IMAGE RECONSTRUCTION AND PROCESSING FOR QUANTITATIVE IMAGING USING STATIONARY DIGITAL TOMOSYNTHESIS

Gongting Wu

A dissertation submitted to the faculty of the University of North Carolina at Chapel Hill in partial fulfillment of the requirements for the degree of Doctor of Philosophy in the Department of Physics and Astronomy.

Chapel Hill
2017

Approved by:

Jianping Lu

Otto Z. Zhou

Yueh Z. Lee

David Lalush

Charles Evans

©2017
Gongting Wu
ALL RIGHTS RESERVED

ABSTRACT

GONGTING WU: Image reconstruction and processing for stationary digital tomosynthesis systems
(Under the direction of Jianping Lu and Otto Zhou)

Digital tomosynthesis (DTS) is an emerging x-ray imaging technique for disease and cancer screening. DTS takes a small number of x-ray projections to generate pseudo-3D images, it has a lower radiation and a lower cost compared to the Computed Tomography (CT) and an improved diagnostic accuracy compared to the 2D radiography. Our research group has developed a carbon nanotube (CNT) based x-ray source. This technology enables packing multiple x-ray sources into one single x-ray source array. Based on this technology, our group built several stationary digital tomosynthesis (s-DTS) systems, which have a faster scanning time and no source motion blur.

One critical step in both tomosynthesis and CT is image reconstruction, which generates a 3D image from the 2D measurement. For tomosynthesis, the conventional reconstruction method runs fast but fails in image quality. A better iterative method exists, however, it is too time-consuming to be used in clinics. The goal of this work is to develop fast iterative image reconstruction algorithm and other image processing techniques for the stationary digital tomosynthesis system, improving the image quality affected by the hardware limitation.

Fast iterative reconstruction algorithm, named adapted fan volume reconstruction (AFVR), was developed for the s-DTS. AFVR is shown to be an order of magnitude faster than the current iterative reconstruction algorithms and produces better images over the classical filtered back projection (FBP) method. AFVR was implemented for the stationary digital breast tomosynthesis system (s-DBT), the stationary digital chest tomosynthesis system (s-DCT) and the stationary intraoral dental tomosynthesis system (s-IOT). Next, scatter correction technique for stationary digital tomosynthesis was investigated. A new algorithm for estimating scatter profile was developed, which has been shown to improve the image quality substantially. Finally, the quantitative imaging was investigated, where the s-DCT system was used to assess the coronary artery calcium score.

ACKNOWLEDGMENTS

This thesis would not be possible without the help and support from many people. First and foremost, I would like to thank my advisor Dr. Jianping Lu and Dr. Otto Zhou for giving me the opportunity to explore the interesting research area of medical imaging. I am deeply grateful for their guidance and encouragement throughout my graduate study. Their enthusiasm and dedication to the research have truly inspired me. Dr.Lu and Dr.Zhou are always happy to discuss research with me and provide helpful insights and guidance. It is a great fortune to have advisors with open doors all the time.

I also greatly appreciate all members of my committee, Dr. Charles Evans, Dr. David Lalush, and Dr. Yueh Z. Lee for their guidance and advice. I would like to give special thanks to Dr. Lee for his insightful and practical guidance and advice to my research. In addition, I would like to thank Dr. Christopher Clemens for his help and encouragement during my research. Many thanks to each member of our research group who has helped me in my projects, including Christina Inscoe, Jing Shan, Jabari Calliste, Allison Hartman, Jiong Wang, Marci Potuzko, Pavel Chtcheprov, Emily Gidcumb, Andrew Tucker, Lei Zhang and Soha Bazyar.

To my collaborators at UNC dental school, XinRay Systems Inc. and XinVivo Inc., including Jing Shan, Brian Gonzales, Andrew Tucker, Laurence Gaalaas, Andre Mol and Enrique Platin, I would like to offer my sincerest thanks for their invaluable discussions. I would also like to thank National Cancer Institute grant (R01 CA134598, R21 HL109832, and R01 HL094740), Lineberger Comprehensive Cancer Center of University of North Carolina at Chapel Hill, UNC School of

Medicine Translational Team Science Award, UNC Graduate School Dissertation Completion Fellowship, and UNC Horizon Award for the funding and support for the research projects.

Finally, I want to thank all my friends and family for their support and encouragement throughout my time in graduate school. Most of all, I am grateful for my parents, Zhongyue Wu and Zhuwei Cao, for their love and unconditional support.

TABLE OF CONTENTS

LIST OF TABLES x

LIST OF FIGURES xi

LIST OF ABBREVIATIONS xvii

Chapter 1: Introduction 1

- 1.1 Dissertation Overview 1
- 1.2 Research Objective 3
- 1.3 Outlines of Dissertation 4
- 1.4 Publications 4

Chapter 2: X-ray Imaging 7

- 2.1 X-ray Interactions with Matters 7
- 2.2 X-ray Attenuation and the Beer–Lambert law 10
- 2.3 X-ray Imaging Modalities 12
- 2.4 Stationary Digital Tomosynthesis 22

Chapter 3: Image Reconstruction 30

- 3.1 System Modelling 30
- 3.2 Analytical Image Reconstruction 35
- 3.3 Algebraic Reconstruction Methods 44
- 3.4 Statistical Iterative Reconstruction 49
- 3.5 Tomosynthesis Reconstruction 56

Chapter 4: Linear Tomosynthesis Image Reconstruction and Processing.................................. 59
4.1 Introduction 59
4.2 Adapted Fan Volume Reconstruction 61
4.3 Projection Model 67
4.4 Evaluation... 75
4.5 s-DCT Reconstruction.. 80
4.6 s-IOT Reconstruction 86
4.7 Discussion and Conclusion 89
4.8 Image Artifacts Reduction 93
4.9 Synthetic Mammography 102
Chapter 5: Scatter Correction for Digital Tomosynthesis.. 112
5.1 Introduction 112
5.2 Method 114
5.3 Results 124
5.4 Discussion 131
5.5 Conclusion... 137
Chapter 6: Assessing Heart Calcium Score Using Stationary Digital Chest Tomosynthesis..... 139
6.1 Introduction 139
6.2 Methods... 141
6.3 Results 145
6.4 Discussion and Conclusion 150
Chapter 7: Summary and Future Direction.. 153
7.1 Summary 153

7.2 Future Direction 154

APPENDIX 157

A.1 Overview of the Reconstruction Software 157

A.2 Key Modules 158

A.3 How to Use the Reconstruction Software 159

A.4 Common Problems and Solutions 159

REFERENCES 163

LIST OF TABLES

Table 3-1: Examples of potential functions and the corresponding weighting function.[83] 52

Table 4-1: Reconstruction time.. 76

Table 4-2: Frequency at 10% MTF.. 78

Table 6-1: Grading table for evaluating the extent of CAD based on the calcium score 141

Table 6-2: Calcification density factor in Agatston score 144

Table 6-3: Calcium scores of heart samples derived from CT and tomosynthesis..................... 149

LIST OF FIGURES

Figure 2-1: the X-ray picture of Röntgen’s wife’s hand. [24] 7

Figure 2-2: Interactions of x-ray. (A) X-ray beam does not interact with the material, (B) Photoelectric absorption and characteristic x-ray, (C) Rayleigh scattering, (D) Compton scattering where recoiled electron is generated. [25] 9

Figure 2-3: Mass attenuation of tissues at different photon energy.[27] 11

Figure 2-4: Schematic diagram of x-ray chest radiography.[29] 13

Figure 2-5: Illustration of the mammogram.[32] 15

Figure 2-6: Digital mammography in (a) CC view and (b) MLO view.[33] 16

Figure 2-7: Third generation axial fan-beam CT geometry.[34] 18

Figure 2-8: Schematic diagram of tomosynthesis. (a) Three projection images with different source projection were acquired. Each projection image is a unique function of the source position and the imaged object or patient. (b) A shift-and-add reconstruction for tomosynthesis. The in-focus plane is obtained by shift each projection image and add together. Features start to show up in the in-focus plane. [5] 20

Figure 2-9: Illustration of DCT.[41] 21

Figure 2-10: Illustration of the field emission. [46] 23

Figure 2-11: Illustration of the CNT nanostructure.[48] 24

Figure 2-12: A schematic diagram of the triode-type field emission x-ray source. Electron emission controlled by the voltage applied to the SWNTs. Electrons accelerate inside the vacuum chamber and x-rays are generated when accelerated electrons hit the copper target.[49] 25

Figure 2-13: (a) A micro-CT system using a CNT-based x-ray source. (b) a desktop microbeam radiation therapy system with CNT-based x-ray sources 26

Figure 2-14: Schematic of stationary digital tomosynthesis using CNT-based x-ray source array. 27

Figure 2-15: (a) A picture of the stationary digital breast tomosynthesis system. The linear source array with CNT-based x-ray sources is retrofitted onto a Hologic Selenia Dimensions tomosynthesis system. 28

Figure 3-1: (a) Line profile of the rectangle function used in pixel basis with the pixel size of 1. (b) a smooth signal that is represented with pixel basis. [57] 33

Figure 3-2: (a) Profile of a blob function. (b) Signal represented with blobs. [57] 33

Figure 3-3: Pixel-driven forward and back projector. [57] 35

Figure 3-4: Schematic illustration of Radon transform.[60] 36

Figure 3-5: (a) Shepp-Logan phantom. (b) The sinogram of the Shepp-Logan phantom. 37

Figure 3-6: Schematic illustration of the Fourier slice theorem. The radon transform $p\theta t$ of a function fx, y is equaled to the line profile of the Fourier transform of the same function at the angle θ.[60] 38

Figure 3-7: Schematic illustration of (a) Pseodopolar fast Fourier transform, (b) iterative reconstruction with constraints based on the Fourier slice theorem.[64] 40

Figure 3-8: A collection of filters used in FBP. [65] 43

Figure 3-9: Principle of the ART method.[73] 47

Figure 3-10: (a) Reference image. Reconstruction images using simultaneous iterative reconstruction technique with 20 iterations (b) at 8 deg angular coverage, (c) at 15 deg angular coverage, (d) at 30 deg angular coverage, (e) at 60 deg angular coverage, (f) at 120 deg angular coverage. 57

Figure 3-11: Patient with pulmonary nodules imaged by (A) chest radiography, (B)-(C) digital chest tomosynthesis, (D) CT.[41] 58

Figure 4-1: (a) Schematic diagram of the s-DBT system. The dots on the linear source array indicates multiple equal-spaced x-ray sources. (b) A picture of the stationary digital breast tomosynthesis system. 62

Figure 4-2: (a) Schematics of the AFVR. The linear source array and each detector row cut the image space into a series of thin slabs. (b) A side view of image space, three fan volumes corresponding to three detector rows are marked in the diagram. 63

Figure 4-3: A flow chart of the AFVR. 66

Figure 4-4: Illustration of two classical ray-driven models: (a) Siddon's algorithm with intersection length, (b) Joseph's linear interpolation method.[93] 68

Figure 4-5: Schematic diagram of (a) 2D distance-driven method, and (b) 3D distance-driven method.[93] 69

Figure 4-6: FBP reconstruction of a head section: reference image, pixel-driven FBP, normalized ray-driven FBP, and distance-driven FBP.[115] 70

Figure 4-7: Iterative reconstruction of a head section using maximum likelihood (ML) algorithm: reference image, pixel-driven ML reconstruction, ray-driven ML reconstruction, and distance-driven ML reconstruction.[115] 71

Figure 4-8: Enlarged view of (a) a Shepp-Logan phantom, AFVR-SIRT reconstruction of the Shepp-Logan phantom (b) using ray-driven projection model, and (c) using the distance-driven projection model. 73

Figure 4-9: Reconstruction slice using (Left) ray-driven projection model, and (Right) distance-driven projection model. 74

Figure 4-10: Line profile of the reconstruction slice using the ray-driven projector and the distance-driven projector 75

Figure 4-11: Normalized MTF curves 77

Figure 4-12: Image of a fatty breast reconstructed by AFVR-SIRT and RTT. 79

Figure 4-13: Reconstructed breast image with carcinoma. 80

Figure 4-14: s-DCT system. 81

Figure 4-15: Reconstruction slices of an anthropomorphic chest phantom using two reconstruction methods. Left: AFVR reconstruction. Right: RTT reconstruction. 83

Figure 4-16: Reconstruction slices of an anthropomorphic chest phantom using two reconstruction methods. Left: AFVR reconstruction. Right: RTT reconstruction. 83

Figure 4-17: Reconstruction slices at 4 different positions of a chest phantom reconstructed by AFVR. 84

Figure 4-18: A reconstruction slice of a patient imaged by s-DCT (a) before correction (b) after correction 85

Figure 4-19: A prototype s-IOT system.[118] 87

Figure 4-20: (a) Conventional dental radiography, (b) and (c) reconstruction slices of tooth phantom imaged by the s-IOT system.[118] 88

Figure 4-21: Tooth phantom imaged by four imaging modalities: standard 2D digital bitewing, standard PSP bitewing, s-IOT, and micro-CT. [118] 89

Figure 4-22: Skin line artifacts in the breast tomosynthesis image. 94

Figure 4-23: Schematic of the skin line artifact reduction method.[119] 95

Figure 4-24: Reconstruction of one 2D fan volume (Top) without the skin line artifact reduction, (Bottom) with the skin line artifact reduction. 96

Figure 4-25: Breast reconstruction slices after the correction. 97

Figure 4-26: A schematic of the truncation artifact reduction method. [119] 98

Figure 4-27: Cross-sectional reconstruction images of a patient's breast (Top) without any correction, (Bottom) with the data truncation correction. 100

Figure 4-28: Reconstruction slices of a patient's breast (a) without any correction, (b) with the data truncation correction.. 101

Figure 4-29: Reconstruction slices of a patient's breast (a) without any correction, (b) with the data truncation correction.. 102

Figure 4-30: Breast segmentation using (a) Otsu's threshold method (b) iterative Otsu's method. 105

Figure 4-31: 2D projection images with and without the density correction. 107

Figure 4-32: (a) Digital mammography image, (b) Synthetic mammography with density correction and contrast enhancement 109

Figure 5-1: Flow chart of the f-SPR scatter estimation method. 119

Figure 5-2: (a) Stationary digital breast tomosynthesis (s-DBT) system with PSD installed. (b) The primary sampling device (PSD) designed for the s-DBT system is placed on the compression paddle. (c) Breast biopsy phantom. (d) BR3D breast imaging phantom. 122

Figure 5-3: Top: scatter profile of the central projection view estimated by (a) SI, (b) ISPR and (c) f-SPR method. The scatter signal outside the phantom is set to be zero to avoid artifact during reconstruction. All scatter profiles are shown in the same display window. Bottom: (d) Line profile of the projection image before scatter correction. The position is indicated by the blue dashed line on the biopsy phantom. (e) Profiles of scatter estimated by different methods along the same line. The SI estimated scatter is very smooth and does not contain any noise. The ISPR estimated scatter though over/under estimates the scatter in the region with object features. The f-SPR estimation captures both the large scale smooth variation and the local fluctuation of the scatter profile. 126

Figure 5-4: (a) Central projection view of the breast biopsy phantom. The index marks seven regions that are used in CR and SDNR analysis. (b) Enlarged views of region 1 and region 2 (from left-to-right: without scatter correction, SI corrected, ISPR corrected, and f-SPR corrected images). (c) The contrast ratio and SDNR for the seven ROIs. Both SI and f-SPR corrected images show a significant improvement in contrast ratio, but only f-SPR shows significant enhancement in SNDR. On average, a 58% increase in CR and 51% increase in SDNR are observed with f-SPR scatter correction method. 127

Figure 5-5: In-focus reconstruction slice of the BR3D feature slab: (a) without scatter correction, (b) with ISPR, (c) with SI, and (d) with f-SPR scatter correction. All images are displayed at the same window width. The window level is set to be the average of the image intensity. Reconstruction with *f*-SPR correction has a significantly better SDNR compared to reconstruction with other scatter correction methods, and a CR comparable to that in the reconstruction with SI correction. 128

Figure 5-6: Top left: in-focus reconstruction slice of two spheroid masses in the BR3D phantom (a) without scatter correction, (b) with ISPR, (c) with SI and (d) with f-SPR scatter correction. Top right: in-focus reconstruction slice of micro-calcifications in the BR3D phantom (a) without scatter correction, (b) with ISPR, (c) with SI and (d) with f-SPR scatter correction. All images are displayed at the same window width. Bottom: CR and SDNR of three spheroid masses. 129

Figure 5-7: Human cadaver imaged by s-DCT. Projection image of the central view (a) without scatter correction, (b) with f-SPR scatter correction. Reconstruction image (c) without scatter correction, (d) with scatter correction. Images before and after f-SPR scatter correction are displayed at the same window width, but different window level, which is set to be the mean gray value of the image. 131

Figure 5-8: Correlation of the scatter profile between the f-SPR estimation and the SI/ISPR estimation. The white line on the scatter map indicates the area that is used to compute the correlation. 133

Figure 5-9: The contrast ratio of (a) mass 1, (b) mass 2, and (c) mass 3. SDNR of (d) mass 1, (e) mass 2, and (f) mass 3. The solid blue line depicts the f-SPR scatter-corrected reconstruction, while the red dashed line depicts the ISPR scatter-corrected reconstruction. The CR and SDNR in the SI scatter-corrected reconstruction are the same as those of the f-SPR with no filtering. The x axis is the standard deviation of the Gaussian filter. 134

Figure 5-10: Left: enlarged view of micro-calcifications in the in-focus reconstruction slice of the BR3D phantom: (a) without scatter correction, (b) with *f*-SPR scatter correction and (c) with direct Gaussian filtering on the SI corrected projection data (*f*-SI). Right: system MTF curve using different processing methods. It is clear that the *f*-SPR method has a negligible impact on the spatial resolution, while direct filtration of the SI corrected image with the same filter size dramatically reduces the spatial resolution.. 135

Figure 6-1: (a) Anatomy of a heart and the coronary artery. (b) A cross-section image of the coronary artery with plaque buildup and a blood clot, which blocks the blood flow inside the heart.. 140

Figure 6-2: An image of the coronary calcification imaged by CTA.[162] 141

Figure 6-3: (a) CT images, and (b) CT numbers of mimic coronary calcifications with different calcium concentrations. 142

Figure 6-4: (a) Stationary digital chest tomosynthesis system developed by our team. (b) Explant heart model with injected calcium simulants. (c) The porcine heart inside an anthropomorphic chest phantom with inflated porcine lung. Unfortunately, the lung was damaged by the butcher and did not stay inflated during the scan. 143

Figure 6-5: Mimic CAC in explant heart model imaged by both s-DCT and CT. Red and yellow circles mark the locations of the CAC. 146

Figure 6-6: Calcium score derived from CT and tomosynthesis images. 147

Figure 6-7: Reconstruction slices of heart samples with the anthropomorphic chest phantom. Mimic CACs are shown in (a), (c) tomosynthesis reconstruction slices, and (b), (d) CT reconstruction slices. 148

Figure 6-8: Calcium scores of the heart samples inside chest phantom derived from CT and tomosynthesis images.. 149

LIST OF ABBREVIATIONS

2D	Two Dimensional
3D	Three Dimensional
AVFR	Adapted Fan Volume Reconstruction
BLOBS	Kaiser-Bessel Basis Functions
BP	Back Projection
CAC	Coronary Artery Calcification
CACS	Coronary Artery Calcium Scores
CC	Cranial Caudal
CG	Conjugate Gradient
CNT	Carbon Nanotube
CR	Contrast Ratio
CPU	Central Processing Unit
CT	Computed Tomography
CTA	Computed Tomography Angiography
CXR	Chest X-ray Radiography
DBT	Digital Breast Tomosynthesis
DCT	Digital Chest Tomosynthesis
DD	Distance-driven
DE	Dual Energy
DICOM	Digital Imaging and Communications in Medicine
DM	Digital Mammography
DTS	Digital Tomosynthesis System

EM	Expectation Maximization
FBP	Filtered Back Projection
FDA	Food and Drug Administration
GPU	Graphics Processing Units
***f*-SPR**	Filtered Scatter-to-primary Ratio
ICD	Iterative Coordinate Descent
ISPR	Interpolated Scatter-to-primary Ratio
LAD	Left Anterior Descending Artery
LCX	Left Circumflex Artery
LM	Left Main Artery
MLO	Mediolateral oblique
MTF	Modulation Transfer Function
OS	Ordered Subs et
PCG	Preconditioned Conjugate Gradient
PD	Pixel-driven
PDA	Posterior Descending Artery
PSD	Primary Sampling Device
RCA	Right Coronary Artery
RD	Ray-driven
ROI	Region of Interest
RTT	Real Time Tomography
s-DBT	Stationary Digital Breast Tomosynthesis
s-DCT	Stationary Digital Chest Tomosynthesis

SDNR	Signal difference to noise ratio
SI	Direct Scatter Interpolation
s-IOT	Stationary Intraoral Tomosynthesis
SIR	Statistical Iterative Reconstruction
SIRT	Simultaneous Iterative Reconstruction Technique
SNR	Signal to noise ratio
SPR	Scatter to primary ratio
TV	Total Variation
UNC	University of North Carolina
WLS	Weighted Least Square

CHAPTER 1: Introduction

1.1 Dissertation Overview

Lung cancer and breast cancer are the two leading causes of cancer death in the United States. Based on a recent study by American Cancer Society, an estimated of 220,000 new cases of lung cancer and 250,000 new cases of breast cancer are diagnosed in 2016, and about 200,000 deaths from breast and lung cancers.[1] For both cancers, early detection is extremely important as it can dramatically reduce the mortality rate.

Currently, two dimensional (2D) x-ray imaging modalities, such as chest radiography and digital mammography, are widely used for non-invasive cancer and disease screening. The 2D x-ray imaging techniques have the advantages of low cost and low radiation dose, therefore they are well suitable for large population disease screening. However, in 2D images, the depth information of the three dimensional (3D) object is missing; structures at different depths overlap on each other, severely degrading the image contrast and cause image artifacts. As a result, the 2D imaging techniques suffer from low diagnostic sensitivity and specificity.

Computed Tomography (CT) was invented to address the drawbacks of 2D x-ray imaging. In CT, hundreds of 2D x-ray measurements are acquired at various imaging angles and are used to compute the 3D image of the object. This completely removes the structure overlapping artifact found in the 2D x-ray image and improves the image contrast. Despite the good image quality, CT is relatively expensive and it exposes high radiation dose to the patient, which increases the risk of radiation-induced cancer especially for pediatric patients.

Digital tomosynthesis (DTS) is another tomographic technique which produces pseudo-3D images at a radiographic dose level. Unlike CT which acquires hundreds of x-ray images, DTS only take a few x-ray projections to compute the 3D image, this results in a much lower radiation dose and a lower-cost system compared to CT. It has been shown that DTS has an improved diagnostic accuracy over the 2D radiography in many clinical applications, including abdominal, breast, chest, dental, musculoskeletal and sinonasal imaging.[2]–[7] Most DTS systems use a single x-ray source and a mechanical moving gantry to shoot X-ray at different imaging positions. This mechanical translating design leads to image blur and slows down the scanning speed which potentially causes more patient motion blur.

Stationary digital tomosynthesis (s-DTS) system eliminates the source motion in the conventional DTS system with a source array consisted of multiple fixed carbon nanotube (CNT) based x-ray sources.[2], [8]–[10] Each CNT source in s-DTS is switched electronically, thus the s-DTS is capable of performing cardiac gated imaging which can significantly reduce the patient motion blur in the cardiac imaging and the pediatric imaging.[11] Previous studies have shown that the s-DTS has improved image resolution as well as faster scanning time compared to the conventional DTS.[8], [10], [12]

Image reconstruction is the process to reconstruct 3D images of the scanned object from 2D x-ray measurement. It is a crucial component in tomosynthesis imaging as the reconstruction algorithm would directly affect the final image quality. Compared to regular CT, DTS suffers from insufficient projection data and data truncation. As a result, classical image reconstruction method, which is based an analytical model and relies on data completeness, does not work well for the tomosynthesis reconstruction.[13]–[16] Statistical iterative reconstruction (SIR), on the other hand, is based on a statistical model and it uses the iterative solver.[17]–[19] Numerous studies have shown that SIR produces better reconstruction images over the classical filtered back projection (FBP) algorithm.[13], [20]–[22] However, SIR is computationally expensive. The reconstruction could take several hours, and it is not practical in a clinical setting.

In this dissertation, a fast iterative image reconstruction algorithm, named adapted fan volume reconstruction, for linear tomosynthesis systems will be proposed. The image artifact reduction methods and the synthetic mammography technique will be discussed. Next, a measurement-based scatter correction algorithm will be introduced. The feasibility of assessing heart calcium score using stationary digital chest tomosynthesis (s-DCT) will be investigated.

1.2 Research Objective

1.2.1 Iterative Reconstruction for s-DTS

In this aim, a fast iterative reconstruction algorithm, named adapted fan volume reconstruction (AFVR), was developed to reconstruct s-DTS images with linear source array. A comparison study was performed to investigate the reconstruction image quality of the proposed AFVR and the classical FBP algorithm. In addition, two different forward projectors were investigated and image processing techniques for image artifacts reduction were implemented. Furthermore, the AFVR was implemented on three s-DTS system: the s-DBT, the s-DCT, and the stationary intraoral dental tomosynthesis (s-IOT) system. Finally, the method for generating synthetic mammography was investigated.

1.2.2 Scatter Correction

A measurement-based scatter correction method for DTS was developed. This work includes two parts: the hardware development of the primary sampling device (PSD) and the scatter correction algorithm development for scatter estimation and compensation. The scatter correction method was evaluated on the s-DBT system using breast phantom, and it was also implemented on the s-DCT system to remove scatter in human cadaver images.

1.2.3 Quantitative Tomosynthesis Imaging

In this phase, the feasibility of assessing heart calcium score using the s-DCT system was studied. A heart model was developed, and imaged by both CT and s-DCT ex vivo. The calcium score metric for chest tomosynthesis was then developed, and the correlation between CT-derived calcium score and the tomosynthesis-derived calcium score was studied.

1.3 Outlines of Dissertation

This dissertation is organized in the following order: (1) background of tomosynthesis imaging, (2) iterative reconstruction for tomosynthesis, (3) measurement-based scatter correction algorithm, (4) quantitative tomosynthesis imaging. Chapter 2 introduces the underlying principles of x-ray imaging, the DTS and s-DTS. Chapter 3 provides the mathematical foundation of image reconstruction. In Chapter 4, a fast iterative reconstruction algorithm for s-DTS is reported. Chapter 5 investigates the scatter correction methods for s-DTS and reports the filtered scatter-to-primary ratio (*f*-SPR) scatter estimation. Chapter 6 studies the feasibility of assessing calcium score using s-DCT. Finally, in Chapter 7, the dissertation is summarized and the future direction of the research is discussed.

1.4 Publications

Certain results of this thesis have previously been published as:

- C. R. Inscoe, G. Wu, *at el* (2017)

  Stationary intraoral tomosynthesis for dental imaging.

- C. Puett, J. Calliste, G. Wu, *at el* (2017)

  Contrast enhanced imaging with a stationary digital breast tomosynthesis system.

- J. Calliste, G. Wu, *at el* (2016)

  A new generation of stationary digital breast tomosynthesis system with wider angular span and faster scanning time.

- J. L. Goralski, A. Hartman, G. Wu, *at el* (2016)

  Digital chest tomosynthesis as a novel method for 3d lung imaging.

- Y. Z. Lee, J. L. Goralski, A. Hartman, G. Wu, *at el* (2016)

  Stationary digital chest tomosynthesis of cystic fibrosis.

- A. E. Hartman, J. Shan, G. Wu, *at el* (2016)

  Initial clinical evaluation of stationary digital chest tomosynthesis.

- G. Wu, *at el* (2016)

  Stationary digital chest tomosynthesis for coronary artery calcium scoring.

- C. R. Inscoe, G. Wu, *at el* (2015)

  Low dose scatter correction for digital chest tomosynthesis.

- J. Shan, A. Tucker, L. R. Gaalaas, G. Wu, *at el* (2015)

  Stationary intraoral digital tomosynthesis using a carbon nanotube X-ray source array.

- J. Shan, L. Burk, G. Wu, *at el* (2015)

  Prospective gated chest tomosynthesis using CNT X-ray source array

- G. Wu, *at el* (2015)

Adapted fan-beam volume reconstruction for stationary digital breast tomosynthesis.

Parts of the work presented in the thesis has resulted in the following patent applications:

- Digital tomosynthesis systems, methods, and computer readable media for intraoral dental tomosynthesis imaging”

  U.S. Patent: 15/205,787. Filing on Jul 8, 2016.
- Intraoral tomosynthesis systems, methods, and computer readable media for dental imaging

  U.S. Patent: 14/741,041. Filing on Jun 16, 2015.

CHAPTER 2: X-ray Imaging

2.1 X-ray Interactions with Matters

X-ray is discovered by German physicist Wilhelm Röntgen, who studied the Crooks tubes and noticed a green glow on a nearby fluorescent screen even though the tube was wrapped by black cardboards. Röntgen realized that it must be due to some invisible rays generated from the Crooks tube, and he referred the rays as “X-rays” to indicate the unknown type of this radiation. Röntgen also took a picture of his wife’s hand on a photographic plate using x-ray (Figure 2-1), which became the first medical use of x-ray. [23]

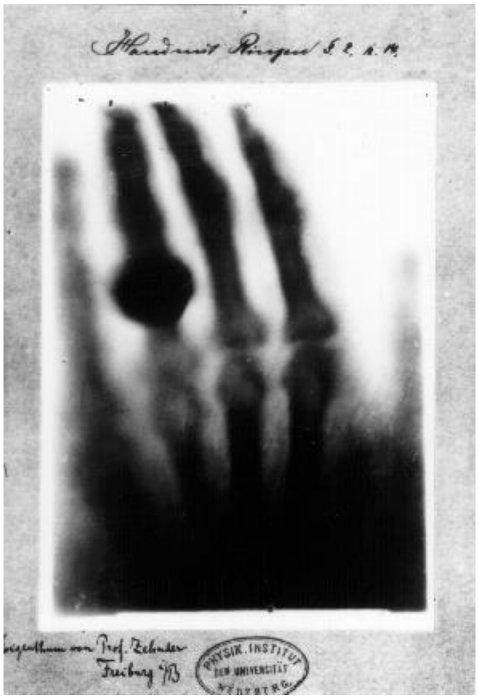

Figure 2-1: the X-ray picture of Röntgen’s wife’s hand. [24]

As we now understand, x-rays are a form of electromagnetic radiation similar to visible light. The difference between x-ray and visible light is that x-ray has a much smaller wavelength that ranges from 0.1 pm to 10 nm, corresponding to an energy level from 100 eV to 10 MeV. The smaller wavelength and higher energy of x-rays give it the ability to penetrate through most materials. This ability, however, does not come without any cost. The x-ray interacts with the matters while it penetrates through, and these interactions weaken the x-ray intensity until finally, it reaches zero. In medical imaging, the three major types of interactions between x-ray and matters are (1) Photoelectric absorption, (2) Compton scattering, and (3) Rayleigh scattering. These interactions are illustrated in Figure 2-2.[25] Here, we briefly introduce the three major x-ray interactions as they directly contribute to the contrast in x-ray imaging.

2.1.1 Photoelectric Absorption

In Photoelectric absorption, an electron of the atom is freed by the incident x-ray photon, and be emitted from the atom. (Figure 2-2B) The difference between the incident photon energy and the binding energy of the electron becomes the kinetic energy of the emitted electron, which is also called photoelectron. When the emitted electron is at a low state, electrons at high energy state will jump to this lower state, resulting the characteristic x-ray with energy equals to the energy difference between the two states.

Approximately, the occurrence rate of photoelectric absorption is proportional to Z^3/E^3, where Z is the atomic number of the material and E is the energy of the incident x-ray photon.[26] When the photon energy is low, the photoelectric absorption is more likely to occur. In fact, the photoelectric absorption is the dominant interaction for low-energy x-ray. At the same time, heavy atoms (high Z value) would have a higher probability of having photoelectric absorption, therefore they attenuate x-ray more than the light atoms. Photoelectric absorption is generally considered as harmful to the human body, as it ironizes the atoms and could potentially breaks the molecular bonds of DNA and proteins.

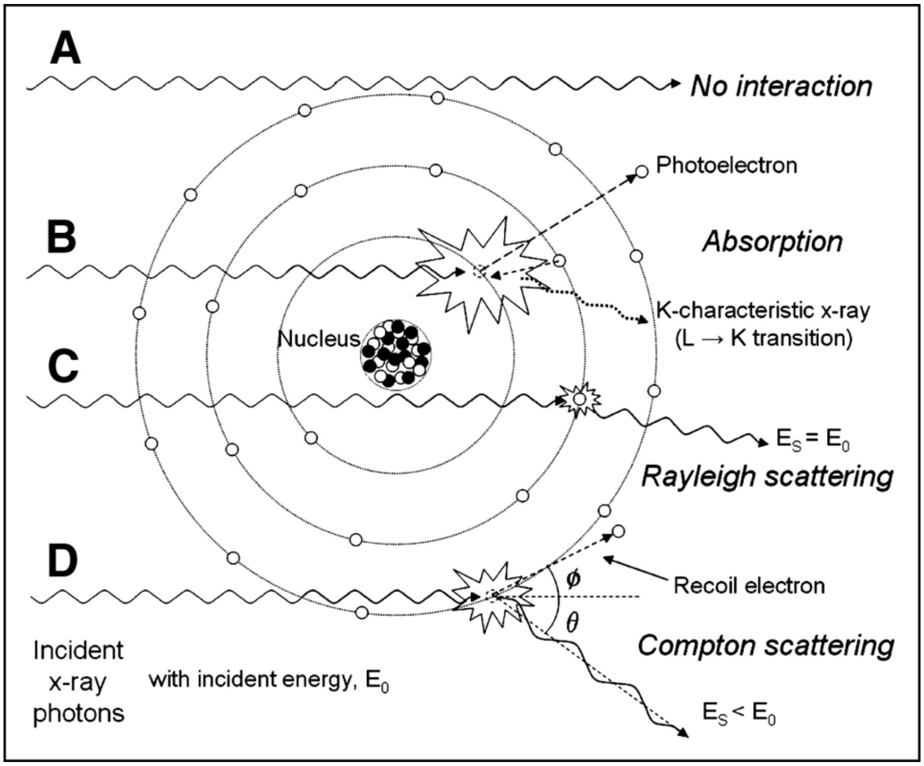
A
No interaction
Photoelectron
B
Absorption
K-characteristic x-ray
(L → K transition)
Nucleus
C
$E_S = E_0$
Rayleigh scattering
D
ϕ
Recoil electron
θ
Compton scattering
Incident
x-ray
photons
with incident energy, E_0
$E_S < E_0$

Figure 2-2: Interactions of x-ray. (A) X-ray beam does not interact with the material, (B) Photoelectric absorption and characteristic x-ray, (C) Rayleigh scattering, (D) Compton scattering where recoiled electron is generated. [25]

2.1.2 Compton Scattering

Compton scattering is the predominant interaction in the diagnostic energy range with soft tissue, it is illustrated in Figure 2-2. In Compton scattering, the incident photon transfers a portion of its energy to the electron, which causes a recoil and removal of the electron, the incident photon will change direction after the interaction. However, the total energy and momentum are conserved in this process. Compton scattering ionizes the tissue and contributes to the radiation dose to the patient. The probability of Compton scattering depends on the photon energy. For energy between 10 keV and 100 keV, the probability is approximately proportional to $Z \cdot E$; while at high energy

(> 100 keV), the probability is approximately proportional to Z/E.[25] As shown in Figure 2-3, Compton scattering consists the majority of scatter radiation, which is an important issue for diagnostic imaging as it reduces the image contrast and causes artifacts.

2.1.3 Rayleigh Scattering

In Rayleigh scattering, the incident photon temporarily excites an electron without freeing it from the atom. When the electron returns to its original state, it emits an x-ray photon with the same energy but a different direction of the incident photon. This process is also known as coherent or elastic scattering, where the photon energy does not change. Rayleigh scattering does not transfer the energy of x-ray photon to the material, therefore, it does not contribute to patient radiation dose. However, Rayleigh scattering is an important issue for x-ray imaging as it can be up to 20% of the scattering. The probability of the Rayleigh scattering is approximately proportional to Z^2/E^2, therefore, it is more likely to occur with low energy x-ray photons and high Z materials.[25]

2.2 X-ray Attenuation and the Beer–Lambert law

The interactions of x-ray with matters have a combined effect of attenuating the x-ray intensity, this relationship is experimentally determined and it can be approximated as:

$$\Delta I/I = -\mu \Delta x, \tag{2-1}$$

where I is the ray intensity, ΔI is the change of the intensity, μ is the linear attenuation coefficient, and Δx is the distance the ray travels. This model indicates that the percentage change of the ray intensity is proportional to a coefficient times the distance the ray travels. The mass attenuation coefficient is a function of the photon energy and the material composition, although most of the time, it is considered to only depends on the material composition. Figure 2-3 illustrates the relationship between the mass attenuation and the x-ray photon energy, and the contributions on the attenuation from different x-ray interactions.[27] For the x-ray used in medical imaging (30 keV – 120 keV), the major mass attenuation comes from the Compton scatter.

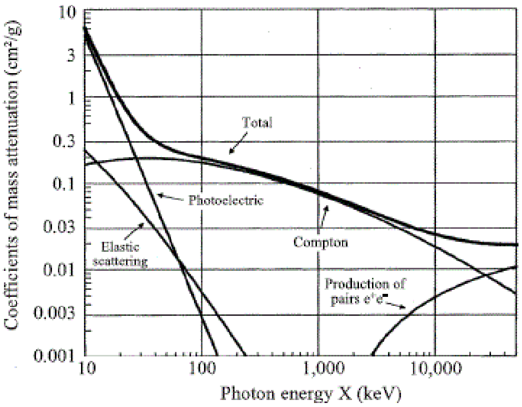

Figure 2-3: Mass attenuation of tissues at different photon energy.[27]

The relationship described by Equation 2-1 is often written in an integral format:

$$\boldsymbol{I = I_0 e^{-\sum_i \mu_i x_i}}, \tag{2-2}$$

where I is the x-ray intensity after it leaves the medium, I_0 is the ray intensity before the x-ray enters the medium and interacts with the matters, μ_i is the mass attenuation within the medium i, and x_i is the distance the ray travels within medium i. This exponential decay relationship is also referred as Beer–Lambert law, and will be used to model the image reconstruction problem. The linear attenuation coefficient μ is a function of the interacted material and the x-ray energy spectrum, this forms the physics foundation of many x-ray imaging modalities.

2.3 X-ray Imaging Modalities

An x-ray image measures the interactions of x-ray and matters. The most widely used x-ray image is the attenuation image, where the x-ray photons that leave the materials after being attenuated are recorded. As the x-ray attenuation depends on the atomic number of the material, the attenuation value can differentiate/visualize materials with different densities. Besides attenuation, other physical effects, such as characteristic x-ray emission and scatter interactions, are also utilized to develop imaging techniques, such as x-ray spectroscopy, x-ray crystallography and x-ray scatter imaging. In this study, we will only focus on the x-ray attenuation imaging techniques used in medical applications.

2.3.1 Radiography

Radiography is probably the oldest x-ray imaging technique, which is discovered along with x-ray. In x-ray radiography, the patient is illuminated by a short x-ray pulse, and the x-ray photons exit patient are recorded in a 2D image. Due to the simplicity of the imaging system and the low cost, radiography is widely used in many medical applications, such as screening lung and heart diseases in chest imaging, diagnosing abdominal diseases, detecting gallstones or kidney stones, detecting bone fractures as well as tooth cavities. Radiography image is originally recorded on photographic films.

Based on the image receptor, radiography can be classified into three types: conventional radiography with photographic film, computed radiography which uses imaging cassette and later scans the cassette to produce digital images, and digital radiography which directly produces digital images with a digital detector. Nowadays, the conventional film and the imaging cassette are replaced by the digital detector for better transferring and storing patient data. In addition to those benefits, the digital detector also has a high radiation dose efficiency and it lowers the radiation dose delivered to the patients.[28] The image post-processing and computer aided diagnosis also become much easier on digital images.

One of the most common uses of x-ray radiography is in chest imaging for patients with known or suspected lung diseases. The chest x-ray radiography (CXR) often acquire multiple views images with each view obtained at different orientations of the chest and the x-ray beam directions. Common CXR views include posteroanterior view, anteroposterior view, and lateral view. As CXR only produces 2D images, multi-view radiographic images can help to visualize features at various positions inside the patient's body. A schematic diagram of the CXR is shown in Figure 2-4. [28]

Based on the characteristics of x-ray attenuation, the higher energy of the x-ray, the fewer interactions the x-ray would have with materials. Thus, high energy x-ray photons are much easier to penetrate through the human body, however, they would have a lower sensitivity on differentiating different organs due to fewer interactions. CXR typical uses an x-ray source operated at 120 kVp, which is optimized to balance body penetration as well as tissue contrast.

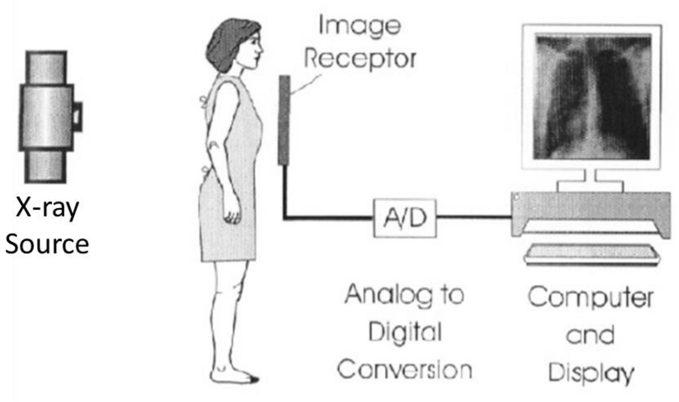

Figure 2-4: Schematic diagram of x-ray chest radiography.[28]

Although digital radiography works well on high contrast organs, it has poor contrast on soft tissues. The main reason lies in the imaging mechanism, in which radiography projects the 3D object onto a 2D detector and the depth information of that object is lost in the radiographic image. As a result, features, such as different organs, overlap each other on the radiographic images, which blurs the images and reduces the contrast, making it harder to identify diseases and extract useful diagnostic information.

2.3.2 Mammography

Mammography is another 2D radiographic imaging technique. Unlike radiography which is used in various different applications, mammography is only used for breast imaging and it has a unique system design optimized for this specific goal. Originally, like radiography, mammography is recorded on the photographic film. Currently, the conventional film is replaced by the digital detector. Equipped with a digital detector, the name of the imaging technology changes digital mammography (DM). A mammography exam, often called a mammogram, aids in the early detection and diagnosis of breast diseases in women. It has been shown that mammogram is effective in screening breast cancer and reducing the mortality rate of the breast cancer.[29], [30] In fact, the American College of Radiology recommend screening mammography every year for women, beginning at age 40.

As breast consists mostly of the soft tissue, the x-ray source used in digital mammography has a much softer energy spectrum with the mean energy typically around 35 kVp, compared to that of most digital radiography systems. The soft x-ray provides a better contrast of the soft tissue in the breast, however, it would more likely to be absorbed/scattered by the breast and harder to reach to the detector. Modern DM system uses automatic exposure control (AEC) to apply customized x-rays for different patients. For example, for patients with thick breast, a longer pulse of higher energy x-rays would be generated to image breast. In DM, there is compression paddle that compresses and fixes the breast on the detector during the scan. The compression paddle not only reduce the motion artifact, but it also measures the thickness of the breast which is used by AEC to determine the source energy and exposure time for the specific patient. An illustration of the mammogram is shown in Figure 2-5.[31]

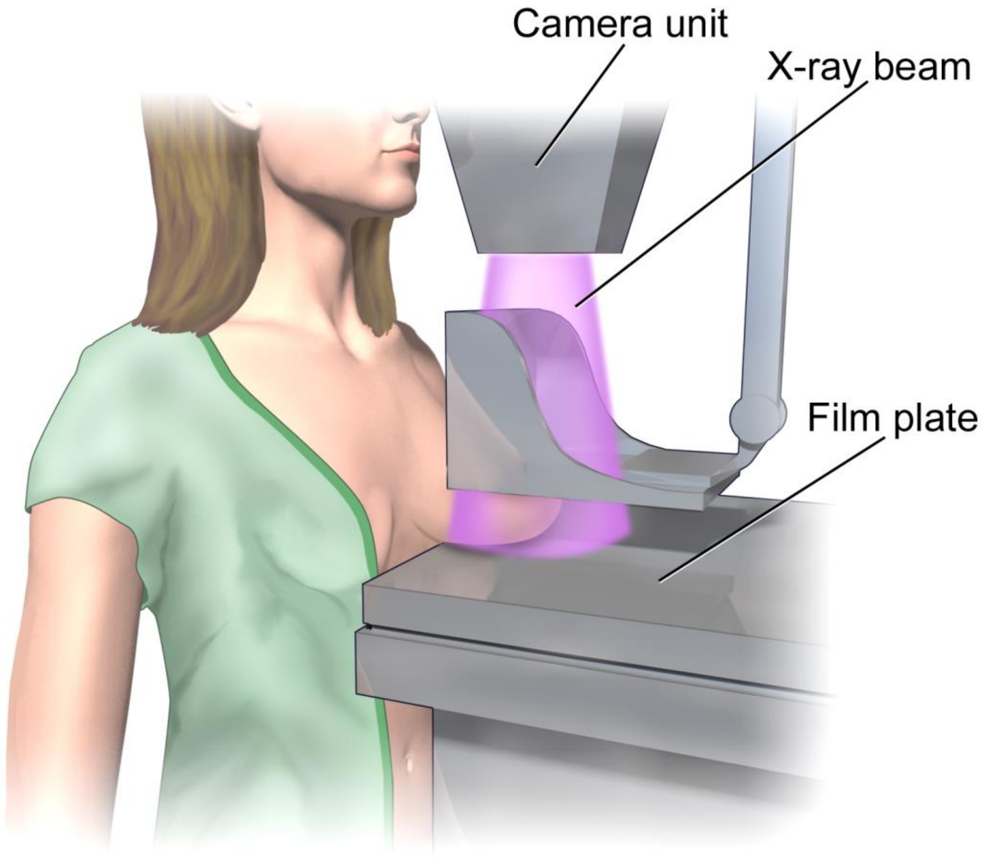

Figure 2-5: Illustration of the mammogram.[31]

DM uses a high-resolution detector with a pixel size around or smaller than 100 μm, to visualize small features such as microcalcifications which are an early sign of breast cancer. Normally, a mammography exam includes two-view images: one cranial caudal (CC) view, and one mediolateral oblique (MLO) view. CC view is the top-down view, where the x-ray is fired right above the patient. CC view clearly depicts the entire breast including the nipple, the fat and the fibro-glandular tissue. MLO view images breast from the center of chest outward to the side, it gives the best lateral view of the breast where pathological changes are most likely to occur. Examples of CC view and MLO view mammography images are shown in Figure 2-6.[32]

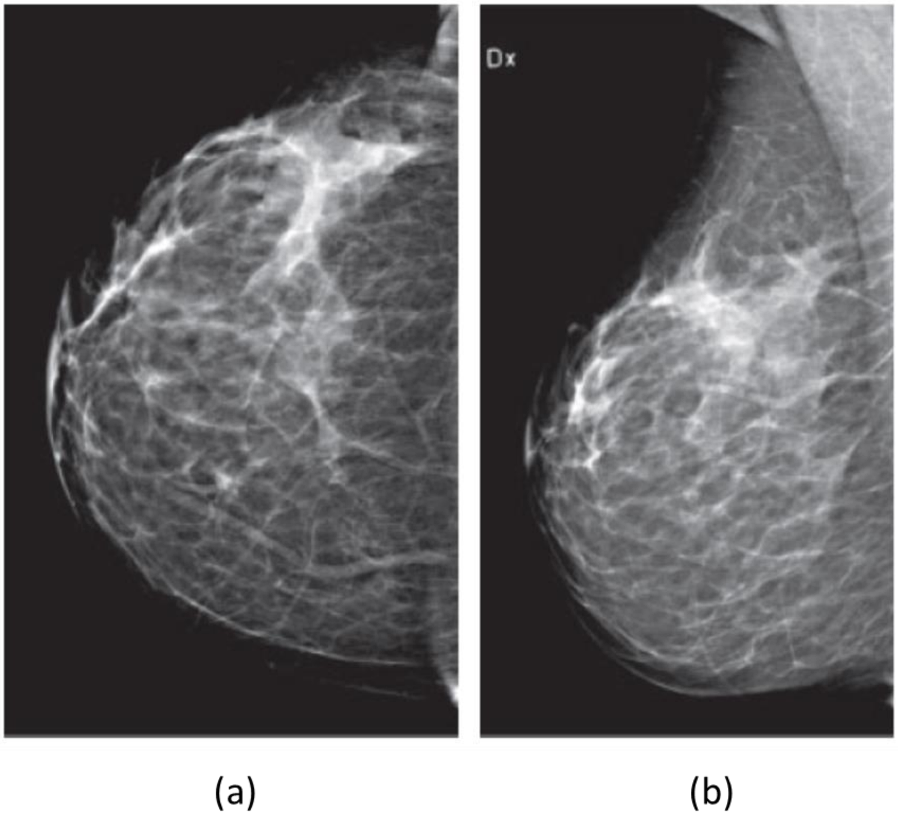

Figure 2-6: Digital mammography in (a) CC view and (b) MLO view.[32]

2.3.3 Computed Tomography

Computed tomography (CT) was invented in the 1970s by Godfrey Hounsfield and Allan Cormack. The basic idea of CT is using multiple 2D radiography images acquired at different angles to estimate the 3D attenuation map of the object. Driven by the clinical demands, the system design of CT has been evolving ever since its invention. The first generation CT system uses parallel beam design, it is soon being replaced by fan beam x-ray radiation for faster scanning speed. The initial axial imaging scheme is replaced by a helical or spiral scan for the purpose of scan the entire organs in a single breath hold. Later, the cone beam CT is developed to achieve isotropic spatial resolution and an even faster scanning speed. Despite different system designs, a typical CT system has one x-ray source tube mounted on a mechanical moving gantry and a digital detector that measures the x-ray radiation. The x-ray source rotates and fires x-rays at different spatial positions, the detector moves together with the source and measures the x-ray radiation for each shoot. Each x-ray shoot forms a projection image in the CT exam, the x-ray source typically moves between 180 to 360 deg around the object and it generates hundreds of projection images during one scan. The projection images are then transferred to a computer, and a specific computer software computes the 3D attenuation images of the object based on the projection images as well as the imaging geometry for each projection. This process is also called image reconstruction, which will be intensively discussed in Chapter 3 and Chapter 4. A schematic diagram for a fan-beam axial CT is shown in Figure 2-7.[33]

In CT images, the image brightness, or image intensity, represents the linear attenuation, and the difference in the x-ray attenuation creates the contrast between different materials. The linear attenuation has a physical unit of cm^{-1}. It is normally not necessary to record the exact value of the attenuation which would cost extra storage space, and it is also not convenient to interpret diagnostic information using a float number. Thus, in CT, the linear attenuation is truncated and converted to an integer with a special unit called Hounsfield unit (HU), or CT number. The conversion from cm^{-1} to HU is:

$$\mu(in\ HU) = 1000 \cdot \frac{\mu - \mu_{water}}{\mu_{water} - \mu_{air}}, \tag{2-3}$$

where μ_{water} and μ_{air} are the linear attenuation of water and air, respectively. The CT images are typically stored as a 16 bit image in the Digital Imaging and Communications in Medicine (DICOM) format. The HU is converted to non-negative integer for storage and transfer, the conversion parameters are stored in the image header, or DICOM header.

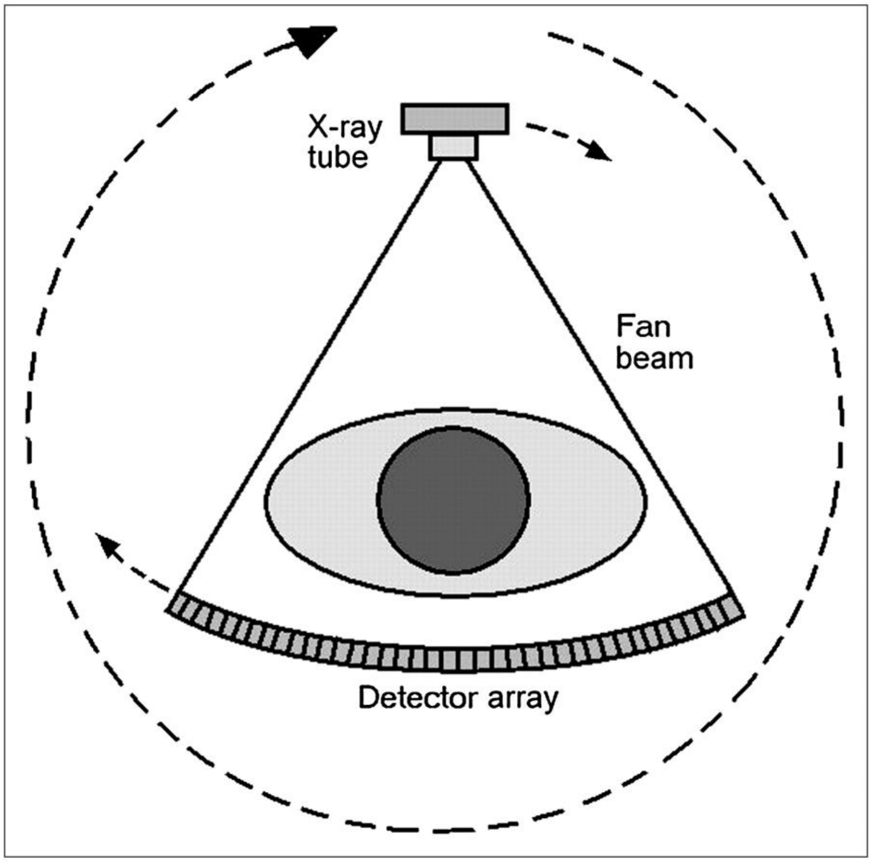

Figure 2-7: Third generation axial fan-beam CT geometry.[33]

CT produces 3D images of the patient anatomy with no tissue overlapping artifact, this dramatically improves the image contrast and consequently the diagnostic accuracy over the conventional radiography. However, due to the large numbers of projection images acquired, CT delivers a significant amount of radiation dose to the patient, which is about 100 times the radiographic dose. This increases the risk of radiation-induced cancer, especially for pediatric patients. In addition, the complex system design of CT raises the cost of the CT exam. Recent studies on advanced image reconstruction algorithms showed promising results in reducing the radiation dose of CT, however, the diagnostic accuracy of those techniques are still the subject of debate and more investigations need to be performed before the dose can be reduced clinically.[18], [34]–[36] In summary, although CT has many successful medical applications, it is not a good choice for disease screening in the general public, and low dose 3D imaging modalities are still needed.

2.3.4 Digital Tomosynthesis

Digital tomosynthesis (DTS) is another tomographic imaging technique. Similar to CT, DTS also produces 3D images from multiple projections acquired during one scan. However, DTS only acquires a few projection images, which is only a fraction of the projection images in CT, within a much smaller angular coverage. This imaging mechanism simplifies the system design, as a result, DTS has lower cost over CT and it delivers a radiographic dose level radiation dose to the patient. A schematic diagram of tomosynthesis is illustrated in Figure 2-8(a), where three projection images are acquired at different source position. Figure 2-8(b) demonstrate the principle of the 3D tomosynthesis. In single x-ray projection image, features in various depths of the imaged object overlap each other. By shift-and-add multiple projection images with different imaging geometries, in-focus planes with different features will be obtained and the overlapping artifact is substantially reduced.

The most well-known application of DTS is breast imaging, where the DTS system is called digital breast tomosynthesis (DBT), or 3D mammography. In breast cancer screening, an abnormal dense tissue called mass or lesion and the small micro-calcification are generally used as markers for early breast cancer. The lesion typically has a low contrast, when it overlaps with other normal tissues in the 2D mammography, its contrast further reduces. As a result, the call back rate is quite high for digital mammography as doctors cannot tell whether the suspected lesion truly exist. DBT has been demonstrated to significantly improve the contrast of the lesion by reducing the overlapping artifact with the 3D images.[3], [32], [37], [38] For microcalcifications, however, the digital mammography performs better than DBT as the source motion in DBT blurs the small calcifications.[4], [39] As a result, DBT is FDA-approved to be used together with DM for breast cancer screening, where DBT is used for confirming lesions and DM is used for visualizing micro-calcifications. Some DBT systems, such as the SenoClaire 3D Breast Tomosynthesis manufactured by GE Healthcare, use step-and-shoot imaging to reduce the source motion artifact. However, this also increases the scanning time, which potentially introduces more patient motion, as well as the patient discomfort.

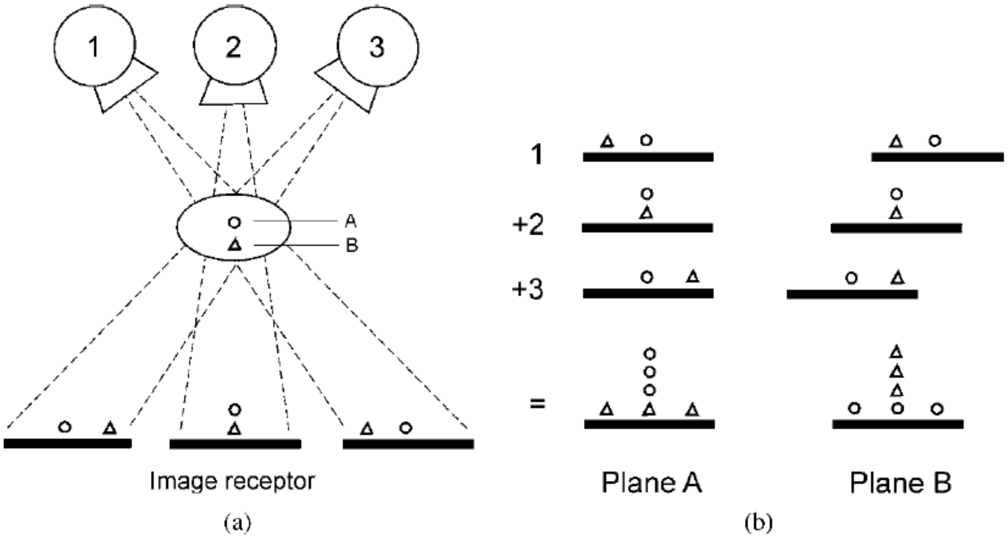

Figure 2-8: Schematic diagram of tomosynthesis. (a) Three projection images with different source projection were acquired. Each projection image is a unique function of the source position and the imaged object or patient. (b) A shift-and-add reconstruction for tomosynthesis. The in-focus plane is obtained by shift each projection image and add together. Features start to show up in the in-focus plane. [5]

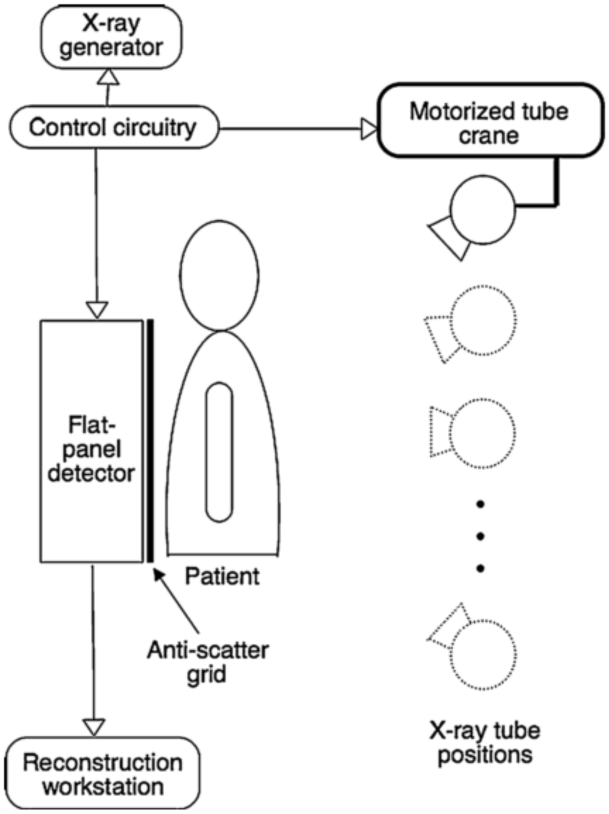
X-ray generator
Control circuitry
Motorized tube crane
Flat-panel detector
Patient
Anti-scatter grid
X-ray tube positions
Reconstruction workstation

Figure 2-9: Illustration of DCT.[40]

Another important application for DTS is chest imaging, in which the DTS is called digital chest tomosynthesis (DCT). The basic principle of DCT is similar to DBT. As illustrated in Figure 2-9,[40] DCT consists an x-ray source mounted on the moving gantry, a digital detector and the control electronics. The gantry moves the source to various projections and multiple projection images are acquired. The difference between DCT and DBT are in the system design, where harder x-rays, larger angular span, and more projection images are used in DCT. For chest imaging, the most challenging task is the detection of pulmonary nodules, which are strongly related to the lung cancer.[41] Due to the severe tissue overlapping in chest imaging, chest x-ray radiography (CXR) has poor diagnostic accuracy on small nodules. DCT has demonstrated to dramatically improve the diagnostic accuracy of lung nodules over CXR with a comparable sensitivity as CT for large lung nodules.[41]–[43]

The 3D tomosynthesis images reduce the overlapping artifact and lead to higher diagnostic accuracy over the 2D radiography in many applications. However, DTS has many challenges as well. First, the limited angular coverage and the small projection images in DTS are mathematically not sufficient to restore the full 3D information of the imaged object. As a result, tomosynthesis images have a poor depth resolution, lower contrast and move artifacts over CT. Secondly, the mechanical moving gantry slows down the scanning speed and introduces two types of motion artifact. First, the rotating source introduces motion blur to the projection image, which in terms adversely affect the image resolution and the diagnostic accuracy for small features. For example, DBT suffers from the source motion blur and performs worse than 2D mammography in detecting microcalcifications. Another type of motion artifact is the indirect patient motion artifact caused by long scanning time. In fact, the patient motion blur, including heart beats and respiration, is the most destructive image artifact for chest imaging.

2.4 Stationary Digital Tomosynthesis

2.2.1 Field Emission Effect

Field emission, also known as field electron emission, is the emission of electron induced by an external electric field. Field emission is first observed in eighteen centuries, but not until 1928 has the effect been fully explained and understood using quantum tunneling.[44] In field emission, the external electric field lowers the effective barrier and increases the probability that electrons tunnel through. An illustration of the field emission effect is shown in Figure 2-10.[45] The emission current is determined by the Fowler-Nordheim equation:

$$I = aV^2 \exp\left(\frac{-b\phi^3}{\beta V}\right), \tag{2-4}$$

where a, b are two constants, and I, V, ϕ, β are the emission current, voltage of the applied field, work function, and field enhancement factor, respectively.

An important application of field emission is making field electron emitters or electron gun source. Traditionally, electrons are generated based on thermal electron emission, where electrons are emitted when the metallic emitter is heated up to a high temperature. However, the field emission only requires external electric field and it has no requirement of the temperature. Hence, field emission is often called "cold emission" or "cold cathode emission", and the electron generated from field emission is often all "cold electrons".

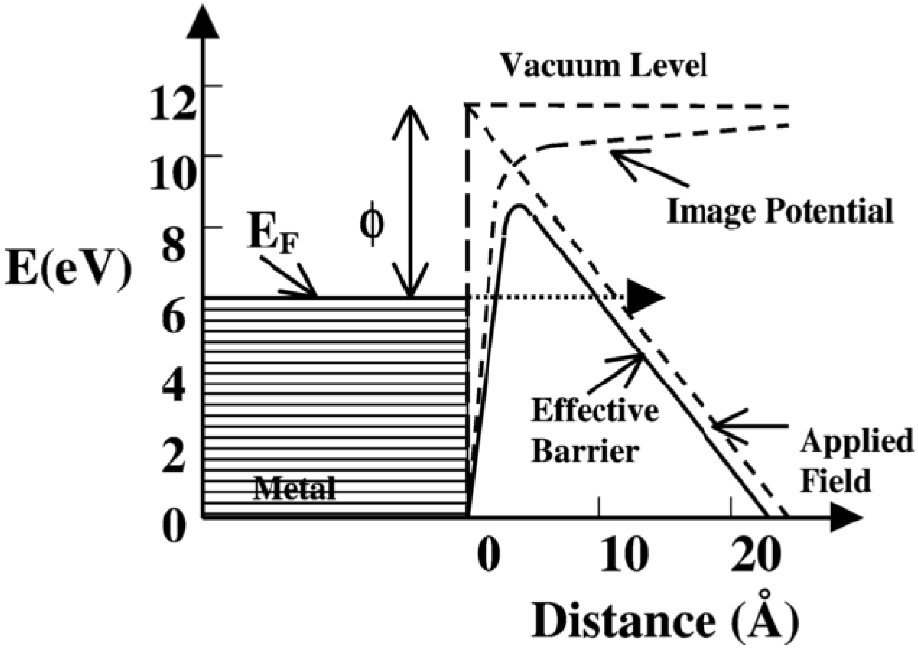

Figure 2-10: Illustration of the field emission. [45]

2.2.2 CNT Field Emitter

A carbon nanotube is a material with cylindrical nanostructure made of graphene. It is first synthesized on 1991 by Sumio Iijima using the arc discharge method, which generated unprecedented interest in the CNT and opened a new era of nanotechnology.[46] Figure 2-11 illustrates the nanostructure of a single wall CNT.[47] Based on the number of layers, CNT can be categorized as single-walled nanotubes (SWNTs) or multi-walled nanotubes (MWNTs). The diameter varies between SWNTs and MWNTs. The diameter for SWNTs ranges from 0.4 nm to 10 nm, while those of MWNTs are much larger, which ranges from 2 nm to over 100 nm. Depends on the nanostructure or the ways that CNT is created, CNT can have a variety of mechanical, optical and electrical properties, leading to wide applications including medical implant, semiconductors, batteries and more.[47]

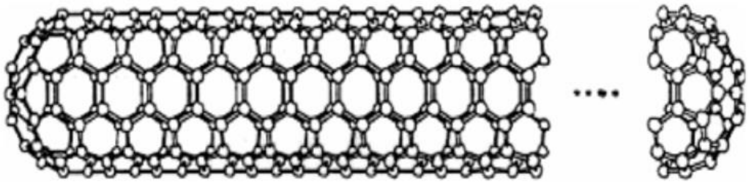

Figure 2-11: Illustration of the CNT nanostructure.[47]

CNT has been extensively studied as a field emitter. The main reason is that CNT has a high aspect ratio, which allows the electron tunneling the energy barrier more easily and makes the field emission to be naturally enhanced. CNT field emitter presents many advantages over thermionic emission. First, CNT field emitters do not require heating to generate electron, which is more energy efficient and produces more stable electron focusing. The cold nature of field emission also simplifies the cooling system design. Secondly, CNT field emitter could be electronically switched on and off, which is faster than the thermionic emitter and eliminates the need of a mechanical shutter. Finally, the CNT field emitter has more compact design over the thermionic emitter, and theoretically generate less outgassing which would contaminate the vacuum chamber.

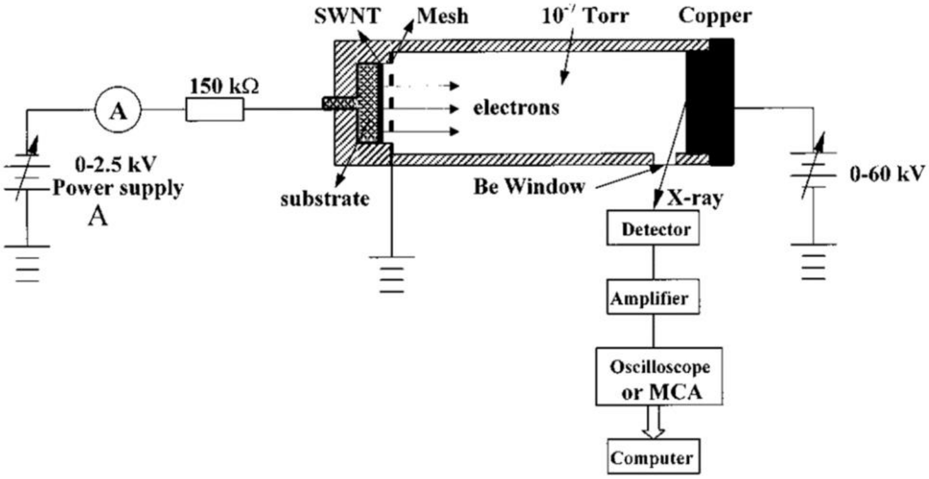
SWNT
Mesh
10⁻⁷ Torr
Copper
150 kΩ
A
electrons
0-2.5 kV
Power supply
A
substrate
Be Window
X-ray
0-60 kV
Detector
Amplifier
Oscilloscope
or MCA
Computer

Figure 2-12: A schematic diagram of the triode-type field emission x-ray source. Electron emission controlled by the voltage applied to the SWNTs. Electrons accelerate inside the vacuum chamber and x-rays are generated when accelerated electrons hit the copper target.[48]

Our lab developed the first CNT-based x-ray source using a cold cathode made of SWNTs.[48] A systematic diagram of the first CNT-based radiography system is shown in Figure 2-12. The source target was made of copper, and the anode voltage was set to be 14 kV. The whole assembling was sealed inside a vacuum chamber. Over the past decade, our lab has developed several CNT-based x-ray source and source array with various source voltage, focal spot size, and tube output for different applications, including micro-CT system,[49]–[51] microbeam radiotherapy system,[52], [53] stationary CT system,[54] stationary digital breast tomosynthesis system,[9], [10], [55] stationary digital chest tomosynthesis system and the stationary intraoral tomosynthesis system.[2], [8] Figure 2-13(a) shows a micro-CT system using a CNT-based x-ray source, and Figure 2-13(b) shows a desktop microbeam radiotherapy system using CNT-based x-ray sources.

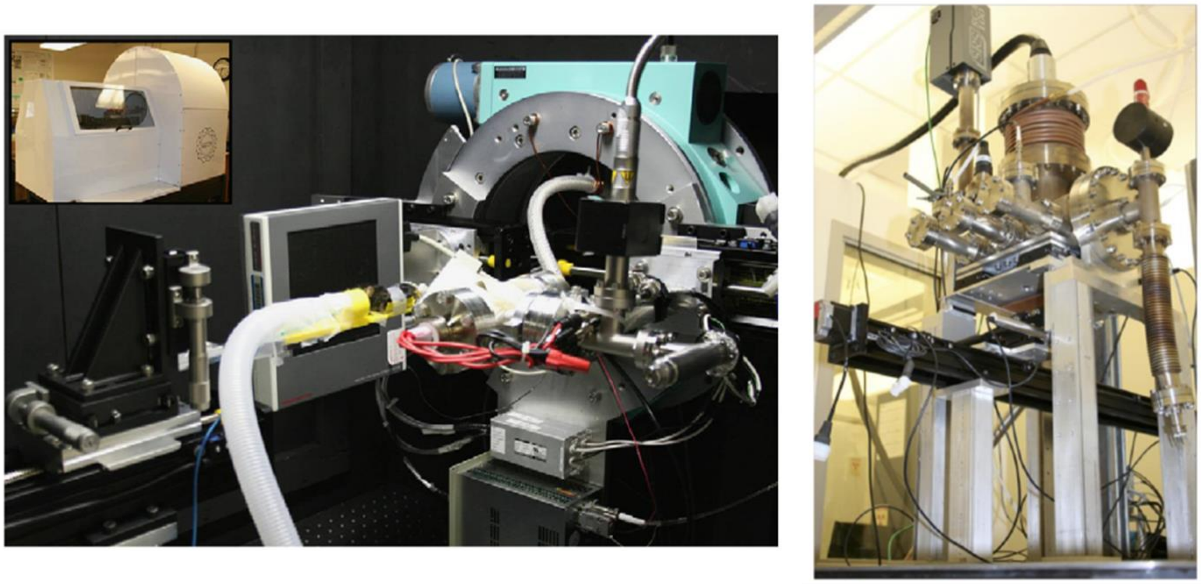

(a) (b)

Figure 2-13: (a) A micro-CT system using a CNT-based x-ray source. (b) a desktop microbeam radiation therapy system with CNT-based x-ray sources.

2.2.3 Stationary Digital Tomosynthesis

As mentioned previously, the mechanical translating gantry used in DTS has several drawbacks, it slows down the scanning speed and introduces source motion blur. Based on the field emission technique, our lab developed a stationary digital tomosynthesis (s-DTS) technology, where the sources stay stationary during the scan. As shown in Figure 2-14, in s-DTS, the moving gantry and the "hot" x-ray source are replaced by a "cold" source module made with multiple CNT-based x-ray sources. All CNT-based x-ray sources are fixed on the source ensemble, each CNT-based x-ray source or focal spot has its unique spatial position on the source ensemble and it is responsible for one projection images. During the scan, x-rays are fired sequentially from the first focal spot to the last focal spot, and each firing from a focal spot creates a projection image with the unique source position. Due to the compact size of the CNT-based x-ray source, it is relatively easy to pack multiple CNT-based sources in a flexible geometry that is hard to achieve with the translating gantry. For instance, we have developed a source ensemble with crossing lines geometry where two linear arrays of sources crossed at the middle, and a square-shaped source array where sources are distributed along the edge of the square.

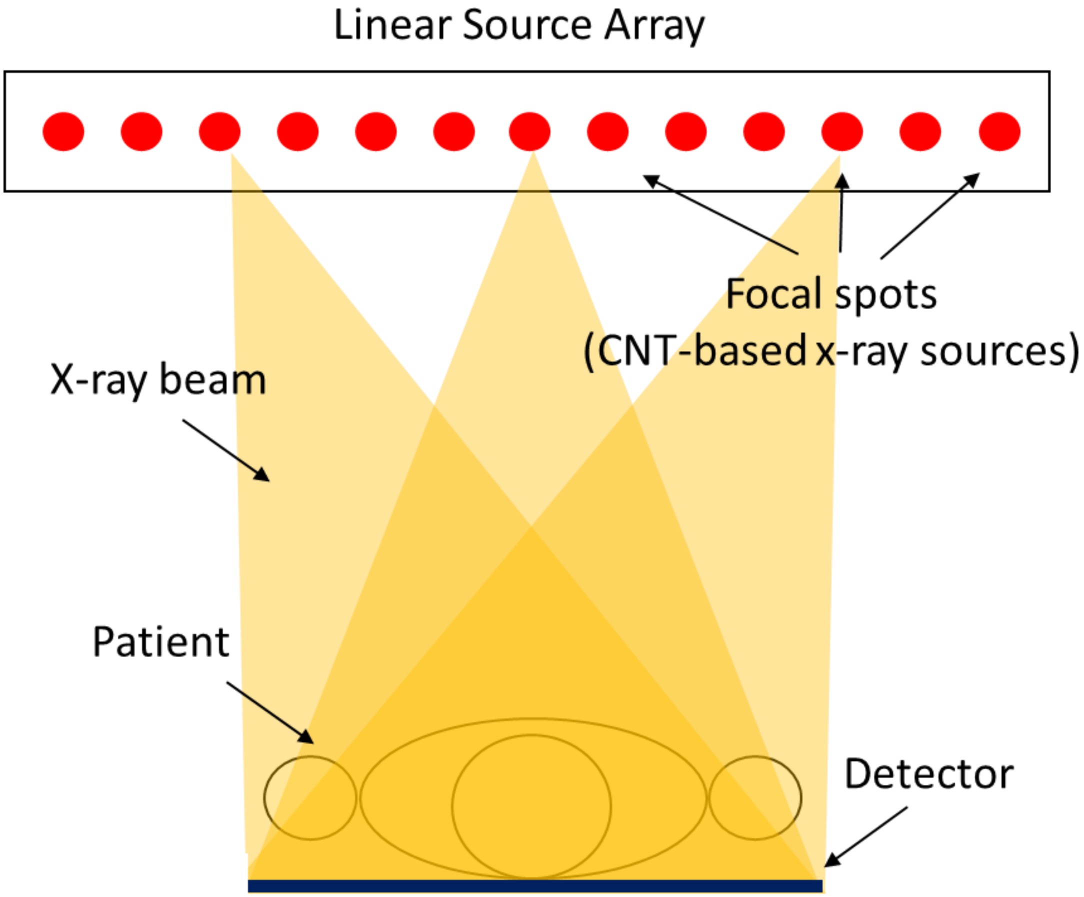
Linear Source Array
Focal spots
(CNT-based x-ray sources)
X-ray beam
Patient
Detector

Figure 2-14: Schematic of stationary digital tomosynthesis using CNT-based x-ray source array.

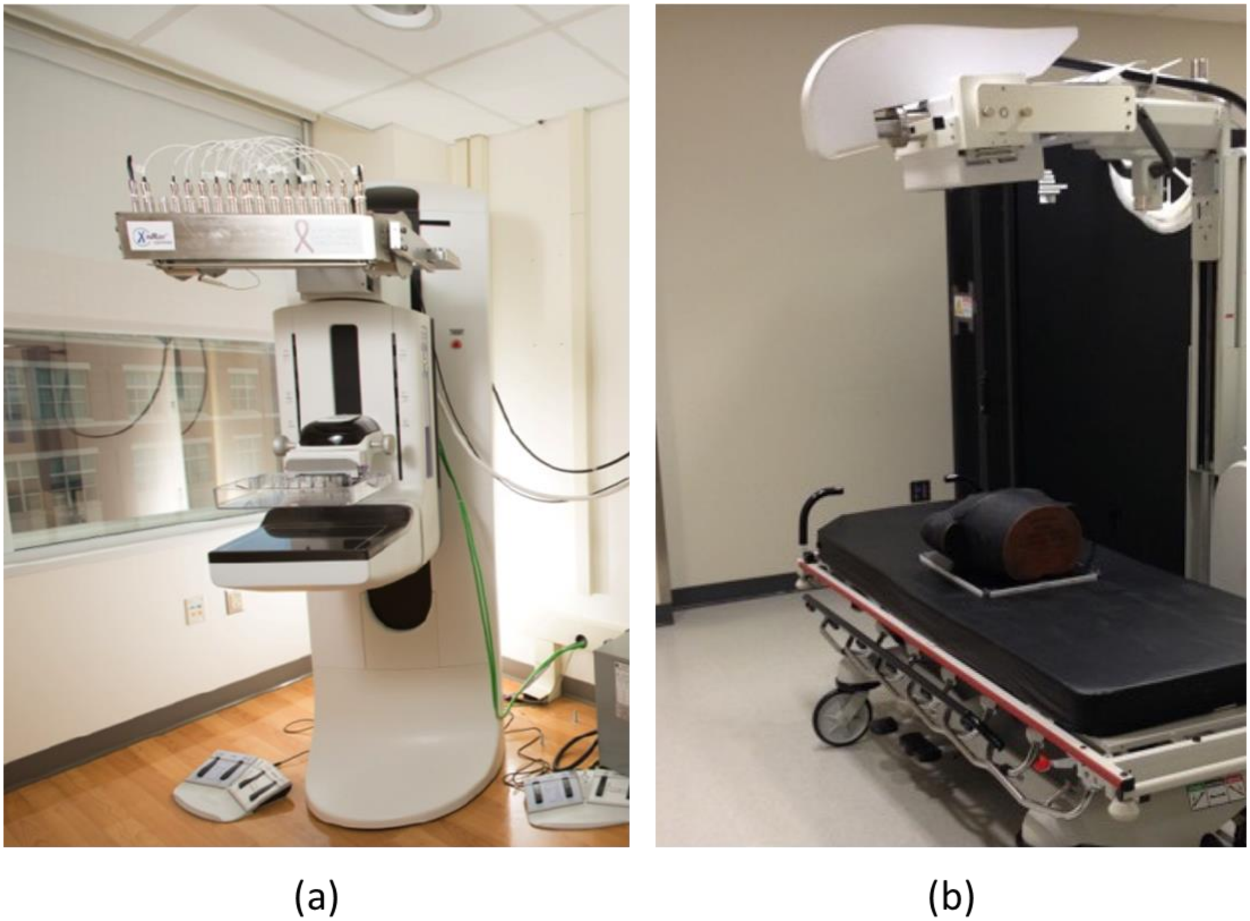

(a) (b)

Figure 2-15: (a) A picture of the stationary digital breast tomosynthesis system. The linear source array with CNT-based x-ray sources is retrofitted onto a Hologic Selenia Dimensions tomosynthesis system.

Based on the clinical applications, three s-DTS systems have been developed in our lab: the stationary digital breast tomosynthesis, the stationary chest tomosynthesis, and the stationary intraoral tomosynthesis. Pictures of s-DBT and s-DCT are shown in Figure 2-15. Each tomosynthesis system targets a unique clinical application. As a result, the x-ray sources used in each system are designed to have different tube voltage, tube current, and focal spot size. For example, the source voltage in s-DBT is around 35 kVp, while that in s-DCT is 80 kVp. Despite all the difference, all s-DTS systems use a linear-sources design, where all focal spots are distributed along a line that is parallel to the detector. It makes the manufacturing of the source array much easier, and also, as we will discuss later, allows a unique way to reconstruct images which turns out to be significantly faster than the conventional reconstruction algorithms.

s-DTS has a couple advantages over conventional DTS: first, the source motion, as well as the induced image blur are eliminated in s-DTS, resulting in an improved image resolution at the same detector and source focal spot; second, by eliminating the gantry motion in DTS, the total scanning time reduces in s-DCT. Consequently, the patient motion blur is also reduced; thirdly, each CNT-based x-ray source is electronically switched on and off, this enables precise control of the x-ray firing and makes s-DTS capable of cardiac gated imaging; fourthly, the fixed source array enables a simpler and a more portable system design.

CHAPTER 3: Image Reconstruction

Image reconstruction is a crucial part for 3D imaging modalities, including CT and DTS, as it converts the 2D raw data to nice 3D images and directly affects the quality of the images used for disease diagnosis. In this chapter, we will briefly introduce the fundamentals of image reconstruction, the system modeling including basis function, forward and back projection. We will then walk through different reconstruction methods, from the analytical filtered back projection method to the algebraic iterative reconstruction method, and finally, the statistical iterative reconstruction method which works extremely well for low dose and under-sampling image reconstruction problems. Since most reconstruction algorithms are originally developed with the assumption of complete sampling, we will introduce the concept of each reconstruction method in the context of CT reconstruction.

3.1 System Modelling

3.1.1 Linearization

As Beer's law suggests, the x-ray imaging is a non-linear process since the number of x-ray photons decreases exponentially as the x-rays pass through materials. Solving this non-linear problem is typically much harder than solving a linear problem. Therefore, many reconstruction algorithms, including the famous FBP algorithm, first convert the imaging process to a linear system and then solve the linear problem. Note that the Beer's law (Equation 2-2) states an exponential decay of the x-ray beam intensity, thus, the linearization can be achieved by applying a logarithmic transformation to both the blank data $\boldsymbol{I}_0$, a measurement of x-ray beam intensity without any attenuation, and the raw data $\boldsymbol{I}$:

$$\ln(\boldsymbol{I}) = \ln\left(\boldsymbol{I_0}\boldsymbol{e}^{-\sum_i \mu_i x_i}\right)$$

$$\ln \boldsymbol{I} = \ln \boldsymbol{I}_0 \cdot \left(-\sum\nolimits_{\boldsymbol{i}} \boldsymbol{\mu_i x_i}\right) \tag{3-1}$$

$$\ln\left(\frac{\boldsymbol{I}_0}{\boldsymbol{I}}\right) = \sum\nolimits_{\boldsymbol{i}} \boldsymbol{\mu_i x_i} \,.$$

The result of the linearization is often called a line integral image, where the photon counts in the raw data are converted to a summation of the linear attenuation coefficients for each source detector pair.

It should be noted that some reconstruction algorithms, e.g. the Maximum Likelihood Expectation Maximization algorithm, do not require the linearization step and uses photon counts during the reconstruction.[56], [57] Although these methods model the system more accurately, they generally run slower than those algorithms require linearization. In this thesis, I will focus on the group of reconstruction methods that requires linearization, and the measurement or the measured data mentioned shown later in the thesis refers to the projection data after the logarithmic transformation.

3.1.2 Basis Function

Inside the computer, all data is stored and processed in discretized digits. A continuous attenuation image $\mu(\boldsymbol{r})$, therefore, is discretized in both space and intensity. While the intensity of the linear attenuation is discretized into a fixed precision (i.e. single precision or double precision), the space is discretized using a set of basis functions $\{b_i(\boldsymbol{r}) : i = 1, \dots, n_v\}$:

$$\mu(r) \approx \sum_{i=1}^{n_v} \mu_i b_i(r). \tag{3-2}$$

where n_v is the number of basis functions. The more basis functions used, the more accurate will be the discretization. Substituting the above expression for $\mu(\boldsymbol{r})$ to Equation 3-3, we will have:

$$\int_l \mu(r)dr \approx \int_l \sum_{i=1}^{n_v} \mu_i b_i(r)dr = \sum_{i=1}^{n_v} \mu_i \int_l b_i(r)dr$$
$$= \sum_{i=1}^{n_v} A_{ij}\mu_i \equiv \mathbf{A}\boldsymbol{\mu}, \tag{3-3}$$

and

$$\mathrm{A}_{ij} = \int_\mathrm{l} \mathrm{b}_i(\mathrm{r})\mathrm{dr}. \tag{3-4}$$

The matrix **A** in Equation 3-3 is called the system matrix or the system model, as it describes the imaging process. Applying the system matrix **A** on the image $\boldsymbol{\mu}$ is called a forward projection, as it projects $\mu(\boldsymbol{r})$ to the measured data. On the other hand, applying the transpose of the system matrix $\mathbf{A}^T$ on a data vector is called a back projection and it is often used to update the current estimation of μ. Forward projection and back projection are two key elements in the image reconstruction, they consume the most of the computation time in iterative reconstruction methods.

Basis function determines the accuracy of the discrete representation of the continuous object. In addition, basis function affects the implementation of the system model and the convergence rate of the iterative reconstruction algorithms. It is preferred to use basis function that is computationally efficient without scarifying the representation accuracy. Pixel (or voxel for 3D images) is a widely used basis which represents a continuous image with a rectangle function as shown in Figure 3-1(a):

$$b(r) = \begin{cases} 1, & |r - r_0| < p/2 \\ 0, & otherwise \end{cases}, \tag{3-5}$$

where *p* is the pixel size. Pixel basis is simple and computationally inexpensive. With pixel basis, several computationally efficient projection models have been developed, including pixel-driven model, ray-driven model, distance driven model, separate footprint model, and Fourier space model. Pixel basis is not smooth, as shown in Figure 3-1(b). Furthermore, as the Fourier transform of a rectangle function has a large side-lobe amplitude, pixel basis could amplify errors.

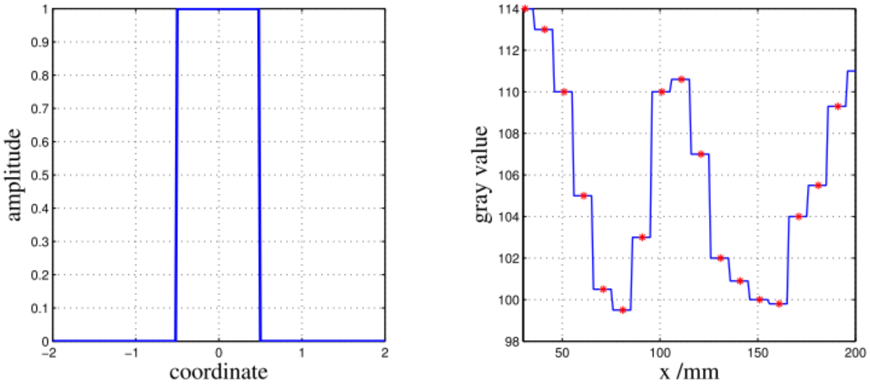

(a) profile of a pixel **(b)** approximation by pixels

Figure 3-1: (a) Line profile of the rectangle function used in pixel basis with the pixel size of 1. (b) a smooth signal that is represented with pixel basis. [58]

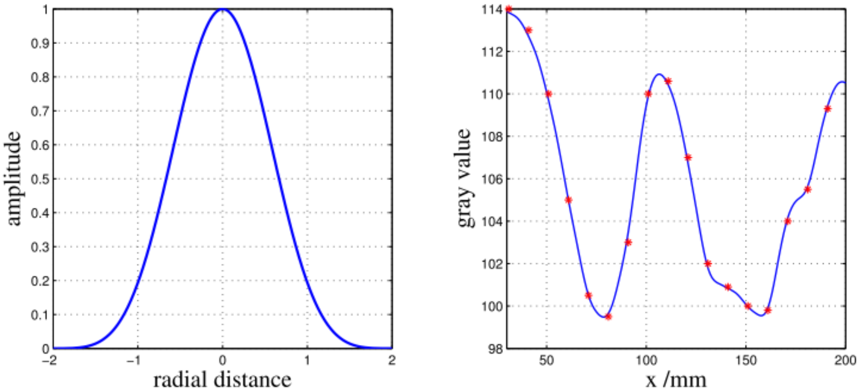

(a) profile of a blob **(b)** approximation by blobs

Figure 3-2: (a) Profile of a blob function. (b) Signal represented with blobs. [58]

Smooth basis functions, such as blobs and B-splines, have been proposed as attractive alternatives. Introduced by Lewitt,[59] the Kaiser-Bessel basis functions (blobs) are spherically symmetric function as shown in Figure 3-2(a):

$$b(r) = \begin{cases} \frac{I_m\left(\alpha\sqrt{1-(r/a)^2}\right)}{I_m(\alpha)}\left(\sqrt{1-(r/a)^2}\right)^m, & 0 < r < a \\ 0, & otherwise \end{cases}. \tag{3-6}$$

where I_m is a modified Kaiser-Bessel function of order m, $\boldsymbol{r}$ is the radial distance. α is a parameter that controls the shape of the blob, a smaller α will result a fatter shape of the blob. a is the radius of the blob. A blob with larger radius would lead to more overlaps with neighboring blobs and consequently more expensive computation.

3.1.3 Pixel-driven Method

The pixel-driven (PD) model is the first proposed projection method for CT reconstruction.[60] As shown in Figure 3-3, in PD projection model, both the image voxel and the detector pixel are modeled as points. Each image voxel, shown as P_{12} in Figure 3-3, is projected onto the detector, which is indicated as a red dot in Figure 3-3. The contribution of the attenuation from this pixel to the detector pixels, D_{23} and D_{34}, is inverse proportional to the distance between the intersection point and the detector pixels. A linear (1D case) or bi-linear (2D case) interpolation is typically used to compute the weighting. Similarly, for back projection, a detector pixel is back projected, based on the imaging angle, onto the image space. Based on the distance between the intersection point and its surrounding voxels, an interpolation is perform and the weightings are calculated. PD forward and back projector will introduce high-frequency artifact to the reconstruction images, thus, it should be avoid in the iterative reconstruction. This model, however, is preferred in FBP algorithm since it is computationally inexpensive and the errors introduced by the projector is not severe as FBP has only one back projection. Improvements on

PD model, such as reducing the size of the voxel, have been investigated, which were shown to reduce the aliasing artifact but with a more expensive computation.

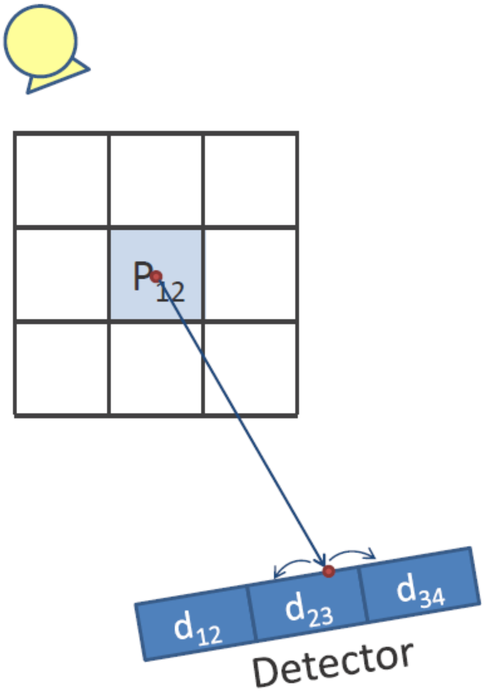

Figure 3-3: Pixel-driven forward and back projector. [58]

3.2 Analytical Image Reconstruction

3.2.1 Radon Transform

The x-ray project a high dimensional object to a lower dimensional detector measurement, this process is mathematically described by the Radon transform, which was introduced in 1917 by Johan Radon. More strictly, the Radon transform is the integral transform which takes a high dimensional function f to a low dimensional function $R(f)$. The Radon transform is schematically illustrated in Figure 3-4. A function $f(x, y)$ which represents the imaged object is defined in x-y coordinate, a line integral $L(\theta, t)$, which represents the an x-ray beam, is performed at an angle θ with respect to the positive y axis to the detector, the detector measured multiple line integrals and the detector function $p_\theta(t)$ is obtained. We say the detector function $p_\theta(t)$ is the Radon transform of the function $f(x, y)$:

$$\mathcal{R}f(\theta, t) = \int_{L(\theta,t)} f(x, y) ds = p_\theta(t). \tag{3-7}$$

The x-y and the θ-t follows the relationship:

$$x \cos\theta + y \sin\theta = t. \tag{3-8}$$

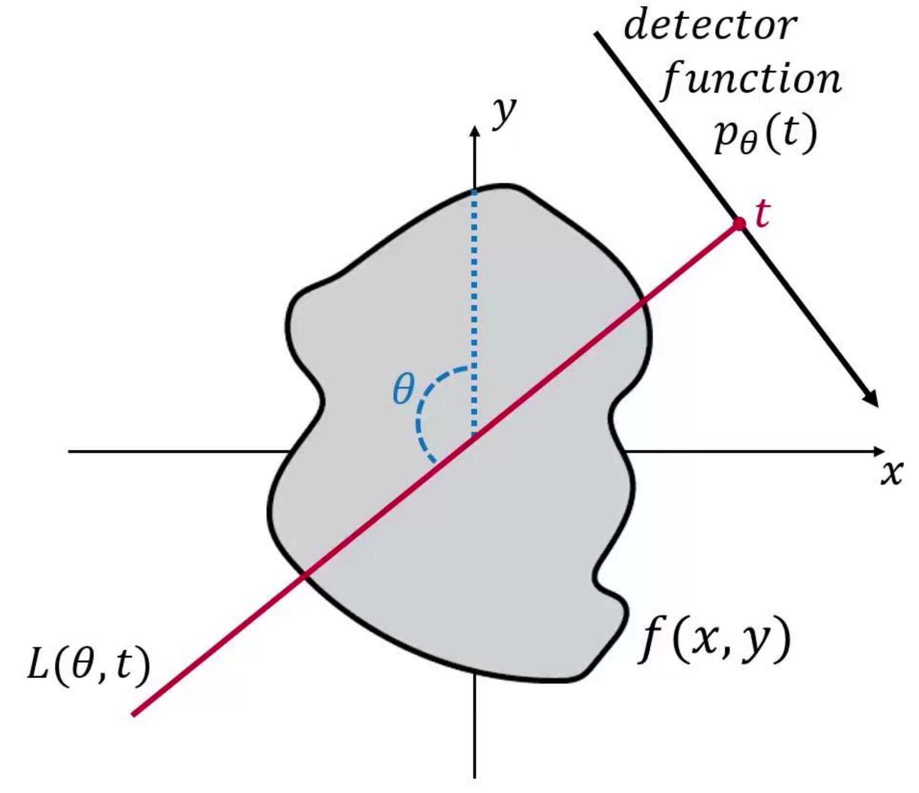

Figure 3-4: Schematic illustration of Radon transform.[61]

The detector function $p_\theta(t)$ at each imaging/integral angle θ is called an x-ray projection. If we measure the detector functions $p_\theta(t)$ over all imaging angles and combine them together into a single graph, we will obtain the full representation of the Radon transform, also called sinogram. The name “sino-” comes from the fact that a point signal will appears like a sinusoidal curve in the sinogram and the whole sinogram is a combination of multiple sinusoidal-like curves.

An example of sinogram from a Shepp-Logan phantom is shown in Figure 3-5.

In practice, only limited number of projection images are acquired during one CT scan, which varies from one hundred to three hundred projections, and there is a small gap between two projections. In addition, the detector function $p_\theta(t)$ will be discretized to pixels, which have a finite size. Therefore, the continuous Radon transform becomes a discretized format, shown as:

$$p_i = \frac{1}{\Delta t}\int_{-\Delta t/2}^{\Delta t/2} \mathcal{R}f(\theta, t + t')dt'. \tag{3-9}$$

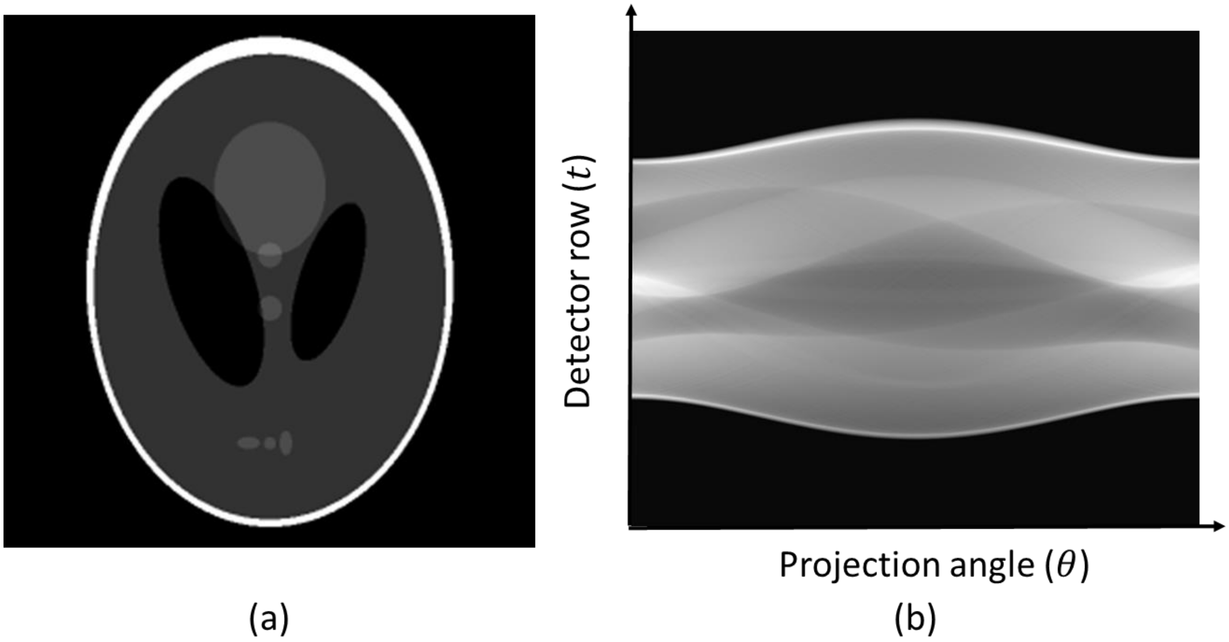

Figure 3-5: (a) Shepp-Logan phantom. (b) The sinogram of the Shepp-Logan phantom.

3.2.2 Fourier Slice Theorem

From the Radon transform, we can derive an important theorem, called Fourier slice theorem or projection slice theorem, which is the fundamental of all analytical reconstruction algorithms. The Fourier slice theorem states that the Fourier transform of a detector function $p_\theta(t)$, which is the Radon transform of the function $f(x, y)$ at an imaging angle of θ, is indeed the same as the line profile of the Fourier transform of the same object function $f(x, y)$, as illustrated in Figure 3-6.[61] Fourier slice theorem indicates a connection between the low dimension detector function and the high dimension object function through Fourier transform, thus it provides a way to restore the object function from the measurements.

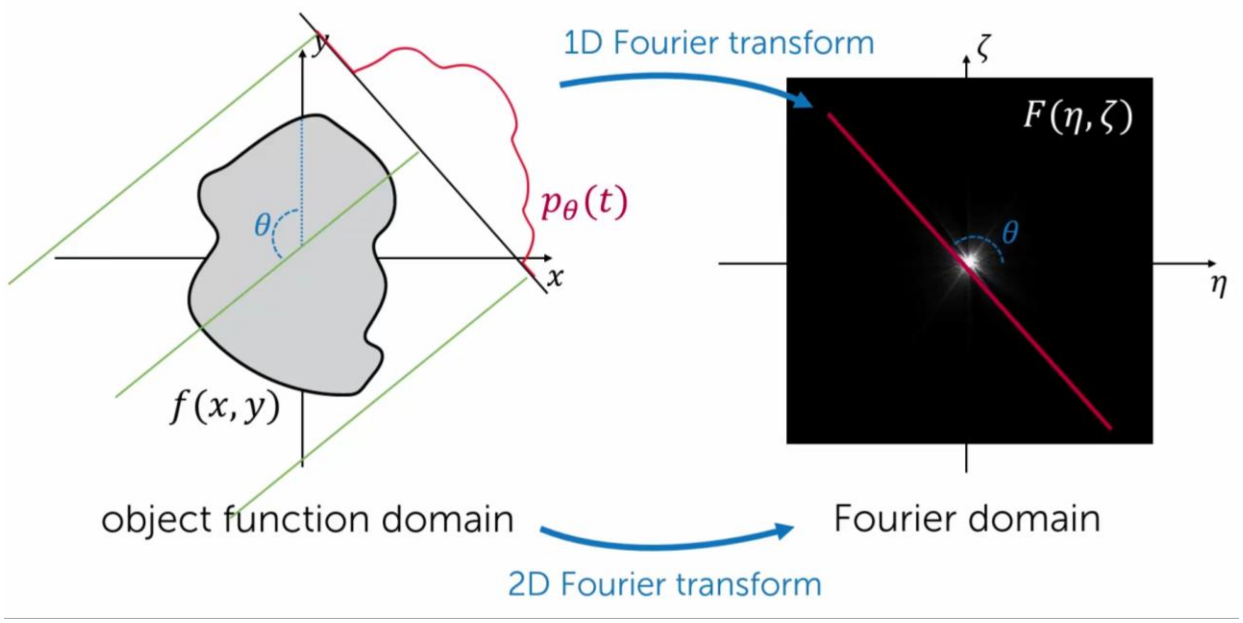
1D Fourier transform
y
θ
x
$p_\theta(t)$
$f(x, y)$
ζ
$F(\eta, \zeta)$
θ
η
object function domain
Fourier domain
2D Fourier transform

Figure 3-6: Schematic illustration of the Fourier slice theorem. The radon transform $p_\theta(t)$ of a function $f(x, y)$ is equaled to the line profile of the Fourier transform of the same function at the angle θ.[61]

The Fourier slice theorem can be proved as the following. Consider the Fourier transform of the object function $f(x, y)$:

$$\mathcal{F}(\zeta, \eta) = \int_{-\infty}^{\infty}\int_{-\infty}^{\infty} f(x, y)e^{-i2\pi(\zeta x + \eta y)}dxdy, \tag{3-10}$$

where $\mathcal{F}(\zeta, \eta)$ is the Fourier transform of the object function $f(x, y)$, and ζ, η is the coordinate of the Fourier space. Remember the Fourier transform of the detector function $p_\theta(t)$ is:

$$\mathrm{P}(\omega) = \int_{-\infty}^{\infty} p_\theta(t)e^{-i2\pi\omega t}dt, \tag{3-11}$$

where $\mathrm{P}(\omega)$ is the Fourier transform of the detector function $p_\theta(t)$. Substitute Equation 3-7 and

3-8 into Equation 3-11, we obtain:

$$\begin{aligned}\mathrm{P}(\omega) &= \int_{-\infty}^{\infty}\int_{-\infty}^{\infty} f(x,y)e^{-i2\pi\omega(x\cos\theta+y\sin\theta)}dxdy \\ &= \mathcal{F}(\omega\cos\theta\,,\omega\sin\theta).\end{aligned} \tag{3-12}$$

Since $\mathcal{F}(\omega\cos\theta\,,\omega\sin\theta)$ is the line profile of the $\mathcal{F}(\zeta,\eta)$ at the angle θ, the Fourier slice theorem is proved.

3.2.3 Reconstruction Based on Fourier Slice Theorem

Based on the Fourier slice theorem, one can Fourier transform each projection in the sinogram, map the results to the Fourier space in the polar coordinate, then interpolate the Fourier space to find the values of Fourier space in Cartesian coordinate, and finally perform an inverse Fourier transform to obtain the original image. However, this approach has two main drawbacks: first, the interpolation that transforms the polar coordinate to the Cartesian coordinate is prone to errors. Second, the Fourier space is well-sampled in the low-frequency regions but not in the high-frequency region. This would result in a loss of high-frequency information in the original image and introduce image blur. To fix this problem, several Fourier projectors have been investigated. Fessler proposed a non-uniform fast Fourier transform, in which the inverse Fourier transform in the last step is performed on a non-uniform grid.[62]–[64] An iterative reconstruction algorithm is also developed based on the pseudo-polar fast Fourier transform, as shown in Figure 3-7.[65] These algorithms produce better image quality than the original Fourier-based method, however, they are computationally more demanding or hard to adapt to complex imaging geometries such as the helical CT scan.

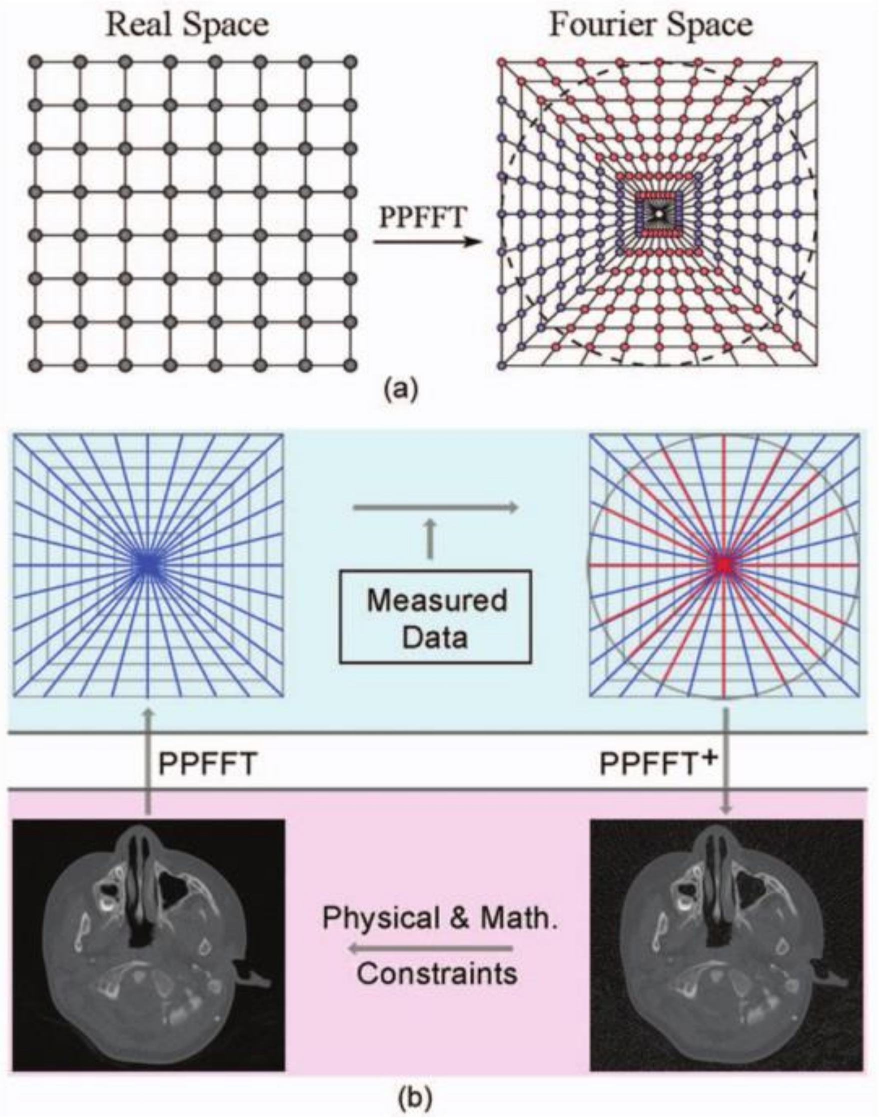
Real Space
Fourier Space
PPFFT
(a)
Measured Data
PPFFT
PPFFT+
Physical & Math.
Constraints
(b)

Figure 3-7: Schematic illustration of (a) Pseodopolar fast Fourier transform, (b) iterative reconstruction with constraints based on the Fourier slice theorem.[65]

3.2.4 Filtered Back Projection

Filtered back projection (FBP) is another image reconstruction method that is also based on the Fourier slice theorem but avoids the drawbacks of direct interpolation on the Fourier sampling space. There are two steps in FBP method: filtering and back projection (BP). The filtering can either be performed on the object image after BP or on the detector function before BP. However, most FBP algorithms apply filtering on the measurement data, which is more efficient and computationally faster. The filtered back projection algorithm can be derived using the Fourier slice theorem. Mathematically, BP is a summation of detector functions over all imaging angles, and it can be expressed as:

$$f_{BP}(x,y) = \int_0^{2\pi} p_\theta(t)d\theta = \int_0^{2\pi} p_\theta(x\cos\theta + y\sin\theta)d\theta. \tag{3-13}$$

where $f_{BP}(x,y)$ is the image obtained by BP the detector function $p_\theta(t)$. We can then substitute the detector function $p_\theta(t)$ with its Fourier transform $p_\theta(t) = \mathcal{F}^{-1}\big(\mathrm{P}(\omega)\big)$ and obtained:

$$\begin{aligned} f_{BP}(x,y) &= \int_0^{2\pi} p_\theta(t)d\theta = \int_0^{2\pi} \mathcal{F}^{-1}\big(\mathrm{P}(\omega)\big)d\theta \\ &= \int_0^{2\pi} \mathcal{F}^{-1}\big(\mathcal{F}(\omega\cos\theta\,, \omega\sin\theta)\big)d\theta \\ &= \int_0^{2\pi}\int_{-\infty}^{\infty} \mathcal{F}(\omega\cos\theta\,, \omega\sin\theta)e^{i2\pi\omega t}d\omega d\theta \\ &= \int_0^{2\pi}\int_{-\infty}^{\infty} \mathcal{F}(\zeta,\eta)e^{i2\pi(\zeta x\,+\,\eta y)}d\omega d\theta\,, \end{aligned} \tag{3-14}$$

where we also used the Fourier slice theorem: $\mathrm{P}(\omega) = \mathcal{F}(\omega\cos\theta\,, \omega\sin\theta)$ and the coordinate transformation $t = x\cos\theta + y\sin\theta$. Note that the Fourier transform of the original object function is:

$$f(x,y) = \int_{-\infty}^{\infty}\int_{-\infty}^{\infty} \mathcal{F}(\zeta,\eta)e^{i2\pi(\zeta x\,+\,\eta y)}dxdy. \tag{3-15}$$

Equation 3-15 is surprisingly similar to this expression, except that Equation 3-14 is written in polar coordinate. We then transform the Cartesian coordinate in Equation 3-15 to the polar coordinate and obtain:

$$f(x,y) = \int^{2\pi}\int^{\infty} \mathcal{F}(\zeta,\eta)e^{i2\pi(\zeta x\,+\,\eta y)}\omega d\omega d\theta \tag{3-16}$$

$$= \int_0^{2\pi} \left(\int_{-\infty}^{\infty} \mathcal{F}(\zeta, \eta) e^{i2\pi(\zeta x + \eta y)} \omega d\omega \right) d\theta$$

$$= \int_0^{2\pi} \mathcal{F}^{-1}\left(\widetilde{\mathrm{P}(\omega)}\right) d\theta = f_{FBP}(x, y),$$

where $\widetilde{\mathrm{P}(\omega)}$ is the filtered $\mathrm{P}(\omega)$ on the Fourier space:

$$\widetilde{\mathrm{P}(\omega)} = \mathrm{P}(\omega) \cdot |\omega|. \tag{3-17}$$

Equation 3-16 and 3-17 suggests that the image obtained from BP is a blurred version of the original object function $f(x, y)$. By filtering the detector function $p_\theta(t)$ on the Fourier domain and then BP the result, an exact solution of the original object function will be obtained, and this is the exactly how FBP reconstructs images. Equation 3-16 also suggests that a filtering can be done after the BP, however, it is rarely implemented for computational speed reason.

The filter design is critical in FBP, as it strongly affects the reconstruction image quality. A high-pass ramp filter with a cut-off frequency is often used in FBP, which is defined as:

$$h(\omega) = \begin{cases} |\omega|, & |\omega| < \omega_0 \\ 0, & |\omega| \geq \omega_0 \end{cases}, \tag{3-18}$$

where ω_0 is the cut-off frequency that controls how much high-frequency information is passed to the final reconstruction images. Generally, a larger cut-off frequency would result a better spatial resolution, but at the same time the high-frequency noise also increases. In contrast, a small cut-off frequency would reduce the noise in the reconstruction image, however, it reduces the image resolution as well and the reconstruction will look blurry. Examples of filters used in FBP are BlackMan filter, Butterworth filter, Cosine filter, Hamming filter, Shepp-Logan filter and RamLak filter. Each filter has different shape and different cut-off frequency, which changes the image characteristic at different frequencies. The filter performance is application dependent (noise level in the raw data and imaging geometry). In certain applications, some filters might perform better than the other. With that being said, despite different designs, all filters have to trade off one or the other between the image resolution and the image noise. A collection of FBP filters are shown in Figure 3-8.[66]

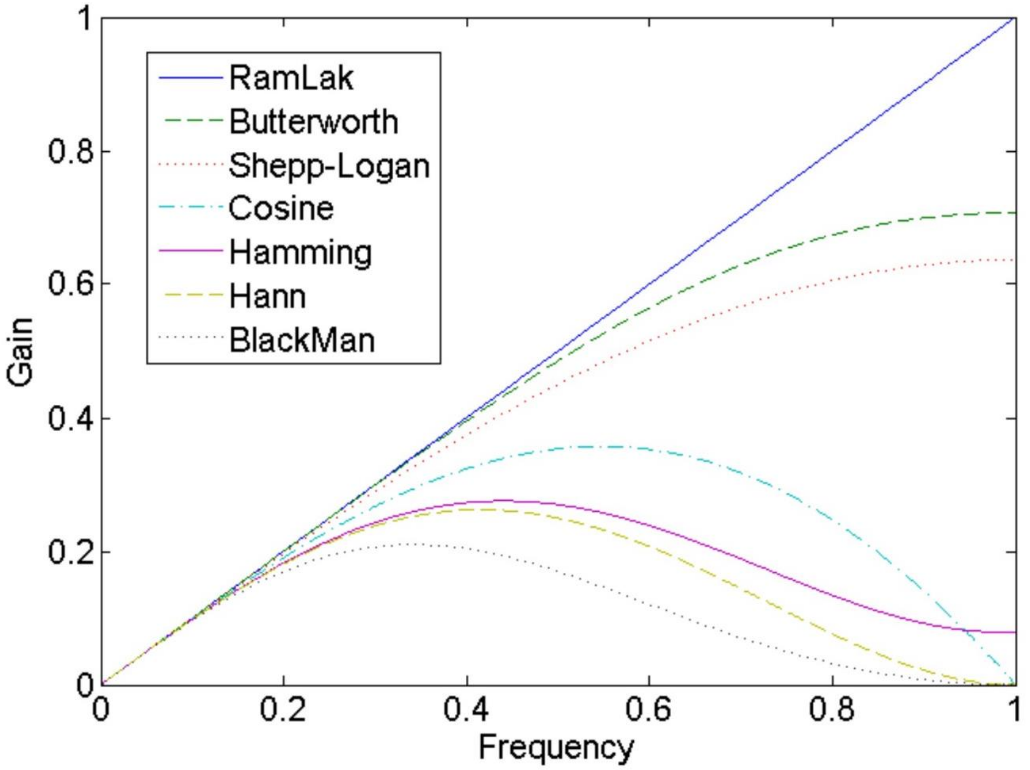

Figure 3-8: A collection of filters used in FBP. [66]

For many years, FBP is the predominant image reconstruction algorithm, it generates sharp images within a reasonable time. Nowadays, it is still widely used in many CT and DTS systems. Thanks to the fast Fourier transform, FBP algorithm is computationally efficient, and doctors can see the reconstruction images in a short time. However, as an analytical method, FBP requires a sufficient sampling size, which should be above the Nyquist rate and it assumes no noise in the raw data. These two conditions ensure the accuracy of the FBP reconstruction, however, they could be hard to achieve in certain clinical applications. For example, the number of projection images in tomosynthesis imaging is far below than the Nyquist requirement, and image noise always exists in the raw data especially with low dose imaging. Currently, with the increasing concerns of radiation-induced cancer, tremendous effects are made on developing low dose clinical protocols and imaging techniques, where the image noise can no longer be ignored and/or the projection data becomes insufficient. This facilitates the development of a new reconstruction method which produces better images with noisy and/or insufficient data.

3.3 Algebraic Reconstruction Methods

3.3.1 Kaczmarz's Method

Algebraic reconstruction methods are a group of methods that solve the reconstruction problem numerically and iteratively. In contrast to FBP or Fourier filtering method, which is based on an exact mathematical solution, the algebraic reconstruction method models the imaging system as a system of linear equations (after linearizing the raw data):

$$\boldsymbol{Ax} = \boldsymbol{b} + \boldsymbol{\varepsilon}, \tag{3-19}$$

where *x* is the unknown attenuation image to be solved (in another word, $\mu(\boldsymbol{r})$), *A* is the system matrix, which models the interaction between x-rays and the object, b is the measured data recorded on the detector (a collection of $p_\theta(t)$ over all imaging angle θ), and ε is the noise. Consequently, the reconstruction problem becomes finding the solution x of a set of linear equations: $\boldsymbol{Ax} - \boldsymbol{b} = 0$, which is totally algebraic.

At first glance, it might seem that Equation 3-19 could be solved by simply applying the inverse of matrix *A* on both sides of the equation. In practice, however, it is rarely done due to two reasons: first, the reconstruction is a large size inverse problem. The system matrix *A* is a sparse matrix, whose size can go up to the order of 10^{17}, which makes it impractical to store the matrix in memory and computationally quite expensive to compute the inverse of *A* matrix and then solve the problem in one step using $x = A^{-1}b$. Secondly, the inverse of the system matrix generally does not exist, such as the case in the tomosynthesis. In fact, the system matrix for many imaging geometries does not have a full row/column rank, which is the necessary and sufficient condition for an inverse matrix to be exist.

A more general way to solve this linear system of equations is using iterative algorithms, where a coarse initial guess is iteratively updated and finally converges to the true solution after several iterations. Historically, this problem was first studied by Polish mathematician Stefan Kaczmarz and the Italian mathematician Gianfranco Cimmino in the early 20th century, both independently developed iterative algorithms for solving linear systems of equations. In 1970, the Kaczmarz method was rediscovered by Gordon et al.[67] and be applied to 3D image reconstruction with the new name of algebraic reconstruction technique (ART). Later Hounsfield included this method in his patent of the first CT-scanner.[68] Since then, numerous variants of the ART methods have been developed and used for tomographic image reconstruction problem.[69]–[72]

ART is computationally intense, as it iterates through all equations in the linear system. The computation time for ART can be up to two magnitudes of that for FBP algorithm. However, ART is more flexible on imaging geometry than FBP. ART works quite well in clinical protocols such as digital tomosynthesis, where the number of projection images is far from sufficient. It has been shown that ART type reconstruction algorithms produce better reconstruction images over FBP in limited-angle and limited-projection CT.[13], [15]

3.3.2 Algebraic Reconstruction Technique (ART)

In Equation 3-19, each row in the system matrix *A* together with unknown object function *x* forms a linear equation. ART treats these equations sequentially from the top of the matrix to the bottom and updates the solution after evaluating each equation. The updating step can be expressed as:

$$\boldsymbol{x_{k,i}} = \boldsymbol{x_{k,i-1}} + \lambda_k \boldsymbol{A_i}^{\boldsymbol{T}} \frac{\boldsymbol{b_i} - \boldsymbol{A_i x}}{\|\boldsymbol{A_i}\|_2^2}, \tag{3-20}$$

where *k*, *i*, λ_k, $\boldsymbol{A_i}$, $\boldsymbol{b_i}$, $\|\boldsymbol{A_i}\|_{\boldsymbol{2}}^{\boldsymbol{2}}$ are the current number of iteration, the index of current update, the relaxation parameter, the i-th row of the system matrix, the i-th element in the measurement, and the square of the L-2 norm of A_i, respectively. $\boldsymbol{b_i} - \boldsymbol{A_i x}$ is the error of the current guess, it is normalized by $1/\|\boldsymbol{A_i}\|_{\boldsymbol{2}}^{\boldsymbol{2}}$ and back project to *x*. The relaxation parameter controls the speed of the convergence, it stabilizes the convergence when the update term is either too large or too small. In the absence of noise, it has been proven mathematically that the solution of Equation 3-23 converges when $0 < \lambda_k < 2$, and the solution converges to the solution of minimum L-2 norm when $x^0 \in \mathcal{R}(A^T)$.[73]

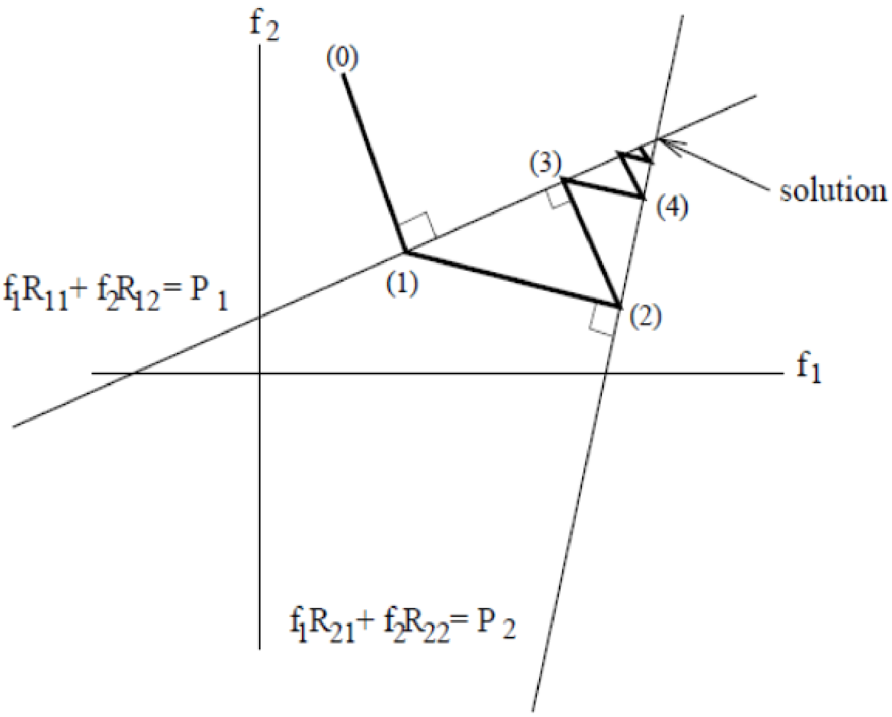

Figure 3-9: Principle of the ART method.[74]

The principle of ART is iteratively projecting solution onto the hyperplanes and finding the solution where all hyperplanes intersect. Figure 3-9 illustrates a case of two linear equations with two unknown variables (f_1, f_2). At the beginning, an initial "guess" is made at position 0 in the space. It is then projected to the first plane: $R_{11}f_1 + R_{12}f_2 = P_1$ at position 1. After that, the error, which is the difference between the true solution and the position 1, is projected to the second plane: $R_{21}f_1 + R_{22}f_2 = P_2$ at postion 2, and again the error term is calculated and back project to plane 1. This process goes back and forth until the solution converges or the stopping criteria is meet.

In the original Kaczmarz method, the relaxation parameter λ_k is set to be 1 and the order of each update step is sequential, from the first row to the last row. Other update schemes have proposed, such as symmetric Kaczmarz and randomized Kaczmarz to accelerate the convergence of the method. [75], [76]

3.2.3 Simultaneous ART methods

The original Kaczmarz method is slow due to the large number of accesses to update the solution. Soon it is realized that the update steps can be grouped to speed up the computation (similar to the original Cimmino’s method). Many algorithms have been developed based on this idea, including the famous simultaneous algebraic reconstruction technique (SART), and the simultaneous iterative reconstruction technique (SIRT). The update step in the simultaneous ART methods can be generalized as:

$$\boldsymbol{x}_{k+1} = \boldsymbol{x}_k + \lambda_k {\boldsymbol{D}_c}^{-\mathbf{1}} \boldsymbol{A}^{\boldsymbol{T}} {\boldsymbol{D}_r}^{-\mathbf{1}} (\boldsymbol{b} - \boldsymbol{A}\boldsymbol{x}_k), \tag{3-21}$$

where D_c and D_r are diagonal matrice defined as the column and the row sum of the system matrix A:

$$\boldsymbol{D_c} = diag\left(\|\boldsymbol{a_j}\|_{\mathbf{1}}\right), \quad \boldsymbol{D_r} = diag\left(\|\boldsymbol{a^i}\|_{\mathbf{1}}\right). \tag{3-22}$$

where i, j represent the row and the column index, respectively. In SIRT, the solution is updated after all projections are considered; while in SART, the solution is updated after each projection. It is demonstrated that SART has a faster convergence speed than SIRT, however, the images reconstructed by SART have a higher noise level and they are not as smooth as those reconstructed by SIRT.

The order of projection data used to update the solution will strongly affect the convergence speed of the SART method. It is known that the sequential update, in which the order of projection update is the same as the order of imaging process, has the slowest convergence. Many update schemes have been proposed to improve the convergence speed of SART. [77]–[79] van Dijke proposed to use a random permutation of the projection order. A constant angular increment determined by golden ratio is proposed by Kohler.[80] Mueller proposed using a weighted distance scheme which minimizes the correlation between used projections.[81]–[83] Guan proposed to use a multilevel scheme which minimizes the geometrical correlation between projection data and use the least correlated projection to update the solution.[77] In summary, all proposed update schemes speed up the convergence of SART by minimizing the correlation between the two adjacent projection updates. Depends on the imaging geometry, the performance of various update schemes might varies on different imaging systems.

3.4 Statistical Iterative Reconstruction

3.4.1 Overview of SIR

Statistical iterative reconstruction (SIR) is another group of iterative algorithms that solve the reconstruction problem iteratively. What sets SIR apart from the classical ART methods is that SIR models the noise in the imaging process and takes the prior knowledge of the imaged object into consideration. More importantly, the SIR is formed under an optimization framework, where the goal is to find the optimized solution rather than the exact solution. The optimization framework used in SIR is a more powerful tool than the algebraic approach used in ART methods, it offers flexibility on more sophisticated system modeling.

A SIR method consists two parts: the objective function, or cost function, and the algorithm that minimizes the objective function. The physical characteristics of the imaging system, the characteristics of the imaged object, the detector measurement of a scan, and the imaging system settings are all modeled as different parts in the objective function. The objective function maps the reconstruction images into the real numbers, which are used to evaluate the quality of the reconstruction. The objective function is designed in such way that the solution at its minimum is close to the true image of patient's anatomy. The algorithm is a numerical solver that minimized the objective function. Similar to the algebraic approaches in ART methods, most algorithms in SIR are iterative.

3.4.2 Noise Modeling

The noise present in the measurement is usually modeled using a probability density function. Other physical processes, such as detector afterglow, detector off-gain correction, are typical pre-corrected in the sinogram before reconstruction. The noise statistics depends on the physical processes, which varies on different imaging systems, however, there are two popular noise models that are generally used in SIR: (1) Compound Poisson noise, and (2) Compound Poisson noise with Gaussian readout noise.

In the compound Poisson noise model, the observation b_i for the source-detector-pair i is modeled as:

$$\boldsymbol{b_i} \sim Poisson\left(\boldsymbol{c_i} \boldsymbol{e}^{-[\boldsymbol{Ax}]_i}\right) + \boldsymbol{r_i}, \tag{3-23}$$

where $\boldsymbol{c_i}$ is the unattenuated beam intensity for source-detector-pair i (blank scan count), and $\boldsymbol{r_i}$ is the corresponding read-out noise and scatter.

For the compound Poisson noise with Gaussian read-out noise, a weighted least square (WLS) model can be used, where the negative log-likelihood of Poisson noise model is approximated and replaced with a quadratic function. The photon counts is replaced with the attenuation line integral variable l_i in the WLS model: $\boldsymbol{l}_i \equiv \ln\left(\boldsymbol{c}_i - \boldsymbol{r}_i / \boldsymbol{b}_i\right)$. In the quadratic approximation, the $\boldsymbol{l}_i$ follows a normal distribution with the mean of $[\boldsymbol{Ax}]_{\boldsymbol{i}}$ and variance of $\boldsymbol{b_i}/(\boldsymbol{b_i} - \boldsymbol{r}_i)^2$. Thus, the WLS model can be expressed as:

$$\boldsymbol{l}_i \sim \mathcal{N}([\boldsymbol{Ax}]_i,\ \boldsymbol{b}_i/(\boldsymbol{b}_i - \boldsymbol{r}_i)^{\mathbf{2}}), \tag{3-24}$$

Practically, the quadratic function is easier to solve than the likelihood function as many fast numerical solvers have already developed for this problem. Consequently, many SIR methods use this compound Poisson noise with Gaussian read-out noise model.

3.4.3 Formation of Objective Function with Regularization

The cost function consists the negative log-likelihood function, which is computed using the probability density function from the statistical model. In addition, a penalty function, or a Bayesian prior of the images, is added to the cost function. The penalty function is used to model the physics of the imaged object, including but not limited to, the smoothness of the image, the edge preservation, the nonnegative image pixels and statistical prior of the images. Consequently, the cost function can be generalized as:

$$\Phi(\boldsymbol{x}) = -L(\boldsymbol{x}) + \beta R(\boldsymbol{x}), \tag{3-25}$$

where $\boldsymbol{L}(\boldsymbol{x})$ is the log-likelihood function, which is also called the data fidelity term, β is the weighting of the overall penalty, $R(\boldsymbol{x})$ is the penalty function, which is also called the regularization. And the reconstruction image, $\boldsymbol{x}$, is obtained by minimizing the cost function:

$$\boldsymbol{x} = arg\ \min_x \Phi(\boldsymbol{x}). \tag{3-26}$$

The log-likelihood function for the Poisson model and WLS model can be expressed as:

$$\begin{gathered} -\mathrm{L}(\boldsymbol{x}) = \sum_{\boldsymbol{i}=\boldsymbol{1}}^{\boldsymbol{n}} \boldsymbol{h}_{\boldsymbol{i}}([\boldsymbol{A}\boldsymbol{x}]_{\boldsymbol{i}}) \\ h_{\boldsymbol{i}}(\boldsymbol{q}_{\boldsymbol{i}}) = \begin{cases} \bar{\boldsymbol{b}}_{\boldsymbol{i}} - \boldsymbol{b}_{\boldsymbol{i}} \ln\left(\bar{\boldsymbol{b}}_{\boldsymbol{i}}\right), & \bar{\boldsymbol{b}}_{\boldsymbol{i}} = \boldsymbol{c}_{\boldsymbol{i}} \boldsymbol{e}^{-\boldsymbol{q}_{\boldsymbol{i}}} + \boldsymbol{r}_{\boldsymbol{i}}, \qquad \text{Poisson} \\ \dfrac{1}{2} \boldsymbol{b}_{\boldsymbol{i}} (\boldsymbol{q}_{\boldsymbol{i}} - \boldsymbol{l}_{\boldsymbol{i}})^2, & \qquad\qquad\qquad\qquad \text{WLS} \end{cases} . \end{gathered} \tag{3-27}$$

The regularization or penalty function has the general form:

$$R(\boldsymbol{x}) = \sum_{k=1}^{\boldsymbol{n}} \omega_{\psi}([\boldsymbol{Dx}]_i) \cdot \psi([\boldsymbol{Dx}]_i), \tag{3-28}$$

where $\boldsymbol{D}$ is an operator that maps the solution $\boldsymbol{x}$ to a value in the sparse space. $\psi(t)$ is called the potential function, it controls the amount of regularization for a particular value in the sparse space projected by operator $\boldsymbol{D}$. $\omega_{\psi}(t)$ is the weighting function. The penalty function is normally used to reduce noise and preserve edges in the reconstruction images. Although there exist many designs of the transformation function, an L-p norm is generally used as the transformation operator. Depends on the application, different p values could be used. For example, in discrete tomosynthesis, p can be set to 0 and $\boldsymbol{D}$ becomes the L-0 norm. The penalty function in this case ensures that the number of non-negative voxel is sparse. For low-dose CT imaging, the p can be set to be between 1 and 2. When the p is 1, the penalty function becomes the total variation of the reconstruction images.

The potential function $\psi(t)$ could strongly influence the reconstructed images. For example, a quadratic potential function would suppress the noise in the reconstruction, but at the same time, it also blur the edges. Adaptive function, like Huber function, would be used to preserve the edges while still reducing the noise. Examples of often used potential functions and their weighting functions are shown in Table 3-1.[84]

Table 3-1: Examples of potential functions and the corresponding weighting function.[84]

Potential Function	$\psi(t)$	$\omega_{\psi}(t)$
Quadratic	$t^2/2$	1
Huber	$\begin{cases} t^2/2 & \lvert t\rvert \le \delta \\ \delta\lvert t\rvert - \delta^2/2 & \lvert t\rvert \le \delta \end{cases}$	$\begin{cases} 1 & \lvert t\rvert \le \delta \\ \delta/\lvert t\rvert & \lvert t\rvert \le \delta \end{cases}$
Hyperbolic	$\delta\left[(1+(t/\delta)^2)^{1/2} - 1\right]$	$\dfrac{1}{(1+(t/\delta)^2)^{1/2}}$

q-GGMRF[85]	$\frac{\lvert t\rvert^{p}}{1+\lvert t/\delta\rvert^{p-q}}$	$\frac{\lvert t\rvert^{p-2}}{1+\lvert t/\delta\rvert^{p-q}}\left(p-(p-q)\frac{\lvert t\rvert^{p-q}}{1+\lvert t/\delta\rvert^{p-q}}\right)$

The weighting β controls the amount of the penalty in the overall cost, the value of which is usually determined empirically. If the observation is enough-sampled and has low noise level, then the regularization term should be small compared to the data fidelity term. Criteria, such as cross-validation, bias-variance trade-off, L-curves, and local-resolution, have been proposed to determine the proper β. In general, β will depends on the quality of the observation, such as noise in the projection data, the number of the projections and completeness of the Fourier space, as well as the size of the patient.

3.4.4 Minimization Algorithms

The minimization algorithm minimizes the cost function in an iterative manner. In each iteration, the cost is reduced and a new solution that is closer to the true solution is obtained. The minimization process stops once the convergence criteria are met. The computation time of the minimization algorithm is the product of two variables: the number of iterations and the average time taken to execute one iteration. A faster convergence speed would lead to fewer iterations before the minimization meets the stopping criteria, and, consequently, reduces the computation time.

A good initial guess is important if the cost function does not converge to a single global minimum. Quite often, a reconstruction image using FBP is used as an initial guess in the SIR. Although initial guess might not affect the final result in the case that the cost function is convergence, it is helpful to use a good initial guess as it would reduce the number of iterations and thus reduce the computation needed to find the cost function minimum.

Most minimization algorithms are based on the gradient. When the cost function is non-differentiable, a differentiable approximation of the cost function can be used to compute the reconstruction. More generally, one can use the optimization transfer methods or MM algorithms to solve the optimization problem.[86] In optimization transfer methods, a surrogate of the cost function will be used. The surrogate function has a special property that the minimization of the surrogate function would lead to the minimization of the cost function, as such, the optimization problem of the original cost function becomes the optimization of the surrogate function. The surrogate function can take different forms, but typically it is designed to be a quadratic function for fast convergence and a guaranteed monotonicity. A quadratic surrogate also allows both unconstrained and constrained optimizations with many existing mathematical tools. A notable example of the optimization transfer methods is the expectation maximization (EM) algorithm, where a large number of surrogates can be used including the quadratic surrogate function.

Ordered subset (OS) is a method that minimizes the cost function with an approximated gradient that computed from a subset of the observed data. Subsets are used in a cyclic order. When all the subsets are used, a new iteration starts and this process repeats itself. The theoretical foundation of the OS methods is an assumption called subset balance, in which the gradients computed from each subset are nearly the same. When this condition is valid, the gradient of the cost function computed using the complete observation would approximately equal to the gradient computed from a subset of the observation times the number of subsets. OS significantly reduces the size of gradient computation, and consequently, reduces the reconstruction time. However, OS is not monotonic, and thus it does not follow a stringent convergence because the gradient approximation would fail when the cost function is close to the true minimum. Recently, convergent OS algorithms have been proposed. However, they have a large memory requirement which is impractical to use for the current imaging systems.[87], [88]

When using the gradient to minimize the cost function, the direction of the gradient might not be the best search direction. Sometimes, the gradient even points to a direction away from the global minimum. Conjugate gradient (CG) is a minimization algorithm, in which the gradient at the current iteration and the descent direction at the previous iteration are used to the current descent direction. CG is based on the theory of the Krylov space method; it has a huge success in solving the symmetric positive definite optimization problem. A preconditioner can be used in CG method to reduce the complexity of the reconstruction problem, which leads to so-called preconditioned conjugate gradient algorithm (PCG). In PCG, the preconditioner is either an easily invertible matrix that approximates the Hessian matrix or an approximation of the inverse of the Hessian. Unlike OS, PCG is monotonic as long as a valid preconditioner is used.

One unique minimization algorithm that is worth noting here is the iterative coordinate descent (ICD) algorithm, which, unlike other algorithms that update the whole solution in each iteration, updates one voxel at a time.[85], [89] Currently used in GE's proprietary model-based iterative reconstruction software, ICD is one of the algorithms that have the highest convergence rate and is known to produce high-quality reconstruction images. However, ICD is not perfect. As ICD "randomly" choose a voxel to update, the memory access of ICD is not sequential. Therefore, the computation is hard to parallelize by either CPU or GPU. Currently, a GPU accelerated ICD algorithm is reported by grouping a patch of related voxels into a SuperVoxels. The algorithm is not fully automatic in the current version and it still requires manual tweaks for different imaging geometries.[90]

3.5 Tomosynthesis Reconstruction

The tomosynthesis image reconstruction is similar to CT, except that tomosynthesis only has a limited number of projection images as well as angular coverage. The unique characteristic results in an incomplete Fourier space and thus a limited depth resolution. Figure 3-10 illustrates the influence of angular coverage on the final reconstruction images. All images are reconstructed using 120 projections with SIRT. The reconstruction images at small angular coverage, such as 8 *deg* and 15 *deg*, are blurred with poor depth-resolution, and features with low contrast could hardly be identified. When the angular coverage increases, the depth resolution improves as well. It is not until 60 *deg* that the low contrast features start to show up in the reconstruction images. This characteristic also shows in the patient images. Figure 3-11 shows images of a patient with pulmonary nodules imaged by DXR, DCT, and CT. As can be seen, the DXR has the worst overlapping artifact. DCT provides some tissue separation and has less overlapping artifact over DXR. As a result, some pulmonary nodules that are not seen in DXR is shown in DCT. CT has no overlapping artifact, tissues at different depth are totally separated.

Due to insufficient observations, FBP algorithm could produce severe image artifacts with excessive noise for the tomosynthesis reconstruction. The iterative algorithm, on the other hand, works well with insufficient measurement as it seeks for the optimized solution rather than the exact solution. Studies have shown that iterative reconstruction produces better quality reconstruction than FBP algorithm.[13]–[15] However, iterative reconstruction algorithms are generally much slower than FBP. For DTS where typically a high-resolution detector is used, iterative reconstruction can take several hours to complete, which is impractical to use in a clinical setting that requires fast workflow.

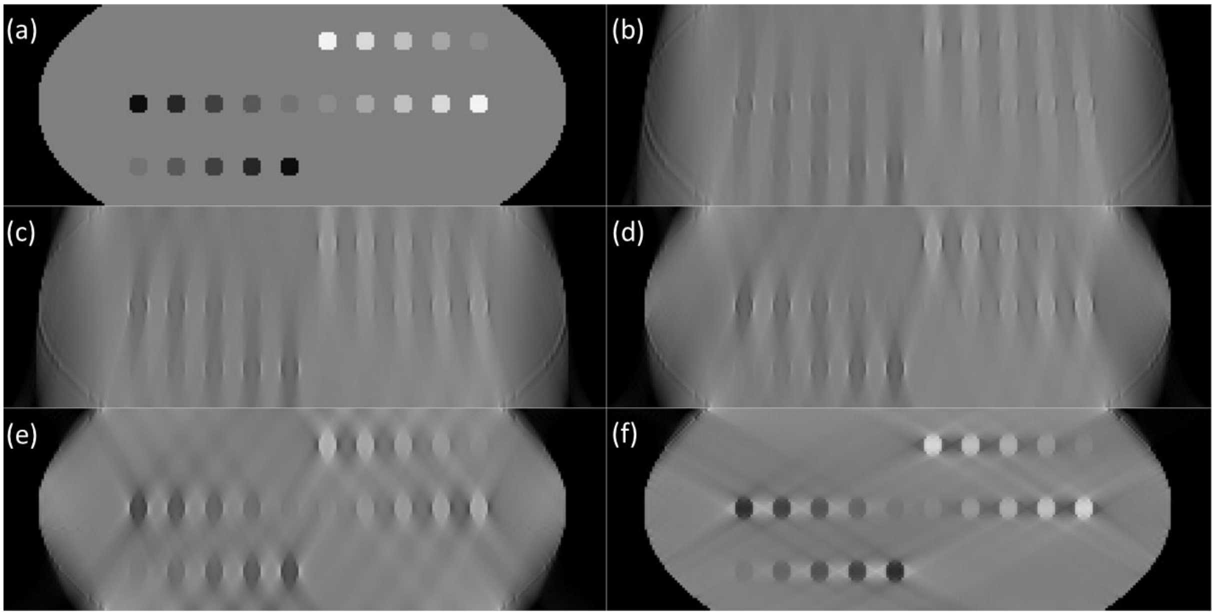

Figure 3-10: (a) Reference image. Reconstruction images using simultaneous iterative reconstruction technique with 20 iterations (b) at 8 deg angular coverage, (c) at 15 deg angular coverage, (d) at 30 deg angular coverage, (e) at 60 deg angular coverage, (f) at 120 deg angular coverage.

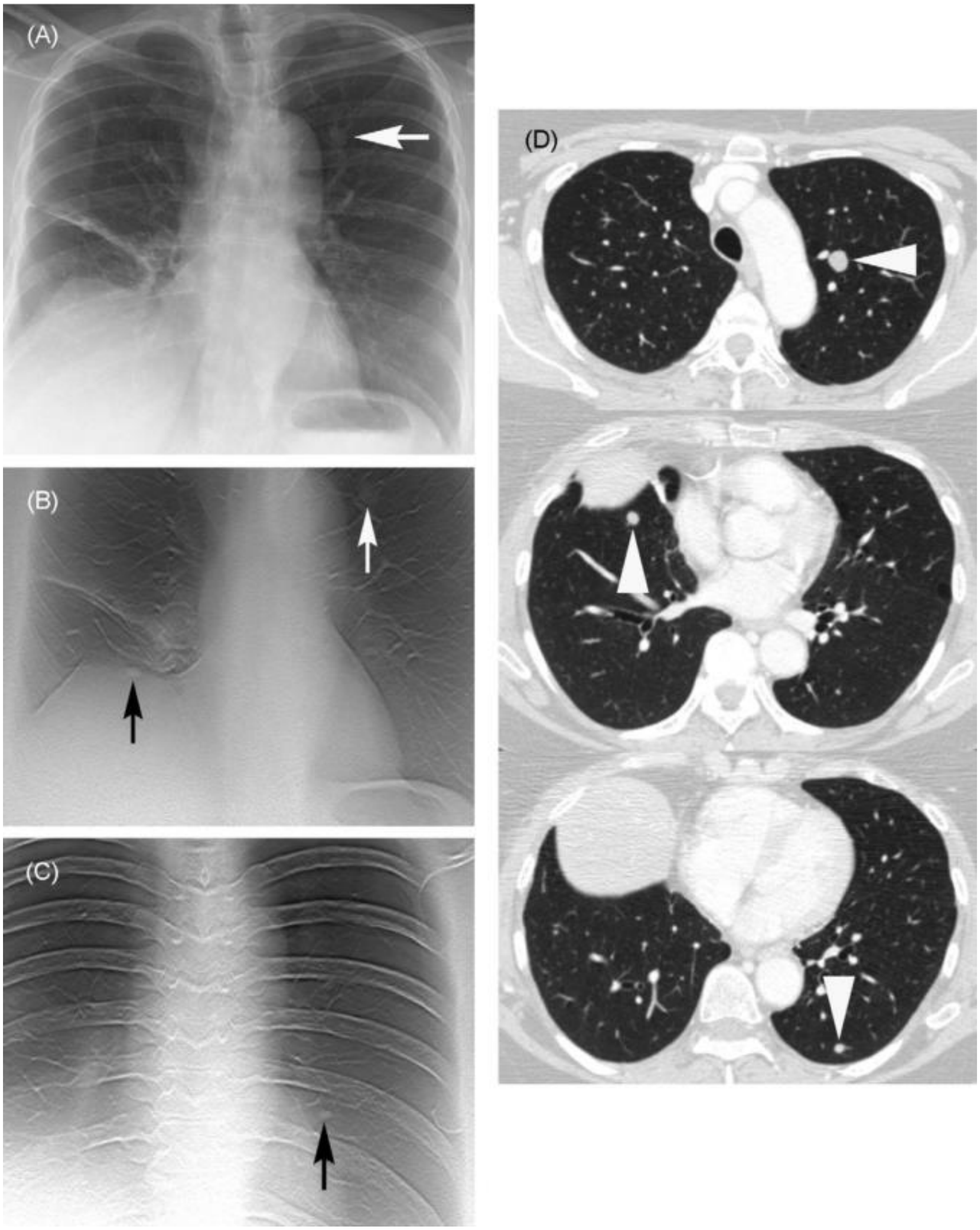

Figure 3-11: Patient with pulmonary nodules imaged by (A) chest radiography, (B)-(C) digital chest tomosynthesis, (D) CT.[40]

CHAPTER 4: Linear Tomosynthesis Image Reconstruction and Processing

In this chapter, a fast iterative reconstruction specifically designed for stationary digital tomosynthesis systems is discussed. The reconstruction algorithm, named adapted fan volume reconstruction (AFVR), breaks the 3D reconstruction problem in linear tomosynthesis into a series of 2D reconstruction, which significantly reduces the computation needed for iterative reconstruction and makes IR practical for clinical use. The AFVR algorithm is tested using both digital phantom as well as physical breast phantom on an s-DBT system. Then, the AFVR reconstruction is compared with FBP and the image quality is evaluated. Next, the implementations of AFVR on other s-DTS systems, including the s-DCT system and the s-IDT system are demonstrated. Finally, discussion and conclusion of the AFVR are discussed. In addition to the reconstruction method, I will discuss two artifact reduction techniques for both s-DBT and s-DCT imaging as well as a preliminary study of synthetic mammography technique.

4.1 Introduction

Digital tomosynthesis (DTS) is a limited-angle tomographic technique, it generates pseudo three dimensional (3D) image at a radiographic dose level.[5] By producing a 3D image, DTS reduces the tissue overlapping artifact found on two dimensional (2D) radiographic images, consequently, it has an improved diagnostic accuracy over radiography. Due to the unique combination of radiation dose and diagnostic accuracy, DTS has gained tremendous interests as a promising imaging technique for early disease screening.[3], [41], [91] Recently, several DTS systems have been developed and used in clinics, including the digital breast tomosynthesis systems by Hologic and GE as well as the chest tomosynthesis developed by GE. Clinical studies had shown that DTS greatly improves the diagnostic accuracy of disease screening over the traditional radiography or mammography.[4], [32], [38], [41], [92], [93]

A crucial step of tomosynthesis imaging is the production of 3D images from 2D measurement, which is called image reconstruction. The image reconstruction methods can be classified into two categories: the filtered back projection (FBP) algorithm, and the iterative reconstruction (IR) algorithm.[16], [18], [72], [57] FBP is based on an analytical mathematical model, it directly solves the reconstruction in two steps, filtering and back projecting the observed data.[94] IR, on the other hand, starts with an initial guess of true image and iteratively refines the estimation based on the observed data until convergence criteria are met.[17], [89], [95] A variety of physics can be modeled in the IR, such as system noise, the statistical prior of the image, and the x-ray energy spectrum. FBP is computationally fast. However, it requires sufficient measurement to produce good reconstruction images. For low dose and limited projection imaging, FBP would introduce severe artifacts to the reconstruction image. In contrast, IR is computationally expensive, but it is more flexible on the imaging geometry, and it is more tolerant to the noise in the projection data. It has been shown that IR produces significantly better reconstruction at a low dose or with limited projections.[54], [96], [97] For DTS reconstruction which is an ill-posed problem with insufficient measurement, several studies have shown that IR outperforms FBP regarding image quality.[13], [15], [22], [98]–[100] Despite the recent advances in GPU accelerated reconstruction,[34], [101]–[104] the demanding computation is still a major concern that prevents the wide acceptance of IR on clinical systems.

Our group has developed a stationary digital tomosynthesis (s-DTS) technique, using a linear x-ray source array with multiple carbon nanotube based x-ray sources.[2], [9], [10], [37], [105] This fixed-source configuration eliminates the source motion in conventional DTS system, and the electronically controlled x-ray sources also reduce the scanning time. s-DTS has a linear source geometry; this unique characteristic allows us to break the 3D reconstruction problem into a series of 2D reconstruction and dramatically speed up the computation.[106] In this paper, we demonstrate the adapted fan volume reconstruction (AFVR) algorithm for s-DTS reconstruction. The algorithm was investigated using both digital and a physical breast phantom. The reconstruction speed was evaluated and compared to the conventional 3D cone beam reconstruction algorithm. Lastly, the AFVR was used to reconstruct clinical images, and the image quality was assessed against that from a commercial software using an FBP-based reconstruction algorithm.

4.2 Adapted Fan Volume Reconstruction

4.2.1 Stationary Digital Tomosynthesis

Stationary digital tomosynthesis uses a linear source array with multiple carbon-nanotube-based x-ray sources and a fixed digital detector. Compared to the conventional DTS systems with a rotating x-ray source, the fixed source geometry in s-DTS eliminates the source motion blur and has a reduced scanning time. Figure 4-1(a) illustrates a stationary digital breast tomosynthesis (s-DBT) system, in which the x-ray source array is parallel to the detector. X-ray sources in the linear array fire x-rays sequentially, each firing creates a projection image with a unique imaging position. After all sources fire and the projection images are acquired, a computer is used to reconstruct the 3D object from the measured data.

In this study, an s-DBT system previously developed by our lab is used to demonstrate and to evaluate the proposed AFVR algorithm.[10], [55] The s-DBT system is built by retrofitting a linear source array with 31 CNT-based x-ray sources on a Hologic Selenia Dimensions mammography system, the angular span of the source array is 30 degree. The digital detector in the s-DBT has 3328 by 4096 pixels, the size of each pixel is 70 um. The s-DBT system is currently undergoing clinical trial at N.C. Women's hospital.[107] Figure 4-1(b) shows a picture of the s-DBT system.

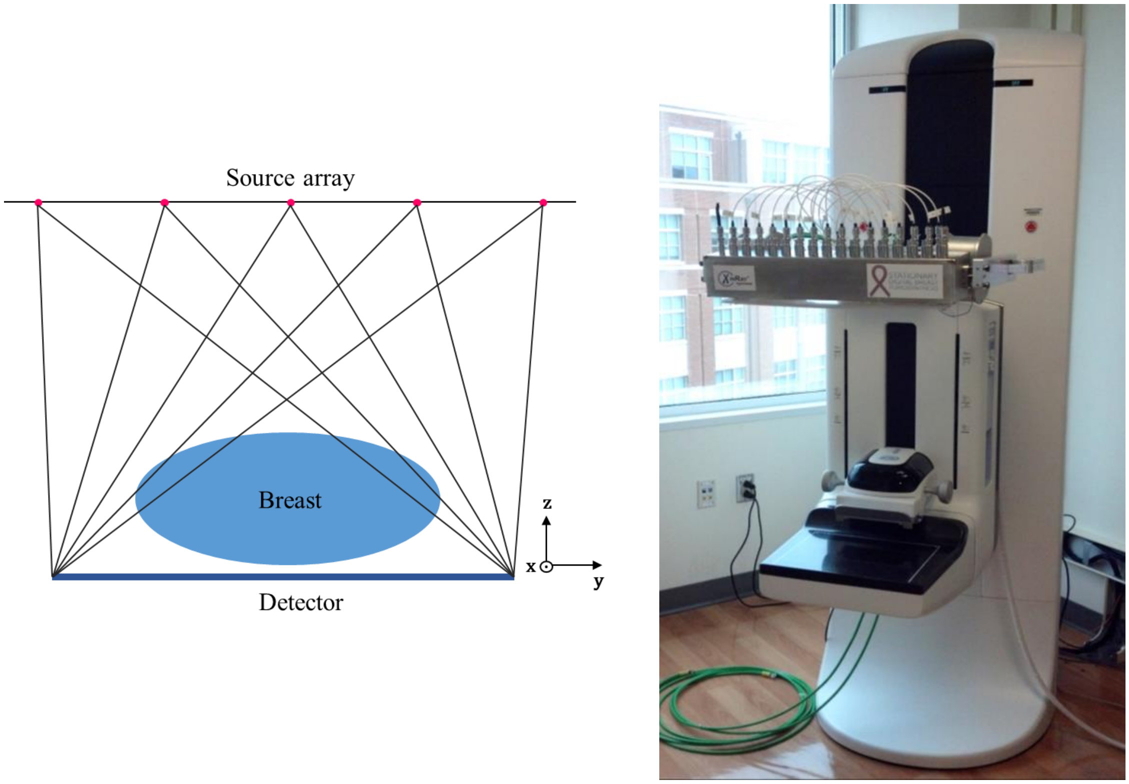

Figure 4-1: (a) Schematic diagram of the s-DBT system. The dots on the linear source array indicates multiple equal-spaced x-ray sources. (b) A picture of the stationary digital breast tomosynthesis system.

4.2.2 Adapted Fan Volume Reconstruction

In iterative reconstruction, the imaging process is modeled as a system of linear equations:

$$\boldsymbol{b} = \boldsymbol{A} \cdot \boldsymbol{x} + \boldsymbol{\varepsilon}\,, \tag{4-1}$$

where $\boldsymbol{b}$ is the measured projection data, $\boldsymbol{x}$ is the imaged object to be reconstructed, $\boldsymbol{\varepsilon}$ is the additive noise, and $\boldsymbol{A}$ is the system matrix, or projection matrix, which models the interaction between x-ray and the imaged object. Due to the size of the problem, direct solving $\boldsymbol{x}$ in a one-step is difficult. IR starts with an initial guess of $\boldsymbol{x}$, and update the solution iteratively until certain convergence criteria is met. Each iteration in IR consists a forward projection and a back projection. In forward projection, a simulated measurement based on the current guess of the solution will be generated. In back projection, the simulated measured is compared with the true measurement $\boldsymbol{b}$ and the difference between the two is used to update the solution for next iteration. The system matrix $\boldsymbol{A}$ is used in both forward projection and back projection. The size of the system matrix is generally quite large for both CT and tomosynthesis, for example, the size of $\boldsymbol{A}$ is in the order of 10^{17} for the s-DBT system. As a result, the matrix $\boldsymbol{A}$ is usually computed on-the-fly repeatedly in each iteration, which is computationally expensive.

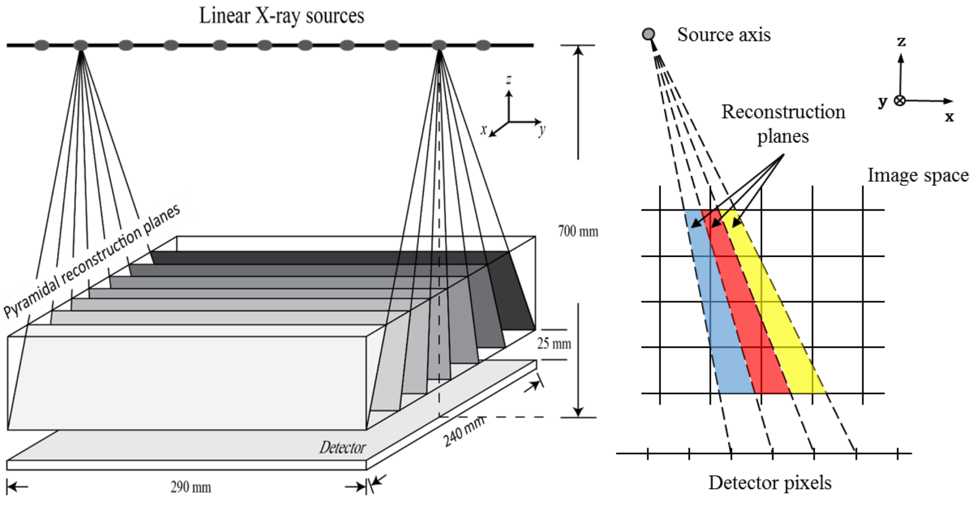

(a) (b)

Figure 4-2: (a) Schematics of the AFVR. The linear source array and each detector row cut the image space into a series of thin slabs. (b) A side view of image space, three fan volumes corresponding to three detector rows are marked in the diagram.

In linear tomosynthesis, the linear source array is parallel to each detector row. This unique imaging geometry allows a fast reconstruction technique, named adapted fan volume reconstruction (AFVR).[106], [108] As shown in Figure 4-2, the line of the source array and a detector row intersect the image space into multiple thin slabs, each can be considered as a 2D plane. Consequently, we can transform the 3D cone beam reconstruction into a series of 2D reconstructions, each has a significantly small problem size. The system of linear equations in AFVR can then re-written as:

$$\boldsymbol{b} = \boldsymbol{A} \cdot \boldsymbol{x} + \boldsymbol{\varepsilon} \rightarrow \begin{cases} \boldsymbol{b_1} = \boldsymbol{A_1} \cdot \boldsymbol{x_1} + \boldsymbol{\varepsilon_1} \\ \boldsymbol{b_2} = \boldsymbol{A_2} \cdot \boldsymbol{x_2} + \boldsymbol{\varepsilon_2} \\ \cdots \\ \boldsymbol{b_n} = \boldsymbol{A_n} \cdot \boldsymbol{x_n} + \boldsymbol{\varepsilon_n} \end{cases}, \tag{4-2}$$

where n is the total number of fan volumes. By transforming the 3D reconstruction to a series of 2D reconstruction, AFVR dramatically reduces the complexity of the reconstruction and offers a straightforward implementation of parallelization. In addition, as the problem size is reduced, the system matrix of each fan volume can be stored in the memory and no need to be computed in every iteration. As such, accurate but computationally demanding projection model can be used without significantly reduce computation speed. Lastly, the fan volume reconstruction improves the data locality of the computation, consequently, improves the reconstruction speed.

For many forward projection models involving intersection length, such as ray-driven model and distance-driven model.[70], [57], [109] Furthermore, additional optimization can be performed to speed up the computation further. Considering two adjacent fan volumes, one can be viewed as a stretched version of the other. The dimension in the y direction shown in Figure 2 remains the same between the two fan volumes, while the dimension in the beam transmission direction, referred as *t* direction, is stretched. Since length can be computed uses its components in every direction, one can pre-compute two components of the system matrix, $\boldsymbol{A}_y$ and $\boldsymbol{A}_t$, of a reference fan volume, and quickly compute the matrix for each fan volume using:

$$\boldsymbol{A}_i = \sqrt{{\boldsymbol{A}_y}^2 + \lambda_i {\boldsymbol{A}_t}^2}\,, \tag{4-3}$$

where λ_i is the stretch ratio of the i-th fan volume respect to the reference fan volume. If the reference volume is set to be the fan volume that is perpendicular to the detector, then the stretch ratio is

$$\lambda_i = \frac{SDD^2 + (x_i - x_{source})^2}{SDD^2}\,, \tag{4-4}$$

where SDD is the source to detector distance, x_i is the i-th fan volume detector row position and x_{source} is the source position in x direction. This provides a more efficient way to compute the system matrix $\boldsymbol{A}$ than individually computing each element of the matrix.

Figure 4-3 shows a flow chart of the AFVR. The first step is preprocessing the raw projection data and re-group the data for fan volume reconstruction. Next, all fan volumes are reconstructed parallel. After the reconstruction complete, all fan volumes will be stitched together. As the voxel closer to the source has a thinner width in each fan volume (as shown in Figure 4-2(b)), an additional correction will be performed to compute the 3D image with correct dimension.

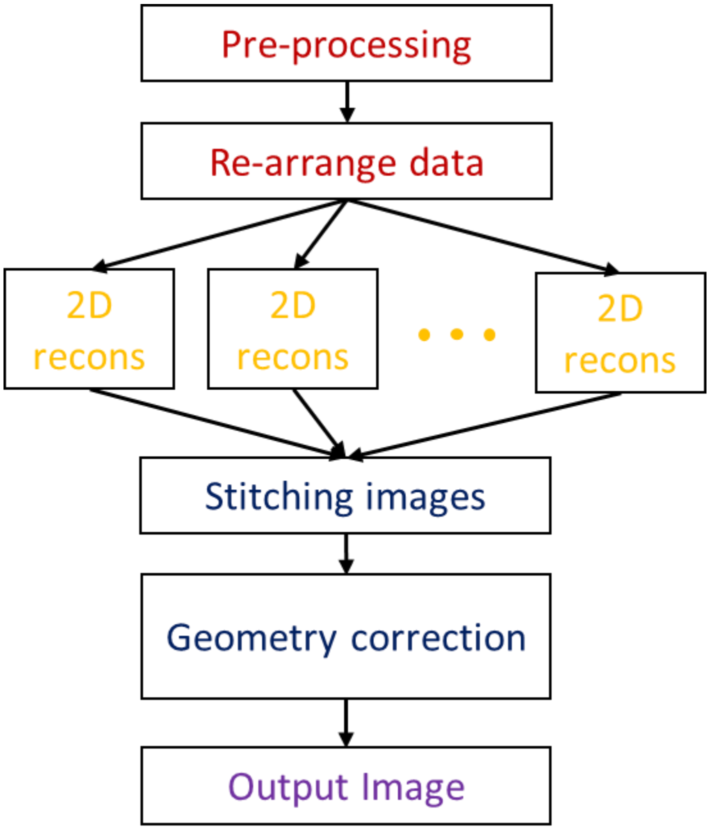
Pre-processing
Re-arrange data
2D recons
2D recons
• • •
2D recons
Stitching images
Geometry correction
Output Image

Figure 4-3: A flow chart of the AFVR.

4.2.3 Reconstruction Kernel

A variety of reconstruction algorithms can be used to reconstruct the fan volumes in AFVR. In this study, we used a simple simultaneous iterative reconstruction technique (SIRT) for the fan volume reconstruction.[72] The update step in SIRT can be expressed as:

$$\boldsymbol{x}_{k+1} = \boldsymbol{x}_k + \alpha_k \boldsymbol{D}_c{}^{-1} \boldsymbol{A}^T \boldsymbol{D}_r{}^{-1} (\boldsymbol{b} - \boldsymbol{A}\boldsymbol{x}_k)\,, \tag{4-5}$$

where $\boldsymbol{x}_{k+1}$ and $\boldsymbol{x}_k$ are the solution at *k+1* iteration, *k* iteration, α_k is the relaxation parameter that controls the amount of update, $\boldsymbol{D}_c$ and $\boldsymbol{D}_r{}^{-1}$ are diagonal matrices defined as:

$$\boldsymbol{D_c} = diag\left(\|\boldsymbol{a}_j\|_1\right), \quad \boldsymbol{D_r} = diag\left(\|\boldsymbol{a}^i\|_1\right), \tag{4-6}$$

where $\left\|\boldsymbol{a}_{\boldsymbol{j}}\right\|_{\mathbf{1}}$ and $\left\|\boldsymbol{a}^{\boldsymbol{i}}\right\|_{\mathbf{1}}$ are the L-1 norm of the j-th column and that of the i-th row of the system matrix, respectively.

4.3 Projection Model

4.3.1 Ray-driven Method

In the ray-driven (RD) model, the x-ray beam is modeled as a pencil beam emitted from the point source to the center of a detector pixel. The x-ray beam intersects with several voxels before it arrives the detector, and the intersection length is then used to compute the weighting coefficient for each voxel, which is the element A_{ij} in the system matrix. There are several implementations of this RD model, the two classical approaches are Siddon's algorithm and Joseph's algorithm, as shown in Figure 4-4(a) and 4-4(b) respectively. In Siddon's algorithm, the intersection length is used directly as the contribution of each voxel to the attenuation line-integral. In Figure 3-4(a), the contribution of voxels 1 and 2 to the projection line *i* is computed as:

$$p_i \mathrel{+}= L_1\mu_1 + L_2\mu_2. \tag{4-7}$$

In Joseph's method, the projector coefficient is computed as a product of the intersection length times the interpolation of the nearest voxels. This method is shown schematically in Figure 3-4(b), where the contribution of voxels 1 and 2 to the projection line *i* is computed as:

$$p_i \mathrel{+}= L\frac{a_2\mu_1 + a_1\mu_2}{a_1 + a_2}. \tag{4-8}$$

Alternative implementations of the RD model have also been proposed, such as a general step-size approach with interpolation using more nearest voxels and the strip integral method.[110], [111] Those algorithms generally improve the smoothness of the reconstruction; however, they are typically more computationally expensive.

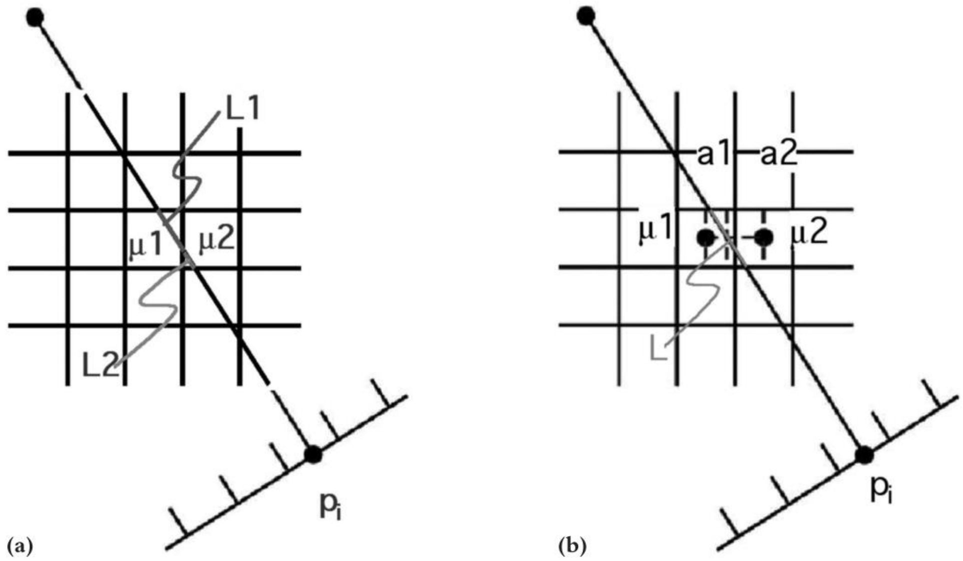

Figure 4-4: Illustration of two classical ray-driven models: (a) Siddon's algorithm with intersection length, (b) Joseph's linear interpolation method.[57]

3.3.2 Distance-driven Method

In both PD model and the RD model, the forward and back projection are not the transpose of the other. As a result, iteratively apply forward and back projection would amplify errors and cause high-frequency artifacts. Several approaches have been proposed to address this issue, including using an unmatched projection pair,[112] Fourier-based projection,[62], [63], [65] pixel decomposition,[113] and projector with different interpolation methods.[114]

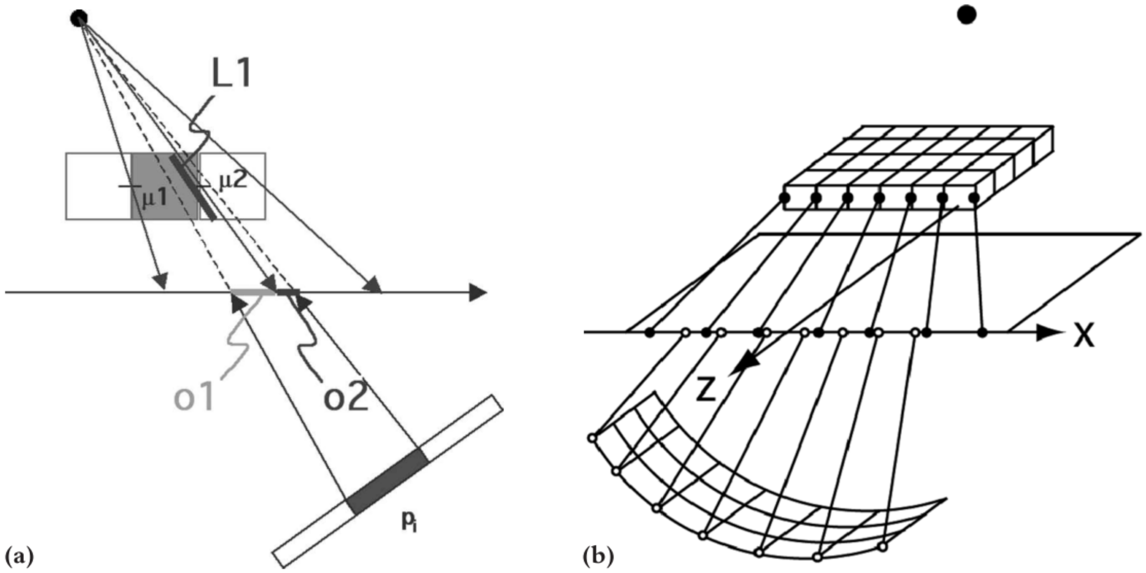

Figure 4-5: Schematic diagram of (a) 2D distance-driven method, and (b) 3D distance-driven method.[57]

De Man proposed a different projection model, called distance-driven (DD) model, which has mathematically transposed forward and back projector.[109], [115], [116] In DD model, the detector pixel and the image voxel are modeled with a finite width, as illustrated in Figure 4-5(a). The weightings are computed by projecting the boundaries of detector pixels and image voxels onto the same axis, and the overlap length is used as the weighting coefficient. In Figure 3-5(a), the contribution of the voxels 1 and 2 to the projection line *i* is computed as:

$$p_i \mathrel{+}= L_1 \frac{o_1\mu_1 + o_2\mu_2}{o_1 + o_2}. \tag{4-9}$$

DD method has a low arithmetic cost and a sequential memory access; therefore, it is computationally efficient. DD method is also fairly accurate as an approximation to the true integral method. Reconstruction images using three different projection methods are shown in Figure 4-6 (FBP reconstruction) and Figure 4-7 (MLEM reconstruction).[115] Compared to PD method and RD method, DD method generates smoother images with less high-frequency artifacts.

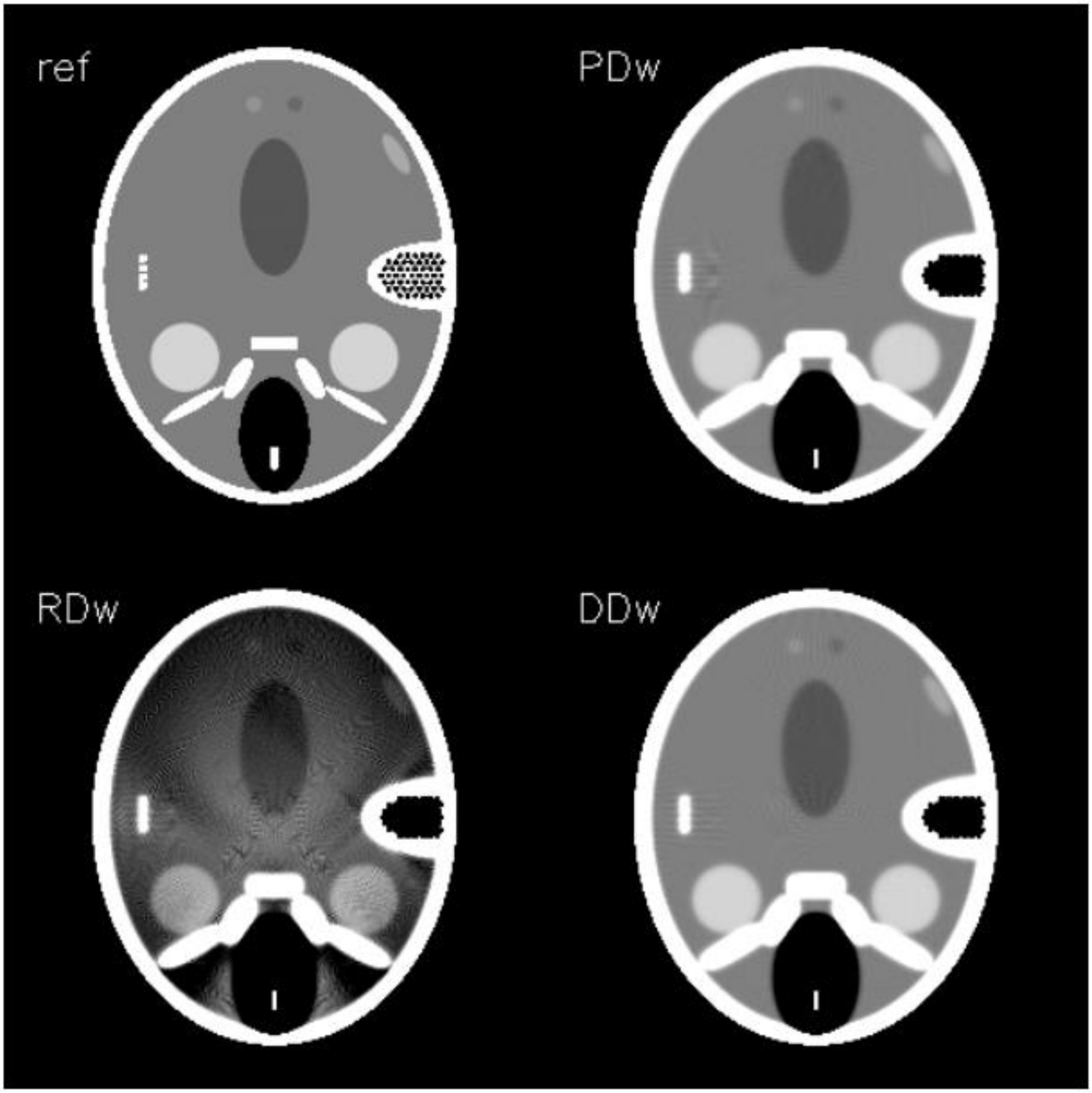

Figure 4-6: FBP reconstruction of a head section: reference image, pixel-driven FBP, normalized ray-driven FBP, and distance-driven FBP.[115]

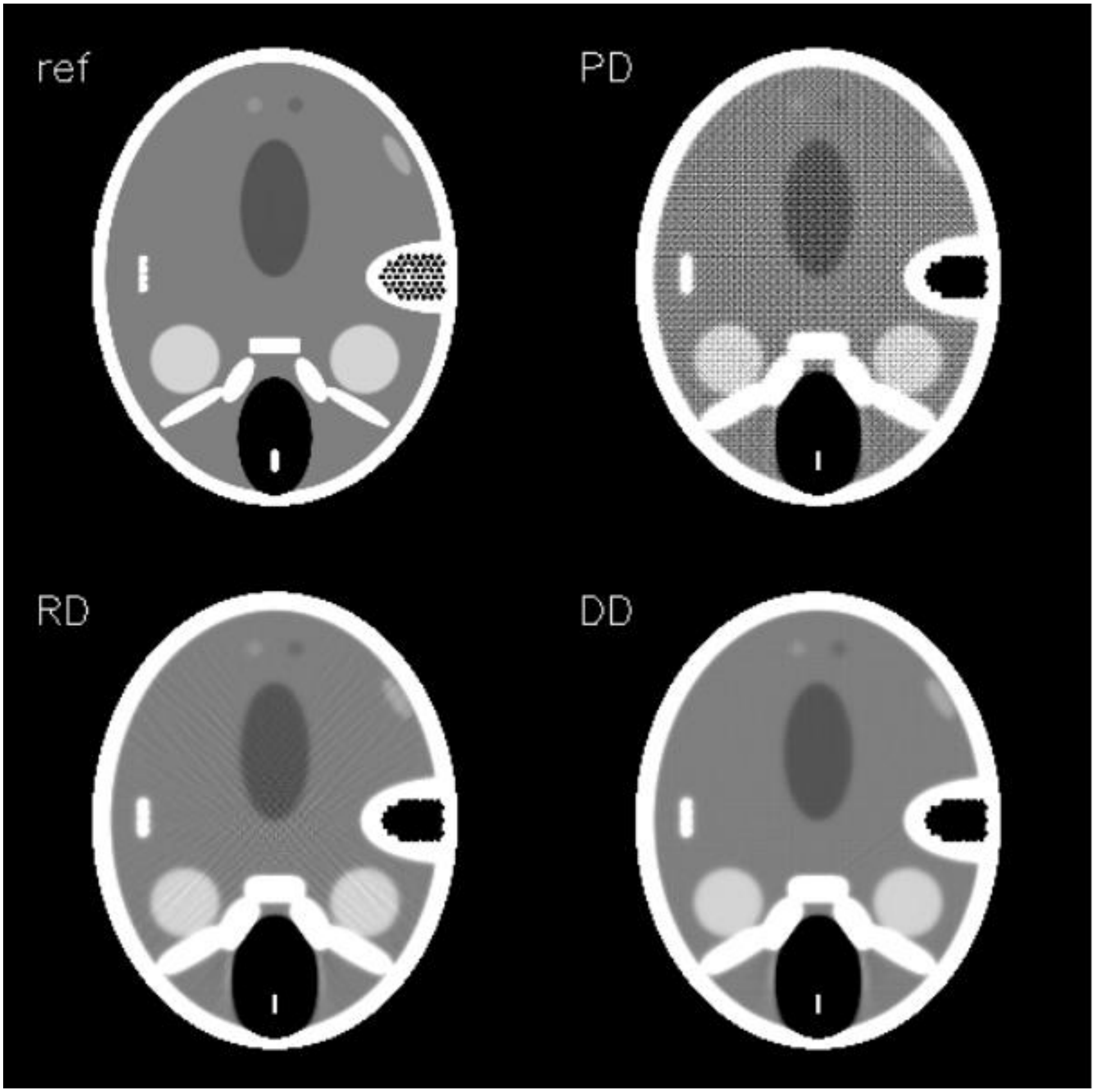

Figure 4-7: Iterative reconstruction of a head section using maximum likelihood (ML) algorithm: reference image, pixel-driven ML reconstruction, ray-driven ML reconstruction, and distance-driven ML reconstruction.[115]

4.3.3 Use Distance-driven Model to Remove the Line Artifact

It is known that primitive projection models, such as pixel-driven model and ray-driven model, would introduce the high-frequency artifact in the reconstruction image. Especially for iterative reconstruction, where the projection error accumulates in every iteration. This high-frequency artifact can be reduced or eliminated by using a more accurate projection models at the cost of more computation. In the conventional 3D cone beam reconstruction, a trade-off is typically required between the accuracy of the projection model and the computation time. In AFVR, the system matrix for each fan volume is only required to compute once, and the result will be stored in the memory. Therefore, a more accurate projection model can be used, and the computational cost will be amortized among all iterations. Here, we demonstrate the reduction of the high-frequency noise by implementing the distance-driven projection model in the AFVR. Figure 4-8 shows the tomosynthesis reconstruction images of a Shepp-Logan phantom using the ray-driven model and the distance driven model. The reconstruction is performed using AFVR and SIRT algorithm with 20 iterations; the s-DBT imaging geometry is used in this simulation. As can be seen from the figure, the reconstruction using RD model has many high-frequency line artifacts; with the DD model, the artifacts are significantly reduced. It should be noted that the high-frequency artifact is the combined result of both the simple projection model and the limited number of projections in tomosynthesis imaging. The artifact also reduces when the number of projection increases.

Figure 4-9 shows reconstruction slices of a patient's breast imaged by s-DBT. Multiple line artifacts are observed on the reconstruction slices with the RD projector. On the other hand, the reconstruction slice with the DD projector is quite smooth without any noticeable line artifacts. A line profile of the reconstruction slices is shown in Figure 4-10. The spikes shown in the line profile of the RD modeled reconstruction are eliminated in that of the DD modeled reconstruction.

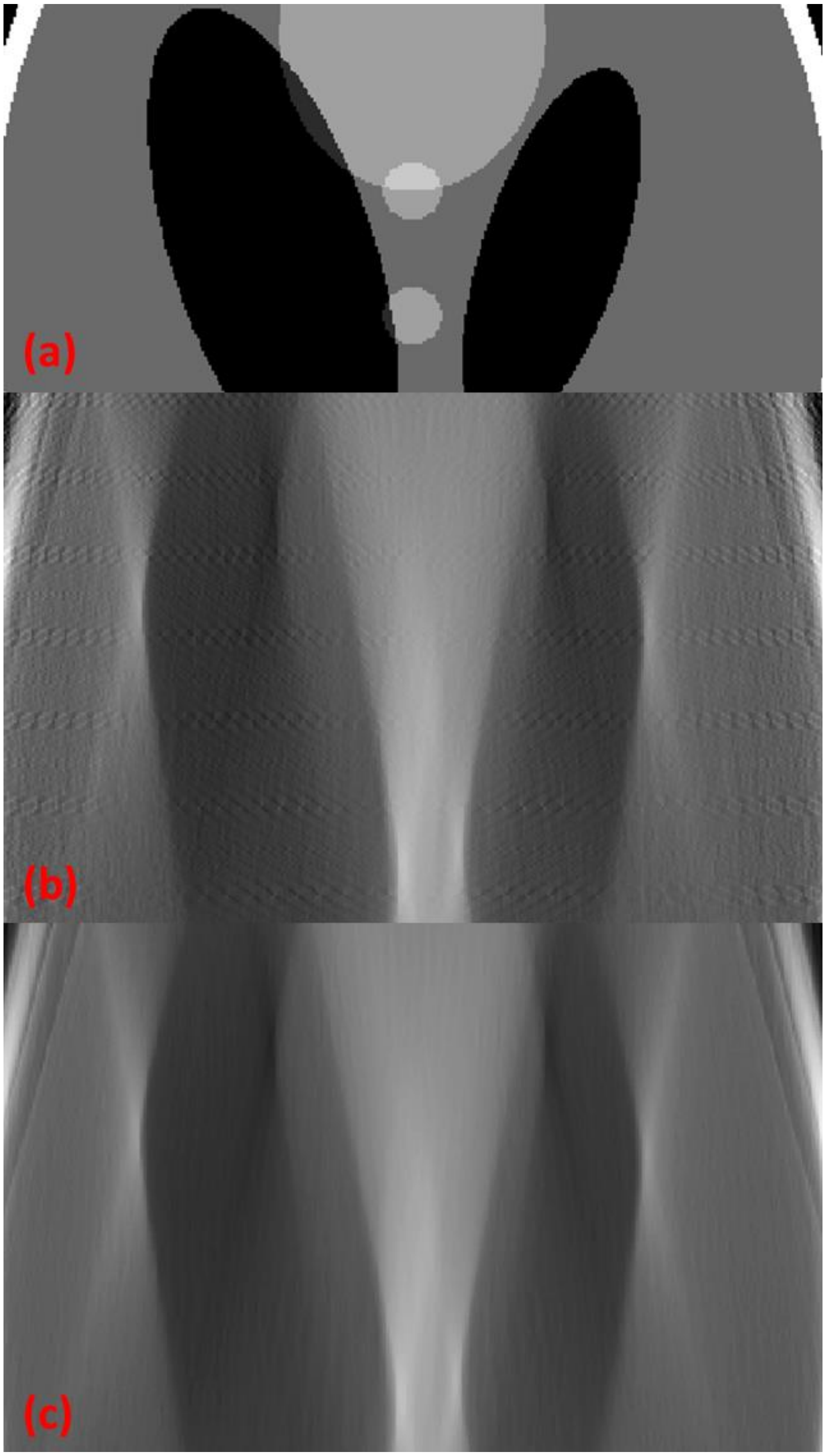

Figure 4-8: Enlarged view of (a) a Shepp-Logan phantom, AFVR-SIRT reconstruction of the Shepp-Logan phantom (b) using ray-driven projection model, and (c) using the distance-driven projection model.

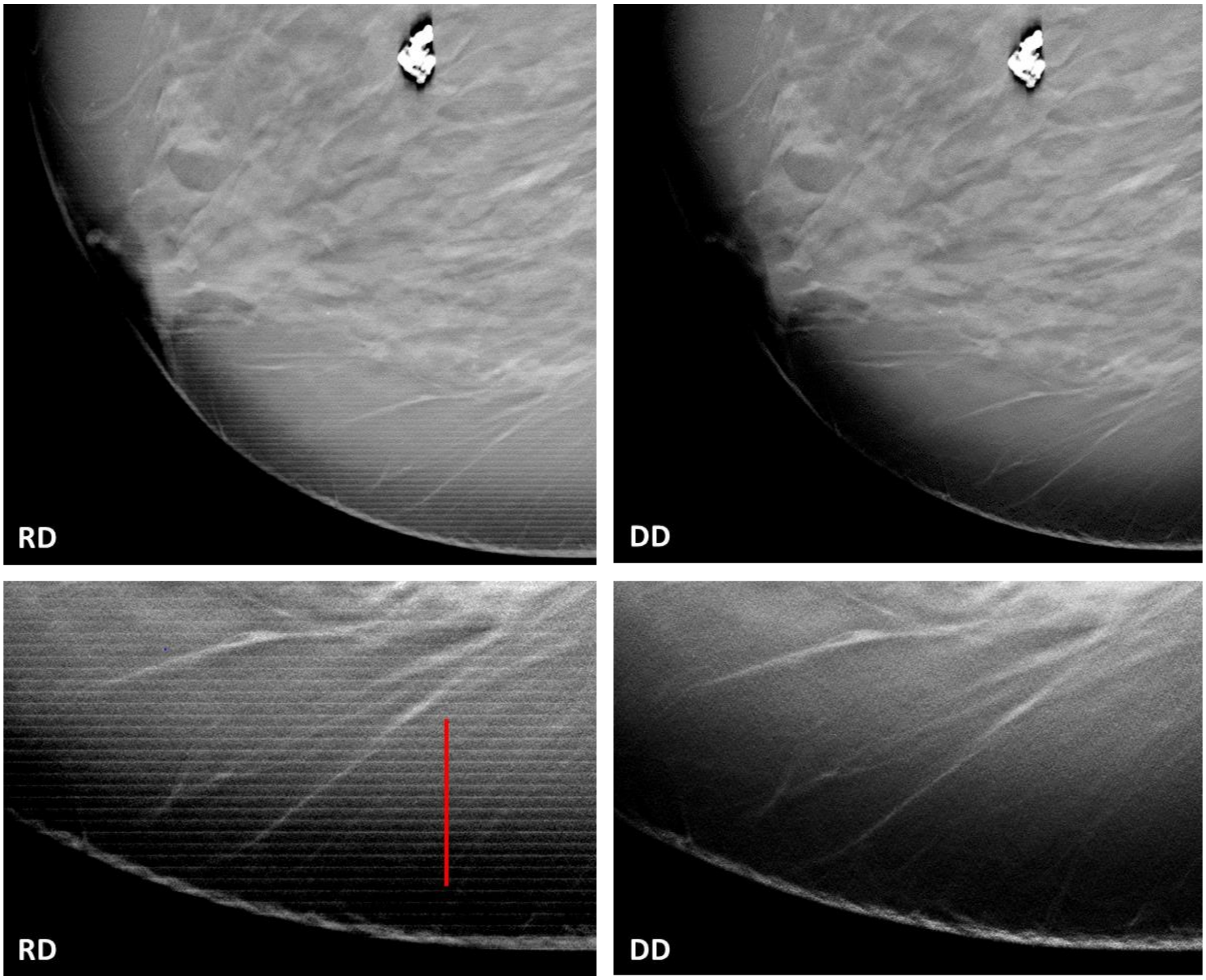

Figure 4-9: Reconstruction slice using (Left) ray-driven projection model, and (Right) distance-driven projection model.

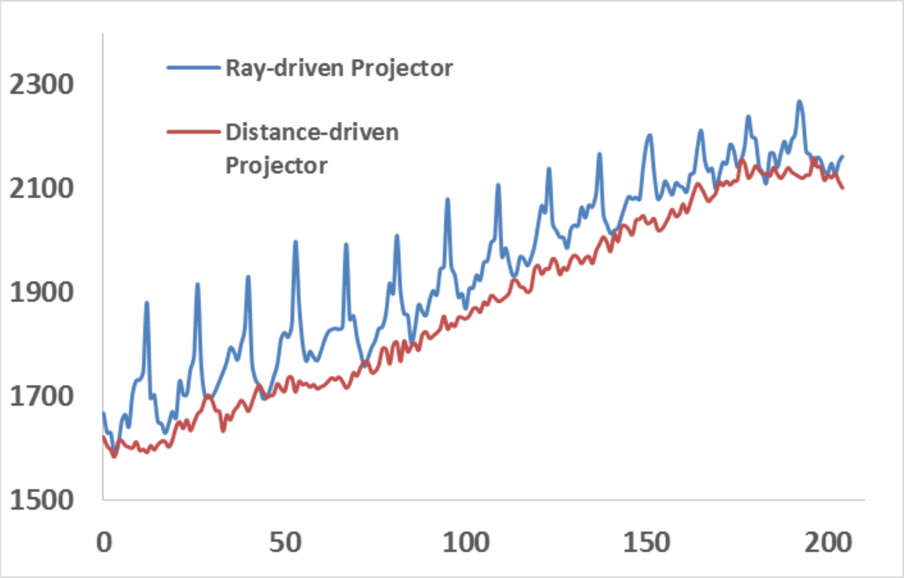

Figure 4-10: Line profile of the reconstruction slice using the ray-driven projector and the distance-driven projector

4.4 Evaluation

4.4.1 Reconstruction Time

AFVR improves the reconstruction speed from several aspects. First, the problem size is significantly reduced in AFVR compared to the conventional 3D reconstruction. Consequently, the system matrix in AFVR has a much smaller size and can be stored in the computer memory. This avoids repeatedly computing the system matrix in every iteration and speeds up the computation. Secondly, AFVR is highly parallelizable as each fan volume can be fully reconstructed without knowing other fan volumes. Without much efforts or utilizing the GPU hardware, the reconstruction can be easily accelerated using multiple-core CPU. Finally, AFVR allows a more sequential data access, as such, the CPU cache can be utilized to improve the computation speed further.

Based on the imaging geometry of the s-DBT system, we quantitatively measured the computation time of AFVR and convention 3D cone beam reconstruction. SIRT algorithm was used as the back projection method. Three reconstruction settings were used, namely 5, 10, and 20 iterations. The reconstruction was run on a customized workstation with 6-cores Intel Core i7-5790K CPU and 32 GB memory, and the AFVR is accelerated with the 6 cores. Each reconstruction was run three times, and the results are shown in Table 4-1. Compared to the conventional 3D reconstruction, AFVR speeds up the computation by 30 to 50 times.

Table 4-1: Reconstruction time

Reconstruction Method	Reconstruction Time (mins)		
	5 iterations	10 iterations	20 iterations
AFVR-SIRT	7.4 ± 0.2	9.7 ± 0.2	13.1 ± 0.3
3D cone beam recon	185 ± 3	360 ± 2	704 ± 2

4.4.2 Image Resolution

It has been well-known that FBP reconstruction produces excessive noise for ill posed imaging problem, e.g. digital tomosynthesis with insufficient projection or low dose imaging problem. The increased noise strongly affect the overall image quality, especially it degrades the detectability of low-contrast or small features. Practically, a de-noise filter is usually used in FBP to reduce the noise in the final reconstruction image, which, at the same time, reduce the spatial resolution, causing image blur.

Iterative reconstruction, in contrast, has demonstrated a better noise-resolution trade-off, as the noise is better modeled and the imaging geometry is less important in IR. In this part, we compared the reconstruction image resolution between the AFVR and an FBP-based reconstruction for the s-DBT system. For FBP reconstruction, a commercial image reconstruction software, RTT, which is specialized for digital breast tomosynthesis reconstruction (Real time tomography, LLC. USA) was used. For AFVR, SIRT algorithm together with the distance driven projector was used, the number of iteration number was set to be 20. Two detector modes were investigated, namely the full resolution mode with a pixel size of 70 um and the 2 by 2 binning mode with an effective pixel size of 140 um. Hologic Selenia Dimensions DBT system (Hologic, Inc. USA) was also added into the comparison.

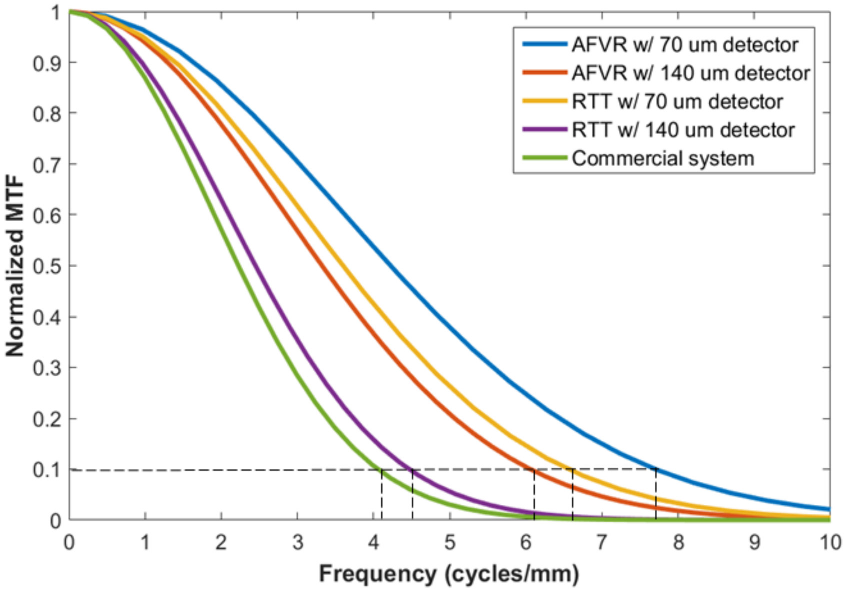

Figure 4-11: Normalized MTF curves

The image resolution was quantified using the frequency at 10% modulation transfer function (MTF). A tungsten wire phantom was used to measure the system MTF curve. The wire phantom was first imaged by the s-DBT system and then reconstructed through two different methods. From the in-focus reconstruction slices, the modulation transfer function curves were calculated using the super-sampling method. The MTF curves at different settings are shown in Figure 4-11, the frequencies at 10% MTF are shown in Table 4-2. With the same reconstruction

(RTT), s-DBT showed a better image resolution, i.e. a higher frequency at 10% MTF, in the binning mode. This is because s-DBT eliminates the source motion blur found in the conventional DBT systems with a mechanical moving source. Comparing IR and FBP for s-DBT reconstruction, IR produced better image resolutions in both full resolution mode and binning mode. Overall, AFVR with SIRT improves the image resolution by 26% in full resolution and 47% in binning mode.

Table 4-2: Frequency at 10% MTF

		Full resolution (line per mm)	Binning mode (line per mm)
s-DBT	AFVR	7.7	6.6
	FBP	6.1	4.5
Hologic DBT system (FBP)		NA	4

4.4.3 Clinical Images

Figure 4-12 and Figure 4-13 are two examples of reconstructed breast images in CC view from the s-DBT system. Figure 4-12 shows a fatty breast, where the AFVR reconstructed image shows better contrast and more details over the image from RTT. Figure 4-13 shows reconstructed images of a breast with a malignant tumor. The tumor is located in the top-left region of the breast with several blood vessels extended to the skin. AFVR reconstructed image shows better contrast too for this breast; also the image looks smoother compared to the RTT reconstructed breast image (lower noise level).

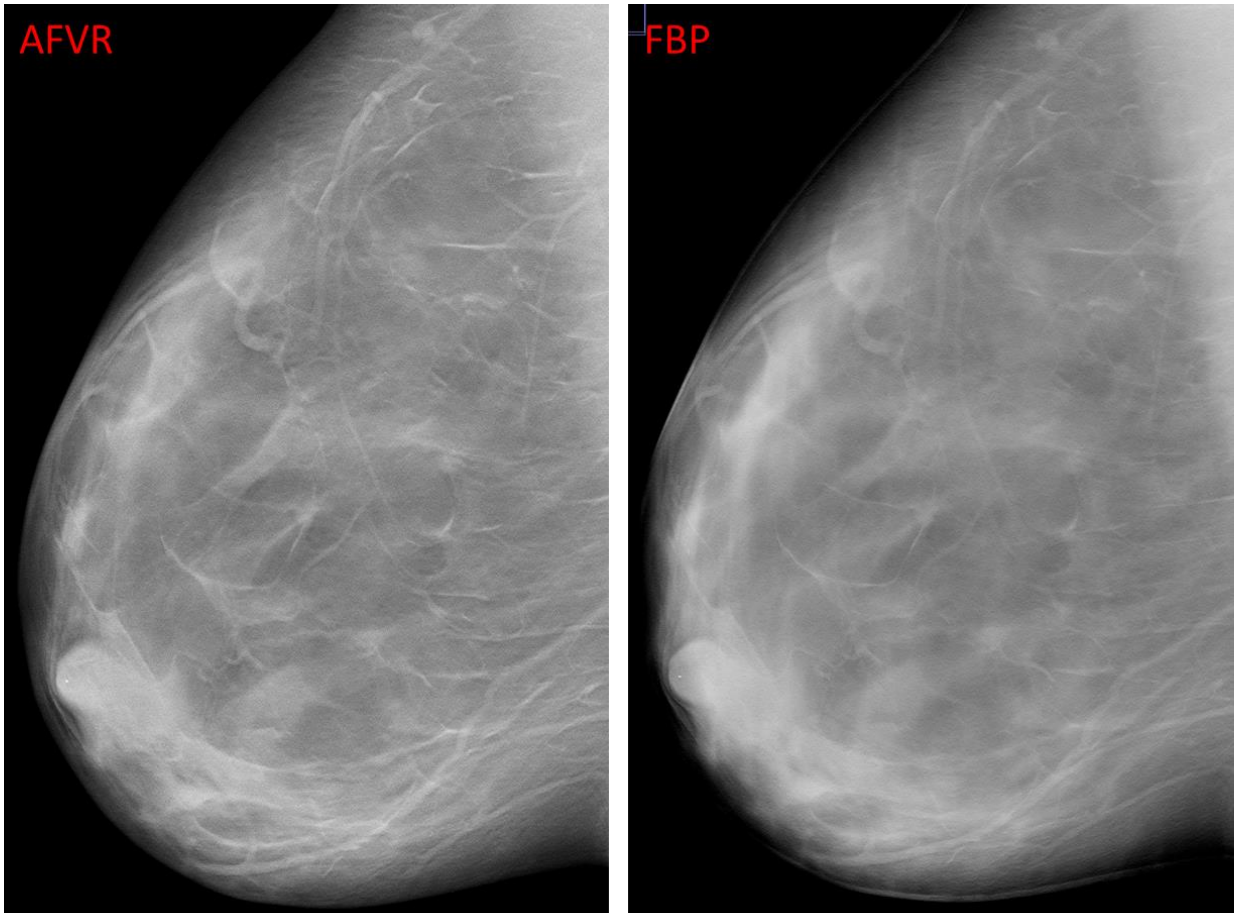

Figure 4-12: Image of a fatty breast reconstructed by AFVR-SIRT and RTT.

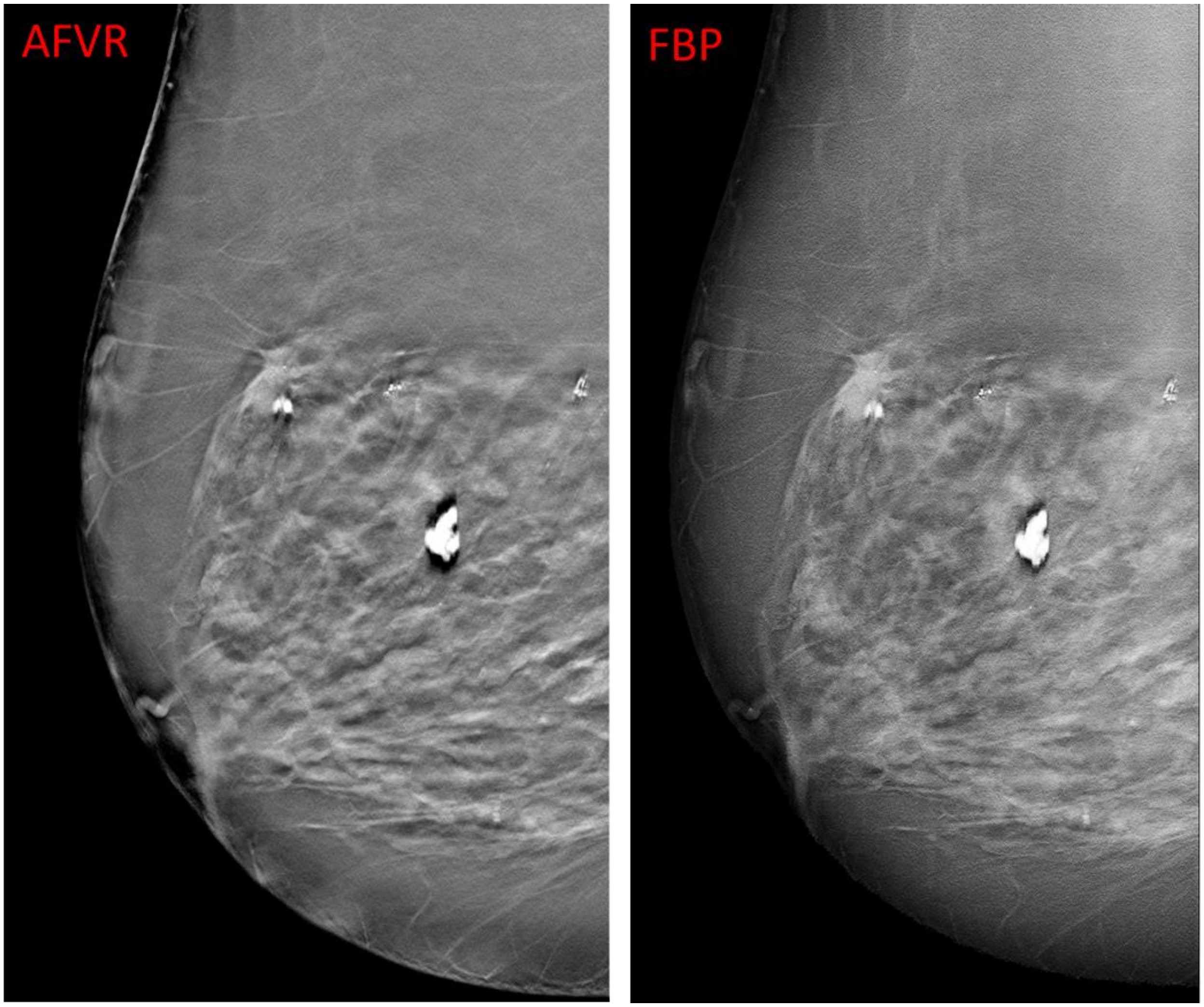

Figure 4-13: Reconstructed breast image with carcinoma.

4.5 s-DCT Reconstruction

4.5.1 s-DCT System

The s-DCT system has a similar system setup as the s-DBT system, namely a linear source array combined with a flat panel detector. The system specification of the s-DCT system, however, is different as it is optimized for the chest imaging. Specifically, the x-ray tube is operated at 80 kVp for a better penetration through the thick body, the SID is 100 cm to 130 cm adjustable, the angular coverage is 15 degree, and the detector pixel size is 194 µm. A second generation of the x-ray source array for the s-DCT system, which is operated at 120 kVp and has a wider angular coverage, is currently being developed. Figure 4-14 shows the s-DCT system which is undergoing clinical trials at the biomedical research imaging center at UNC Chapel Hill.[8], [117]

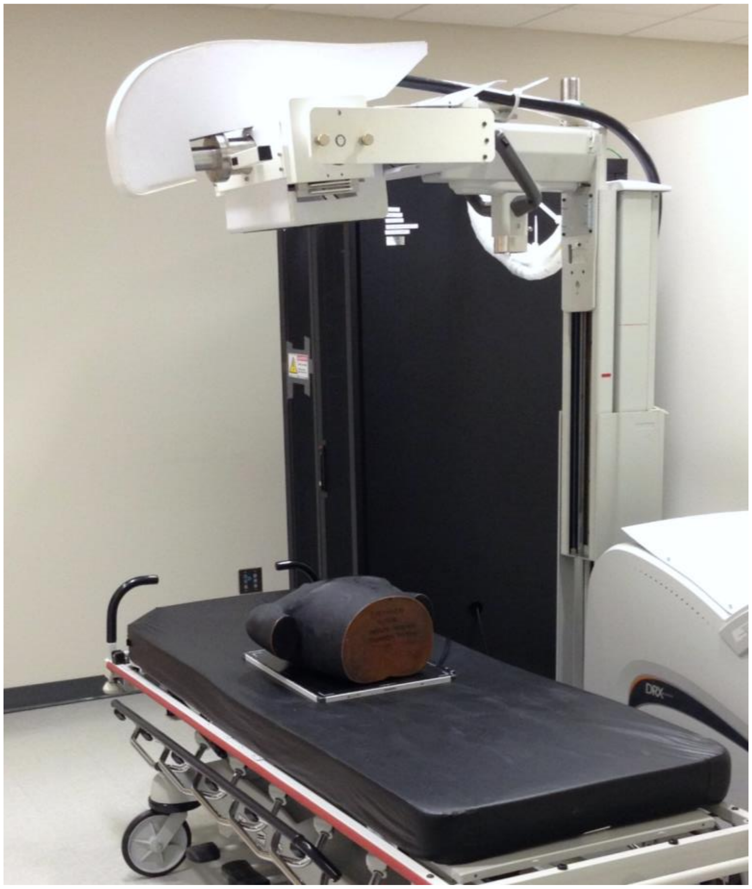

Figure 4-14: s-DCT system.

4.5.2 Projection Data Alignment

Unlike the s-DBT system where both the source array and the detector are fixed on the system, the s-DCT system has adjustable source array and detector. Consequently, the source detector position varies and the source array might not be parallel to each detector row in practice. In order to use AFVR, the raw projection data needs to be resampled so that the data is “aligned” with the source array before reconstruction. The resampling is performed in the following steps:

first, the tilted angle is computed from the imaging geometry. Second, the raw projection data is padded on the boundary to increase the FOV artificially. Thirdly, a bi-cubic interpolation is performed, and the interpolated projection data is cropped so that FOV stays the same. After the resampling, the projection data is sent to AFVR for reconstruction.

4.5.3 Clinical Images

Here we show two examples of s-DCT images reconstructed using AFVR and RTT. The imaged object is an anthropomorphic chest phantom (Model RS-320, Radiology Support Devices, Long Beach, CA) with porcine lung and heart placed inside. An air pump was used to inflate the porcine lung through a plastic tube into the lung airway. In-focus slices of lung airways are shown in Figure 4-15, and the in-focus slices of the spine are shown in Figure 4-16. As demonstrated, the AFVR reconstructed image shows a higher contrast of the lung airways as wells as more details such as bone structure, while the RTT reconstructed image looks blurry. It should be noted that RTT is specifically designed and optimized for digital breast tomosynthesis, which could contribute to its mediocre image quality. A human chest phantom was also imaged using the s-DCT system, the reconstruction images using AFVR are shown in Figure 4-17. As can be seen from the figure, tomosynthesis significantly reduce the overlapping tissue problem in conventional chest radiography, different organs are well separated and clearly shown in different reconstruction slices. A typical s-DCT reconstruction takes about 10 to 15 minutes on MATLAB.

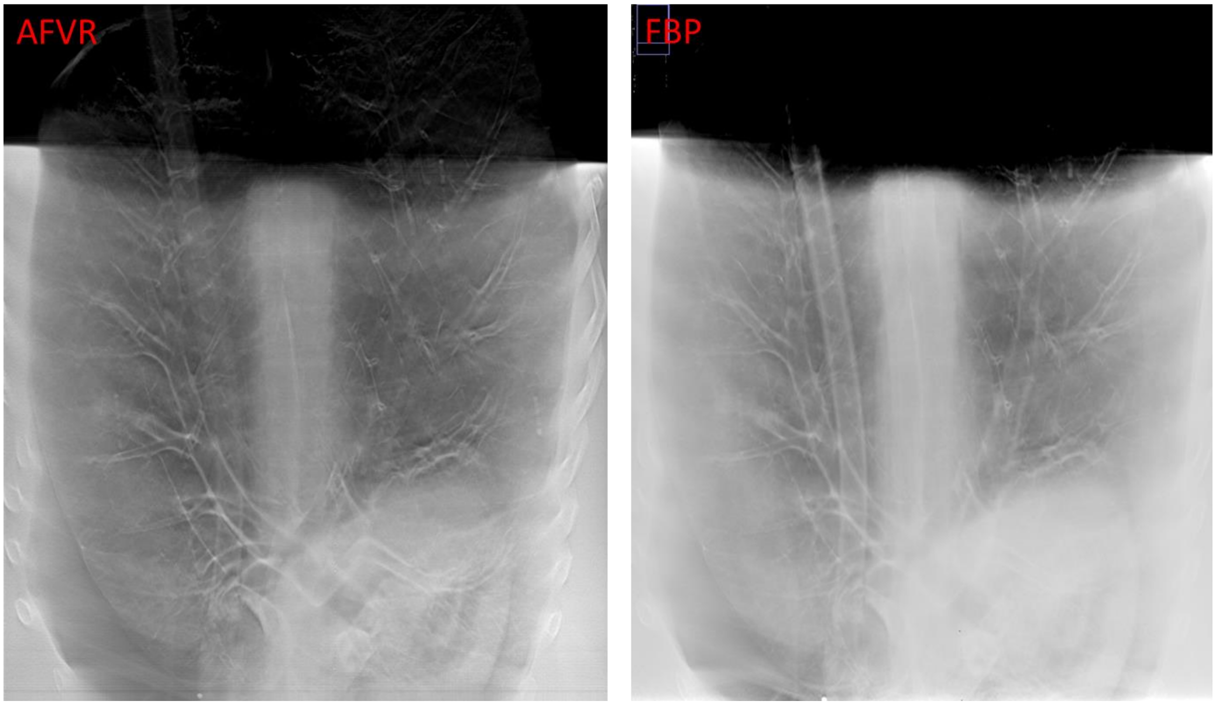

Figure 4-15: Reconstruction slices of an anthropomorphic chest phantom using two reconstruction methods. Left: AFVR reconstruction. Right: RTT reconstruction.

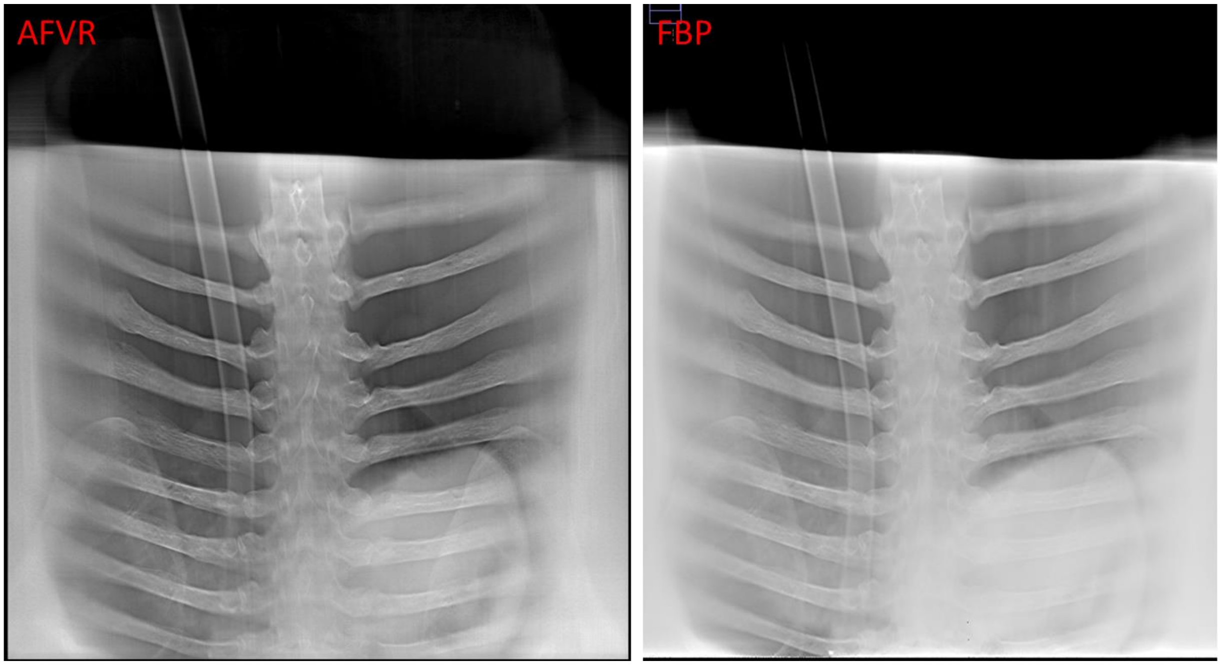

Figure 4-16: Reconstruction slices of an anthropomorphic chest phantom using two reconstruction methods. Left: AFVR reconstruction. Right: RTT reconstruction.

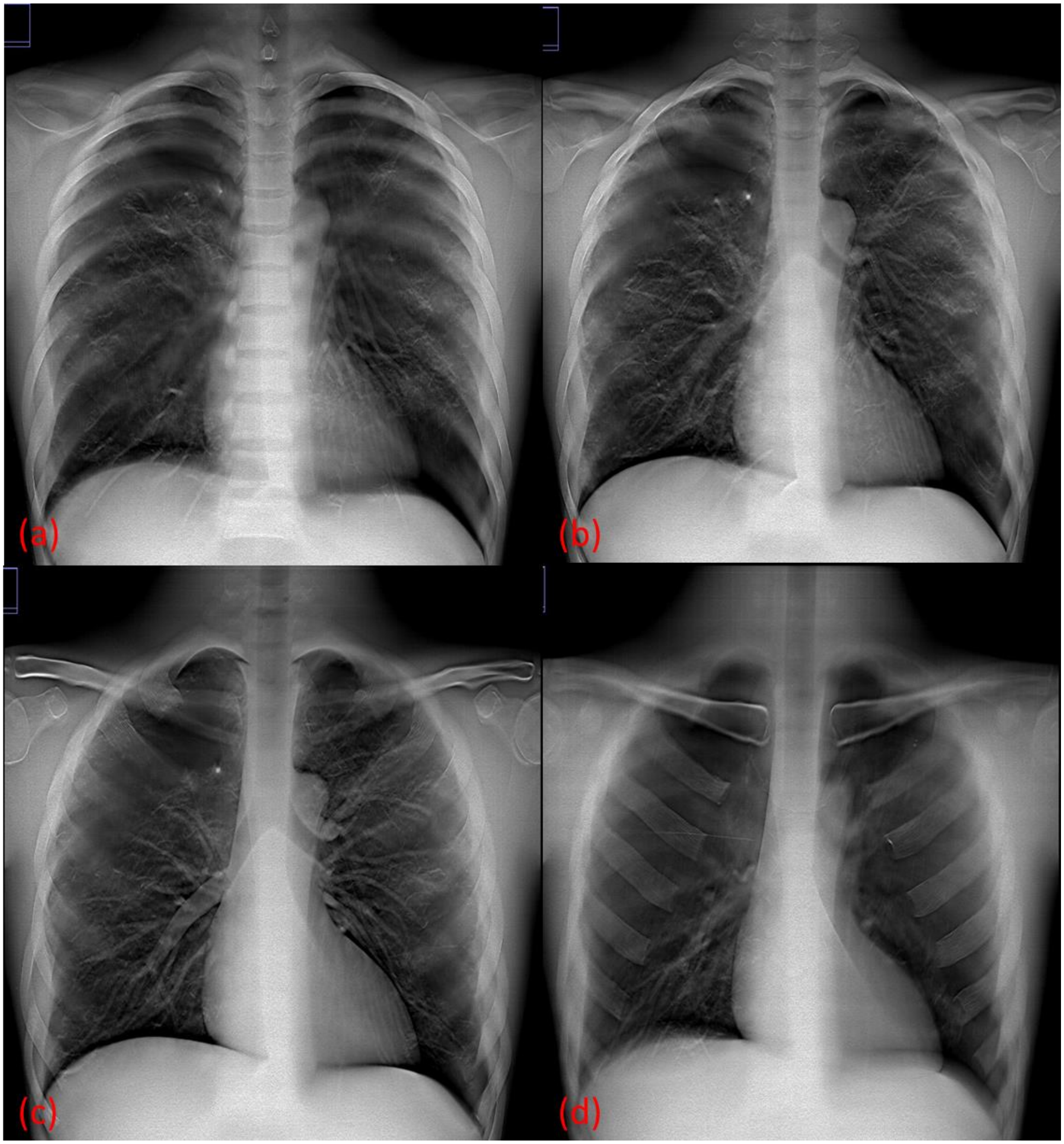

Figure 4-17: Reconstruction slices at 4 different positions of a chest phantom reconstructed by AFVR.

4.5.4 Image Artifact Reduction

Due to the unique image acquisition practice, s-DCT has a special type of data truncation artifact, shown in Figure 4-18(a). This artifact is caused by the lead cover, which is placed on top of the patient to protect the patients from harmful radiation during the scan. The lead cover would highly attenuate the x-ray beam and blocks it from reaching the detector. However, this lead cover only shows up in a few projection views. As s-DCT only acquires limited projections, the fact that some projection views do not contain the lead cover while others do causes a data inconsistency which in terms creates image artifacts.

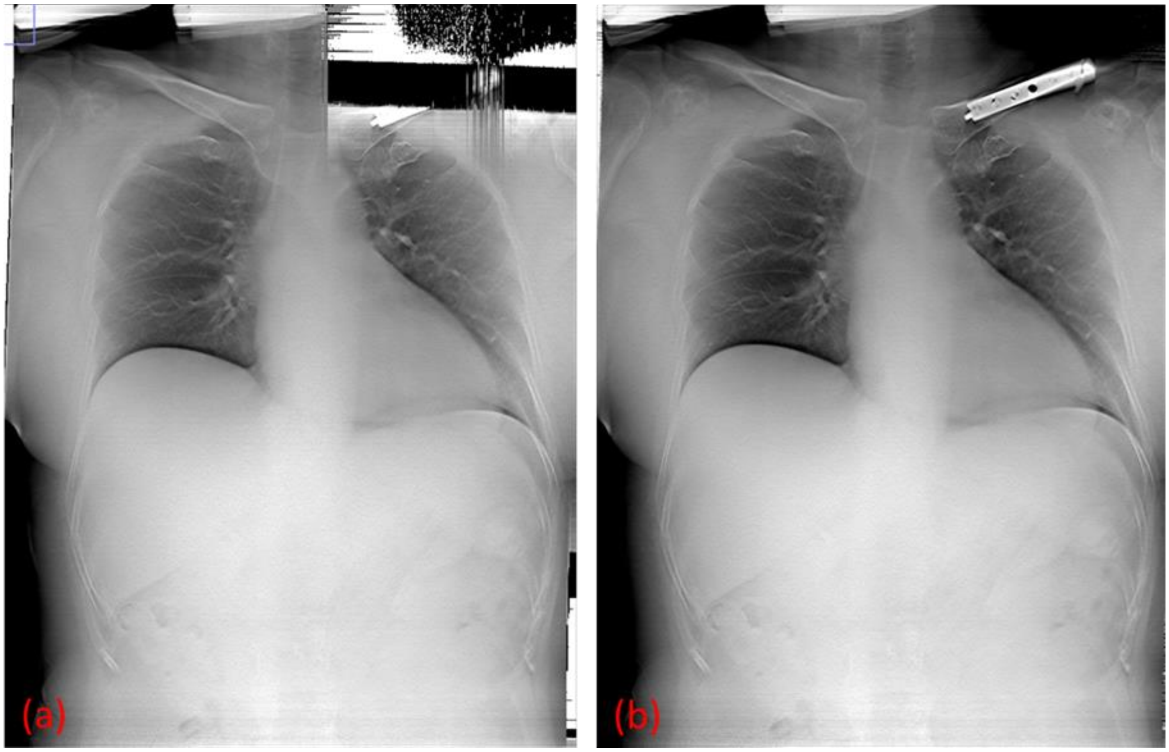

Figure 4-18: A reconstruction slice of a patient imaged by s-DCT (a) before correction (b) after correction

We applied two correction methods in our reconstruction to reduce this artifact. First, we threshold the linear attenuation to a pre-determined maximum value in the reconstruction. Second, during the rotation step in the sinogram pre-processing, we interpolate the observed data using the attenuation map outside the lead cover region, which prevents the wrong interpolation. The reconstruction slice after the corrections is shown in Figure 4-18(b), where the missing information is recovered, and the image artifact is reduced.

4.6 s-IOT Reconstruction

4.6.1 s-IOT System

The s-IOT system consists of a linear CNT-based source array and a flat panel detector. A picture of the prototype s-IOT system is shown in Figure 4-19. The whole system is mounted on a robotic arm, a flexible holder is used to hold the detector inside the patient's mouth. The x-ray coming from the linear source will be collimated to cover only the area of the detector. Once the imaging position is set up, the system stays stationary during the image acquisition. In this prototype system, 7 CNT-based x-ray sources are used with an angular coverage of about 10 degrees. This technology is patented by UNC and XinVivo LLC. As the patent is currently pending, the full system specifications of the s-IOT system are not available for disclosure at this point.

Due to the small FOV and a relatively large imaging angle, s-IOT images can have severe data truncation artifacts around the edges in the scanning direction. Truncation data correction method that is mentioned previously, therefore, has been implemented in the s-IOT reconstruction. One thing that should be noted here is that the x-ray source array is not guaranteed to be parallel to the detector. Therefore, the projection data "alignment" is needed before reconstruction using

AFVR. Same as the reconstruction for s-DBT and s-DCT systems, SIRT with 20 iterations is used for the s-IOT reconstruction.

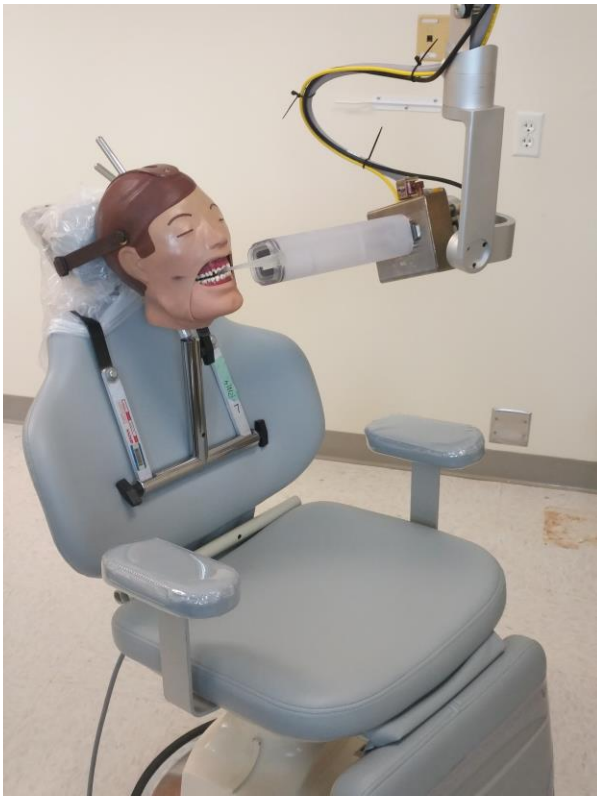

Figure 4-19: A prototype s-IOT system.[118]

4.6.2 Clinical Images

Figure 4-20 shows a comparison between conventional dental bitewing image and the s-IOT image. Both the filing (white disk shown in the image) and the cavity (dark disk shown in the image) have a better contrast in the s-IOT image (Figure 4-20(b)). The two fractures in the tooth, which is clearly shown in the s-IOT image, are not shown in the bitewing image. This suggests that s-IOT provides better contrast on the tooth cavity and it improves the diagnosis of tooth fracture.

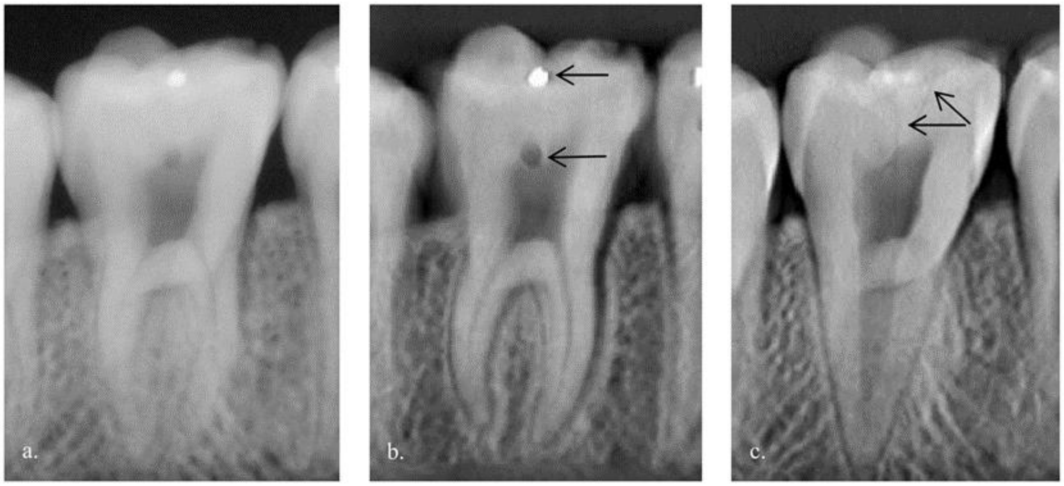

Figure 4-20: (a) Conventional dental radiography, (b) and (c) reconstruction slices of tooth phantom imaged by the s-IOT system.[118]

Figure 4-21 shows another comparison between the conventional dental radiography and the s-IOT on extracted teeth. Bitewing images from two dental radiography systems were acquired, the standard 2D digital bitewing, and the standard PSP bitewing. The micro-CT images for the central teeth were also acquired, which serve as a ground truth of the lesion status. The middle two teeth are the teeth of interest in each image, each has a lesion on the surface. The lesions were confirmed in the micro-CT images. As can be seen in Figure 4-21, the two lesions showed up clearly in the s-IOT image, however, they are hardly identified in both dental radiography images.

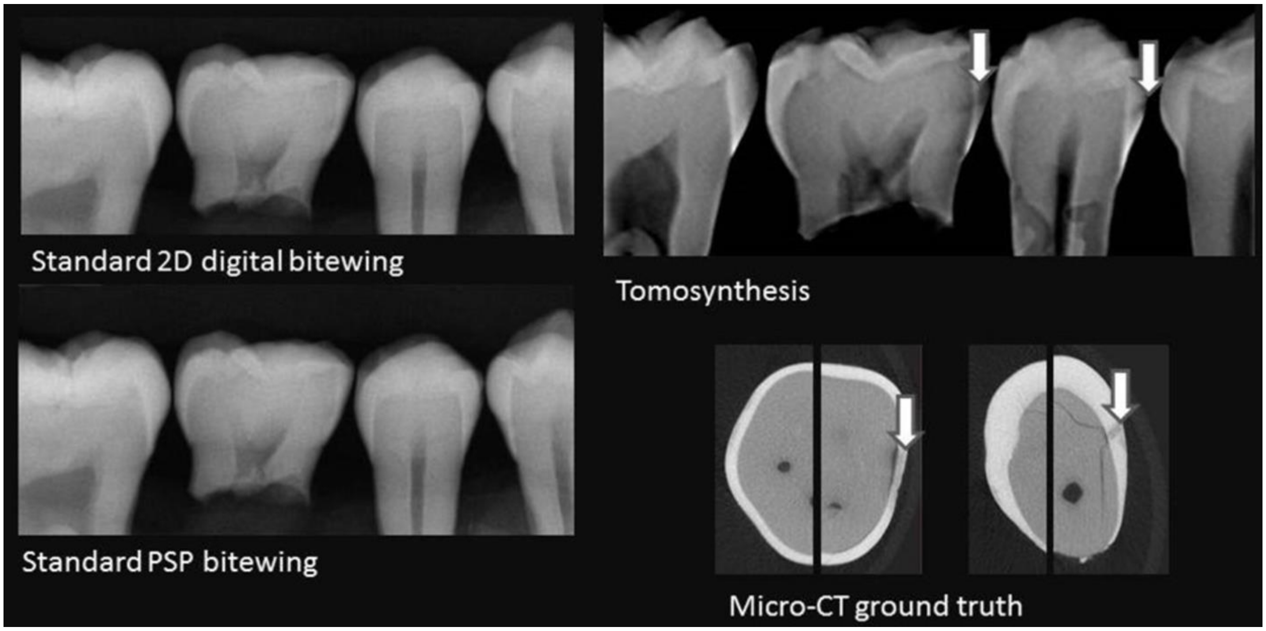

Figure 4-21: Tooth phantom imaged by four imaging modalities: standard 2D digital bitewing, standard PSP bitewing, s-IOT, and micro-CT. [118]

4.7 Discussion and Conclusion

4.7.1 Discussion

With the increased public awareness and concerns about x-ray radiation, the diagnostic imaging is heading to the direction of a safer diagnosis with reduced radiation dose. However, lower radiation dose reduces the x-ray photons that reach the detector, thus lowering the signal strength and negatively affect the image quality, and consequently affect the diagnosis. This raises a question to the research community: how to achieve better image quality at low dose. Many efforts have been made to the imaging hardware, including better detectors, phase-contrast imaging, and innovative imaging geometry. As hardware is heavily constrained by the physics, the improvement in imaging hardware is slow. Recent advances in software, mainly the image reconstruction and processing algorithms, have shone a light into this dilemma. Statistically modeling incorporated with prior knowledge and the efficient iterative algorithm have shown to be able to recover information that is not captured by the hardware, and the reconstruction from the statistical iterative reconstruction has demonstrated a superior image quality over the conventional FBP reconstruction. The only drawback is that such iterative reconstruction is time-consuming, which is not practical in a clinical setting. For digital tomosynthesis where the measured data are insufficient and truncated, the iterative reconstruction can greatly improve the final image quality which in terms benefits the diagnostic accuracy.

The adapted fan volume reconstruction that we developed for the stationary tomosynthesis systems can significantly improve the reconstruction speed. In our result, we observed 30 to 50 times' speed up compared to the conventional 3D cone beam reconstruction on a six-core desktop. Several aspects contribute to this improvement. First, each fan volume can be treated as independent of the adjacent fan volume. Therefore, each fan volume reconstruction can be carried out separately, enabling a straightforward parallelization. Utilizing this advantage, we speed up the reconstruction by 6 times through parallel computing on MATLAB. Secondly, as the size of each reconstruction in AFVR is smaller than that in conventional cone-beam reconstruction, the size of the system matrix is dramatically reduced. Therefore, we are able to store the system matrix in the memory. This avoids the computation of the forward projector in each iteration, and thus reduces the reconstruction time. In addition, the system matrix of each fan volume is related, by the tilted angle of the fan volume. As a result, the computation of system matrix can be much more efficient. Thirdly, AFVR improves the data locality, which allows a performance improvement through the caching mechanism.

AFVR is designed for linear tomosynthesis, and it will not reconstruct images for conventional tomosynthesis systems with a curved line source motion, as generally, the source positions in those systems will be different in height. This picture becomes clearer when one thinks of two source positions and connect them with one randomly-chosen detector row. The connections create two planes in the 3D space, each consists the same detector row but different sources. Since these source positions have different height, the two planes will cut the image space differently, or in another word, one voxel cut or included by the one plane might not be cut (included) in another plane. As a result, the value of those voxels can no longer be entirely determined by the projection data of a single detector row. With that being said, there is data redundancy even in the conventional tomosynthesis imaging (The value of one voxel is fully determined by only a fraction of the measurement), and one might be able to use that characteristic to design an algorithm to speed up the reconstruction.

In this study, we used an FBP-based commercial software, RTT, to compare with the AFVR. While RTT can be used for a general tomosynthesis reconstruction, it is designed and optimized for the breast imaging. Therefore, it might not be fair to compare image quality between RTT and the proposed AFVR algorithm when reconstructing for a different imaging system. In addition, as commercial software, RTT may consist of proprietary imaging processing besides the reconstruction, which may affect the final reconstruction image. Therefore, our result may not apply to a general setting, i.e. the difference in image quality between AFVR and FBP reconstruction. Currently, the AFVR is coupled with SIRT, which is relatively simple and the reconstruction image quality is generally believed to be mediocre. We expect that the image quality can be further improved by incorporating a more sophisticated statistical model with AFVR.

AFVR applies re-sampling twice during the reconstruction. At first, resampling is applied to align the projection data to the source array. After all 2D reconstructions are completed, resampling is used again to combine all 2D images into a 3D image, during which the irregular aspect ratio from the fan-shaped volume is corrected. Theoretically, the image resolution will compromise whatever a resampling is applied. In practice, we have not observed any noticeable degradation in image resolution in our data. Based on our observations, the tilted angle between the source array and each detector row is found to be around ± 3 degrees, which is relatively small. Thus, the effect of rotating and resampling the projection data is small. The difference in aspect ratio between the top and bottom reconstruction slices, however, varies for different imaging systems. In the s-DBT system, the difference is about 8%; while in the s-DCT system, the difference can be as large as 25%. At first glance, one might think that the resampling process could change the image resolution for difference slices, i.e. image resolution in the top reconstruction slice is different from that in the bottom slice. This is not entirely true as the reconstruction for the top slice is super-sampled at the beginning, where the voxel used in the reconstruction is smaller than the actual voxel. Therefore, before the resampling, ideally, the top slice will have a better resolution than the lower slices. The resampling indeed normalizes the difference in image resolution, as such, difference in image resolution is not noticeable. With that being said, a more strict measurement of image resolution at various depths might be beneficial to understand this effect fully.

Future improvement of the AFVR can include several aspects. First, the back projection algorithm for each 2D volume reconstruction can be improved. By incorporating a statistical noise model, one can design a reconstruction algorithm that could further reduce the image noise and improve both the resolution and the quantitative accuracy. Prior knowledge can also be utilized in the reconstruction for better convergence and lower noise level. Secondly, the reconstruction speed can be further improved by implementing the reconstruction on GPU hardware. With the parallel computing power GPU provided, the reconstruction speed is expected to increase by another order of magnitude. Thirdly, for tomosynthesis imaging, techniques for artifact reduction can be investigated, which can dramatically improve the diagnostic accuracy of the tomosynthesis.

4.7.2 Conclusion

A fast iterative reconstruction algorithm has been developed. The new algorithm, named adapted fan volume reconstruction, utilizes the unique geometry of the imaging system and speeds up the computation by transforming a large reconstruction problem, which is computationally expensive, into a number of small problems that are computationally more efficient to solve. Implemented this algorithm on MATLAB, we observed that the new algorithm speed up the computation by one order of magnitude, from 30 to 50 times. The image quality produced by AFVR was also investigated. Comparing the reconstruction from AFVR with that from RTT, we found that the image resolution was much higher on AVFR, ranging from 30% to 50% higher than that in RTT reconstruction while the noise was on the same level between the two reconstruction methods. Looking at the clinical images, we observed that AFVR produced images looked much sharper, which benefits the diagnosis. Finally, AFVR was implemented to reconstruct images for the s-DBT, the s-DCT, and the s-IOT system. The reconstruction has been optimized for different applications in each imaging system.

4.8 Image Artifacts Reduction

4.8.1 Skin Line Artifact

Radiologists often use breast skin line as a reference to diagnose malignant tumors. In digital mammography, the skin line is quite clear. However, in DBT, the skin line is often contaminated by tomosynthesis artifacts, which add multiple “faked” skin lines on the breast image as shown in Figure 4-22. Although ultimately, the artifact is caused and limited by the data insufficiency of the tomosynthesis, it can be mitigated with certain imaging processing techniques.

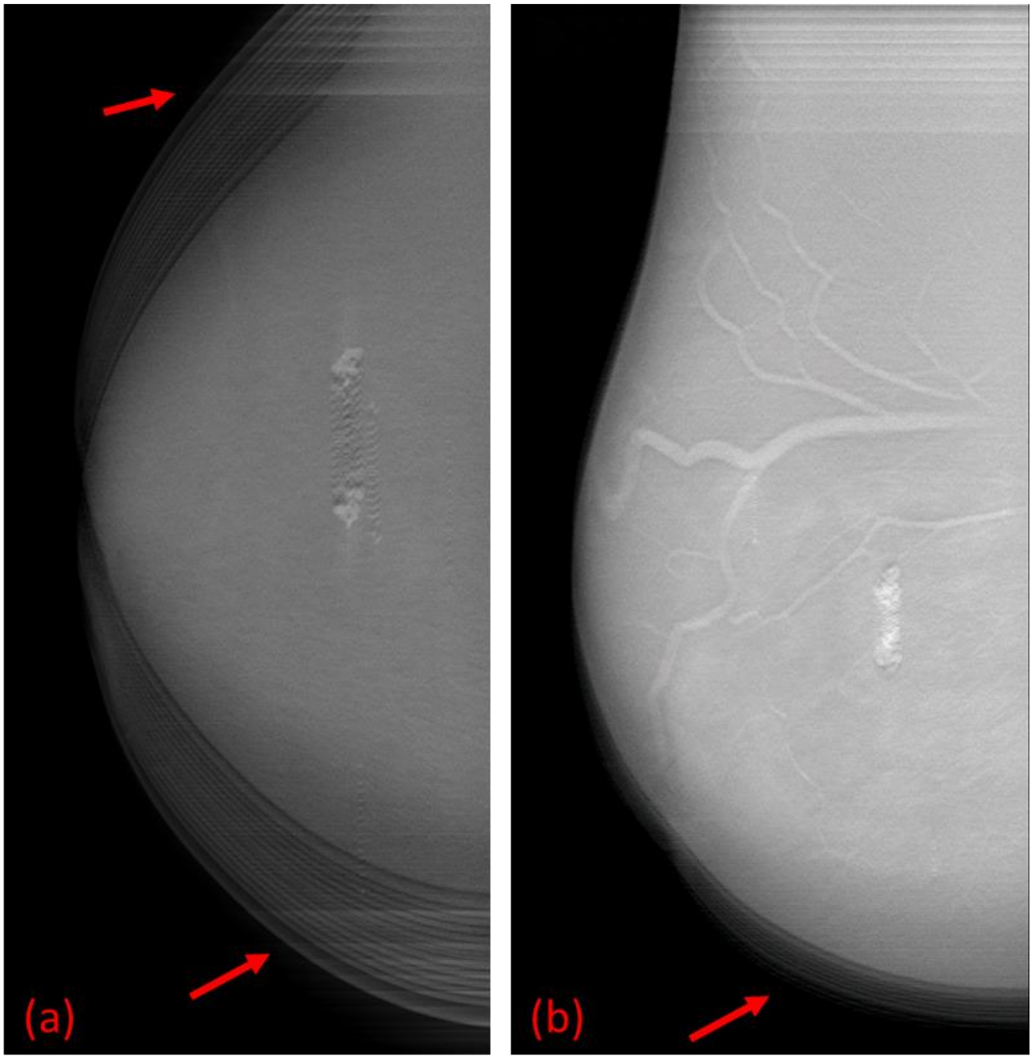

Figure 4-22: Skin line artifacts in the breast tomosynthesis image.

Here, we present one method that reduces the skin line artifact in breast tomosynthesis, originally proposed by Zhang *et al*.[119] The idea of presented method is to confine the reconstruction space and force the reconstruction to converge. The method is implemented as follows: first, segment out the breast and identify the breast edge in each projection image; then back project the breast edge to the image space to find a tighter space where the breast locates;

Repeat this step for every projection images and obtain a trimmed space where the breast should locate, the segmentation information obtained from each projection are used to reconstruct the 3D volume of the breast; Finally, restrict the reconstruction only within the identified breast region, namely set everything outside the breast region to be zero. A schematic diagram of the method is shown in Figure 4-23. It should be noted that this method is still suffered from data insufficiency of the tomosynthesis imaging. As indicated in the figure, there are missing gaps even after taking all projections into consideration, and the tomosynthesis artifact, or particularly the skin line artifact, might still show up in those regions.

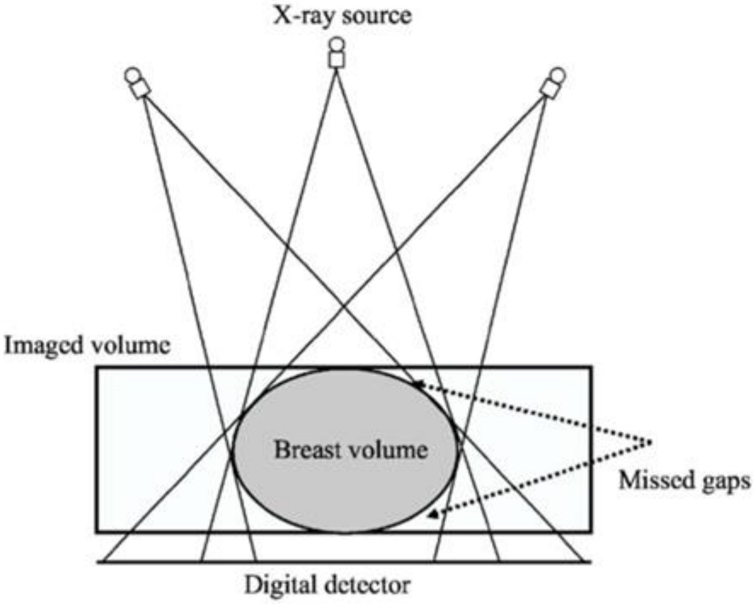

Figure 4-23: Schematic of the skin line artifact reduction method.[119]

We implemented this method in the s-DBT reconstruction and tested the method using real patient data. Figure 4-24 shows a 2D fan volume reconstruction (cross-sectional image) of a patient's breast without and with the skin line artifact reduction. The out-of-plane artifact was significantly reduced after the correction is applied. Note that the 2D fan volume image is a cross-sectional image of the breast, as such, the reduction of the tomosynthesis artifact would translate to the reduction of the skin line artifact in the 3D image in the top-down view. Figure 4-25 shows the reconstruction slices of the same breast as shown in Figure 4-22 but with the skin-line artifact reduction applied. We observed that the attenuation values in the periphery region decrease slightly after applying the correction, further investigation is required to understand and fix this side effect.

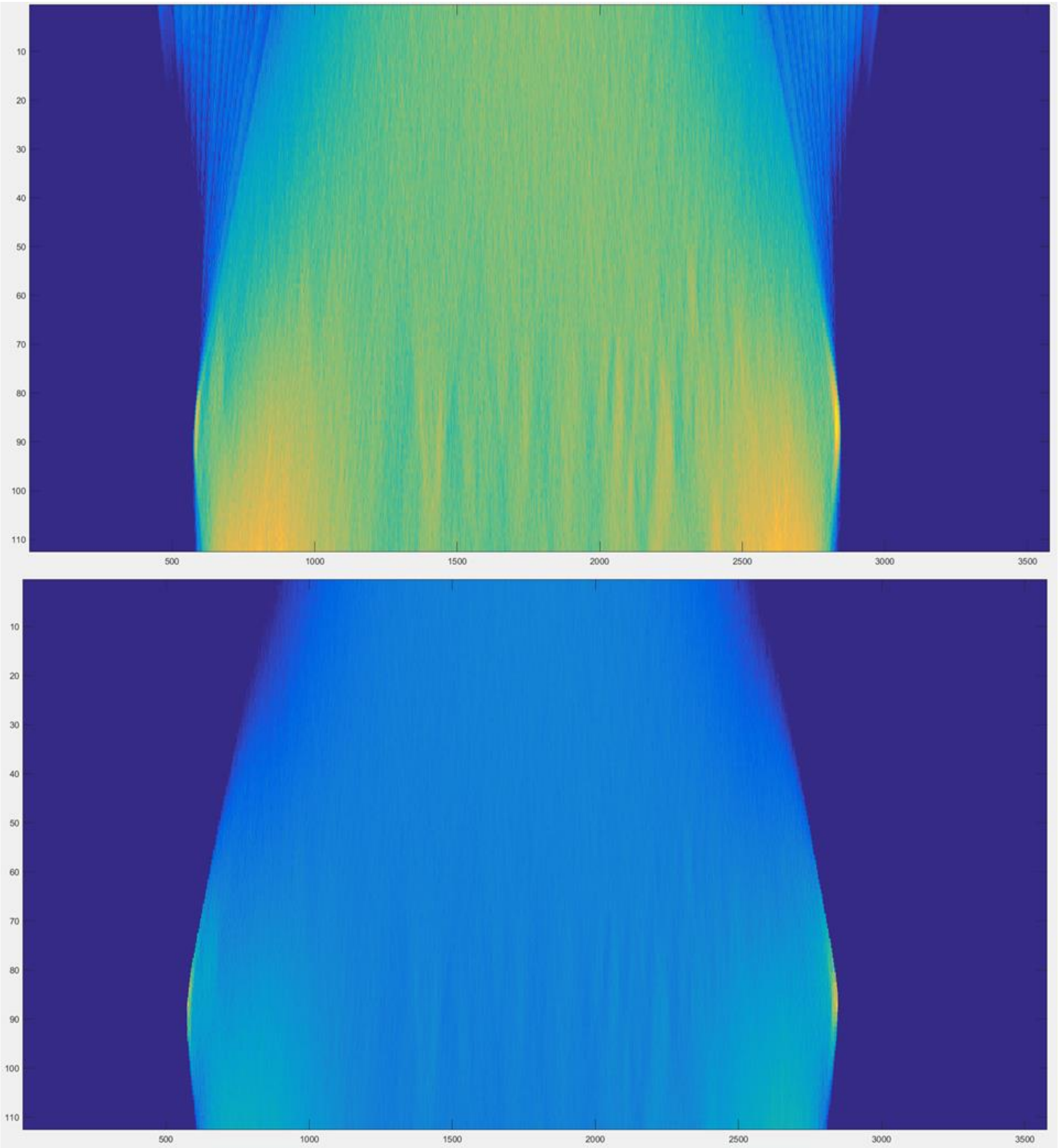
10
20
30
40
50
60
70
80
90
100
110
500
1000
1500
2000
2500
3000
3500
10
20
30
40
50
60
70
80
90
100
110
500
1000
1500
2000
2500
3000
3500

Figure 4-24: Reconstruction of one 2D fan volume (Top) without the skin line artifact reduction, (Bottom) with the skin line artifact reduction.

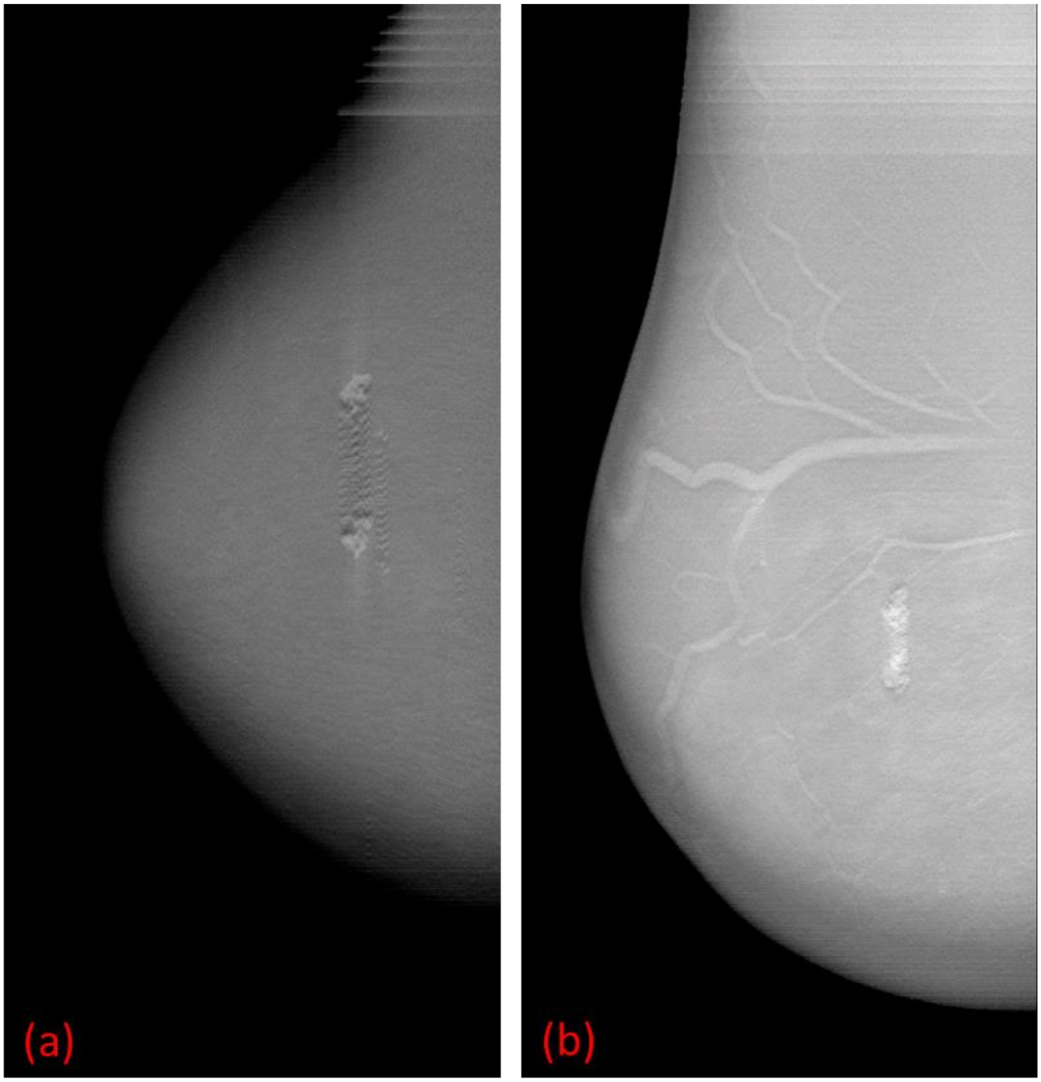

Figure 4-25: Breast reconstruction slices after the correction.

4.8.2 Data Truncation Artifact Reduction

Tomosynthesis, in general, has a small field of view due to its unique imaging geometry (object sits on top of a fixed or semi-fixed detector). The tomosynthesis reconstruction is typically performed within an image space defined based on the size of the detector, materials outside this space will not be taken into account during the reconstruction. Those “outside” materials, however, also attenuate the x-ray during the imaging acquisition at certain imaging positions. When those regions are ignored, the x-ray attenuation that originally belongs to those regions will be mistakenly assigned to other regions in the image space, causing a bright glow artifact near the boundary shown in Figure 4-28(A) and 4-29(A). When the glowing artifact appears, features "underneath" the glow become extremely hard to detect.

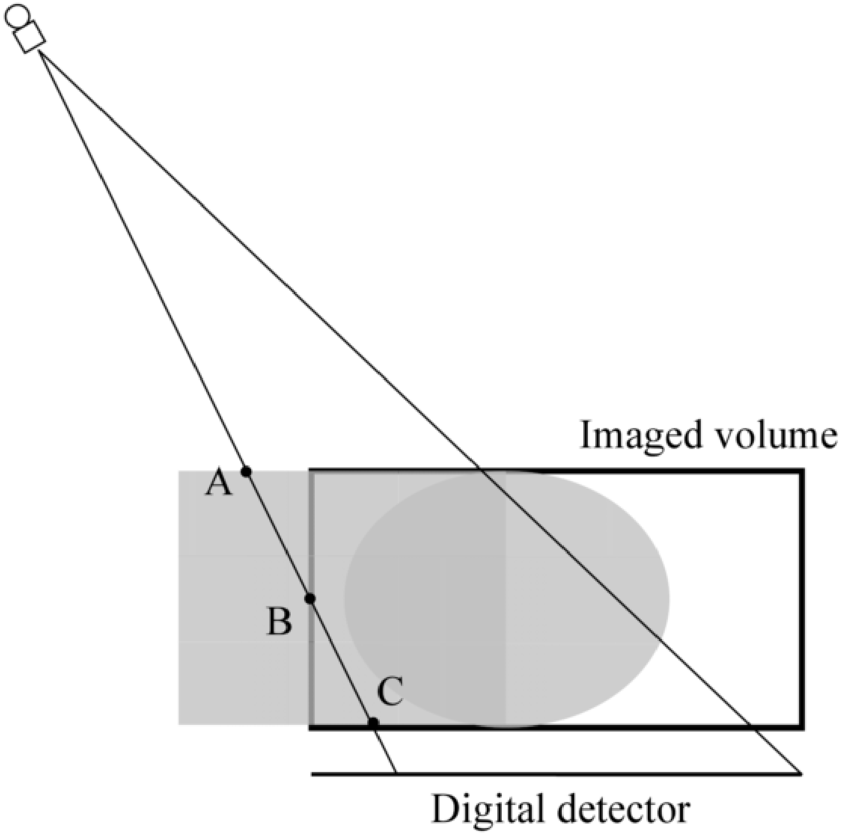

Figure 4-26: A schematic of the truncation artifact reduction method. [119]

We applied a simple correction to mitigate the flow artifact due to the data truncation, which is modified from the Zhang's method.[119] The method assumes that, first, the material in the outside region is nearly uniform thus has a same linear attenuation, and, secondly, the outside region material extends to the top of the image space. Based on these two assumptions, one can identify the projection data which has contributions from outside region materials and scale the data to eliminate the Figure 4-26 shows a schematic of the correction method, and the algorithm goes as follows: first, an average attenuation value is calculated and is used as a threshold in the next step to determine the data that needs to be corrected. Second, in each projection image, identify the regions where the x-ray might have been attenuated outside the image space (black rectangle box in Figure 4-26). Use the average attenuation as a reference to pick the region that has significantly higher line integral value. Lastly, scale the projection data based on the length of the x-ray for each source-detector pair, namely. For example, in Figure 4-26, we scale the line integral data at source detector pair C by a fact of BC/AC.

Figure 4-27 shows a cross-sectional breast image before and after the correction is applied. The data truncation causes consistency projection, which, in terms, causes an artificially high attenuation in the bottom left and a dark region in the top left of the reconstruction image. After the correction had been applied, both the glowing artifact and the dark region disappeared. Reconstruction slices of two patient breast images in MLO view with and without the correction are shown in Figure 4-28 and Figure 4-29. As can be seen in the figures, the glowing artifact due to the data truncation in tomosynthesis imaging is significantly reduced.

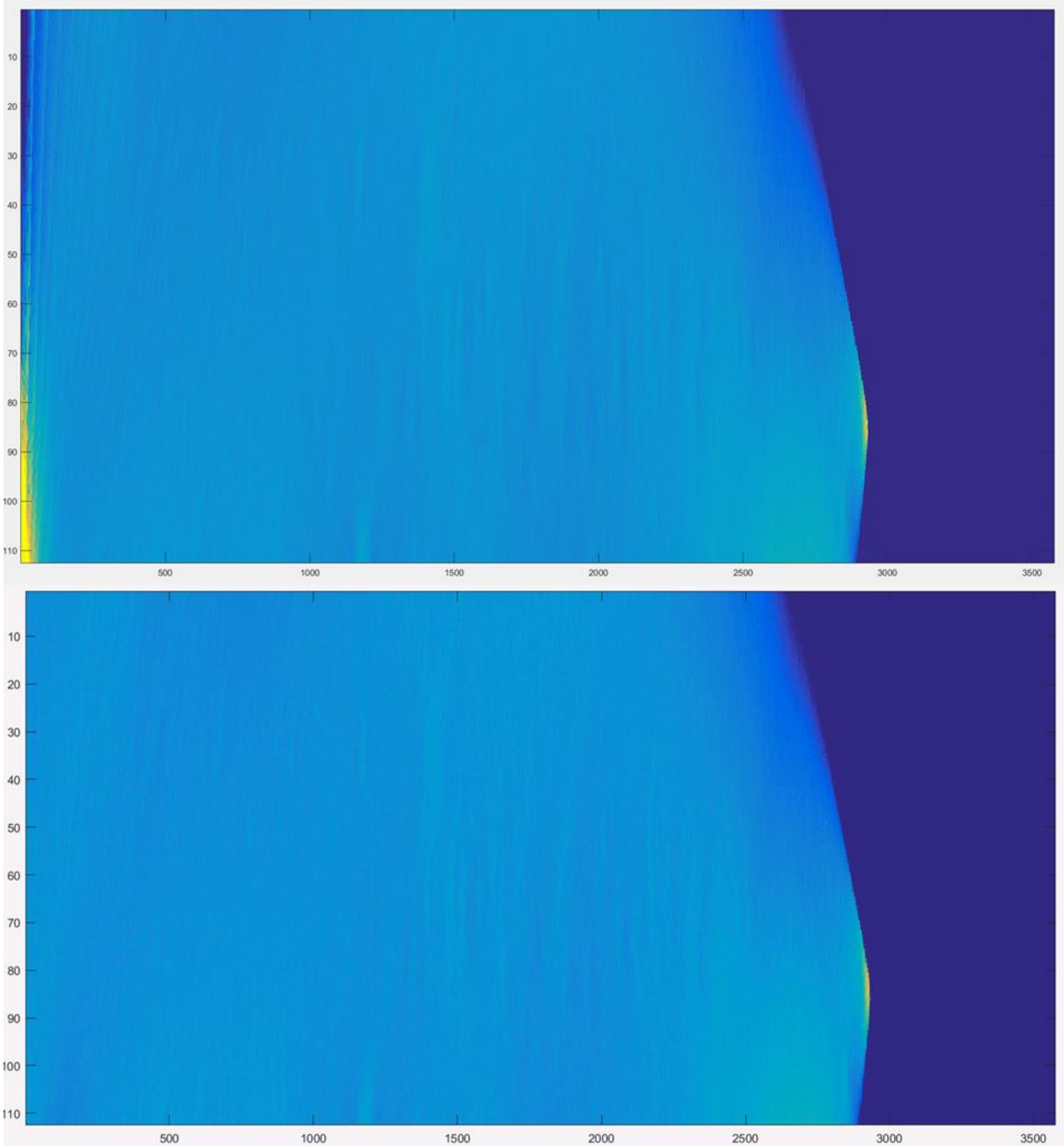
10
20
30
40
50
60
70
80
90
100
110
500
1000
1500
2000
2500
3000
3500
10
20
30
40
50
60
70
80
90
100
110
500
1000
1500
2000
2500
3000
3500

Figure 4-27: Cross-sectional reconstruction images of a patient’s breast (Top) without any correction, (Bottom) with the data truncation correction.

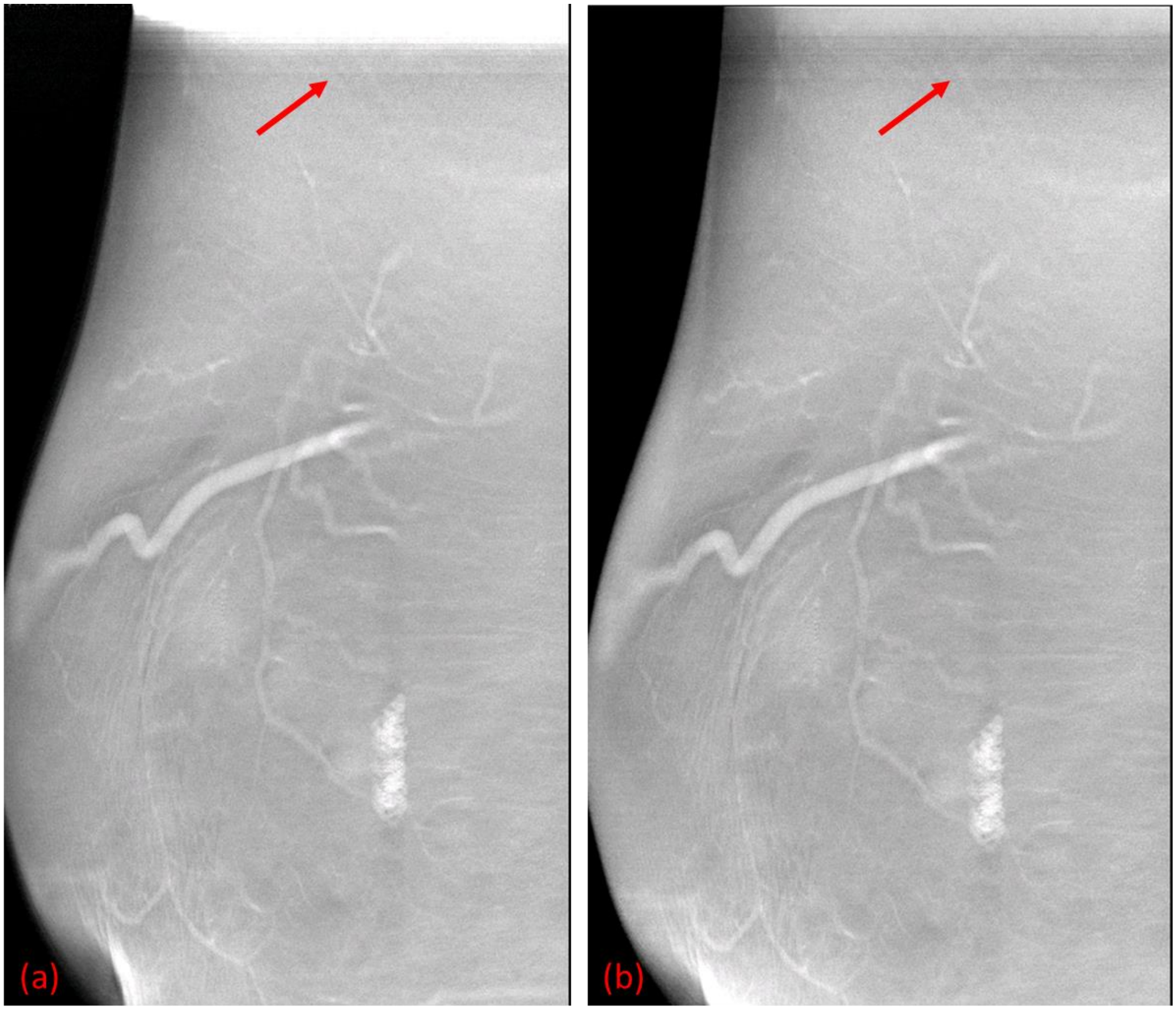

Figure 4-28: Reconstruction slices of a patient’s breast (a) without any correction, (b) with the data truncation correction.

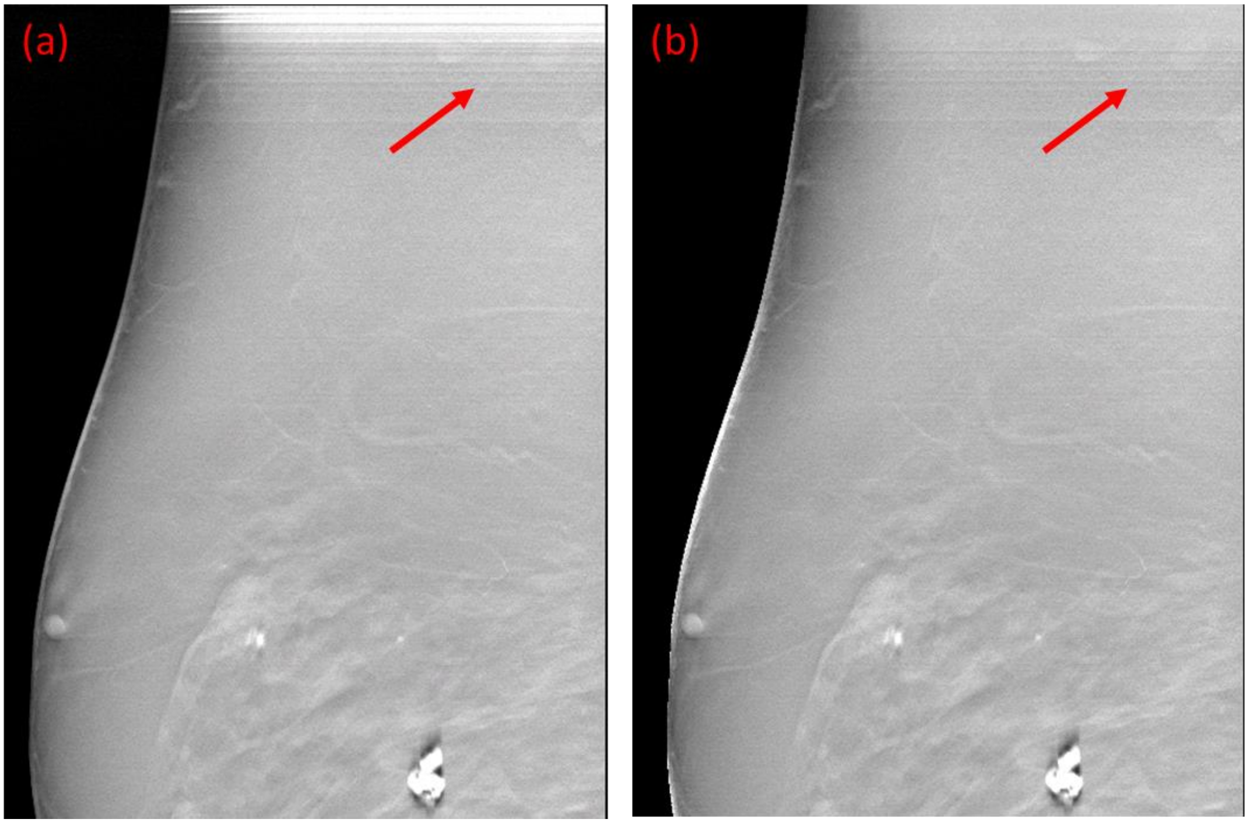

Figure 4-29: Reconstruction slices of a patient's breast (a) without any correction, (b) with the data truncation correction.

4.9 Synthetic Mammography

4.9.1 Motivation

Studies have shown that although DBT has better diagnostic accuracy on the masses, it does not visualize microcalcifications as well as the 2D mammography. Thus, most of DBT systems in the market are FDA approved for use only in combined with the 2D mammography. This doubles the radiation dose and increases the patient discomfort caused by the compression paddle. While the performance of the DBT imaging has improved significantly over the past few years and some researchers argue that DBT and DM perform equally well in microcalcification with the current advances, many radiologists still prefer viewing 2D mammography in addition to the 3D tomosynthesis image. Part of that is because radiologists were trained to read DM early in their careers, the other reason, and probably the more important one, is that DM provides a faster workflow over the tomosynthesis images where radiologists can get diagnostic information in one glance without the need to scroll through hundreds of DBT images.

One solution to reduce radiation dose while still maintain the diagnostic accuracy is the synthetic mammography. The idea is generating a synthetic mammography image from the 3D tomosynthesis reconstruction to replace the physical mammography exam. In this section, the method of generating synthetic mammography from the s-DBT will be investigated, in particular, the method to detect skin line and the algorithm to correct breast density.

4.9.2 Skin Line Detection

Otsu's threshold method is a special case of the more general K-mean clustering method. The basic idea of the K-mean clustering method is to separate data into K-groups by minimizing the intra-group distances. In Otsu's method, a 2-mean clustering is performed on image histogram to separate the image foreground from the background. Although Otsu's method is based purely on the pixel intensity and the local geometry is not used, it is proved to be highly effective in a variety of applications. One drawback of the Otsu's method is that it is hard to determine the number of clusters in the image, sometimes, this number could be more than 2. In other words, there might exist one or more regions in the image that do not belong to either foreground (ROI) or background. Furthermore, the Otsu's threshold method loses its accuracy around the boundary of the clusters. As a result, directly applying Otsu's method to breast image might lead to a mediocre segmentation of the breast.

Figure 4-30(a) shows a breast segmentation using the Otsu's method. The white region is the segmentation of the breast, and dark region is the breast tissue that is not correctly identified. The Otsu's method segmented out the breast, however, the identified boundary or skin line is not accurate. To improve the accuracy of the skin line detection, we applied an improved Otsu's method, where the clustering is performed iteratively around the boundary. A pseudo code of the algorithm is shown in Algorithm 1:

Algorithm 1 Algorithm for detecting breast skin

```
1. Apply Otsu's threshold method on the whole image
2. For i = 1 : number of iteration:
       Find the boundary regions based on the skin line
       Apply Otsu's method on the boundary region
       Segment out the breast region based on the new threshold value
       Save the segmentation for next iteration
```

By iteratively applying the Otsu's method on the boundary, the segmentation accuracy is improved. A result of the segmentation using this improved Otsu's method is shown in Figure 4-30(b). Five iteration was used in the iterative Otsu's method, but the threshold value converges after three iteration. As can be seen, the segmentation accuracy is much improved from the previous the result, and no noticeable segmentation error is observed.

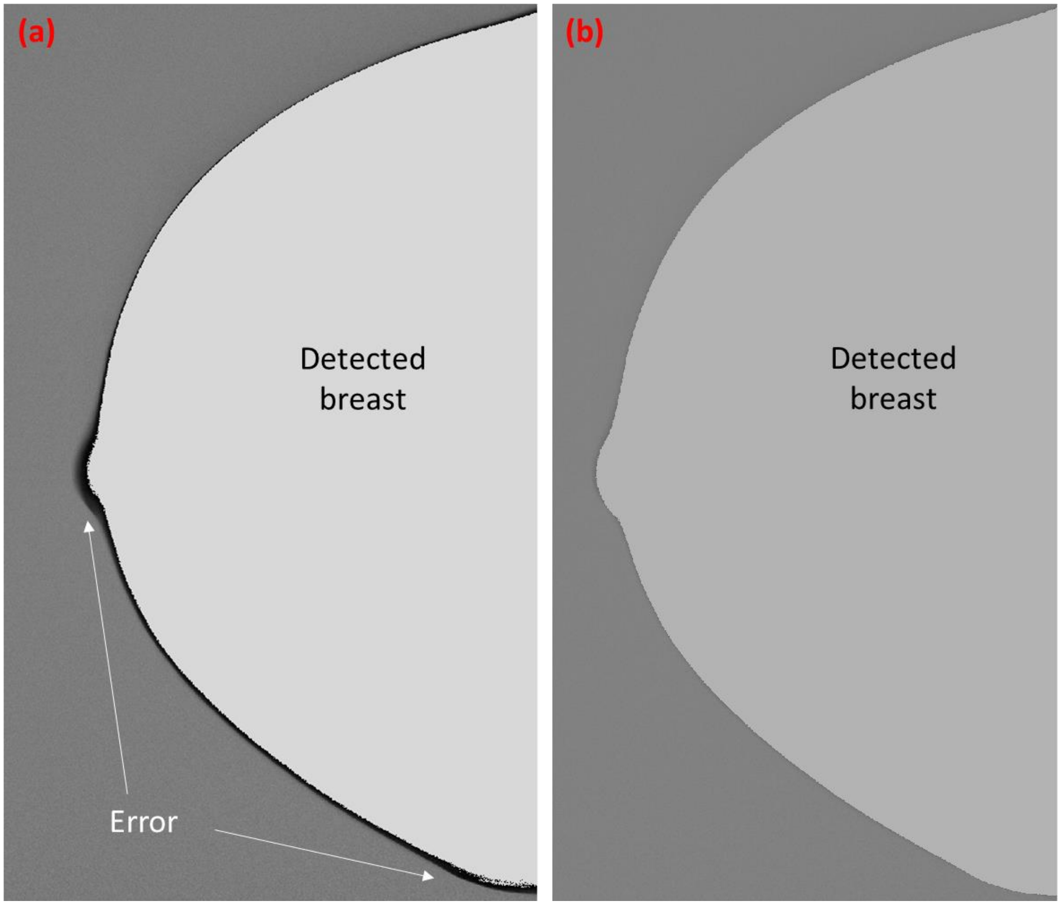

Figure 4-30: Breast segmentation using (a) Otsu's threshold method (b) iterative Otsu's method.

4.9.3 Breast Density Correction

During the exam of both DBT and DM, the breast is compressed and held by the compression paddle. This imaging setting causes a denser tissue in the center of the breast and thinner breast tissue in the periphery region. Consequently, as the x-ray is attenuated much more in the center region than that in the periphery region, the 2D projection image would have a wide dynamic range. It is generally not preferred in diagnosis, as radiologists need to adjust the image display window if they want to exam different regions of the breast. More importantly, the skin line is often used as a reference to diagnose many malignant tumors. When the skin line is not shown up with the breast tissue, it would be hard for the radiologists to make any accurate diagnosis.

One solution is applying breast density correction to the 2D image, which flattens the dynamic range of the breast image and makes all features of the breast to display in one display window. The key challenge in the breast density correction is accurately estimating the breast thickness. In this study, we proposed to use an anisotropic filter and a Gaussian filter to estimate the breast thickness from the 2D projection image. Both filters are used to remove the feature details in the breast and to extract the baseline attenuation that strongly related to the thickness of the breast tissue. The resulting image will then be subtracted from the original breast image, to reduce the dynamic range of the breast. The model assumption behind the anisotropic filter is that two positions with the same distance from the breast skin should have the same breast thickness. Therefore, an estimation of the breast thickness can be obtained by filtering the pixels with the same distance from the skin line. In addition, the Gaussian filter is used to remove the features further from the baseline "thickness" image. The full detailed algorithm is shown in Algorithm 2.

Algorithm 2 Algorithm for the breast density correction

```
1. Find the breast skin line using Algorithm 1
2. Compute the curvature of each pixel on the boundary
3. For each pixel inside the breast:
       Find the closest boundary point and record its curvature.
       Apply an anisotropic filter to itself. The pixel along the curvature will have a high weight,
       while the pixel perpendicular to the curvature will have a smaller weight
4. Apply a Gaussian filter to the whole image to obtain the breast "thickness" image
5. Compensate the periphery region in the original image based on the "thickness" image
```

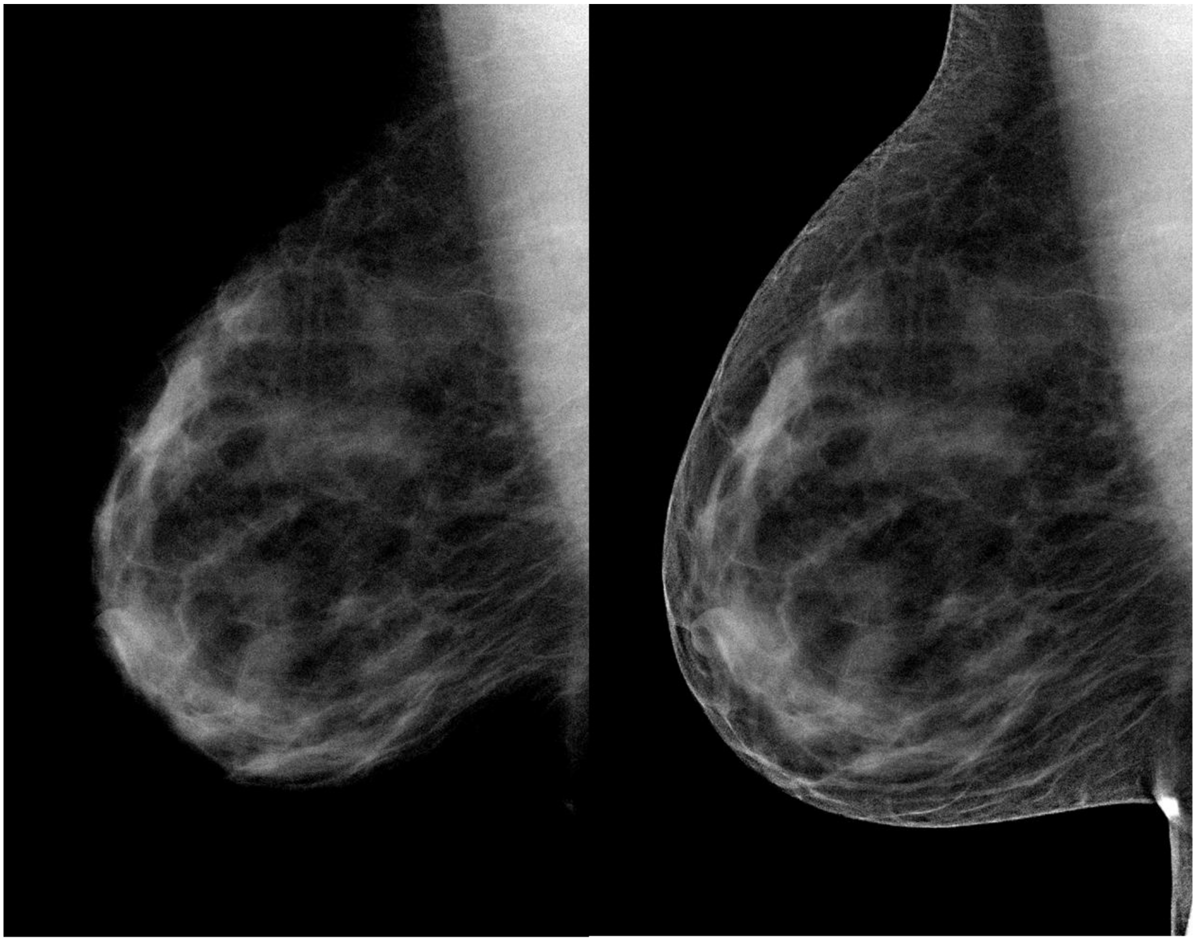

Before correction

After correction

Figure 4-31: 2D projection images with and without the density correction.

Figure 4-31 shows projection images of a patient breast in MLO view without and with the density correction. As can be seen, the density correction successfully recovers the disappeared skin line while maintaining the local contrast of the inner breast. It is interesting that although both images are displayed in the same display window, the image with the density correction shows visually better contrast with the presence of the skin line.

4.9.4 Synthetic Mammography with a Forward Projection

The 2D mammography is simply an x-ray projection image. Therefore, if an accurate 3D reconstruction image exists, one can apply a forward projector to the reconstruction and obtain a synthetic 2D image. It should be noted that the DM image is an x-ray attenuation image while the projection image is a line integral image from the AFVR with SIRT. Therefore, in addition to the forward projection, a conversion is required to convert the line integral image to the attenuation image. In this study, a simulated x-ray source with 10,000 x-ray photons was used for the synthetic image.

Figure 4-32 shows the comparison between the true mammography image, 2D projection image and the synthetic mammography image of the same breast. The 2D projection image and the synthetic image were coming from the same data set, while the mammography image was acquired before the tomosynthesis scan on a different imaging system. Because of different imaging position and deformation of the breast, the 2D projection and the synthetic image will not match exactly the look of the mammography image no matter how good they are. With that being said, the synthetic mammography does look much better than the 2D projection image. The skin line is clearly shown and the contrast of the fibroglandular tissue is enhanced. The appearance of the current synthetic image does not look quite like the true mammography image. However, the synthetic image should not be evaluated purely on its similarity to the true mammography image, and a clinical observers’ study is required to evaluate and compare the two imaging techniques.

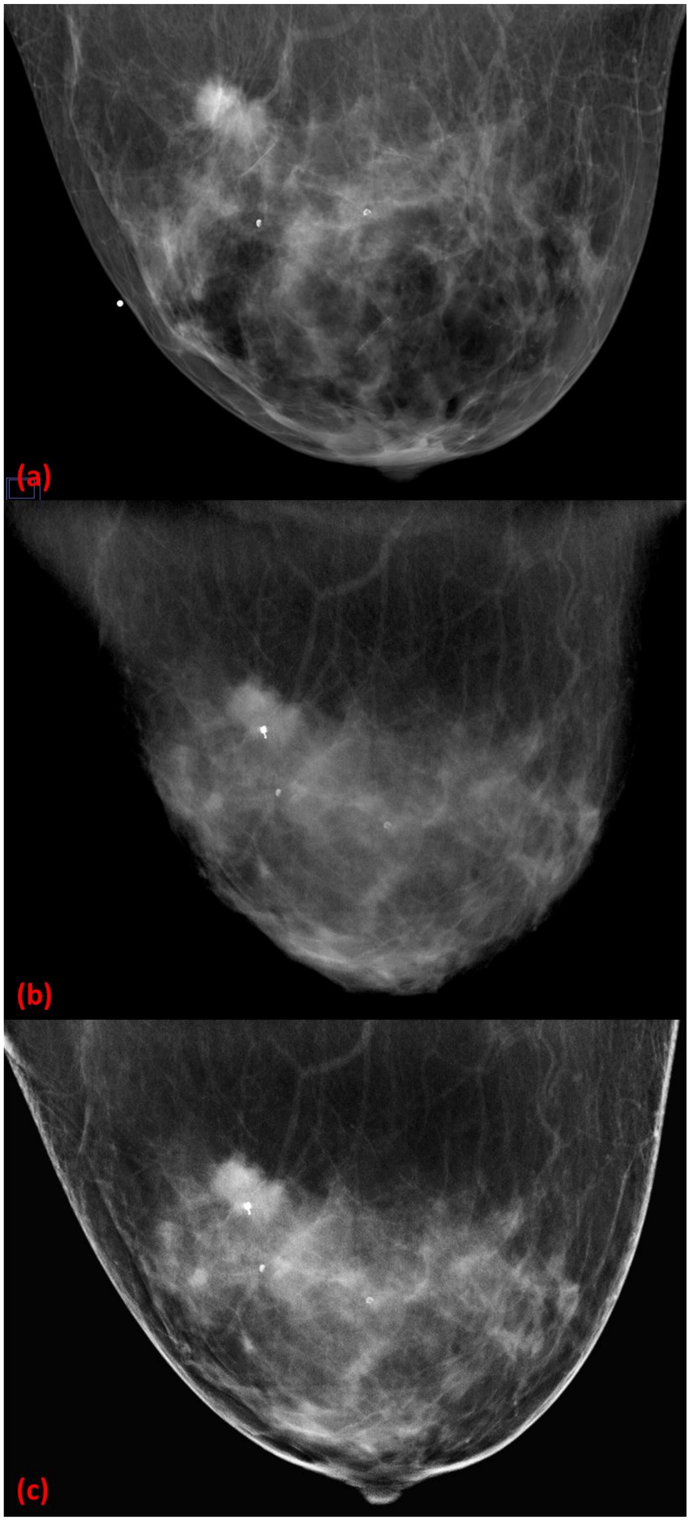

Figure 4-32: (a) Digital mammography image, (b) Synthetic mammography with density correction and contrast enhancement

4.9.5 Discussion and Future Work

In theory, given an accurate reconstruction, the synthetic mammography could be as simple as one forward projection of the reconstruction. In practice, however, obtaining a good synthetic image is more difficult than a simple forward projection. There are mainly two reasons that contribute to the difficulty. First, the reconstruction image obtained in the tomosynthesis imaging is far from accurate. Due to the insufficient data, the tomosynthesis reconstruction does not converge. Even worse, image artifacts appear in the reconstruction because of the data truncation, the image noise, the scatter, and the beam hardening effect. Secondly, in clinics, doctors are more concerned about how clear the diagnostic information is presented in the image rather than the quantitative accuracy of the image. As such, the synthetic image needs to be "engineered" to aid diagnosis, i.e. diagnostic important features will need to be artificially enhanced in the synthetic image, which leads to another interesting research area of computer aided diagnosis.

In this section, we discussed our preliminary approaches for the synthetic mammography, including detection of the breast skin and the breast density correction. Identifying the breast region is generally the first step for performing other more sophisticated image processing, thus, it is of great importance to develop a robust and efficient algorithm for breast skin line detection. Here, we used an improved variant of the Otsu's threshold method, where the clustering is performed iteratively around the breast skin. This improves the accuracy of the original method and it is more robust for different breast images. The breast density correction method proposed here uses the breast line detection and the anisotropic filtering. The breast density correction flattens the dynamic range of the 2D breast image so that all features in the image can be displayed in the same image window which is preferred in clinics. In future, it would be helpful to apply this method to more 2D breast images and to evaluate the robustness of this algorithm.

Due to the complex nature of the synthetic mammography, the methods mentioned here are far from sufficient to obtain a good synthetic image. Future research is required to generate a nice-looking and useful synthetic image. The future research can focus on two areas: the image artifact reduction and the image enhancement. It is known that DBT images contain many image artifacts, including the tomosynthesis artifact (out-of-plane artifact) and data truncation artifact. These image artifacts can severely degrade the image quality in the synthetic mammography, as the artifacts at various depths of the reconstruction will sum up in the synthetic image. To reduce the tomosynthesis artifact, one can either improve the reconstruction, which is a more fundamental way to fix or mitigate the problem, or design a post-processing algorithm to remove the artifacts. The image enhancement is self-explanatory, the purpose is to improve image the quality and to make the diagnostic important features much conspicuous in the image. It should be noted that all DM images nowadays are heavily post-processed for image enhancement. With the extra depth information in DTS imaging, one might come up with an algorithm that takes the advantage of the depths information to better visualize the masses and microcalcifications in the breast.

CHAPTER 5: Scatter Correction for Digital Tomosynthesis

In this chapter, we will present a new approach, referred as filtered scatter-to-primary ratio (*f*-SPR) method, to estimate scatter from sparsely sampled scatter signals. Compared to other scatter correction algorithm, *f*-SPR can substantially improve the image quality of both projection and reconstruction images. We quantitatively evaluated the *f*-SPR method against two direct interpolation methods using breast tomosynthesis data from physical phantoms and demonstrated its effectiveness using chest tomosynthesis data from a human cadaver imaged by a stationary digital chest tomosynthesis (s-DCT) system.

5.1 Introduction

Scatter radiation is a major issue for x-ray imaging systems with cone-beam x-ray radiation and flat panel detectors. It can severely degrade the image quality by reducing the contrast, increasing image noise, and causing image artifacts, such as cupping artifact, ring artifact and streaking artifact.[120], [121] Scatter reduction hardware, such as anti-scatter grids (ASG), is often used to reject the scatter signal physically. The ASG consists of a series of alternating strips which collimate the radiation and reject scatter radiation coming from directions other than the primary beam. Although ASG rejects scatter radiation from reaching the detector, the primary signal is also reduced due to the collimation.[122] For digital breast tomosynthesis, the effectiveness of the anti-scatter grid is still in debate.[123], [124] In addition to physically reject the scatter signal, mathematical model-based scatter estimation has been intensively investigated. This includes convolution-based method, Monte Carlo (MC) simulation method, and a hybrid method.[125]–[129] Among them, the MC simulation method produces the most accurate estimation; however, it requires the most computation time. Convolution-based method estimates scatter by convoluting the projection image with a scatter kernel obtained from MC simulations. The convolution-based method is computationally efficient; however, the scatter estimation is not as accurate. Recent studies showed the computation time of MC simulation could be significantly reduced using advanced graphics processing units (GPU), making this scatter correction method more practical in the clinical setting.[104], [130], [131]

Measurement-based scatter correction method estimates the scatter profile from sparsely sampled scatter/primary signal.[121], [132]–[136] One method uses a beam-stop (beam-absorber) array (BSA) installed close to the x-ray source.[137]–[139] The BSA blocks a fraction of the x-ray photons and creates multiple shadow areas on the detector that consist only of scatter. Scatter map is then estimated by interpolating the measured scatter signal under the BSA shadow area. The scatter map estimated using BSA is relatively accurate. However, BSA is prone to the residual artifact due to the missing data.[140] Other techniques, such as the beam-pass array (BPA) and primary modulation method, have also been investigated for sampling and recovering scatter profile.[133], [141]–[143] Previous, our team demonstrated a scatter correction method for stationary digital breast tomosynthesis (s-DBT) using a primary sampling device (PSD).[144], [145] Different than BSA and BPA, which are installed close to the x-ray source and have a large magnification factor, the PSD is placed in close proximity to the patient. The magnification for the PSD is close to 1, which allows much smaller size sampling holes and a much higher sampling density than either BPA or BSA, therefore increases the accuracy of the scatter profile sampling. We have demonstrated that using PSD only increases the radiation dose by 3% while still obtain a good sampling of the scatter profile, and the method can be easily implemented on other digital x-ray imaging systems.[144], [145]

One critical step in measurement-based scatter correction method is the recovery of the scatter profile from the sparse measurements. The majority of the previous research uses interpolation to generate a smooth scatter profile.[134], [135], [138], [141], [146]–[149] When this scatter profile is subtracted from the projection image, the image noise remains the same. As a result, though the contrast ratio of the image is increased, the signal difference to noise ratio (SDNR) does not change in the projection images. In fact, as shown by Zhu *et al*,[150] subtracting a smooth scatter profile will cause noise amplification in the line integral image after logarithmic transformation, resulting in image quality degradation and image artifacts which may overshadow the benefit of scatter removal.

5.2 Method

5.2.1 Scatter Estimation Using Direct Interpolation

In measurement-based scatter correction, the scatter profile is generally recovered by direct interpolation of the sparse signal samples. There are generally two approaches for scatter estimation. The first approach is to use the measured scatter signal $\bar{S_{\boldsymbol{i}}}$ at each sampling point $\boldsymbol{i}$ to interpolate the whole scatter profile S_{SI}:

$$\begin{gathered} \bar{S_i} = Average(S) \text{ within the } i^{\text{th}} \text{ sampling area} \\ S_{SI} = Interpolation(\bar{S_i}). \end{gathered} \tag{5-1}$$

We will refer this method as direct scatter interpolation (SI) in this Chapter. The scatter profile estimated from the SI method is very smooth, as a result, the noise in the projection image is intact after the scatter subtraction:

$$\begin{aligned} Var(P_{SI}) &= Var(T - S_{SI}) \\ &= Var(T) + Var(S_{SI}) + Cov(T, S_{SI}) \approx Var(T)\ , \end{aligned} \tag{5-2}$$

where P_{SI} stands for the estimated primary signal using SI method and T is the total measured signal. Due to the smoothness of the interpolated scatter profile S_{SI}, $Var(S_{SI})$ and $Cov(T, S_{SI})$ can be approximated to zero. As a result, the signal to noise ratio (SNR) in SI corrected image is reduced:

$$SNR_{SI} = \frac{P_{SI}}{\sqrt{Var(P_{SI})}} \approx \frac{P_{SI}}{\sqrt{Var(T)}} < \frac{T}{\sqrt{Var(T)}}\,. \tag{5-3}$$

Since neither the signal difference nor the noise variance is changed significantly in the SI corrected images, the SDNR remains the same after scatter correction.

The second approach is to use the measured scatter signal to calculate the scatter-to-primary ratio $\overline{SPR_i}$ at each sampling point, then interpolating and extrapolating the SPR to the whole image to obtain the SPR profile SPR_{intp}:

$$\begin{gathered} \overline{SPR}_i = Average(S/(T - S)) \text{ at the } i\text{-th sampling the point} \\ SPR_{intp} = Interpolation(\overline{SPR}_i)\ , \end{gathered} \tag{5-4}$$

from which the scatter profile is computed using

$$S_{ISPR} = T \cdot \frac{SPR_{intp}}{SPR_{intp} + 1}\,. \tag{5-5}$$

We will refer to this approach as the interpolated SPR (ISPR) estimation. The ISPR method uses a smooth SPR profile to estimate a locally fluctuating scatter signal.[134], [148], [149], [151] ISPR has the advantage of ensuring positivity and enabling further modeling of the scatter profile, for example, one could impose an upper or lower bound threshold on the SPR profile in ISPR method. At places where scatter varies significantly between two sampling points, ISPR might recover some structural variation of the scatter signal which SI would fail to estimate. In addition, ISPR method suppresses the noise in the projection image after scatter removal:

$$\begin{aligned} Var(P_{ISPR}) &= Var(T - S_{ISPR}) \\ &= Var\left(T - T \cdot \left(1 - \frac{1}{SPR_{intp} + 1}\right)\right) \\ &= Var\left(T \cdot \left(\frac{1}{SPR_{intp} + 1}\right)\right) \\ &\approx \left(\frac{1}{SPR_{intp} + 1}\right)^2 \cdot Var(T) < Var(T)\,, \end{aligned} \tag{5-6}$$

where we approximate SPR_{intp} as a constant since the spline interpolation is always smooth between two sampling points. Hence, the SNR will be similar to that in the raw image before scatter correction:

$$\begin{aligned} SNR_{ISPR} &= \frac{P_{ISPR}}{\sqrt{Var(P_{ISPR})}} \\ &\approx \frac{T \cdot \left(\frac{1}{SPR_{intp} + 1}\right)}{\sqrt{\left(\frac{1}{SPR_{intp} + 1}\right)^2 \cdot Var(T)}} = \frac{T}{\sqrt{Var(T)}}\,. \end{aligned} \tag{5-7}$$

Since the signal difference is also scaled by the same factor, the CR is not enhanced in the scatter corrected image, and the SDNR is not improved.

In summary, scatter correction using scatter profile estimated from direct interpolation of either scatter or SPR samplings would not improve the SDNR of the image.

5.2.2 *f*-SPR Scatter Estimation

Scatter can be modeled as a convolution of incident x-ray photon *I* and a scatter point spread function *SPSF*:

$$S[\boldsymbol{r}] = \textstyle\sum_u I[\boldsymbol{u}] \cdot SPSF(\boldsymbol{u}, \boldsymbol{r}) \ , \tag{5-8}$$

where $I[\boldsymbol{u}]$ is the total incident photon flux at the image space position $\boldsymbol{u}$, and the scatter point spread function $SPSF(\boldsymbol{u}, \boldsymbol{r})$ describes the scatter kernel from the image space position $\boldsymbol{u}$ to the detector position $\boldsymbol{r}$. This model suggests that scatter is generally a smooth function on the large scale but could still carry local fluctuations. Direct interpolation of the sparsely measured scatter samplings only generates a smooth scatter profile. The high frequency noise associated with scatter is not subtracted from the image. Though there is no accurate way to estimate this high frequency information, to the first order it is reasonable to assume that this part of the signal scale with total local signal measured due to the correlation between S and T. And we can make a heuristic approximation:

$$\sum_u I[\boldsymbol{u}] \cdot SPSF(\boldsymbol{u}, \boldsymbol{r}) \approx P[\boldsymbol{r}] \cdot \sum_{r'} SPR[\boldsymbol{r}'] \cdot G(\boldsymbol{r} - \boldsymbol{r}') \ , \tag{5-9}$$

where the $G(r - r')$ is a convolution kernel depending only on the distance between two points $\boldsymbol{r}$ and $\boldsymbol{r}'$ in the detector coordinate. The scatter profile, therefore, can be approximated to:

$$\begin{aligned} S[\boldsymbol{r}] &\approx P[\boldsymbol{r}] \cdot \sum_{r'} SPR[\boldsymbol{r}'] \cdot G(\boldsymbol{r} - \boldsymbol{r}') \\ &= (T - S) \cdot SPR_f = T \cdot \left(1 - \frac{1}{SPR_f + 1}\right). \end{aligned} \tag{5-10}$$

For the actual calculation, we use the interpolated scatter profile S_{SI} from SI method to estimate $SPR[\boldsymbol{r}']$ using $SPR_0 = S_{SI}/(T - S_{SI})$, and adopt a range bound Gaussian filter kernel as $G(\boldsymbol{r} - \boldsymbol{r}')$:

$$SPR_f = \sum_{r'} \frac{S_{SI}[\boldsymbol{r}']}{T[\boldsymbol{r}'] - S_{SI}[\boldsymbol{r}']} \cdot G(\boldsymbol{r} - \boldsymbol{r}') \, . \tag{5-11}$$

The *f*-SPR estimated scatter then becomes:

$$S_{f-SPR} = T \cdot \left(\frac{SPR_f}{SPR_f + 1} \right). \tag{5-12}$$

Since the filtered SPR profile is a locally smooth function, noise in the projection image will be suppressed after the *f*-SPR scatter correction:

$$\begin{aligned} Var(P_{f-SPR}) &= Var(T - S_{f-SPR}) \\ &= Var\left(T - T \cdot \left(1 - \frac{1}{SPR_{fc} + 1} \right) \right) \\ &= Var\left(T \cdot \left(\frac{1}{SPR_{fc} + 1} \right) \right) \approx \left(\frac{1}{SPR_{fc} + 1} \right)^2 \cdot Var(T) \, , \end{aligned} \tag{5-13}$$

and the SNR is maintained after scatter correction. Consequentially, SDNR is enhanced after *f*-SPR scatter correction.

In Eq. 13, we approximate SPR_{fc} as a constant. This approximation holds when the filtered *SPR* profile is locally smooth. However, if the filter size is close to zero, this approximation fails and the noise variance of the *f*-SPR corrected image converges to that of the SI corrected image. As will be later demonstrated, the filter size controls the amount of the total signal that is scaled and copied to the scatter estimation. When the filter size is zero, *f*-SPR is essentially the SI method; when the filter size increases to the range of the sampling distance, *f*-SPR converges to ISPR. Unlike the ISPR where the true signal is scaled, the signal difference would not be scaled much at small filter size in *f*-SPR. In *f*-SPR, as shown in Eq. 12, the smooth SI scatter profile is adapted to compute SPR before filtering, this sets the baseline of the scatter estimation and prevents the true signal from being copied into the scatter estimation. In essence, the *f*-SPR method combines the advantage of the SI method which enhances the contrast and the ISPR method which reduces the noise to result in an enhanced SDNR. A flow chart of the *f*-SPR method is shown in Fig. 5-1.

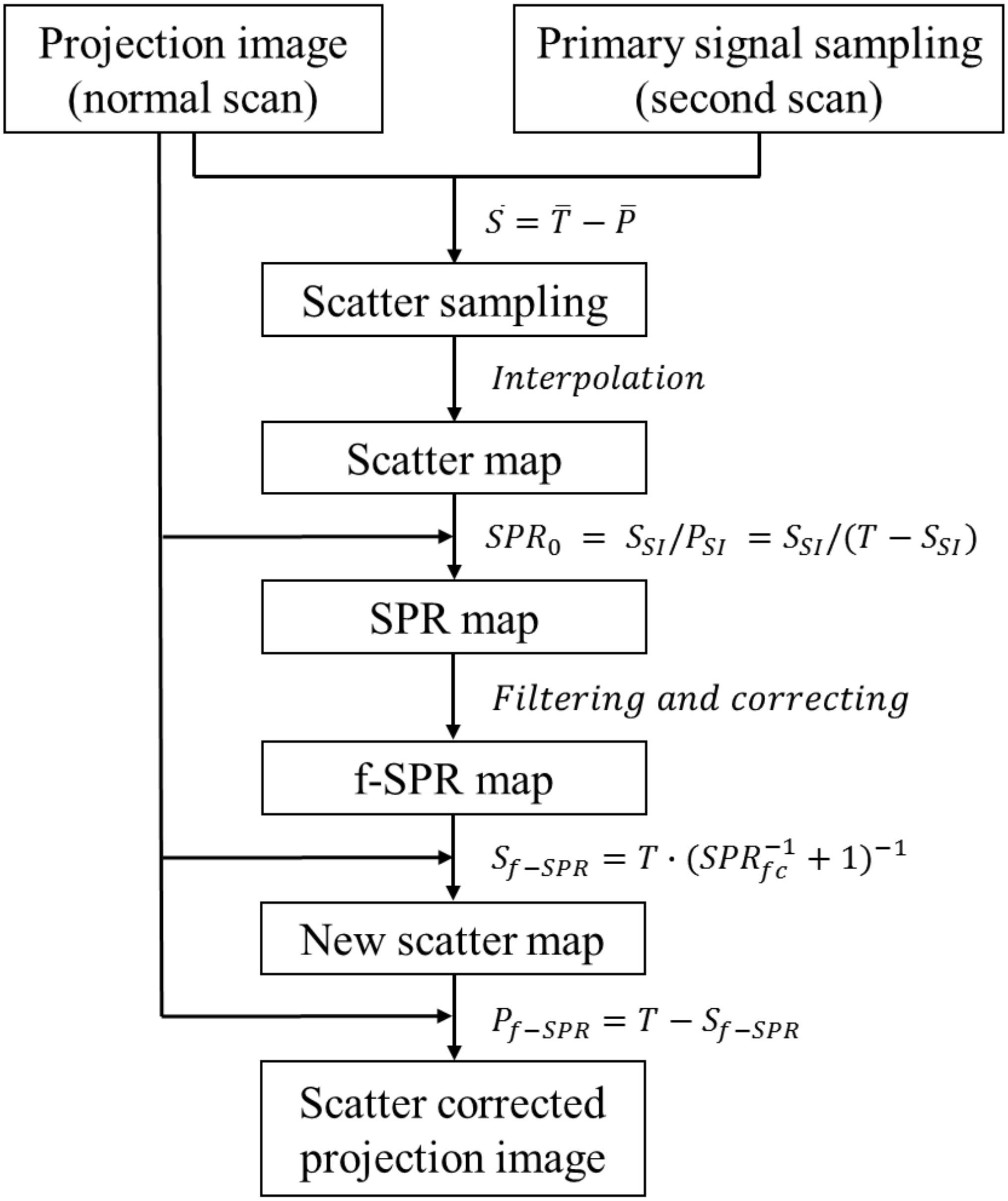
Projection image (normal scan)
Primary signal sampling (second scan)
$\dot{S} = \bar{T} - \bar{P}$
Scatter sampling
Interpolation
Scatter map
$SPR_0 = S_{SI}/P_{SI} = S_{SI}/(T - S_{SI})$
SPR map
Filtering and correcting
f-SPR map
$S_{f-SPR} = T \cdot (SPR_{fc}^{-1} + 1)^{-1}$
New scatter map
$P_{f-SPR} = T - S_{f-SPR}$
Scatter corrected projection image

Figure 5-1: Flow chart of the f-SPR scatter estimation method.

The first step in *f*-SPR is segmenting out the sampling region in the scan with PSD installed. This is done using Otsu's threshold method with a morphological closing operation.[152] To avoid the penumbral effect, the identified sampling area is morphologically eroded by 4 pixels. Next, the center of each sampling area is located, and the average scatter signal of each sampling area is computed using $\bar{S} = \bar{T} - \bar{P}$, where $\bar{P}$ is the average primary signal measured from the PSD scan and $\bar{T}$ is the average total signal measured from the normal scan in the same sampling region. A bi-harmonic spline interpolation and extrapolation is then applied on the sparse scatter samplings and the SI estimated scatter profile S_{SI} is obtained.[153] Based on this smooth scatter profile S_{SI}, the SPR at each pixel is calculated using $SPR = S_{SI}/(T - S_{SI})$.

At regions with structural change, such as places with metal implants, the scatter signal might be overestimated since the finite sampling points might be too sparse to capture the change. To avoid overestimation, the computed SPR profile is corrected using a preset maximum SPR value obtained from previous studies.[154], [155] This structural variation of the scatter signal could also be recovered using the information from the adjacent scatter profile through mathematical modeling.[140] In this study, we set a maximum SPR value of 2 for breast imaging and a maximum SPR value of 10 for thoracic imaging. After correction, the SPR profile is convoluted with a Gaussian filter kernel, and the filtered SPR profile is obtained (Eq. 12). In this study, we used a Gaussian filter with standard deviation σ of 4 pixels and filter size equal to 17 pixels (see discussion section on the choice of filter size). Finally, the scatter-corrected projection image is obtained: $P_{f-SPR} = T - S_{f-SPR} = T \cdot \left(\frac{1}{SPR_{fc}+1}\right)$.

5.2.3 Imaging System

A stationary digital breast tomosynthesis (s-DBT) system was used for breast imaging studies.[8], [10] The s-DBT system uses field emission-based carbon nanotube X-ray source array, which eliminates the mechanical source motion in the traditional tomosynthesis scan. The s-DBT system has a linear x-ray source array with 31 focal spots and an angular coverage of 28 degrees, a typical anode voltage of 31 kVp, a detector pixel size of 70 µm, and an image resolution of 3328×4096.[10] In this study, we only used 15 projection images with 28-degree angular coverage in 2×2 binning mode, with an equivalent pixel size of 140 µm. Fig. 2a shows the s-DBT system, which is undergoing clinical trials at the University of North Carolina Hospitals (NCT01773850, NCT02008032).

The stationary digital chest tomosynthesis (s-DCT) system employees similar x-ray source array technology. It uses a linear source array with 75 focal spots and an angular coverage of 15 degrees at 100 cm source-to-detector distance; the anode voltage is 80 kVp. A flat panel detector is used in the s-DCT system which has 1536×1536 pixels and a pixel size of 194 µm.[8] The s-DCT system is also currently under a clinical trial at the Biomedical Research Imaging Center at University of North Carolina (NCT02075320).

5.2.4 Primary Sampling Device

The primary sampling device is a thin metal plate with an array of small open apertures.[144], [145] As x-ray photons can only penetrate through the open apertures, the projection of the apertures on the detector contains mostly the primary signals, the primary photons in each projection view can, therefore, be sampled using PSD.

During the scatter correction, normal projection images are first acquired without PSD. After the normal scan, a second scan is performed with the PSD installed close to the imaged object. By comparing the total signal intensity from the normal scan and the primary signal intensity from the second scan, samplings of scatter/SPR are obtained, which are used to estimate the full scatter map.

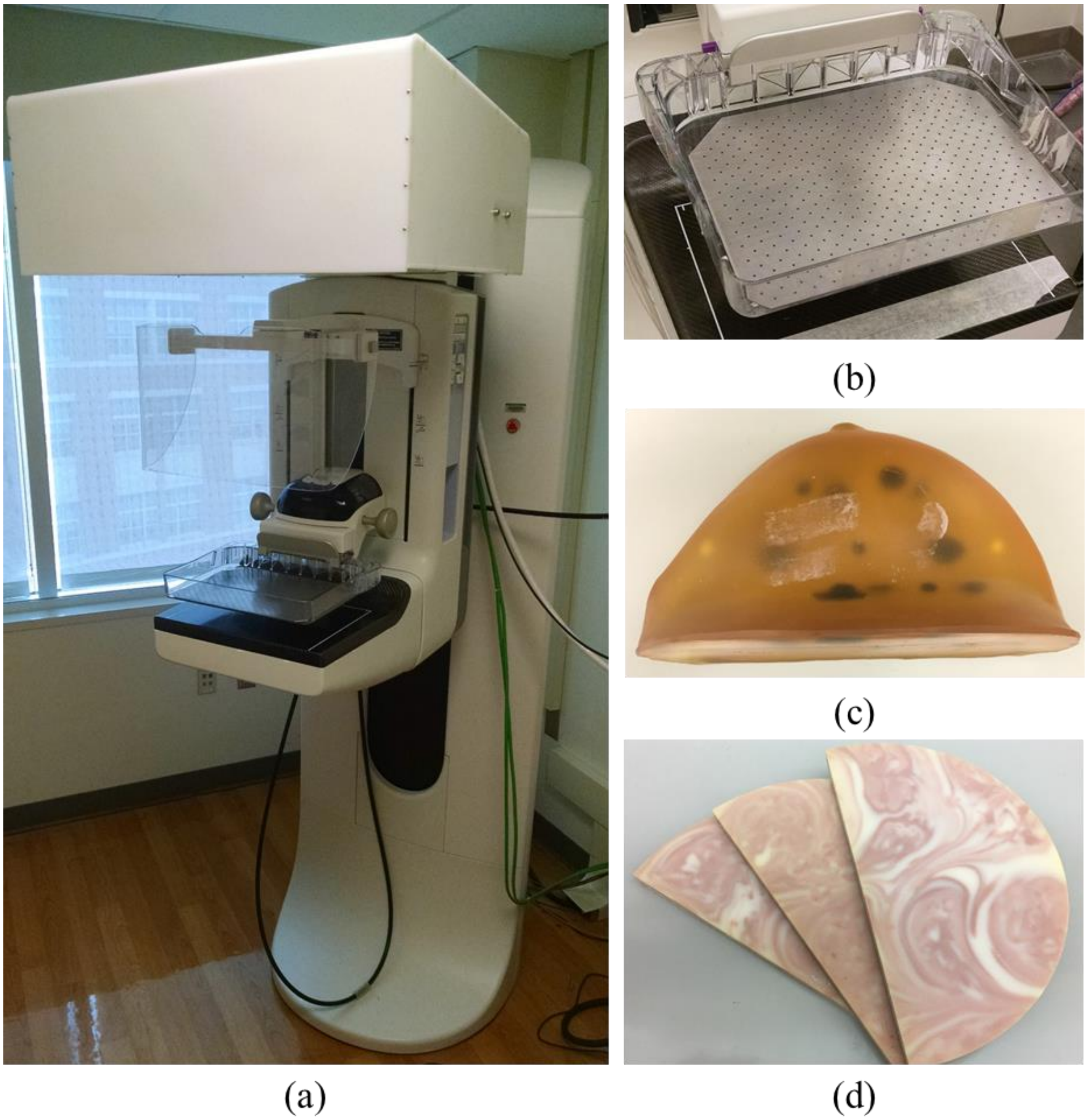

Figure 5-2: (a) Stationary digital breast tomosynthesis (s-DBT) system with PSD installed. (b) The primary sampling device (PSD) designed for the s-DBT system is placed on the compression paddle. (c) Breast biopsy phantom. (d) BR3D breast imaging phantom.

The PSD used with the s-DBT system is made of a 2 mm thick stainless steel plate, it contains apertures of 2 mm diameter with 10.6 mm spacing. This translates to an aperture area of only 3% of the total area, resulting in a minimal additional dose.[144] Figure 5-2(a) and 2(b) show a PSD placed on the compression paddle of the s-DBT system. The PSD used in the s-DCT system is made of a 6 mm thick lead plate, it contains apertures spaced 31 mm apart with a diameter of 6 mm, also occupying about 3% of the total plate area.[145]

5.2.5 Phantom Studies

A breast biopsy phantom and BR3D breast imaging phantom (Computerized Imaging Reference Systems, Virginia, USA) are used in this study to demonstrate and evaluate the *f*-SPR method. Both phantoms were imaged by the s-DBT system. Pictures of the biopsy phantom and the BR3D phantom are shown in Fig. 5-2(c) and 5-2(d), respectively. In this study, we used three BR3D slabs, one feature slab with mass and micro-calcification simulants sandwiched between two breast tissue mimicking slabs. The thickness of each slab is 1 cm. A 50 µm diameter tungsten wire phantom placed on top of three BR3D adipose slabs is used to measure the system's modulation transfer function (MTF).

An adult female thoracic cadaver, obtained through collaboration with the UNC School of Medicine, was imaged by the s-DCT system. The thickness of the thorax is 25cm.

5.2.6 Image Reconstruction

Scatter-corrected projection images are reconstructed using the adapted fan volume reconstruction (AFVR) method.[108] AFVR utilizes the linear source geometry in the stationary tomosynthesis, in which it transforms the 3D cone-beam reconstruction into a series of "2D" fan volume reconstructions. In AFVR, each fan volume reconstruction is independent. In addition, each system matrix of the fan volume is pre-calculated and stored in memory. This makes AFVR extremely fast, even without the GPU implementation. In this study, simultaneous iterative reconstruction technique with twenty iterations was used.[69] The reconstructed slice thickness is 0.5 mm for the biopsy and BR3D phantom, and 3 mm for the human cadaver.

5.2.7 Evaluation Metrics

The effectiveness of the *f*-SPR method is evaluated using the contrast ratio (CR) and SDNR. CR is calculated using $CR = \left(I_f - I_b\right)/I_b$, where I_f is the average pixel value of the foreground (features), and I_b is the average pixel value of the background area around the features.

Practically, the local CR is usually stretched and maximized by adjusting the image display window. A more meaningful metric for measuring the image quality is the ability to differentiate structures/tissues given the presence of the background noise. This is measured using the signal difference to noise ratio (SDNR), defined as $SDNR = \left(I_f - I_b\right)/\sigma_b$, where σ_b is the noise level of the background.

The spatial resolution is characterized by the modulation transfer function (MTF). A 50 μm slanted tungsten wire phantom was used to measure the system MTF. SI, ISPR, and *f*-SPR methods were applied to the projection images, the scatter corrected projection images were then reconstructed using AFVR. Finally, using the slice containing the focused wire, the MTF was obtained using the method described by Fujita *et al.*[156]

5.3 Results

5.3.1 Scatter Correction on Projection Image

Figure 5-3(a)–(c) show the scatter profiles estimated using different methods for the breast biopsy phantom in the central projection view. The SI estimated scatter is very smooth since it is obtained directly from interpolation; the ISPR estimated scatter, on the other hand, is quite noisy and it even shows features from the projection image. The *f*-SPR estimated scatter looks quite similar to SI estimated scatter except that it is locally grainy, since the high-frequency spectra of the total signal are scaled and added into the scatter estimation. The characteristics of three estimated scatter profiles are better illustrated from the line profiles shown in Figure 5-3(e). In ISPR, the SPR map used to estimate scatter is smooth due to direct interpolation. Although the ISPR method has better noise properties, the signal difference is decreased in comparison to the projection image without scatter correction. The SI method estimates a very smooth scatter profile, consequently the noise in the original projection image is unaffected by the scatter correction. Therefore, the scatter-corrected image is quite noisy using the SI method. The *f*-SPR estimated scatter is smooth on a large scale but fluctuates locally. The scatter-corrected image using *f*-SPR maintains the signal difference, as in SI corrected image, but suppresses the noise during the scatter correction. It results in an improved SDNR in the projection image, which consequently leads to a better reconstruction image.

To quantitatively evaluate the projection image quality after scatter correction, we selected seven regions of interest (ROI) across the phantom and computed both CR and SDNR for each ROI. Figure 5-4 shows the locations of each ROI [Fig. 5-4(a)], enlarged views of the central projection images after applying different scatter correction methods [Fig. 5-4(b)], and CR and SDNR of the seven regions [Fig. 5-4(c)]. As seen in the figure, both the SI and *f*-SPR corrected images show a significant improvement in the CR. However, only the *f*-SPR corrected projection image shows an improved SDNR. In the ISPR corrected image, the CR and SDNR are comparable or only slightly better than the projection image without scatter correction. Overall, we observed an average of 58% increment in CR and an average of 51% increment in SDNR in the projection image corrected using the *f*-SPR method.

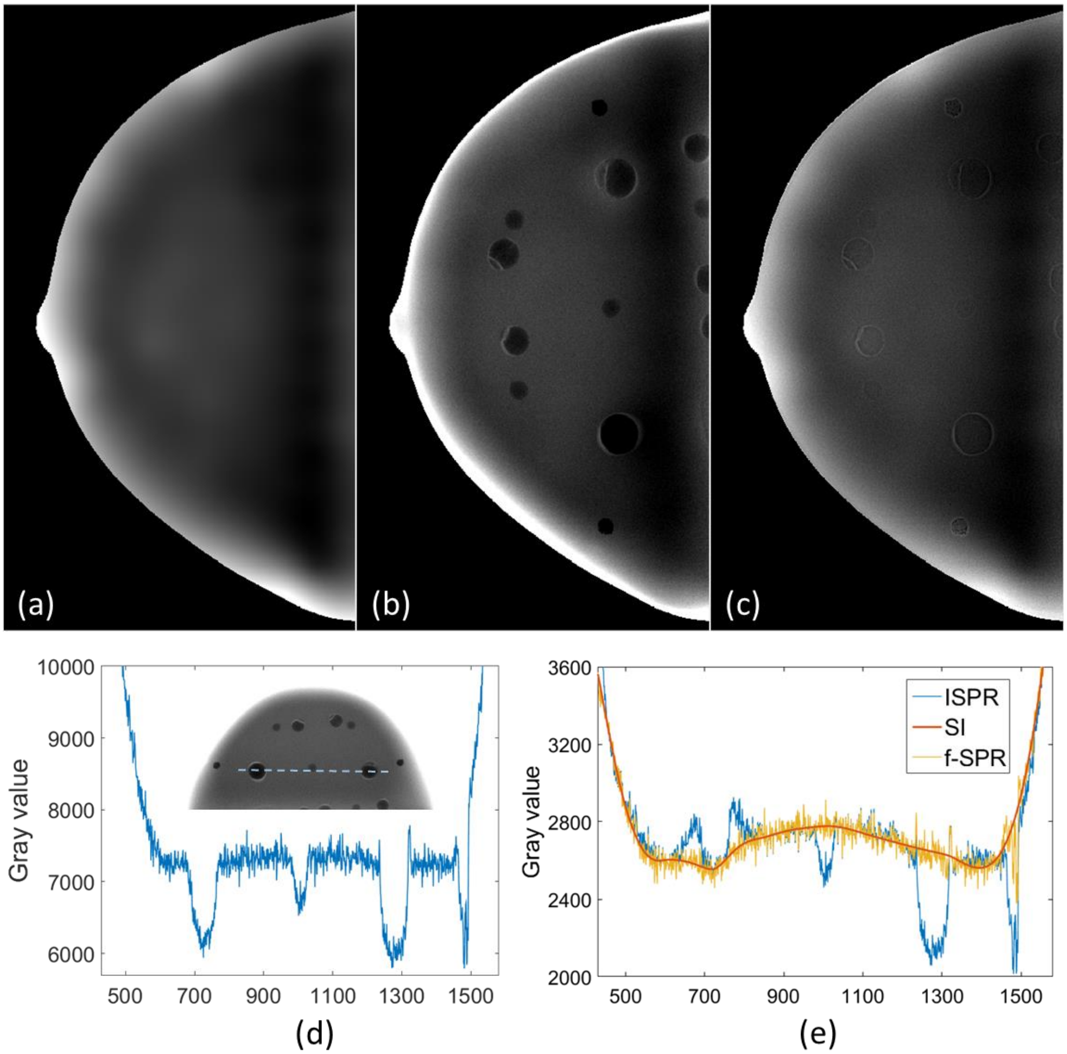

Figure 5-3: Top: scatter profile of the central projection view estimated by (a) SI, (b) ISPR and (c) f-SPR method. The scatter signal outside the phantom is set to be zero to avoid artifact during reconstruction. All scatter profiles are shown in the same display window. Bottom: (d) Line profile of the projection image before scatter correction. The position is indicated by the blue dashed line on the biopsy phantom. (e) Profiles of scatter estimated by different methods along the same line. The SI estimated scatter is very smooth and does not contain any noise. The ISPR estimated scatter though over/under estimates the scatter in the region with object features. The f-SPR estimation captures both the large scale smooth variation and the local fluctuation of the scatter profile.

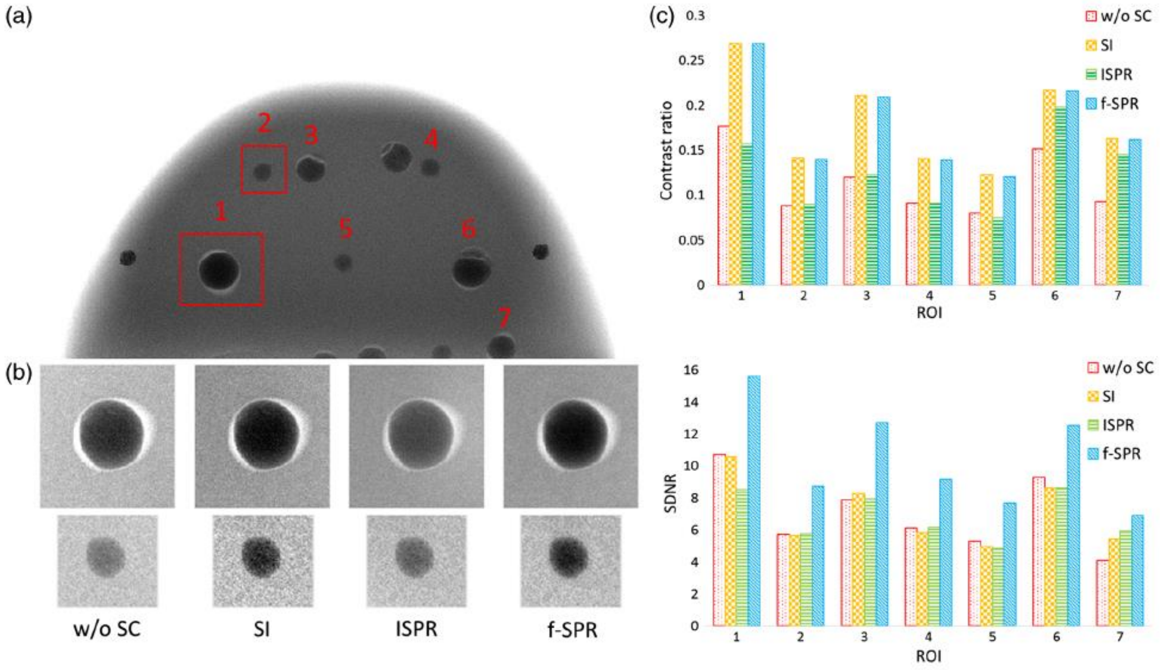

Figure 5-4: (a) Central projection view of the breast biopsy phantom. The index marks seven regions that are used in CR and SDNR analysis. (b) Enlarged views of region 1 and region 2 (from left-to-right: without scatter correction, SI corrected, ISPR corrected, and f-SPR corrected images). (c) The contrast ratio and SDNR for the seven ROIs. Both SI and f-SPR corrected images show a significant improvement in contrast ratio, but only f-SPR shows significant enhancement in SNDR. On average, a 58% increase in CR and 51% increase in SDNR are observed with f-SPR scatter correction method.

5.3.2 Reconstruction Image Quality Analysis

The in-focus reconstruction slices of the BR3D phantom before and after scatter correction are shown in Fig. 5-5. Compared to the reconstruction image without scatter correction, all scatter-corrected reconstruction images show higher contrast and better conspicuity. Both SI and *f*-SPR corrected reconstruction slice shows a noticeably improved contrast, however, the noise is significantly lower in the *f*-SPR corrected image. ISPR corrected reconstruction slices show a low noise level, however, the improvement of the image contrast is not as good as that in the reconstruction corrected using SI or *f*-SPR.

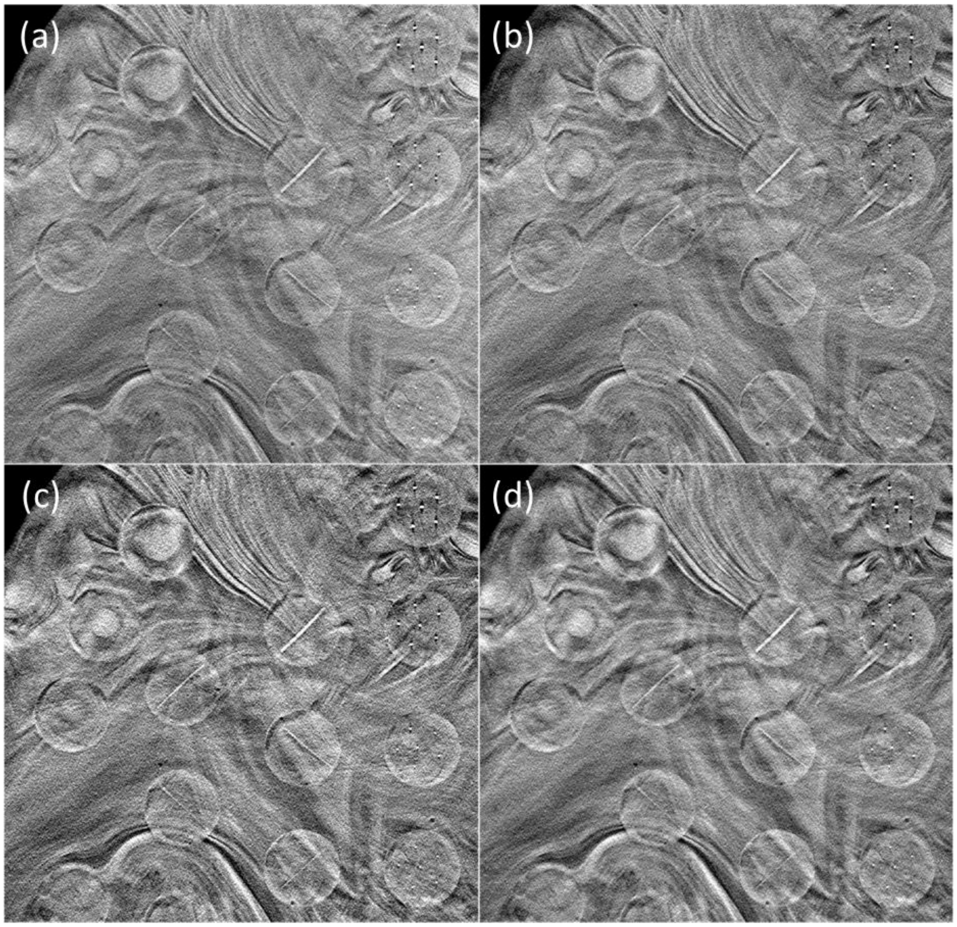

Figure 5-5: In-focus reconstruction slice of the BR3D feature slab: (a) without scatter correction, (b) with ISPR, (c) with SI, and (d) with f-SPR scatter correction. All images are displayed at the same window width. The window level is set to be the average of the image intensity. Reconstruction with *f*-SPR correction has a significantly better SDNR compared to reconstruction with other scatter correction methods, and a CR comparable to that in the reconstruction with SI correction.

Enlarged views of spheroid masses and microcalcifications are shown in Fig. 5-6. Both SI and *f*-SPR corrected reconstructions show significant improvement in contrast; however, the pronounced noise in SI corrected image makes it difficult to identify small features like micro-calcifications from the image. On the other hand, *f*-SPR corrected reconstruction has a noise level similar to the uncorrected and the ISPR corrected reconstructions, but with a much higher CR, making it easy to identify both masses and microcalcifications in the image.

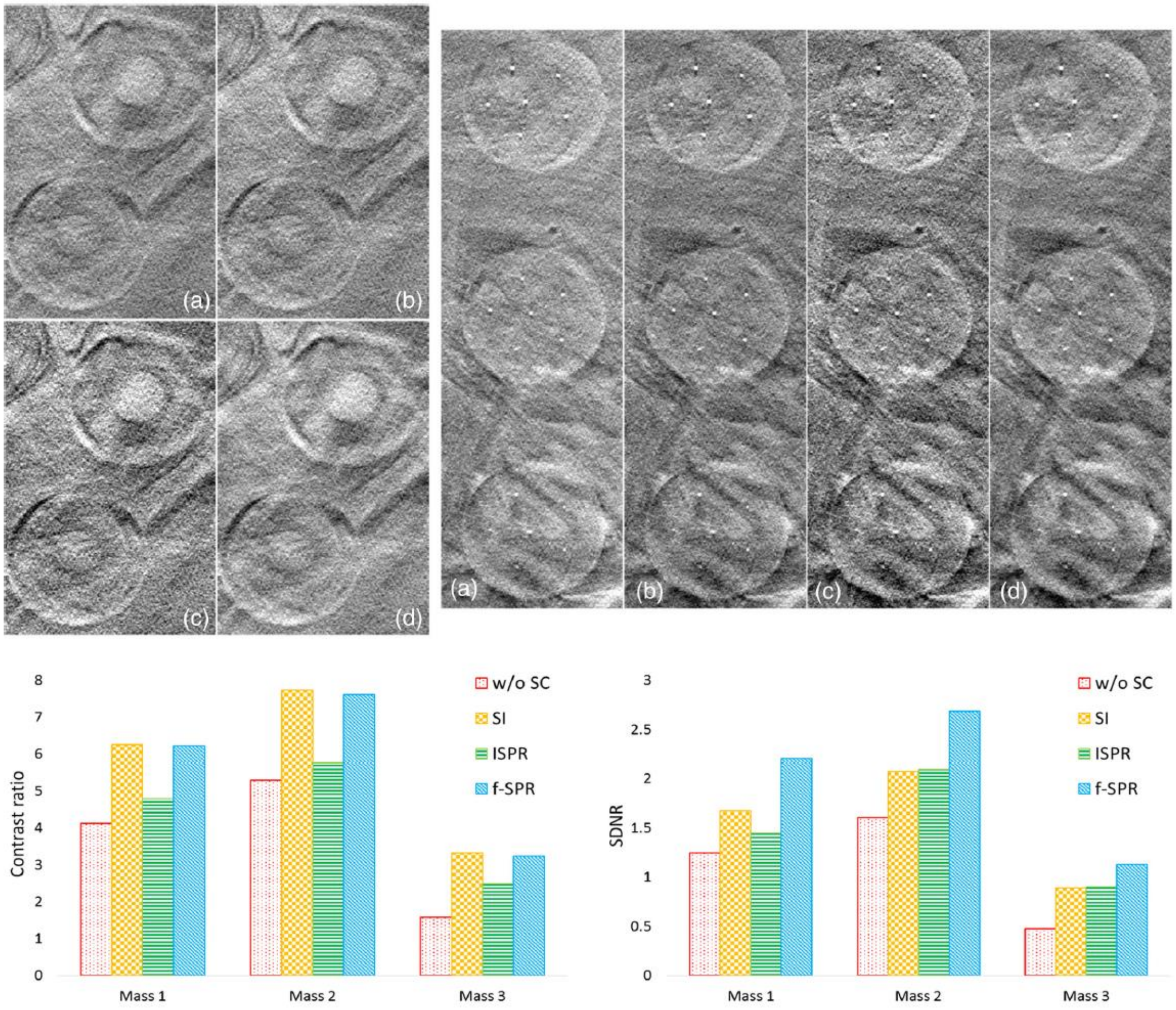

Figure 5-6: Top left: in-focus reconstruction slice of two spheroid masses in the BR3D phantom (a) without scatter correction, (b) with ISPR, (c) with SI and (d) with f-SPR scatter correction. Top right: in-focus reconstruction slice of micro-calcifications in the BR3D phantom (a) without scatter correction, (b) with ISPR, (c) with SI and (d) with f-SPR scatter correction. All images are displayed at the same window width. Bottom: CR and SDNR of three spheroid masses.

Quantitative analysis of CR and SDNR on three spheroid masses are shown in Fig. 5-6. Three largest masses in the BR3D phantom were chosen for this analysis with diameters of 6.3 mm, 4.7 mm and 3.9 mm. For masses, the results show the CR is improved by 69.5%, 27.4% and 66.5% for SI, ISPR and f-SPR corrected reconstruction, respectively. The SDNR is improved by 49.8%, 45.1%, and 93.8% for SI, ISPR, and f-SPR corrected reconstruction, respectively. The results suggest that the f-SPR corrected reconstruction has a comparable increment in the CR, and almost doubles the increment in SDNR compared to SI corrected reconstruction. The ISPR corrected reconstruction has improvement in both CR and SDNR; however, the improvement is not as good as that in either SI corrected or f-SPR corrected reconstruction.

5.3.3 Chest Imaging

We further implemented PSD with the f-SPR correction on an s-DCT system for chest imaging. A human cadaver was imaged using s-DCT with additional PSD scan. The f-SPR scatter correction was then applied to the projection images, which were later reconstructed using AFVR. Both projection views and reconstruction images with and without f-SPR scatter correction are shown in Fig. 5-7. The f-SPR scatter correction improves image contrast in both projection and reconstruction images, body anatomy and small features become more conspicuous after scatter correction.

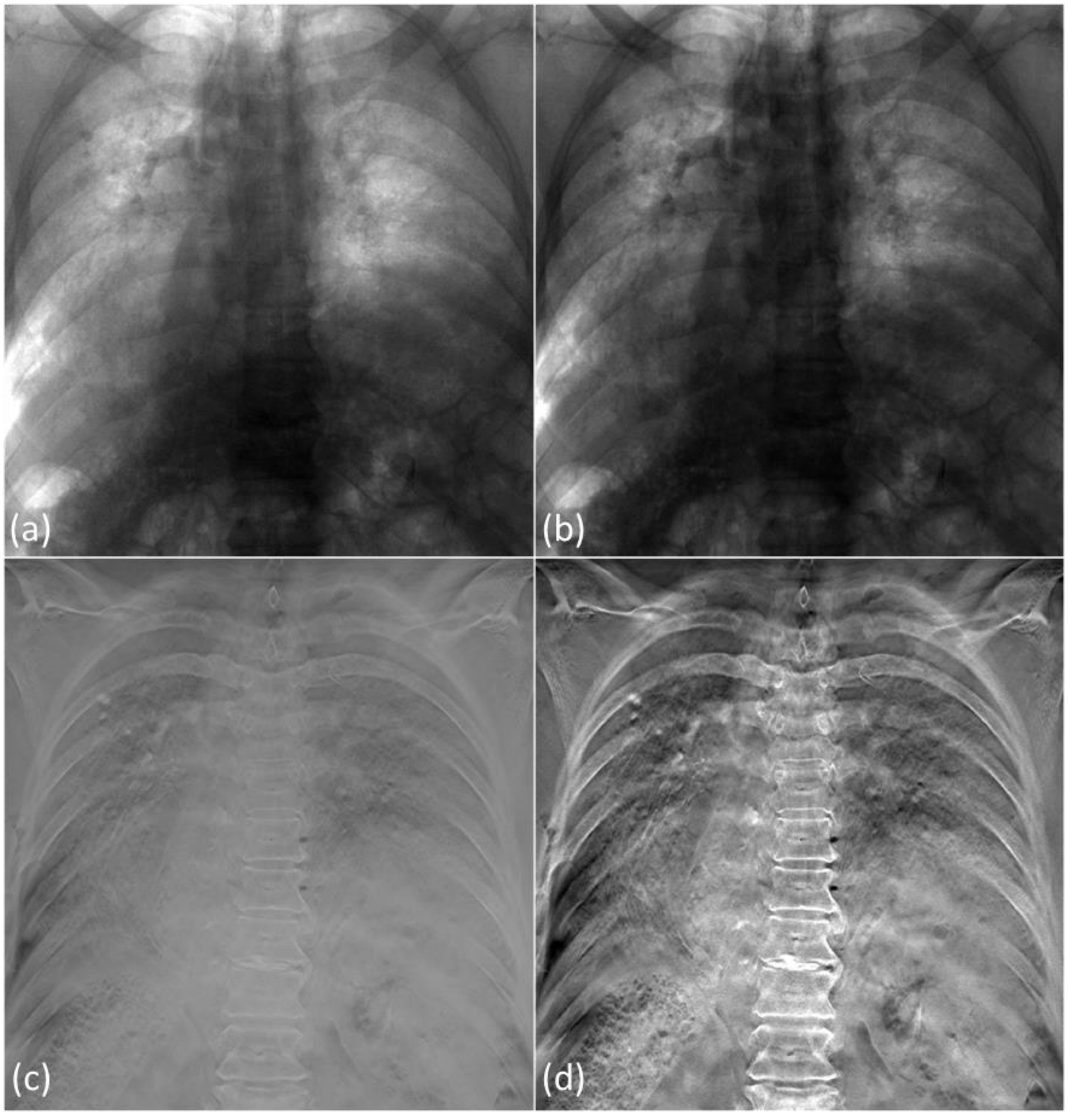

Figure 5-7: Human cadaver imaged by s-DCT. Projection image of the central view (a) without scatter correction, (b) with f-SPR scatter correction. Reconstruction image (c) without scatter correction, (d) with scatter correction. Images before and after f-SPR scatter correction are displayed at the same window width, but different window level, which is set to be the mean gray value of the image.

5.4 Discussion

5.4.1 Filter Size in *f*-SPR Scatter Correction

One of the most important steps in *f*-SPR is the filtering. Using Pearson's correlation[157], we investigated the similarity between the *f*-SPR estimated scatter and direct interpolation estimated scatter when varying filter size. The standard deviation of the Gaussian filter σ is set to be $0.25 \cdot (\text{filter size} - 1)$, and the central region is used for computing Pearson's correlation. The result is shown in Fig. 5-8. When no filtering applied on the SPR map, the f-SPR is equivalent to SI and the Pearson's correlation is one. As the filter size increases, the Pearson's correlation between SI and f-SPR estimated scatter decreases. On the other hand, the correlation between f-SPR and ISPR estimated scatter increases as the filter size increases. When the size of filter reaches the distance between two sampling points, the correlation between f-SPR estimated scatter and ISPR estimated scatter is close to one.

The image quality, in terms of CR and SDNR, is also studied with varying filter size. Three largest spherical masses in the feature slab were chosen for this analysis, with results shown in Fig. 5-9. The results suggest that when the filter size is small, the image quality of the f-SPR corrected reconstruction is similar to that of the SI corrected reconstruction; when the filter size is large, the image quality of f-SPR corrected reconstruction is more similar to the ISPR corrected reconstruction. The SDNR curve increases and then decreases, with a peak value around 4 pixels. The increase in SDNR when the filter size is small is probably due to the plateau region in the CR curve, where CR is maintained as the noise decreases with filter size. As the filter size further increases, the CR starts to drop but the noise level is not further reduced. Hence, the SDNR drops and finally matches the SDNR in the ISPR corrected reconstruction image.

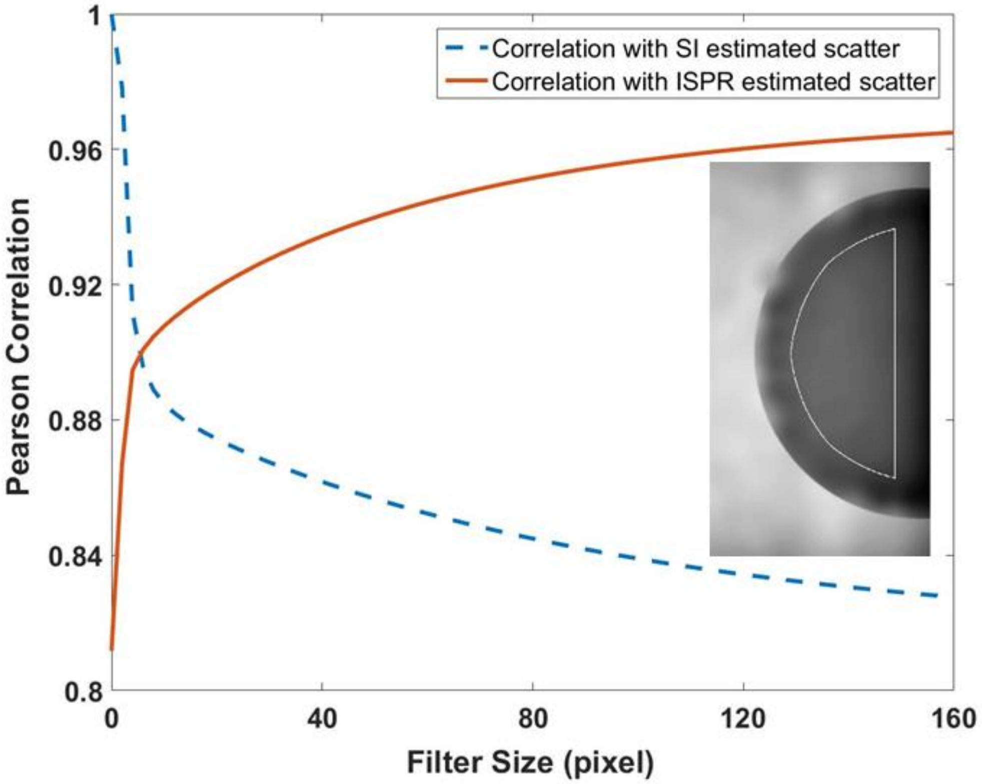

Figure 5-8: Correlation of the scatter profile between the f-SPR estimation and the SI/ISPR estimation. The white line on the scatter map indicates the area that is used to compute the correlation.

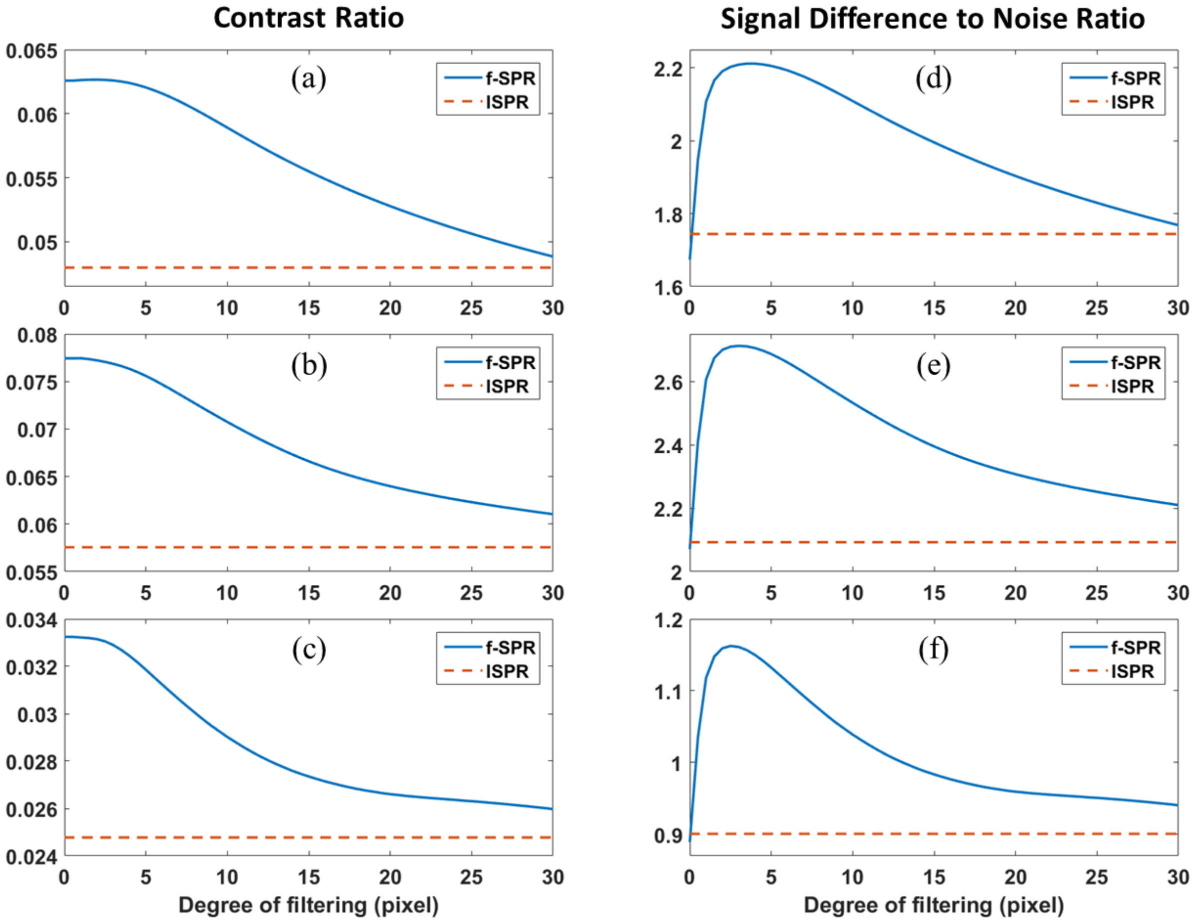

Figure 5-9: The contrast ratio of (a) mass 1, (b) mass 2, and (c) mass 3. SDNR of (d) mass 1, (e) mass 2, and (f) mass 3. The solid blue line depicts the f-SPR scatter-corrected reconstruction, while the red dashed line depicts the ISPR scatter-corrected reconstruction. The CR and SDNR in the SI scatter-corrected reconstruction are the same as those of the f-SPR with no filtering. The x axis is the standard deviation of the Gaussian filter.

5.4.2 Image Resolution with *f*-SPR Scatter Correction

One concern about the *f*-SPR algorithm is the possible loss of the spatial resolution due to the filtering. Visual inspection of the small features, such as micro-calcification shows no image blur on the *f*-SPR corrected reconstruction image. To quantitatively investigate the possible image resolution change, we measured the system MTF before and after scatter correction, the result is shown in Fig. 5-10. The image resolution at 10% MTF before scatter correction is 4.5 line per mm, and it drops slightly to 4.4 line per mm after *f*-SPR scatter correction using a Gaussian filter with a filter size of 17×17 pixel. Both the SI corrected and ISPR corrected reconstruction show similar frequency at 10% MTF. However, the reconstruction from Gaussian filtered SI corrected projection data using the same filter as *f*-SPR shows severe degradation in the image resolution, with the frequency of 10% MTF at 0.8 line per mm. The MTF curves are consistent with our visual observation.

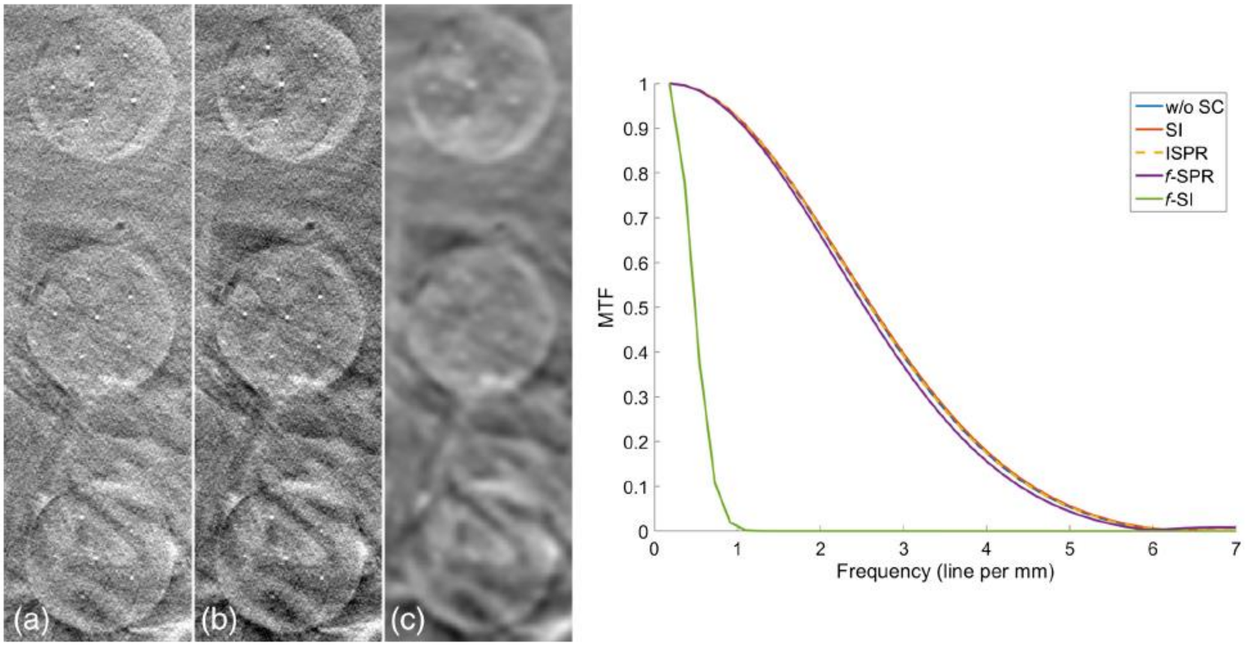

Figure 5-10: Left: enlarged view of micro-calcifications in the in-focus reconstruction slice of the BR3D phantom: (a) without scatter correction, (b) with *f*-SPR scatter correction and (c) with direct Gaussian filtering on the SI corrected projection data (*f*-SI). Right: system MTF curve using different processing methods. It is clear that the *f*-SPR method has a negligible impact on the spatial resolution, while direct filtration of the SI corrected image with the same filter size dramatically reduces the spatial resolution.

5.4.3 Advantages, Limitations, and Future Work

One advantage of using SPR for scatter correction is that the noise in the projection image is suppressed after the scatter removal. An underlying assumption of this approach is that the noise in the scatter signal and the noise in the total signal are correlated. This is a valid assumption considering that a large portion of the total signal is the scatter, especially in the regions with high SPR values. This assumption could be inaccurate in the regions with very low scatter, however, the high-frequency correction that will be applied to those regions is also small. Therefore, the reconstruction image quality significantly improves after the *f*-SPR scatter correction.

Scatter correction using simple scatter interpolation improves the local contrast ratio but it fails to reduce noise, while correction using ISPR reduces the noise level but it fails to improve the local contrast. The *f*-SPR method takes the advantages of both scatter estimations and balances between the two with different levels of filtering. When no filtering is applied, the *f*-SPR is same as the SI scatter correction. When the scale of filtering is close to the PSD sampling distance, the scatter estimated by *f*-SPR and ISPR becomes quite similar to each other.

In this paper, we analyzed the image quality of different scatter correction methods, and shown that the noise is reduced and the SDNR is increased on the projection images using the proposed *f*-SPR method. Due to the nonlinear characteristics of the logarithmic transformation, the noise property would be different on the line integral images.[150] The improvement of image quality, however, is still valid after the logarithmic transformation, since better projection images will lead to better line integral images, which eventually leads to better reconstruction images.

The effect of off-focal radiation has been investigated in a separate study using the stationary digital breast tomosynthesis system. The results showed that the radiation intensity I_0 changes around 5% near the edge of the detector, and only around 2% at the central region of the detector where the breast is imaged. The relatively small change in the radiation intensity is probably due to the fact that the PSD is placed close to the patient and the diameter of the pinhole (2 mm) is much larger than the focal spot size. For this reason, we did not perform any correction for the scatter measurement in this study. With that being said, the off-focal spot radiation correction is necessary and helpful for a more general purpose.[158], [159] Due to limited sampling points, the spatial interpolation of scatter might not be able to restore the structural variation of scatter around object boundaries, leaving an irregular fluctuation in those regions. Local anatomy or metal implants will also create high frequency scatter which might not be sampled. To address this problem, correction is performed on the SPR map based on prior knowledge. In this study, we use a maximum SPR constraint for the correction. When computational time is not a concern, one can also utilize the scatter samples at the neighboring angular projections to restore the variations of scatter as proposed by Yan *et al*[140]. The data redundancy in the projection views might also be used to interpolate the scatter, reducing the number of projections acquired in the additional scan and therefore reducing the scanning time and patient dose.

The *f*-SPR algorithm is implemented in MATLAB and it is run on a customized workstation equipped with an Intel Core i7-5930K CPU. Currently, it takes 30 s to correction one projection image. When utilizing six cores and the MATLAB parallel computing toolbox, the whole scatter correction can be completed in 1.5 min for s-DBT images or 2.5 min for the s-DCT images. The computational time could be further reduced by utilizing GPU hardware.

5.5 Conclusion

A new method, named *f*-SPR, for estimating scatter profile from the sparsely sampled primary signal is proposed. The *f*-SPR method combines the advantages of both the direct scatter interpolation method, which enhances the contrast but fails to reduce noise, and interpolated SPR method, which reduces the noise level but fails to improve the local contrast. With different levels of filtering, it balances between the SI and the ISPR scatter estimations. The *f*-SPR method is demonstrated using breast phantoms and PSD on a stationary digital breast tomosynthesis system, image quality in terms of CR, SDNR and MTF was evaluated and compared with two direct interpolation methods. Significant improvement in image quality was observed using the *f*-SPR method compared to the direct interpolation methods with very small changes in image resolution. Reconstruction of the human cadaver with *f*-SPR scatter correction showed a significantly improved CR and conspicuity while maintaining a similar noise level compared to that without scatter correction. The *f*-SPR method proposed in the paper may be used in any imaging systems where the scatter/primary signal can be sampled accurately. The application of the *f*-SPR scatter correction technique could lead to an improved image quality and reduction in radiation dose in x-ray imaging

CHAPTER 6: Assessing Heart Calcium Score Using Stationary Digital Chest Tomosynthesis

Heart calcium score measures the buildup of calcium inside heart vessels, it is a strong predictor of developing cardiovascular diseases (CVD) and it is widely used clinically to predict the risk of developing CVD. The current standard way of measuring heart calcium score is the computed tomography angiography (CTA), it is expensive and it exposes high radiation dose to patients. In this chapter, we investigate the feasibility of assessing heart calcium score using the stationary digital chest tomosynthesis system developed by our team. We develop the ex vivo heart model as well as the metric for assessing calcium scoring from tomosynthesis images. We then evaluate the tomosynthesis derived calcium score with the CT-derived calcium score in terms of accuracy and consistency, and show that the s-DCT could potentially be a low cost and low radiation dose alternative to the current standard CTA.

6.1 Introduction

Coronary artery calcification (CAC) is the buildup of calcium on the coronary artery wall, it is the early sign of coronary artery disease (CAD). An example of the calcification build up inside the coronary artery is shown in Fig. 6-1.[160] Coronary artery calcium scores (CACS) measures the CAC deposits, it is a strong predictor of CAD. CACS is used clinically to evaluate the extent of CAD and help cardiologists decide the proper medical treatment to their patients (Table 6-1).[161] Computed tomography angiography is currently used to measure the coronary artery calcium score, a CTA image of the coronary artery with calcification is shown in Fig. 6-

2.[162] CTA delivers high radiation to patients (about 8 – 12 mSv), which is 800 times the radiation dose of a single chest radiography. Due to the high radiation dose, CTA would cause a considerable increase in life time cancer risk and therefore it is not suitable for screening purpose.[163], [164]

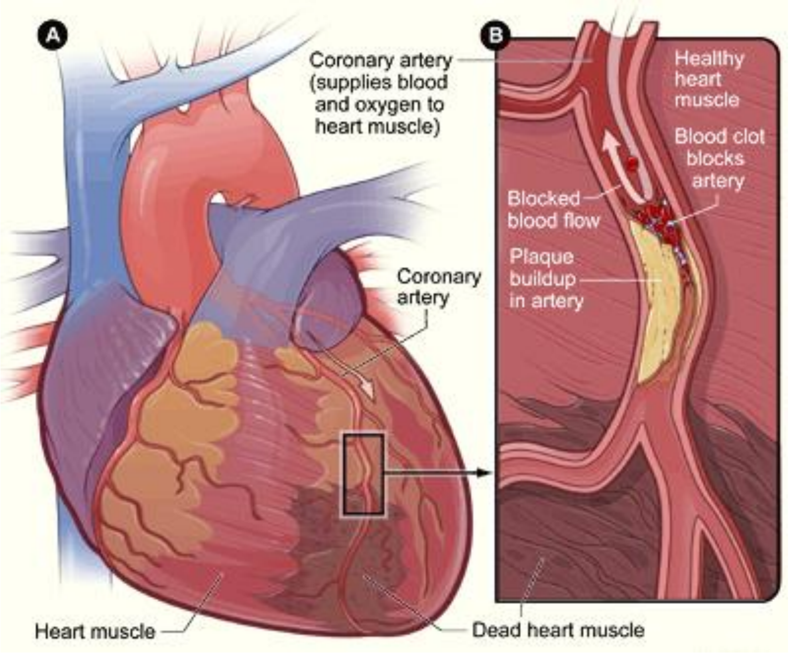
A
B
Coronary artery (supplies blood and oxygen to heart muscle)
Healthy heart muscle
Blood clot blocks artery
Blocked blood flow
Plaque buildup in artery
Coronary artery
Heart muscle
Dead heart muscle

Figure 6-1: (a) Anatomy of a heart and the coronary artery. (b) A cross-section image of the coronary artery with plaque buildup and a blood clot, which blocks the blood flow inside the heart.

Tomosynthesis is a low cost and low dose alternative for CT, it only acquires a small number of projection images to reconstruct 3D structures. Studies have shown chest tomosynthesis has a comparable sensitivity as CT in lung diseases screening, including lung nodule detection and other lung pathologies[92]. However, the current chest tomosynthesis system requires long scanning time and cannot be adapted for high resolution gated cardiac image that is necessary for accurate measurement of CACS. Stationary digital chest tomosynthesis, developed by our team using CNT X-ray source array[8], increases the scanning speed and allows high resolution gated imaging[11].

Table 6-1: Grading table for evaluating the extent of CAD based on the calcium score

Calcium Score (CT)	**Presence of CAD**
0	No evidence of CAD
1-10	Minimal evidence of CAD
11-100	Mild evidence of CAD
101-400	Moderate evidence of CAD
Over 400	Extensive evidence of CAD

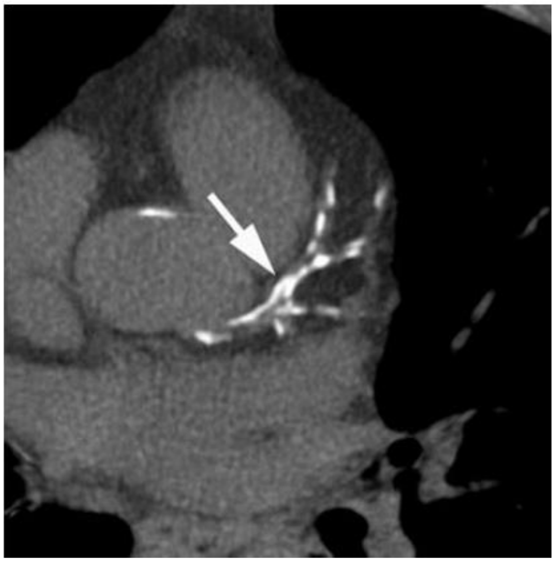

Figure 6-2: An image of the coronary calcification imaged by CTA.[162]

6.2 Methods

6.2.1 Heart Model

Mimic coronary calcifications were created using calcium hydroxyapatite with various volumes and densities from 0.3 g/ml to 0.5 g/ml. This calcium concentration is validated to be clinically realistic, which has an HU value ranges from 130 to 700. The CT images of the mimic coronary calcifications and their CT numbers are shown in Figure 6-3. Calcium mixture was injected into a porcine explant heart through the left anterior descending artery, and the right coronary artery, a picture of the explant porcine hearts is shown in Figure 6-4(b).

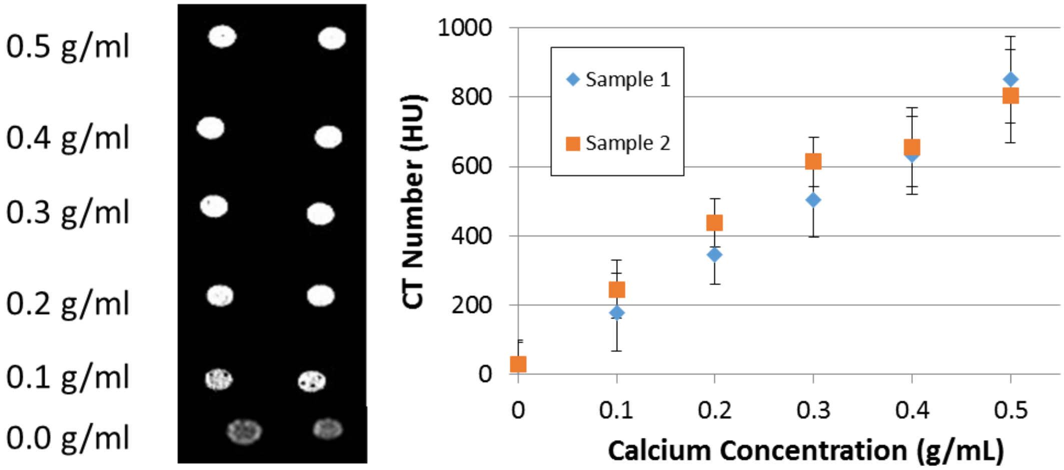

(a) (b)

Figure 6-3: (a) CT images, and (b) CT numbers of mimic coronary calcifications with different calcium concentrations.

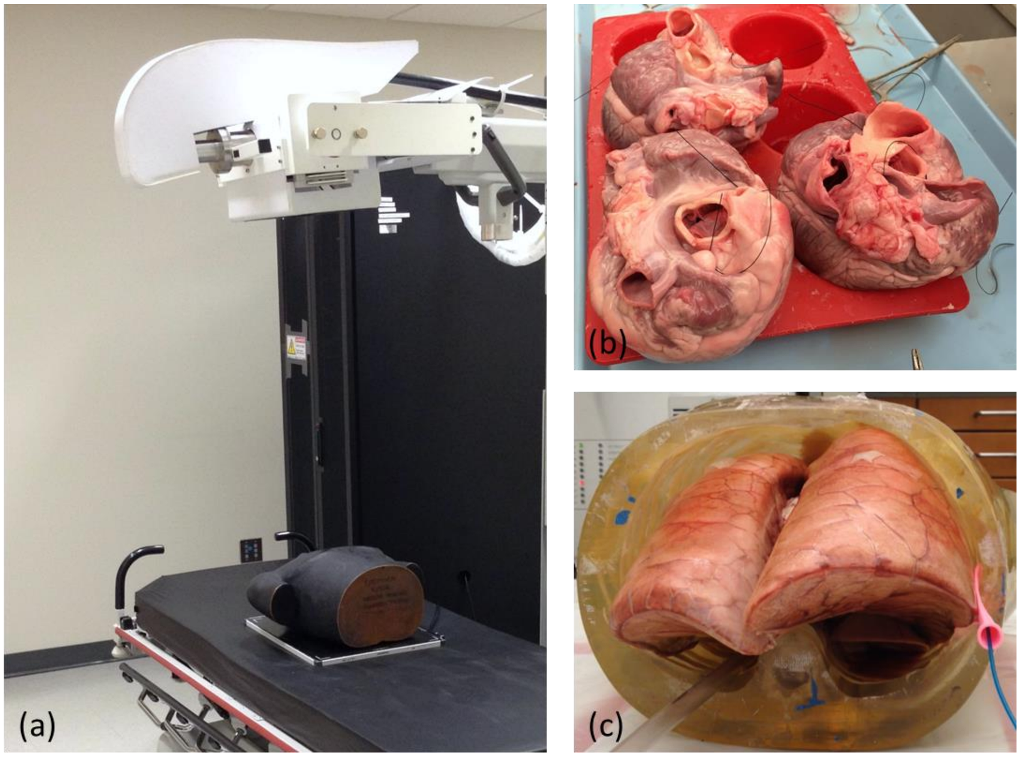

Figure 6-4: (a) Stationary digital chest tomosynthesis system developed by our team. (b) Explant heart model with injected calcium simulants. (c) The porcine heart inside an anthropomorphic chest phantom with inflated porcine lung. Unfortunately, the lung was damaged by the butcher and did not stay inflated during the scan.

6.2.2 Imaging System

The stationary digital chest tomosynthesis system uses a linearly distributed CNT source array containing 75 focal spots and a flat panel detector. The detector pixel number is 2560×3072, and the pixel size is 139 µm. In this study, we only use 31 focal spots with an angular coverage of 17 deg. A photo of the s-DCT system is shown in Fig 6-4(a).

The explant heart phantom was then imaged by both the s-DCT system and a commercial CT system (Siemens SOMATOM Definition, Siemens, Germany) all at 80 kVp. We also imaged the porcine heart inside an anthropomorphic chest phantom (Model RS-320, Radiology Support Devices, Long Beach, CA) with porcine lung, as shown in Figure 6-4(c). Same imaging setting was used for the s-DCT system; however, the CT images were acquired at 120 kVp, which is the default clinical imaging protocol for CT calcium scoring.

Tomosynthesis images were reconstructed using AFVR and SIRT with 20 iterations. For heart samples that were imaged alone, the reconstruction slice thickness is 0.5 mm; for heart samples that were imaged inside the chest phantom, the reconstruction slice thickness is 3 mm. The CT images were reconstruction using the integrated software from Siemens. The reconstruction slice thickness is 1 mm.

6.2.3 Calcium Scoring

Coronary artery calcium score is computed by multiplying the volume of the calcification with its density factor. Agatston score is a widely used metric for measuring the CAC. In Agatston score, the calcifications are separated into four different categories, and a density factor is assigned based on the category of the calcification.[165] The four calcification categories and the corresponding CT number are shown in Table 6-2.

Table 6-2: Calcification density factor in Agatston score

CT Number (HU)	**Density factor**
130 – 199	1
200 – 299	Minimal evidence of CAD
300 – 399	Mild evidence of CAD
Over 400	Extensive evidence of CAD

The CT-derived calcium score is computed using the commercial software integrated with the Siemens SOMATOM Definition CT system. Using the software, the reader (clinical cardiologist) first went through the whole stack of CT images and marked the regions she believed were calcifications, the integrated software then computed the CACS based on the input from the reader using different scoring metrics. In this study, we used Agatston score computed from the Siemens software.[165]

There is no existing standard for the tomosynthesis-derived calcium score. We proposed that the linear attenuation recorded in the tomosynthesis reconstruction images can be used for the density factor of CAC. The tomosynthesis-derived calcium score can then calculated by summing over the product of the linear attenuation and the volume of the calcifications:

$$CACS_{DTS} = \sum_{calcification\ areas} \mu_{cal} \Delta V \ , \tag{6-1}$$

where $CACS_{tomo}$ is the tomosynthesis-derived calcium score, μ_{cal} is the linear attenuation of the calcification in tomosynthesis reconstruction, and ΔV is the volume of the calcification with μ_{cal}. A procedure similar to CT calcium scoring was used: A trained cardiologist first examined all tomosynthesis reconstruction images, marked and segmented out the regions that contain calcifications. Based on the input of the reader, the tomosynthesis-derived CACS is computed using a MATLAB script.

6.3 Results

6.3.1 Explant Heart Model

Figure 6-5 shows the explant heart with mimic calcification imaged by both CT and s-DCT. Mimic calcifications were shown in the right coronary artery (RCA), left main artery (LM) and left anterior descending artery (LAD). Most calcifications that appear in CT images is also shown in the tomosynthesis images except one calcification in the LAD. However, the contrast of the calcification in tomosynthesis images is lower than that in CT images. Six hearts with a total of 12 CAC were imaged by both s-DCT and CT; all 12 CAC were clear in CT reconstruction while only 9 CAC were identified in tomosynthesis reconstruction. As shown in in Figure 6-6, there is a strong correlation between the two calcium scores derived from CT and tomosynthesis.

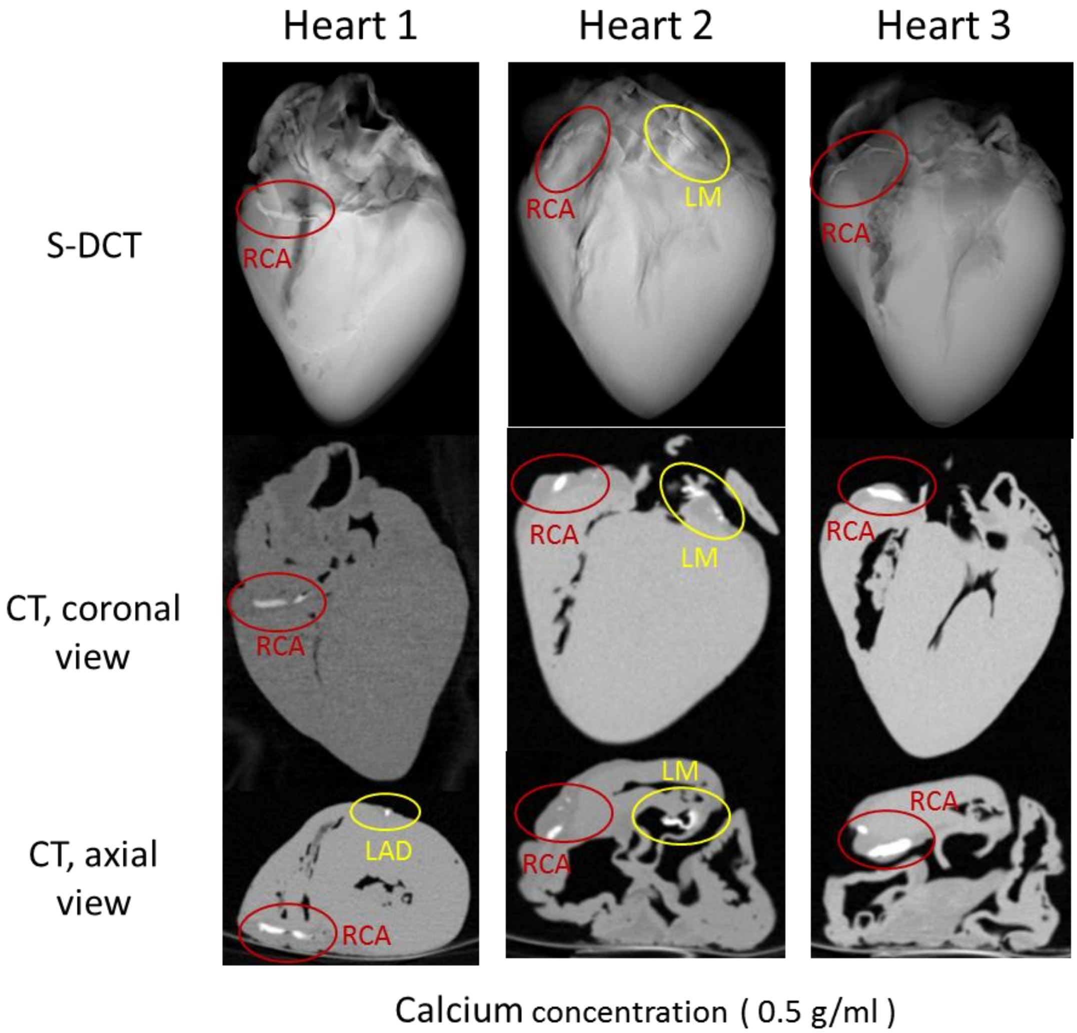
Heart 1
Heart 2
Heart 3
S-DCT
CT, coronal view
CT, axial view
RCA
LM
LAD
Calcium concentration (0.5 g/ml)

Figure 6-5: Mimic CAC in explant heart model imaged by both s-DCT and CT. Red and yellow circles mark the locations of the CAC.

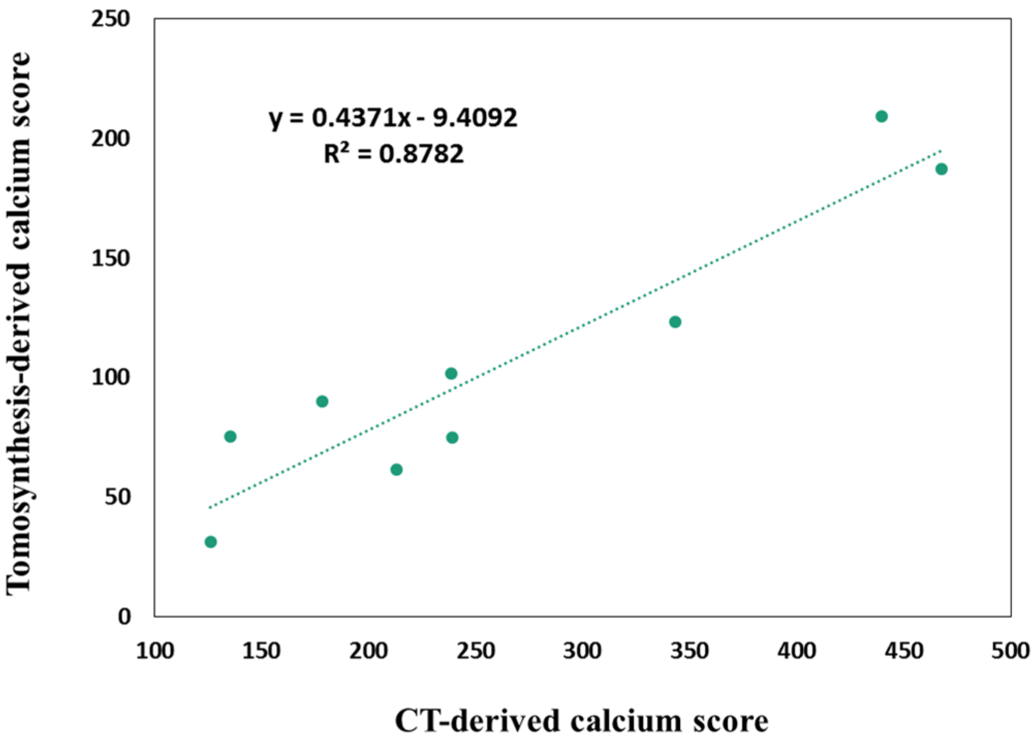

Figure 6-6: Calcium score derived from CT and tomosynthesis images.

6.3.2 Heart inside Chest Phantom

To evaluate this technique in a more realistic setting, we further imaged porcine heart injected with calcium simulants inside an anthropomorphic chest phantom with a porcine lung. The result showed that all CACs were visible in the CT reconstruction, while only five CACs in two hearts were confirmed by the cardiologists in the tomosynthesis images. Two “possible” CACs in one heart were observed. However the cardiologists could not confirm them due to the out-of-plane artifact coming from the lung airway. Due to the fact that the lung was not inflated successfully during this study, two small size hearts were completely wrapped by the lung and lied almost flat close the ribs. The tomosynthesis artifact severely affects the visibility of the CACs. As a result, no CACs were identified in those two hearts. Mimic CACs at the in-focus tomosynthesis reconstruction slices and corresponding CT reconstruction slices are shown in Figure 6-7.

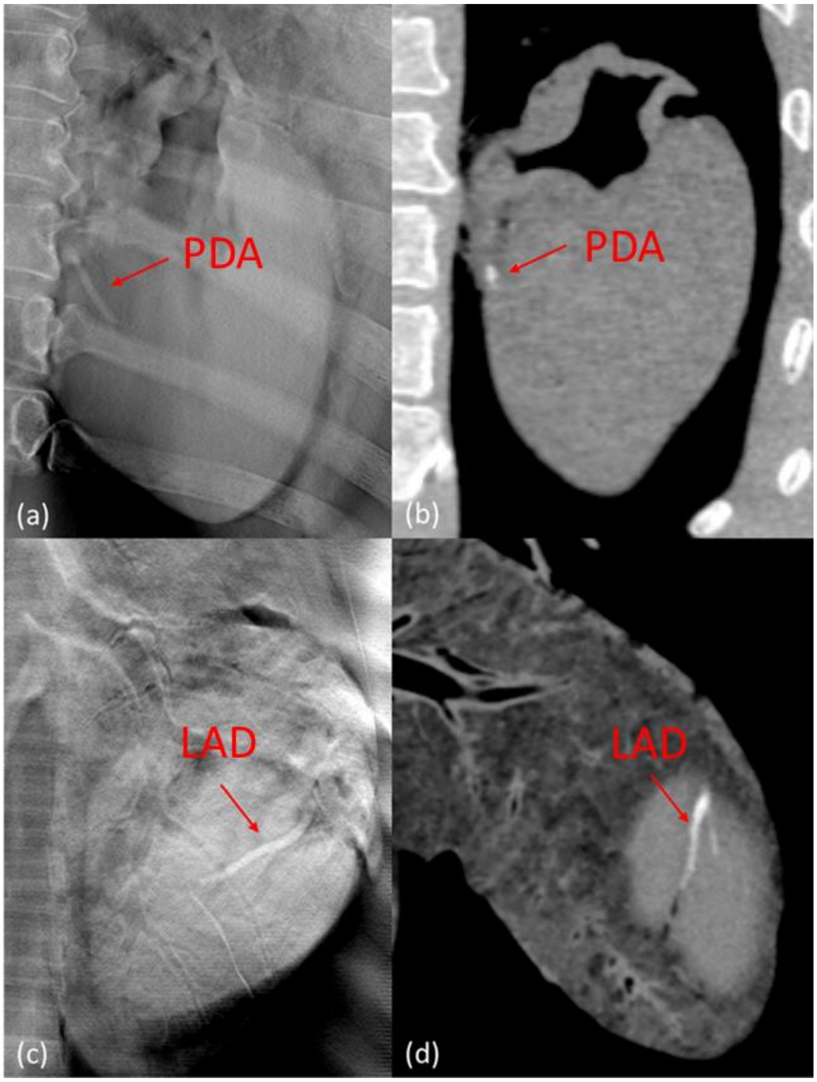

Figure 6-7: Reconstruction slices of heart samples with the anthropomorphic chest phantom. Mimic CACs are shown in (a), (c) tomosynthesis reconstruction slices, and (b), (d) CT reconstruction slices.

The measured CACS is shown in Table 6-3, the same data is plotted in Figure 6-8 and is fitted to a linear relationship. Despite the fact that there are only four data points, a strong correlation was observed between the CT-derived CACS and Tomosynthesis-derived CACS.

Table 6-3: Calcium scores of heart samples derived from CT and tomosynthesis

	Position	Tomosynthesis derived CACS	CT derived CACS
Heart 1	Left circumflex artery	1.076	69.6
	Left anterior descending artery	36.303	908.9
	Right coronary artery	9.864	133.3
Heart 2	Left anterior descending artery	47.103	1127.7
	Right coronary artery	7.765	996.8

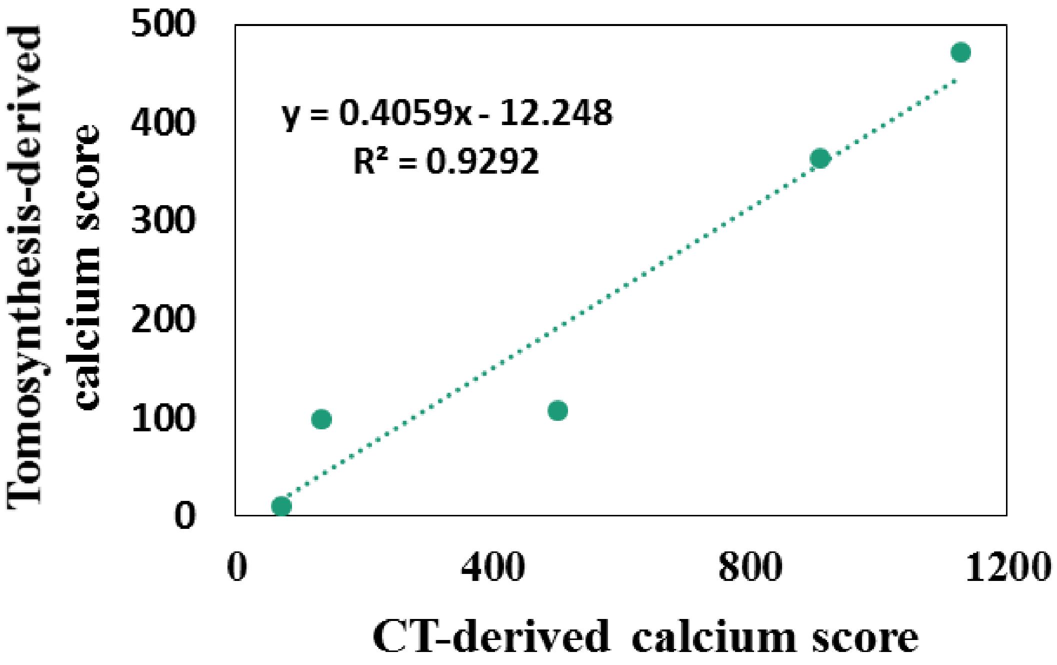

Figure 6-8: Calcium scores of the heart samples inside chest phantom derived from CT and tomosynthesis images.

6.4 Discussion and Conclusion

6.4.1 Discussion

Using the stationary digital chest tomosynthesis and porcine heart models with simulated calcifications, we investigated the correlation between tomosynthesis-derived coronary artery calcium score and the CT-derived calcium score. Strong correlations were observed between CACS for hearts imaged along as well as when they are placed inside an anthropomorphic chest phantom with a porcine lung.

A strong linear relationship between tomosynthesis-derived calcium score and CT-derived calcium score is observed in two imaging settings: the heart was imaged along, and the heart was imaged inside the chest phantom with the lung. This suggests that tomosynthesis derived calcium score could be used as a quantitative measure to evaluate coronary artery calcification. As shown in previous studies, coronary artery calcium score might change at different energy spectrum and with different reconstruction algorithm[166]. In digital tomosynthesis, the source geometry and scanning angle can also alter the calcium score. The purpose of this study is not to establish the standard of calcium scoring using digital tomosynthesis, but rather to demonstrate the potential of stationary digital tomosynthesis to perform calcium scoring. Thorough evaluation and careful calibration must be performed to establish a new norm of calcium scoring using digital tomosynthesis.

The main advantage of using s-DCT for coronary artery calcium scoring is the capability of physiologically gated imaging. Even with all projections acquired within one breath hold, motion blur is still the main factor that degrades the image quality for the current tomosynthesis with a mechanical moving x-ray source[167]. As demonstrated in the previous study, gated imaging using s-DCT can effectively reduce the heart motion blur by 85%, which leads to a higher spatial resolution and a more accurate reconstruction with reduced artifacts[11]. Since the size of CAC can be as small as several millimeters, gated imaging using s-DCT could significantly improve both the diagnostic and measurement accuracy of coronary artery calcium scoring.

One limitation of this study is the identification of CAC from two reconstructions. Since the heart is a deformable soft tissue, the shape and position of heart changed during each scan, making it hard for the cardiologist to identify the specific calcification on the tomosynthesis images relative to the CT images. Another limitation of the study is the porcine lung was not inflated successfully, causing significant tomosynthesis artifacts for small size heart.

Due to the tomosynthesis artifact, some calcifications that are apparent in CT are not visible in tomosynthesis images. For instance, the contrast of CAC significantly degrades when it is close to the spine, ribs or the lung airway. Improvement in the imaging system, such as using a larger scanning angle, could help to reduce the image artifact and improve the conspicuity of CAC[168]. On the other hand, the advances in the image reconstruction algorithm, such as the model-based iterative reconstruction algorithm, has also shown potentials to reduce the image artifact and to improve the overall image quality[16], [18]. As scatter is an important issue for the cone-beam imaging modalities, scatter correction could also help to improve both the reconstruction accuracy as well as the contrast of the CAC[120], [121], [145]. Other image processing methods, including contrast enhancement algorithms, could also be used to improve the local contrast of CAC in tomosynthesis reconstruction, thus helping the diagnosis of CAC[169].

While the CT images were acquired at 120 kVp, the s-DCT was obtained at 80 kVp due to the limitation of the current prototype s-DCT system. The softer energy spectrum would lead to less penetration and low contrast in the x-ray images. In addition, the small angular span of the current s-DCT limits the depth resolution of the tomosynthesis images. Both the source energy spectrum and small angular span of the prototype s-DCT are due to the non-optimal x-ray source array used (the source array was originally designed for a different application). With a dedicated and optimal designed x-ray source array for s-DCT, we expect the future generation of s-DCT will produce significantly better images, further improve the quantitative correlation between the CT derived and tomosynthesis-derived CACSs.

6.4.2 Conclusion

This study demonstrates that it is possible to obtained quantitative coronary artery calcium scores using stationary digital chest tomosynthesis systems. Further work is needed to optimize the s-DCT imaging geometry, upgrading the x-ray source array, and reducing the impact of scatter. With those improvements, it is expected that a gated s-DCT image may become a valuable tool for screening patients with high risk of coronary artery diseases.

CHAPTER 7: Summary and Future Direction

7.1 Summary

Tomosynthesis imaging faces several challenges due to its unique imaging geometry. In this study, we developed a set of image reconstruction and processing algorithms that address and improve three aspects of the stationary tomosynthesis imaging: reconstruction speed, reconstruction accuracy, and reconstruction image quality.

In terms of reconstruction speed, a fast iterative image reconstruction algorithm, namely adapted fan volume reconstruction, was developed for the stationary digital tomosynthesis systems with linear source array. AFVR increases the reconstruction speed compared to other iterative reconstruction algorithms with the cone beam projector, making iterative reconstruction practical for clinical use.

To improve reconstruction accuracy, efficient scatter correction algorithm together with the scatter sampling device was developed. Studies showed that this scatter correction technique can effectively remove scatter radiation from the projection data, resulting in more accurate attenuation values in the reconstruction images. In addition, as the scatter radiation is removed, both the contrast ratio and the signal difference-to-noise ratio were substantially increased on both projection and reconstruction images.

Several image processing algorithms were implemented that improves the reconstruction image quality. Iterative reconstruction was implemented for all CNT-based tomosynthesis systems, including s-DBT, s-DCT, and s-IOT systems. IR improves the image resolution as well as reducing the noise in the reconstruction images. The distance driven projector, as well as the data truncation artifact reduction, were implemented, which removes the horizontal line artifacts and reduces the truncation artifact. Synthetic mammography has also been investigated to further reduce the radiation dose in breast tomosynthesis imaging.

With the improvement in the reconstruction, we evaluate the feasibility of quantitative imaging using s-DTS. The Feasibility of assessing heart calcium score is investigated. An explant heart model with mimic calcifications was developed and imaged in two settings using both CT and s-DCT. The scoring metrics for tomosynthesis imaging was developed, and it was used to compute the tomosynthesis-derived calcium score. Results showed a strong correlation between tomosynthesis-derived calcium score and the CT-derived calcium score, suggesting that tomosynthesis would potentially be used as a low dose and low-cost alternative to CT in evaluating coronary artery calcification score.

7.2 Future Direction

This study marks the first step toward many applications of the quantitative imaging using the stationary digital tomosynthesis. There is still tremendous work that can be done to overcome the hardware limitation and to improve the diagnostic accuracy of this technology further.

The fast iterative reconstruction framework has been developed,[108] however the reconstruction algorithm is not yet optimized. Future implementation of parallel computing on GPU as well as multi-core CPU could further reduce the computation time for reconstruction. With a faster reconstruction speed, more sophisticated system modelings such as modeling the finite-sized focal spot in the reconstruction would be practical.

Currently, the AFVR uses SIRT for each fan volume reconstruction. Statistical iterative reconstruction algorithm, such as maximum-likelihood expectation-maximization,[15], [21] total variation minimization algorithms,[19], [20] and iterative coordinate descent algorithm,[17], [170] could be implemented to improve the image quality as well as reducing the radiation dose used in the s-DTS. Due to the non-isotropic voxel size of the tomosynthesis imaging, investigations on the optimized regularization used in the reconstruction will also improve the overall image quality.[171], [172]

Tomosynthesis is a limited-angle tomographic imaging technique, which is an ill-posed problem with insufficient data by nature. Therefore, reduced contrast, low depth resolution, and image artifacts are pronounced in tomosynthesis images. Implementation of artifact reduction techniques, including out-of-plane artifact reduction and metal artifact reduction would help doctors to better interpret and extract useful diagnostic information from the tomosynthesis images.[94], [173]–[175] Post image processing, such as image super-resolution,[176] synthetic mammography,[177]–[179] contrast enhancement algorithms,[180]–[183] and noise reduction techniques, would also help the disease diagnosis, especially for breast imaging.

One of the biggest advantages of CNT-based stationary digital tomosynthesis is the capability of physiologically gated imaging,[11], [117] where images are acquired precisely at a specific phase of the physiological cycle. Physiologically gated imaging not only can substantially reduce the motion artifact, but it also enables accurate dynamic imaging. For example, the lung motion at a different phase of respiration is of great interest for lung disease diagnosis. Investigation of the four-dimensional image reconstruction algorithms with sparse samplings would enable the dynamic imaging using s-DCT.

The second generation s-DBT system comes with the capability of dual energy imaging. Developing the specific image processing and reconstruction algorithms for the dual energy tomosynthesis imaging would improve the contrast of abnormal tissues, thus aiding disease diagnosis. Investigation of the material decomposition method for dual energy tomosynthesis would add more diagnostic value to the technology.

APPENDIX

This appendix serves as a user manual for the AFVR software that I developed at UNC. First, a brief overview of the reconstruction software is provided. After that, key modules which used in the reconstruction are described. Next, the instruction on how to run the reconstruction software is provided, and finally, common problems and solutions are discussed.

A.1 Overview of the Reconstruction Software

The current reconstruction software is written in MATLAB (version 2015a or later) with its parallel computing toolbox. Thus it requires the user to install MATLAB on the computer. The software will automatically detect the number of CPU cores on the computer and accelerates the reconstruction. Due to the large memory requirement, a 64-bit operating system is recommended. The reconstruction time varies from 8 mins to 20 mins, depends on the computing power and the size of the problem (projection number, detector pixel size, the number of reconstruction slices and etc.).

The current reconstruction does four things: 1. Processes the raw projection data, including cropping, re-grouping, and rotating the raw data. 2. Computes the system matrix for each fan volume, this is also called forward projection. 3. Based on the projection data and the system matrix, computes the fan volume image. 4. Combine all reconstructed fan volume images and resamples the 3D image.

Currently, the ART reconstruction takes the pre-processed projection images (after off-gain correction but before the logarithmic transformation) as the input and the statistical reconstruction, such as maximum likelihood expectation maximization algorithm, takes both the raw projection images and the blank images as the input.

A.2 Key Modules

Several subroutines are used in the AFVR script, including:

- **ddprojector.m** (**ddprojector1.m**):

  This is the subroutine that computes the system matrix **A** using the distance driven method describe by Bruno De Man. The imaging geometry must be provided when **ddprojector** is called.

- **fanbeam1.m:**

  This is the forward projection routine that computes the system matrix using the ray-driven model (intersection length is used as the weighting).

- **sart.m** (**sart1.m, sart2.m, sart3.m**)

  This is the back projection subroutine that takes the pre-computed system matrix and the projection data and computes the object image.

- **mlem.m**

  This is the back projection using the maximum likelihood expectation maximization algorithm. Both the blank projection images and the uncorrected raw projection data are needed as the input to the reconstruction.

- **sampb.m**

This module takes the combined fan volume images as the input, re-samples and outputs the 3D images with correct aspect ratio.

- **calczeta.m**

  This subroutine calculates the step size in each SIRT update.

A.3 How to Use the Reconstruction Software

Below are the steps to run the AFVR-SIRT reconstruction

- Step 1: Pre-processing raw projection data
- Step 2: Obtained the correct imaging geometry
- Step 3: Choose the right reconstruction parameter
  - Folder of the pre-processed projection images
  - Output image folder
  - Location of the imaging geometry
  - Reconstruction space height/reconstruction slice thickness
- Step 4: Run reconstruction

A.4 Common Problems and Solutions

A.4.1 Dimension Mismatch

It is typically caused by incorrect projection data or incorrect geometry calibration data. For example, if one set the number of projection images to be 29, but instead of 29 projection images, there are only 28 projection images in the input folder, then the reconstruction software would crash with an error code “dimension mismatch”. This error would also show up if the geometry calibration input does not contain the geometry of all projection images (i.e. one geometry calibration projection is missing)

A.4.2 Artifacts on the Image Boundary

Certain detectors have dead pixels around the edges; this would cause reconstruction artifacts. Objects that only appear in one or two projection could also introduce reconstruction artifacts. In those scenarios, it is suggested to crop the image for reconstruction. One can set ***cr***, ***cl***, ***ct***, and ***cb*** (crop right, left, top, and bottom pixels) to crop reconstruction image.

A.4.3 Low Contrast (Abnormal)

The reconstruction images will have a low contrast (lower than what it should be) when the preprocessing is not done correctly. The solution introduced here would help reduce the effect caused by incorrect preprocessing. However, it would not help if the contrast between the two materials is INDEED small.

The pre-processing is the step that transforms the raw measurement of the photon counts to the line integral image that used for FBP or ART reconstruction. It computes the ratio of the measured photon intensity and the blank (un-attenuated) photon intensity and performs a logarithmic transformation on the ratio. The value of the resulted line integral image, theoretically, ranges from 0 to 1, with 0 corresponds to all x-ray photon being absorbed, and 1 represents the situation when x-ray beam is not attenuated at all. Sometimes, the x-ray tube shoots a different flux than what we expected. In this case, the pre-processing would be wrong as the pre-recorded blank image does not represent the true blank image for this particular shot.

When the actual flux is lower than what we expected, the region where x-ray would not be attenuated, such as air, will have a photon count lower than that in the pre-measured blank image. As a result, in the reconstruction slice, those regions will have some attenuations and looks grayish, and all objects would appear to have a higher attenuation than their true values. On the other hand, if the actual flux is higher than what we expected, the object would appear to have a low attenuation and low contrast, as the attenuation integral after the preprocessing would be lower than what it should be.

One can adjust the ***ppf*** parameter in the reconstruction script to correct the pre-processing error. For example, when the actual x-ray flux is lower than expected, one can reduce the ***ppf*** value to compensate this effect. In contrast, if the actual flux is higher than expected, one should increase the ***ppf*** value so that the range of the line integral image is still between 0 and 1.

A.4.4 Unable to Write DICOM Header

The reconstruction software automatically writes reconstruction settings in output DICOM images. Those settings are stored in the private sections in the DICOM header, which are not defined in the default lookup table that MATLAB uses. To write customized DICOM header information, one needs to modify the MATLAB DICOM header lookup table first. A MATLAB script, called ***Modify_dicom_dict.m***, has been created for this purpose. The script will atomically revise the DICOM header table in MATLAB, enabling writing customized information in the DICOM images. Currently, the ***Modify_dicom_dict.m*** script only adds certain fields in the MATLAB look-up table, which matches the information that will be saved in the reconstruction. If in the future, it is desired to create and store other information in the DICOM header, one will need to update the ***Modify_dicom_dict.m*** script with the correct DICOM header field information and rerun the script before trying to store that information in the DICOM header.

REFERENCES

[1] American Cancer Society, “Cancer Facts & Figures 2016,” 2016.

[2] J. Shan, a W. Tucker, L. R. Gaalaas, G. Wu, E. Platin, A. Mol, J. Lu, and O. Zhou, “Stationary intraoral digital tomosynthesis using a carbon nanotube X-ray source array,” *Dentomaxillofacial Radiol.*, vol. 44, no. 9, p. 20150098, 2015.

[3] I. Sechopoulos, “A review of breast tomosynthesis. Part I. The image acquisition process.,” *Med. Phys.*, vol. 40, no. 1, p. 14301, Jan. 2013.

[4] I. Reiser and I. Sechopoulos, “A REVIEW OF DIGITAL BREAST TOMOSYNTHESIS,” *Radiographics*, vol. 2, no. 1, pp. 57–66, 2014.

[5] J. T. Dobbins III and D. J. Godfrey, “Digital x-ray tomosynthesis: current state of the art and clinical potential,” *Phys Med Biol*, vol. 48, no. 19, pp. R65--R106, 2003.

[6] T. Gomi and H. Hirano, “Clinical potential of digital linear tomosynthesis imaging of total joint arthroplasty,” *J. Digit. Imaging*, vol. 21, no. 3, pp. 312–322, 2008.

[7] K. Mermuys, F. De Geeter, K. Bacher, K. Van De Moortele, K. Coenegrachts, L. Steyaert, and J. W. Casselman, “Digital tomosynthesis in the detection of urolithiasis: Diagnostic performance and dosimetry compared with digital radiography with MDCT as the reference standard,” *Am. J. Roentgenol.*, vol. 195, no. 1, pp. 161–167, 2010.

[8] J. Shan, A. W. Tucker, Y. Z. Lee, M. D. Heath, X. Wang, D. H. Foos, J. Lu, and O. Zhou, “Stationary chest tomosynthesis using a carbon nanotube x-ray source array: a feasibility study.,” *Phys. Med. Biol.*, vol. 60, no. 1, pp. 81–100, Jan. 2015.

[9] X. Qian, R. Rajaram, X. Calderon-Colon, G. Yang, T. Phan, D. S. Lalush, J. Lu, and O. Zhou, “Design and characterization of a spatially distributed multibeam field emission x-ray source for stationary digital breast tomosynthesis,” *Med. Phys.*, vol. 36, no. 10, p. 4389, 2009.

[10] X. Qian, A. Tucker, E. Gidcumb, J. Shan, G. Yang, X. Calderon-Colon, S. Sultana, J. Lu, O. Zhou, D. Spronk, F. Sprenger, Y. Zhang, D. Kennedy, T. Farbizio, and Z. Jing, “High resolution stationary digital breast tomosynthesis using distributed carbon nanotube x-ray source array.,” *Med. Phys.*, vol. 39, no. 4, pp. 2090–9, May 2012.

[11] J. Shan, L. Burk, G. Wu, Y. Z. Lee, M. D. Heath, X. Wang, D. Foos, J. Lu, and O. Zhou, “Prospective gated chest tomosynthesis using CNT X-ray source array,” *Proc. SPIE*, vol. 9412, p. 941242, Mar. 2015.

[12] A. W. Tucker, Y. Z. Lee, C. M. Kuzmiak, J. Calliste, J. Lu, and O. Zhou, “Increased microcalcification visibility in lumpectomy specimens using a stationary digital breast tomosynthesis system,” *Proc. SPIE, Med. Imaging 2014 Phys. Med. Imaging*, vol. 9033, p. 903316, Mar. 2014.

[13] T. Wu, R. H. Moore, E. a. Rafferty, and D. B. Kopans, “A comparison of reconstruction algorithms for breast tomosynthesis,” *Med. Phys.*, vol. 31, no. 9, p. 2636, 2004.

[14] I. Sechopoulos, “A review of breast tomosynthesis. Part II. Image reconstruction, processing and analysis, and advanced applications.,” *Med. Phys.*, vol. 40, no. 1, p. 14302, Jan. 2013.

[15] Y. Zhang, H.-P. Chan, B. Sahiner, J. Wei, M. M. Goodsitt, L. M. Hadjiiski, J. Ge, and C. Zhou, “A comparative study of limited-angle cone-beam reconstruction methods for breast tomosynthesis,” *Med. Phys.*, vol. 33, no. 10, p. 3781, 2006.

[16] X. Pan, E. Y. Sidky, and M. Vannier, “Why do commercial CT scanners still employ traditional, filtered back-projection for image reconstruction?,” *Inverse Probl.*, vol. 25, no. 12, p. 1230009, Jan. 2009.

[17] Z. Yu, J. Thibault, C. Bouman, K. Sauer, and J. Hsieh, “Fast model-based X-ray CT reconstruction using spatially nonhomogeneous ICD optimization,” *IEEE Trans. Image Process.*, vol. 20, no. 1, pp. 161–175, 2011.

[18] J. Hsieh, B. Nett, Z. Yu, K. Sauer, J.-B. Thibault, and C. a. Bouman, “Recent Advances in CT Image Reconstruction,” *Curr. Radiol. Rep.*, vol. 1, no. 1, pp. 39–51, Jan. 2013.

[19] E. Y. Sidky and X. Pan, “Image reconstruction in circular cone-beam computed tomography by constrained, total-variation minimization.,” *Phys. Med. Biol.*, vol. 53, no. 17, pp. 4777–807, Sep. 2008.

[20] E. Y. Sidky, X. Pan, I. S. Reiser, R. M. Nishikawa, R. H. Moore, and D. B. Kopans, “Enhanced imaging of microcalcifications in digital breast tomosynthesis through improved image-reconstruction algorithms,” *Med. Phys.*, vol. 36, no. 11, p. 4920, 2009.

[21] T. Wu, J. Zhang, R. Moore, E. Rafferty, D. Kopans, W. Meleis, and D. Kaeli, “Digital tomosynthesis mammography using a parallel maximum likelihood reconstruction method,” in *Proceedings of SPIE*, 2004, vol. 5368, no. Cc, pp. 1–11.

[22] Y. Park, H. Cho, U. Je, H. Cho, C. Park, H. Lim, K. Kim, G. Kim, S. Park, T. Woo, and S. Choi, “Evaluation of the image quality in digital breast tomosynthesis (DBT) employed with a compressed-sensing (CS)-based reconstruction algorithm by using the mammographic accreditation phantom,” *Nucl. Instruments Methods Phys. Res. Sect. A Accel. Spectrometers, Detect. Assoc. Equip.*, vol. 804, pp. 72–78, Dec. 2015.

[23] B. Kevles, *Naked to the Bone: Medical Imaging in the Twentieth Century*. Rutgers University Press, 1997.

[24] B. Kevles, *Naked to the Bone: Medical Imaging in the Twentieth Century*. Rutgers University Press, 1997.

[25] J. a. Seibert and J. M. Boone, “X-ray imaging physics for nuclear medicine technologists. Part 2: X-ray interactions and image formation.,” *J. Nucl. Med. Technol.*, vol. 33, no. 1, pp.

3–18, 2005.

[26] J. T. Bushberg and J. M. Boone, *The Essential Physics of Medical Imaging*. Wolters Kluwer Health, 2011.

[27] H. Fanet, *Photon-based Medical Imagery*. Wiley, 2013.

[28] M. J. Yaffe and J. A. Rowlands, “X-ray detectors for digital radiography,” *Phys. Med. Biol.*, vol. 42, no. 1, p. 1, 1997.

[29] S. J. Otto, J. Fracheboud, C. W. N. Looman, M. J. M. Broeders, R. Boer, J. H. C. L. Hendriks, A. L. M. Verbeek, and H. J. De Koning, “Initiation of population-based mammography screening in Dutch municipalities and effect on breast-cancer mortality: A systematic review,” *Lancet*, vol. 361, no. 9367, pp. 1411–1417, 2003.

[30] K. Armstrong, E. Moye, S. Williams, J. a Berlin, and E. E. Reynolds, “Screening Mammography in Women 40 to 49 Years of Age: A Systematic Review for the American College of Physicians,” *Ann. Intern. Med.*, vol. 146, pp. 516–526, 2007.

[31] Blausen.com, “Medical gallery of Blausen Medical 2014,” *WikiJournal of Medicine 1 (2)*, 2014. [Online]. Available: en.wikiversity.org/wiki/WikiJournal_of_Medicine/Medical_gallery_of_Blausen_Medical_2014.

[32] T. M. Svahn, D. P. Chakraborty, D. Ikeda, S. Zackrisson, Y. Do, S. Mattsson, and I. Andersson, “Breast tomosynthesis and digital mammography: a comparison of diagnostic accuracy.,” *Br. J. Radiol.*, vol. 85, no. 1019, pp. e1074-82, Dec. 2012.

[33] L. W. Goldman, “Principles of CT and CT technology.,” *J. Nucl. Med. Technol.*, vol. 35, no. 3, pp. 115-28-30, 2007.

[34] J. C. Park, B. Song, J. S. Kim, S. H. Park, H. K. Kim, Z. Liu, T. S. Suh, and W. Y. Song, “Fast compressed sensing-based CBCT reconstruction using Barzilai-Borwein formulation for application to on-line IGRT.,” *Med. Phys.*, vol. 39, no. 3, pp. 1207–17, Mar. 2012.

[35] M. Katsura, I. Matsuda, M. Akahane, J. Sato, H. Akai, K. Yasaka, A. Kunimatsu, and K. Ohtomo, “Model-based iterative reconstruction technique for radiation dose reduction in chest CT: comparison with the adaptive statistical iterative reconstruction technique.,” *Eur. Radiol.*, vol. 22, no. 8, pp. 1613–23, Aug. 2012.

[36] S. L. Brady, B. S. Yee, and R. a Kaufman, “Characterization of adaptive statistical iterative reconstruction algorithm for dose reduction in CT: A pediatric oncology perspective.,” *Med. Phys.*, vol. 39, no. 9, pp. 5520–31, Sep. 2012.

[37] A. W. Tucker, J. Lu, and O. Zhou, “Dependency of image quality on system configuration parameters in a stationary digital breast tomosynthesis system.,” *Med. Phys.*, vol. 40, no. 3, p. 31917, Mar. 2013.

[38] E. Rafferty, J. Park, L. Philpotts, S. Poplack, J. Sumkin, and E. Halpern, “Assessing radiologist performance using combined digital mammography and breast tomosynthesis compared with digital mammography alone: results of a multicenter, multireader trail,” *Radiology*, vol. 266, no. 1, 2013.

[39] A. Tagliafico, G. Mariscotti, M. Durando, C. Stevanin, G. Tagliafico, L. Martino, B. Bignotti, M. Calabrese, and N. Houssami, “Characterisation of microcalcification clusters on 2D digital mammography (FFDM) and digital breast tomosynthesis (DBT): does DBT underestimate microcalcification clusters? Results of a multicentre study.,” *Eur. Radiol.*, Aug. 2014.

[40] J. T. Dobbins and H. P. McAdams, “Chest tomosynthesis: Technical principles and clinical update,” *Eur. J. Radiol.*, vol. 72, no. 2, pp. 244–251, 2009.

[41] J. T. Dobbins, H. P. McAdams, J.-W. Song, C. M. Li, D. J. Godfrey, D. M. DeLong, S.-H. Paik, and S. Martinez-Jimenez, “Digital tomosynthesis of the chest for lung nodule detection: Interim sensitivity results from an ongoing NIH-sponsored trial,” *Med. Phys.*, vol. 35, no. 6, p. 2554, 2008.

[42] S. G. Langer, B. D. Graner, B. a Schueler, K. a Fetterly, J. M. Kofler, J. N. Mandrekar, and B. J. Bartholmai, “Sensitivity of Thoracic Digital Tomosynthesis (DTS) for the Identification of Lung Nodules.,” *J. Digit. Imaging*, Sep. 2015.

[43] a Terzi, L. Bertolaccini, a Viti, L. Comello, D. Ghirardo, R. Priotto, and M. Grosso, “Lung cancer detection with digital chest tomosynthesis: Baseline results from the observational study SOS,” *J. Thorac. Oncol.*, vol. 8, no. 6, pp. 685–692, 2013.

[44] R. H. Fowler and L. Nordheim, “Electron Emission in Intense Electric Fields,” *Proc. R. Soc. London A Math. Phys. Eng. Sci.*, vol. 119, no. 781, pp. 173–181, 1928.

[45] Y. Cheng and O. Zhou, “Electron field emission from carbon nanotubes,” *Comptes Rendus Phys.*, vol. 4, no. 9, pp. 1021–1033, 2003.

[46] S. Iijima, “Helical microtubules of graphitic carbon,” *Nature*, vol. 354, no. 6348, pp. 56–58, Nov. 1991.

[47] M. Baxendale, “The physics and applications of carbon nanotubes,” *J. Mater. Sci. Electron.*, vol. 14, no. 10–12, pp. 657–659, 2003.

[48] G. Z. Yue, Q. Qiu, B. Gao, Y. Cheng, J. Zhang, H. Shimoda, S. Chang, J. P. Lu, and O. Zhou, “Generation of continuous and pulsed diagnostic imaging x-ray radiation using a carbon-nanotube-based field-emission cathode,” *Appl. Phys. Lett.*, vol. 81, no. 2, pp. 355–357, 2002.

[49] Y. Z. Lee, L. Burk, K.-H. Wang, G. Cao, J. Lu, and O. Zhou, “Carbon Nanotube based X-ray Sources: Applications in Pre-Clinical and Medical Imaging.,” *Nucl. Instrum. Methods Phys. Res. A.*, vol. 648, pp. S281–S283, 2011.

[50] G. Cao, L. M. Burk, Y. Z. Lee, X. Calderon-Colon, S. Sultana, J. Lu, and O. Zhou, "Prospective-gated cardiac micro-CT imaging of free-breathing mice using carbon nanotube field emission x-ray," *Med. Phys.*, vol. 37, no. 10, p. 5306, 2010.

[51] G. Cao, Y. Z. Lee, R. Peng, Z. Liu, R. Rajaram, X. Calderon-Colon, L. An, P. Wang, T. Phan, S. Sultana, D. S. Lalush, J. P. Lu, and O. Zhou, "A dynamic micro-CT scanner based on a carbon nanotube field emission x-ray source.," *Phys. Med. Biol.*, vol. 54, no. 8, pp. 2323–2340, 2009.

[52] L. Zhang, H. Yuan, L. M. Burk, C. R. Inscoe, M. J. Hadsell, P. Chtcheprov, Y. Z. Lee, J. Lu, S. Chang, and O. Zhou, "Image-guided microbeam irradiation to brain tumour bearing mice using a carbon nanotube x-ray source array," *Phys. Med. Biol.*, vol. 59, no. 5, pp. 1283–1303, 2014.

[53] M. Hadsell, J. Zhang, P. Laganis, F. Sprenger, J. Shan, L. Zhang, L. Burk, H. Yuan, S. Chang, J. Lu, and O. Zhou, "A first generation compact microbeam radiation therapy system based on carbon nanotube X-ray technology," *Appl. Phys. Lett.*, vol. 103, no. 18, 2013.

[54] B. Gonzales, D. Spronk, A. W. Tucker, M. Beckman, and O. Zhou, "Rectangular Fixed-Gantry CT Prototype: Combining CNT X-Ray Sources and Accelerated Compressed Sensing-Based Reconstruction," *IEEE Access*, vol. 2, pp. 971–981, 2014.

[55] J. Calliste, G. Wu, P. E. Laganis, D. Spronk, H. Jafari, K. Olson, B. Gao, Y. Z. Lee, O. Zhou, and J. Lu, "A new generation of stationary digital breast tomosynthesis system with wider angular span and faster scanning time," in *SPIE Medical Imaging*, 2016, p. 978304.

[56] D. S. Lalush, R. Rajaram, and O. Zhou, "Tomosynthesis Reconstruction from Multi-Beam X-Ray Sources," *3rd IEEE Int. Symp. Biomed. Imaging Macro to Nano, 2006.*, pp. 1180–1183, 2006.

[57] B. De Man and J. Fessler, "Statistical iterative reconstruction for x-ray computed tomography," *Biomath. Promis. Dir. Imaging, Ther. Planning, Inverse Probl.*, no. m, pp. 1–28, 2010.

[58] Y. Levakhina, *Three-Dimensional Digital Tomosynthesis: Iterative Reconstruction, Artifact Reduction and Alternative Acquisition Geometry*. 2014.

[59] R. M. Lewitt, "Multidimensional digital image representations using generalized Kaiser--Bessel window functions," *J. Opt. Soc. Am. A*, vol. 7, no. 10, pp. 1834–1846, Oct. 1990.

[60] T. M. Peters, "Algorithms for Fast Back- and Re-Projection in Computed Tomography," *IEEE Trans. Nucl. Sci.*, vol. 28, no. 4, pp. 3641–3647, Aug. 1981.

[61] ASTRA-Toolbox, "Analytical Reconstruction," 2015. [Online]. Available: https://www.youtube.com/playlist?list=PLmecqweSELQPgUUG5eIvghR_tzUnK6lD8.

[62] J. A. Fessler, S. Member, and B. P. Sutton, "Nonuniform Fast Fourier Transforms Using Min-Max Interpolation," *IEEE Trans. Signal Process.*, vol. 51, no. 2, pp. 560–574, 2003.

[63] a. Averbuch, R. R. Coifman, D. L. Donoho, M. Elad, and M. Israeli, “Fast and accurate Polar Fourier transform,” *Appl. Comput. Harmon. Anal.*, vol. 21, no. 2, pp. 145–167, Sep. 2006.

[64] A. Averbuch, R. R. Coifman, D. L. Donoho, M. Israeli, and Y. Shkolnisky, “A Framework for Discrete Integral Transformations I—The Pseudopolar Fourier Transform,” *SIAM J. Sci. Comput.*, vol. 30, no. 2, pp. 764–784, 2008.

[65] B. P. Fahimian, Y. Zhao, Z. Huang, R. Fung, Y. Mao, C. Zhu, M. Khatonabadi, J. J. DeMarco, S. J. Osher, M. F. McNitt-Gray, and J. Miao, “Radiation dose reduction in medical x-ray CT via Fourier-based iterative reconstruction.,” *Med. Phys.*, vol. 40, no. 3, p. 31914, Mar. 2013.

[66] B. Kári, K. Karlinger, and D. Légrády, “Reconstruction,” 2011. [Online]. Available: http://oftankonyv.reak.bme.hu/tiki-index.php?page=Rekonstrukció.

[67] R. Gordon, R. Bender, and G. T. Herman, “Algebraic Reconstruction Techniques (ART) for three-dimensional electron microscopy and X-ray photography,” *J. Theor. Biol.*, vol. 29, no. 3, pp. 471–481, 1970.

[68] G. N. Hounsfield, “Computerized transverse axial scanning (tomography): I. Description of system,” *Br. J. Radiol.*, vol. 46, no. 552, pp. 1016–1022, 1973.

[69] A. Andersen and A. Kak, “Simultaneous algebraic reconstruction technique (SART): a superior implementation of the ART algorithm,” *Ultrason. Imaging*, no. 6, pp. 81–94, 1984.

[70] A. Kak and M. Slaney, *Principles of Computerized Tomographic Imaging*. Society for Industrial and Applied Mathematics, 2001.

[71] F. Natterer, *The Mathematics of Computerized Tomography*. Society for Industrial and Applied Mathematics, 2001.

[72] P. C. Hansen and M. Saxild-Hansen, “AIR Tools — A MATLAB package of algebraic iterative reconstruction methods,” *J. Comput. Appl. Math.*, vol. 236, no. 8, pp. 2167–2178, Feb. 2012.

[73] P. P. B. Eggermont, G. T. Herman, and a. Lent, “Iterative algorithms for large partitioned linear systems, with applications to image reconstruction,” *Linear Algebra Appl.*, vol. 40, pp. 37–67, 1981.

[74] I. B. Kabiena, E. Tonye, and P. E. Ntsama, “Algebraic Tomographic Reconstruction by Selective Discrimination (ART -DS),” vol. 3, no. 4, pp. 106–112, 2013.

[75] T. Strohmer and R. Vershynin, “A Randomized Kaczmarz Algorithm with Exponential Convergence,” *J. Fourier Anal. Appl.*, vol. 15, no. 2, p. 262, 2008.

[76] Å. Björck and T. Elfving, “Accelerated projection methods for computing pseudoinverse solutions of systems of linear equations,” *BIT Numer. Math.*, pp. 317–326, 1979.

[77] H. Guan and R. Gordon, "Computed tomography using algebraic reconstruction techniques (ARTs) with different projection access schemes: a comparison study under practical situations.," *Phys. Med. Biol.*, vol. 41, no. 9, pp. 1727–1743, Sep. 1996.

[78] H. Guan, R. Gordon, and Y. Zhu, "Combining various projection access schemes with the algebraic reconstruction technique for low-contrast detection in computed tomography," *Phys. Med. Biol.*, vol. 43, no. 8, p. 2413, 1998.

[79] G. Wu, J. Mainprize, and M. Yaffe, "Characterization of Projection Ordering in Iterative Reconstruction Methods for Breast Tomosynthesis," in *Digital Mammography: 9th International Workshop, IWDM 2008 Tucson, AZ, USA, July 20-23, 2008 Proceedings*, E. A. Krupinski, Ed. Berlin, Heidelberg: Springer Berlin Heidelberg, 2008, pp. 601–605.

[80] T. Kohler, "A projection access scheme for iterative reconstruction based on the golden section," in *IEEE Symposium Conference Record Nuclear Science 2004.*, 2004, vol. 6, p. 3961–3965 Vol. 6.

[81] K. Mueller, R. Yagel, and J. F. Cornhill, "The weighted-distance scheme: a globally optimizing projection ordering method for ART," *IEEE Trans. Med. Imaging*, vol. 16, no. 2, pp. 223–230, Apr. 1997.

[82] K. Mueller, R. Yagel, and J. Wheller, "Fast and accurate projection algorithm for 3D cone-beam reconstruction with the Algebraic Reconstruction Technique (ART)," *Med. …*, 1998.

[83] G. Yang, "Numerical Approaches for Solving the Combined Reconstruction and Registration of Digital Breast Tomosynthesis," 2012.

[84] S. Srivastava, "Accelerated Statistical Image Reconstruction Algorithms and Simplified Cost Functions for X-Ray Computed Tomography," 2008.

[85] J.-B. Thibault, K. D. Sauer, C. A. Bouman, and J. Hsieh, "A three-dimensional statistical approach to improved image quality for multislice helical CT.," *Med. Phys.*, vol. 34, no. 11, pp. 4526–4544, Nov. 2007.

[86] D. R. Hunter and K. Lange, "A Tutorial on MM Algorithms," *Am. Stat.*, vol. 58, no. 1, pp. 30–37, 2004.

[87] S. Ahn, J. A. Fessler, D. Blatt, and A. O. Hero, "Convergent incremental optimization transfer algorithms: application to tomography," *IEEE Trans. Med. Imaging*, vol. 25, no. 3, pp. 283–296, Mar. 2006.

[88] D. Blatt, A. O. Hero, and H. Gauchman, "A Convergent Incremental Gradient Method with a Constant Step Size," *SIAM J. Optim.*, vol. 18, pp. 29–51, 2007.

[89] K. Sauer and C. Bouman, "A local update strategy for iterative reconstruction from projections," *IEEE Trans. Signal Process.*, vol. 41, no. 2, pp. 534–548, 1993.

[90] A. Sabne, X. Wang, S. J. Kisner, C. A. Bouman, A. Raghunathan, and S. P. Midkiff,

“Model-based Iterative CT Image Reconstruction on GPUs,” in *Proceedings of the 22Nd ACM SIGPLAN Symposium on Principles and Practice of Parallel Programming*, 2017, pp. 207–220.

[91] G. A. Kicska and P. Gautham, “Digital Tomosynthesis of the Chest : Current and Emerging,” pp. 359–373, 2014.

[92] J. Vikgren, S. Zachrisson, A. Svalkvist, A. A. Johnsson, M. Boijsen, A. Flinck, S. Kheddache, and M. Båth, “Comparison of chest tomosynthesis and chest radiography for detection of pulmonary nodules: human observer study of clinical cases.,” *Radiology*, vol. 249, no. 3, pp. 1034–1041, 2008.

[93] E. Quaia, E. Baratella, S. Cernic, A. Lorusso, F. Casagrande, V. Cioffi, and M. A. Cova, “Analysis of the impact of digital tomosynthesis on the radiological investigation of patients with suspected pulmonary lesions on chest radiography,” *Eur. Radiol.*, vol. 22, no. 9, pp. 1912–1922, 2012.

[94] Y. Lin and E. Samei, “A fast poly-energetic iterative FBP algorithm.,” *Phys. Med. Biol.*, vol. 59, pp. 1655–78, 2014.

[95] K. Zeng, B. De Man, J.-B. Thibault, C. Bouman, and K. Sauer, “Spatial resolution enhancement in CT iterative reconstruction,” *2009 IEEE Nucl. Sci. Symp. Conf. Rec.*, pp. 3748–3751, Oct. 2009.

[96] J. Tang, B. E. Nett, and G.-H. Chen, “Performance comparison between total variation (TV)-based compressed sensing and statistical iterative reconstruction algorithms.,” *Phys. Med. Biol.*, vol. 54, no. 19, pp. 5781–804, Oct. 2009.

[97] K. Egiazarian, a. Foi, and V. Katkovnik, “Compressed Sensing Image Reconstruction Via Recursive Spatially Adaptive Filtering,” *2007 IEEE Int. Conf. Image Process.*, vol. 1, p. I-549-I-552, 2007.

[98] S. Xu, J. Lu, O. Zhou, and Y. Chen, “Statistical iterative reconstruction to improve image quality for digital breast tomosynthesis,” *Med. Phys.*, vol. 42, no. 9, pp. 5377–5390, 2015.

[99] W. Zhou, J. Lu, O. Zhou, and Y. Chen, “Ray-tracing-based reconstruction algorithms for digital breast tomosynthesis,” *J. Electron. Imaging*, vol. 24, no. 2, pp. 023–028, 2015.

[100] W. Zhou, J. Lu, O. Zhou, and Y. Chen, “Evaluation of Back Projection Methods for Breast Tomosynthesis Image Reconstruction,” *J. Digit. Imaging*, vol. 28, no. 3, pp. 338–345, 2014.

[101] R. Liu, Y. Luo, and H. Yu, “GPU-based acceleration for interior tomography,” *IEEE Access*, vol. 2, pp. 757–770, 2014.

[102] D. Matenine, Y. Goussard, and P. Després, “GPU-accelerated regularized iterative reconstruction for few-view cone beam CT.,” *Med. Phys.*, vol. 42, no. 4, pp. 1505–17, Apr. 2015.

[103] A. Sabne, X. Wang, S. Kisner, C. Bouman, A. Raghunathan, and S. Midkiff, “Model-based Iterative CT Image Reconstruction on GPUs,” pp. 207–220.

[104] X. Jia, H. Yan, L. Cervino, M. Folkerts, and S. B. Jiang, “A GPU tool for efficient, accurate, and realistic simulation of cone beam CT projections.,” *Med. Phys.*, vol. 39, no. 2012, pp. 7368–78, 2012.

[105] C. R. Inscoe, G. Wu, D. E. Soulioti, E. Platin, A. Mol, L. R. Gaalaas, M. R. Anderson, A. W. Tucker, S. Boyce, J. Shan, and others, “Stationary intraoral tomosynthesis for dental imaging,” in *SPIE Medical Imaging*, 2017, p. 1013203.

[106] P. Bleuet, R. Guillemaud, L. Desbat, and I. Magnin, “An adapted fan volume sampling scheme for 3-D algebraic reconstruction in linear tomosynthesis,” *IEEE Trans. Nucl. Sci.*, vol. 49, no. 5, pp. 2366–2372, Oct. 2002.

[107] J. Calliste, A. W. Tucker, E. Gidcumb, C. M. Kuzmiak, J. Lu, O. Zhou, and Y. Z. Lee, “Initial clinical evaluation of stationary digital breast tomosynthesis,” vol. 9412, p. 941228, Mar. 2015.

[108] G. Wu, C. Inscoe, J. Calliste, Y. Z. Lee, O. Zhou, J. Lu, N. Carolina, and C. Hill, “Adapted fan-beam volume reconstruction for stationary digital breast tomosynthesis,” *Proc. SPIE*, vol. 9412, pp. 1–10, Mar. 2015.

[109] B. De Man and S. Basu, “Distance-driven projection and backprojection in three dimensions,” *Phys. Med. Biol.*, vol. 49, no. 11, pp. 2463–2475, Jun. 2004.

[110] S. C. B. Lo, “Strip and line path integrals with a square pixel matrix: a unified theory for computational CT projections,” *IEEE Trans. Med. Imaging*, vol. 7, no. 4, pp. 355–363, Dec. 1988.

[111] G. Wang, M. W. Vannier, and P.-C. Cheng, “Iterative X-ray Cone-Beam Tomography for Metal Artifact Reduction and Local Region Reconstruction,” *Microsc. Microanal.*, vol. 5, no. 1, pp. 58–65, 1999.

[112] G. L. Zeng and G. T. Gullberg, “Unmatched projector/backprojector pairs in an iterative reconstruction algorithm,” *IEEE Trans. Med. Imaging*, vol. 19, no. 5, pp. 548–555, 2000.

[113] M. H. Byonocore, W. R. Brody, and A. Macovski, “A Natural Pixel Decomposition for Two-Dimensional Image Reconstruction,” *IEEE Trans. Biomed. Eng.*, vol. BME-28, no. 2, pp. 69–78, Feb. 1981.

[114] F. Xu and K. Mueller, “A comparative study of popular interpolation and integration methods for use in computed tomography,” in *3rd IEEE International Symposium on Biomedical Imaging: Nano to Macro, 2006.*, 2006, pp. 1252–1255.

[115] B. De Man and S. Basu, “Distance-driven projection and backprojection,” *2002 IEEE Nucl. Sci. Symp. Conf. Rec.*, vol. 3, pp. 1477–1480, 2003.

[116] S. Basu and B. De Man, “Branchless distance driven projection and backprojection,” vol. 6065, p. 60650Y–60650Y–8, Feb. 2006.

[117] A. E. Hartman, J. Shan, G. Wu, Y. Z. Lee, O. Zhou, J. Lu, M. Heath, X. Wang, and D. Foos, “Initial clinical evaluation of stationary digital chest tomosynthesis,” in *SPIE Medical Imaging*, 2016, p. 978366.

[118] C. R. Inscoe, G. Wu, D. E. Soulioti, E. Platin, A. Mol, L. R. Gaalaas, M. R. Anderson, A. W. Tucker, S. Boyce, J. Shan, B. Gonzales, J. Lu, and O. Zhou, “Stationary intraoral tomosynthesis for dental imaging,” in *SPIE Medical Imaging*, 2017, vol. 10132, p. 1013203.

[119] Y. Zhang, H. Chan, B. Sahiner, and J. Wei, “Artifact reduction methods for truncated projections in iterative breast tomosynthesis reconstruction,” *J. Comput. …*, vol. 33, no. 3, pp. 426–435, 2009.

[120] E.-P. Rührnschopf and K. Klingenbeck, “A general framework and review of scatter correction methods in x-ray cone-beam computerized tomography. Part 1: Scatter compensation approaches,” *Med. Phys.*, vol. 38, no. 7, p. 4296, 2011.

[121] E.-P. Ruhrnschopf And and K. Klingenbeck, “A general framework and review of scatter correction methods in cone beam CT. Part 2: scatter estimation approaches.,” *Med. Phys.*, vol. 38, no. 9, pp. 5186–99, Sep. 2011.

[122] H. Aichinger, J. Dierker, S. Joite-Barfuß, and M. Säbel, *Radiation exposure and image quality in X-ray diagnostic radiology: physical principles and clinical applications*. Berlin: Springer, 2012.

[123] H. Aichinger, J. Dierker, S. Joite-Barfus, and M. Säbel, *Physical principles and clinical applications: Radiation exposure and Image quality in X-ray diagnostic radiology*. Berlin, Heidelberg: Springer Berlin Heidelberg, 2012.

[124] T. Patel, H. Peppard, and M. B. Williams, “Effects on image quality of a 2D antiscatter grid in x-ray digital breast tomosynthesis: Initial experience using the dual modality (x-ray and molecular) breast tomosynthesis scanner,” *Med. Phys.*, vol. 43, no. 4, pp. 1720–1735, 2016.

[125] W. Zbijewski and F. J. Beekman, “Efficient Monte Carlo based scatter artifact reduction in cone-beam micro-CT,” *IEEE Trans. Med. Imaging*, vol. 25, no. 7, pp. 817–827, 2006.

[126] H. P. Chan and K. Doi, “The validity of Monte Carlo simulation in studies of scattered radiation in diagnostic radiology,” *Phys. Med. Biol.*, vol. 28, no. 2, p. 109, 1983.

[127] a P. Colijn and F. J. Beekman, “Accelerated simulation of cone beam X-ray scatter projections.,” *IEEE Trans. Med. Imaging*, vol. 23, no. 5, pp. 584–90, May 2004.

[128] A. Miceli, R. Thierry, A. Flisch, U. Sennhauser, F. Casali, and M. Simon, “Monte Carlo simulations of a high-resolution X-ray CT system for industrial applications,” *Nucl. Instruments Methods Phys. Res. Sect. A Accel. Spectrometers, Detect. Assoc. Equip.*, vol. 583, no. 2–3, pp. 313–323, 2007.

[129] Y. Kyriakou, T. Riedel, and W. A. Kalender, "Combining deterministic and Monte Carlo calculations for fast estimation of scatter intensities in CT," *Phys. Med. Biol.*, vol. 51, no. 18, pp. 4567–4586, 2006.

[130] A. Badal and A. Badano, "Accelerating Monte Carlo simulations of photon transport in a voxelized geometry using a massively parallel graphics processing unit," *Med. Phys.*, vol. 36, no. 11, p. 4878, 2009.

[131] K. Kim, T. Lee, Y. Seong, J. Lee, K. E. Jang, J. Choi, Y. W. Choi, H. H. Kim, H. J. Shin, J. H. Cha, S. Cho, and J. C. Ye, "Fully iterative scatter corrected digital breast tomosynthesis using GPU-based fast Monte Carlo simulation and composition ratio update.," *Med. Phys.*, vol. 42, no. 9, pp. 5342–5355, 2015.

[132] R. Ning, X. Tang, and D. Conover, "X-ray scatter correction algorithm for cone beam CT imaging," *Med. Phys.*, vol. 31, no. 5, p. 1195, 2004.

[133] K. P. Maher and J. F. Malone, "Computerized scatter correction in diagnostic radiology," *Contemp. Phys.*, vol. 38, no. 2, pp. 131–148, Mar. 1997.

[134] K. Yang, G. Burkett, and J. M. Boone, "A breast-specific, negligible-dose scatter correction technique for dedicated cone-beam breast CT: a physics-based approach to improve Hounsfield Unit accuracy.," *Phys. Med. Biol.*, vol. 59, no. 21, pp. 6487–505, Nov. 2014.

[135] I. Sechopoulos, "X-ray scatter correction method for dedicated breast computed tomography.," *Med. Phys.*, vol. 39, no. 5, pp. 2896–903, May 2012.

[136] L. Zhu and L. Xing, "Measurement-based scatter correction for cone-beam CT in radiation therapy," *SPIE Med. Imaging*, vol. 7258, p. 72583C–72583C–8, Feb. 2009.

[137] T. Niu and L. Zhu, "Scatter correction for full-fan volumetric CT using a stationary beam blocker in a single full scan.," *Med. Phys.*, vol. 38, no. 11, pp. 6027–38, Nov. 2011.

[138] a. Peterzol, J. M. Létang, and D. Babot, "A beam stop based correction procedure for high spatial frequency scatter in industrial cone-beam X-ray CT," *Nucl. Instruments Methods Phys. Res. Sect. B Beam Interact. with Mater. Atoms*, vol. 266, no. 18, pp. 4042–4054, Sep. 2008.

[139] J. S. Maltz, B. Gangadharan, M. Vidal, A. Paidi, S. Bose, B. a. Faddegon, M. Aubin, O. Morin, J. Pouliot, Z. Zheng, M. M. Svatos, and A. R. Bani-Hashemi, "Focused beam-stop array for the measurement of scatter in megavoltage portal and cone beam CT imaging," *Med. Phys.*, vol. 35, no. 6, p. 2452, 2008.

[140] H. Yan, X. Mou, S. Tang, Q. Xu, and M. Zankl, "Projection correlation based view interpolation for cone beam CT: primary fluence restoration in scatter measurement with a moving beam stop array.," *Phys. Med. Biol.*, vol. 55, no. 21, pp. 6353–75, 2010.

[141] K. Schörner, M. Goldammer, and J. Stephan, "Comparison between beam-stop and beam-hole array scatter correction techniques for industrial X-ray cone-beam CT," *Nucl.*

Instruments Methods Phys. Res. Sect. B Beam Interact. with Mater. Atoms, vol. 269, no. 3, pp. 292–299, Feb. 2011.

[142] L. Zhu, N. R. Bennett, and R. Fahrig, “Scatter Correction Method for X-Ray CT Using Primary Modulation: Theory and Preliminary Results,” *IEEE Trans. Med. Imaging*, vol. 25, no. 12, pp. 1573–1587, Dec. 2006.

[143] L. Ritschl, R. Fahrig, M. Knaup, J. Maier, and M. Kachelrieß, “Robust primary modulation-based scatter estimation for cone-beam CT.,” *Med. Phys.*, vol. 42, no. 1, pp. 469–78, Jan. 2015.

[144] C. R. Inscoe, A. W. Tucker, O. Z. Zhou, and J. Lu, “Demonstration of a scatter correction technique in digital breast tomosynthesis,” in *SPIE Medical ImagingMedical Imaging 2013: Physics of Medical Imaging*, 2013, vol. 8668, p. 86680H.

[145] C. R. Inscoe, G. Wu, J. Shan, Y. Z. Lee, O. Zhou, and J. Lu, “Low dose scatter correction for digital chest tomosynthesis,” *Proc. SPIE*, vol. 9412, pp. 1–8, Mar. 2015.

[146] Y. Kim, H. Kim, H. Park, J. Choi, and Y. Choi, “An experimental study of practical computerized scatter correction methods for prototype digital breast tomosynthesis,” vol. 9033, p. 903314, Apr. 2014.

[147] R. Ning, X. Tang, and D. Conover, “X-ray scatter correction algorithm for cone beam CT imaging,” *Med. Phys.*, vol. 31, no. 5, p. 1195, 2004.

[148] K. Yang, G. Burkett, Jr., and J. M. Boone, “An object-specific and dose-sparing scatter correction approach for a dedicated cone-beam breast CT system using a parallel-hole collimator,” vol. 8313, p. 831303, Feb. 2012.

[149] S. S. Jia Feng and I. Sechopoulos, “A software-based x-ray scatter correction method for breast tomosynthesis.,” *Med. Phys.*, vol. 38, no. 12, pp. 6643–53, Dec. 2011.

[150] L. Zhu, J. Wang, and L. Xing, “Noise suppression in scatter correction for cone-beam CT,” *Med. Phys.*, vol. 36, no. 3, p. 741, 2009.

[151] J. Star-Lack, M. Sun, A. Kaestner, R. Hassanein, G. Virshup, T. Berkus, and M. Oelhafen, “Efficient scatter correction using asymmetric kernels,” *Proc. SPIE*, vol. 7258, no. 12, pp. 72581–12, 2009.

[152] N. Otsu, “A Threshold Selection Method from Gray-Level Histograms,” *IEEE Trans. Syst., Man, Cybern.*, vol. SMC-9, no. 1, pp. 62–66, 1979.

[153] D. Sandwell, “Biharmonic spline interpolation of GEOS-3 and SEASAT altimeter data,” *Geophys. Res. Lett.*, vol. 14, no. 2, pp. 139–142, 1987.

[154] E. Samei, J. Lo, T. Yoshizumi, J. Jesneck, J. Dobbins, C. Floyd, H. P. McAdams, and C. Ravin, “Comparative Scatter and Dose Performance of Slot-Scan and Full-Field Digital Chest Radiography Systems,” *Radiology*, vol. 235, pp. 940–949, 2005.

[155] I. Sechopoulos, S. Suryanarayanan, S. Vedantham, C. J. D'Orsi, and A. Karellas, "Scatter radiation in digital tomosynthesis of the breast," *Med. Phys.*, vol. 34, no. 2, p. 564, 2007.

[156] H. Fujita, D.-Y. Tsai, T. Itoh, K. Doi, J. Morishita, K. Ueda, and A. Ohtsuka, "A simple method for determining the modulation transfer function in digital radiography," *IEEE Trans. Med. Imaging*, vol. 11, no. 1, pp. 34–39, 1992.

[157] K. Pearson, "Note on Regression and Inheritance in the Case of Two Parents," *Proc. R. Soc. London*, vol. 58, no. 58, pp. 240–242, 1895.

[158] X. Dong, T. Niu, X. Jia, and L. Zhu, "Relationship between x-ray illumination field size and flat field intensity and its impacts on x-ray imaging," *Med Phys*, vol. 39, no. 10, pp. 5901–5909, 2012.

[159] E. S. M. Ali and D. W. O. Rogers, "Quantifying the effect of off-focal radiation on the output of kilovoltage x-ray systems," *Med. Phys.*, vol. 35, no. 9, p. 4149, 2008.

[160] NHLBI, "What Is a Heart Attack?," 2014. [Online]. Available: https://www.nhlbi.nih.gov/health/health-topics/topics/heartattack.

[161] D. E. Bild, G. Burke, D. Ph, A. R. Folsom, K. Liu, S. Shea, M. Szklo, D. A. Bluemke, D. H. O. Leary, R. Tracy, K. Watson, N. D. Wong, and R. A. Kronmal, "Coronary Calcium as a Predictor of Coronary Events in Four Racial or Ethnic Groups," *N. Engl. J. Med.*, pp. 1336–1346, 2008.

[162] S. Achenbach and P. Raggi, "Imaging of coronary atherosclerosis by computed tomography," *Eur. Heart J.*, vol. 31, no. 12, pp. 1442–1448, 2010.

[163] S. Motoyama, T. Kondo, M. Sarai, A. Sugiura, H. Harigaya, T. Sato, K. Inoue, M. Okumura, J. Ishii, H. Anno, R. Virmani, Y. Ozaki, H. Hishida, and J. Narula, "Multislice computed tomographic characteristics of coronary lesions in acute coronary syndromes.," *J. Am. Coll. Cardiol.*, vol. 50, no. 4, pp. 319–26, Jul. 2007.

[164] A. J. Einstein, "Estimating Risk of Cancer Associated With Radiation Exposure From 64-Slice Computed Tomography Coronary Angiography," *Yearb. Diagnostic Radiol.*, vol. 2008, no. 3, pp. 155–156, 2008.

[165] J. a Rumberger, B. H. Brundage, D. J. Rader, and G. Kondos, "Electron beam computed tomographic coronary calcium scanning: a review and guidelines for use in asymptomatic persons.," *Mayo Clin. Proc.*, vol. 74, no. 3, pp. 243–252, 1999.

[166] M. Mahesh, S. L. Zimmerman, and E. K. Fishman, "Radiation dose shift in relative proportion: the case of coronary artery calcium studies.," *J. Am. Coll. Radiol.*, vol. 11, no. 6, pp. 634–5, Jun. 2014.

[167] A. A. Johnsson, J. Vikgren, and M. Bath, "Chest tomosynthesis: technical and clinical perspectives.," *Semin. Respir. Crit. Care Med.*, vol. 35, no. 1, pp. 17–26, Feb. 2014.

[168] Y. Zhong, C.-J. Lai, T. Wang, and C. C. Shaw, “A dual-view digital tomosynthesis imaging technique for improved chest imaging,” *Med. Phys.*, vol. 42, no. 9, pp. 5238–5251, Sep. 2015.

[169] S. Dippel, M. Stahl, R. Wiemker, and T. Blaffert, “Multiscale contrast enhancement for radiographies: Laplacian Pyramid versus fast wavelet transform.,” *IEEE Trans. Med. Imaging*, vol. 21, no. 4, pp. 343–53, Apr. 2002.

[170] J. Zheng, S. S. Saquib, K. Sauer, and C. a. Bouman, “Parallelizable Bayesian tomography algorithms with rapid, guaranteed convergence,” *IEEE Trans. Image Process.*, vol. 9, no. 10, pp. 1745–1759, 2000.

[171] J. Webster Stayman and J. a. Fessler, “Regularization for uniform spatial resolution properties in penalized-likelihood image reconstruction,” *IEEE Trans. Med. Imaging*, vol. 19, no. 6, pp. 601–615, 2000.

[172] Y. Lu, H.-P. Chan, J. Wei, and L. M. Hadjiiski, “Selective-diffusion regularization for enhancement of microcalcifications in digital breast tomosynthesis reconstruction,” *Med. Phys.*, vol. 37, no. 11, p. 6003, 2010.

[173] S. Abdurahman, A. Jerebko, and T. Mertelmeier, “Out-of-plane artifact reduction in tomosynthesis based on regression modeling and outlier detection,” *Breast Imaging*, pp. 729–736, 2012.

[174] J. Ge, H.-P. Chan, B. Sahiner, Y. Zhang, J. Wei, L. M. Hadjiiski, C. Zhou, Y.-T. Wu, and J. Shi, “Digital tomosynthesis mammography: Improvement of artifact reduction method for high-attenuation objects on reconstructed slices,” *Proc. SPIE*, vol. 6913, p. 69134O, Mar. 2008.

[175] Z. Zhang, M. Yan, K. Tao, and X. Xuan, “Metal Artifacts Reduction for Tomosynthesis,” pp. 513–516, 2014.

[176] A. Wong, A. Mishra, D. A. Clausi, and P. Fieguth, “Mammogram Image Superresolution Based on Statistical Moment Analysis,” *Comput. Robot Vis. (CRV), 2010 Can. Conf.*, pp. 339–346, 2010.

[177] S. T. Kim, D. H. Kim, and Y. M. Ro, “Generation of conspicuity-improved synthetic image from digital breast tomosynthesis,” *Digit. Signal Process. (DSP), 2014 19th Int. Conf.*, no. August, pp. 395–399, 2014.

[178] S. T. Kim, D. H. Kim, and Y. M. Ro, “Combination of conspicuity improved synthetic mammograms and digital breast tomosynthesis: a promising approach for mass detection,” vol. 9414, p. 941419, 2015.

[179] H. Homann, F. Bergner, and K. Erhard, “Computation of synthetic mammograms with an edge-weighting algorithm,” *SPIE Med. Imaging*, vol. 9412, p. 94121Q, 2015.

[180] S.-C. Huang, F.-C. Cheng, and Y.-S. Chiu, “Efficient contrast enhancement using adaptive

gamma correction with weighting distribution.," *IEEE Trans. Image Process.*, vol. 22, no. 3, pp. 1032–41, Mar. 2013.

[181] M. Prokop, U. Neitzel, and C. Schaefer-Prokop, "Principles of image processing in digital chest radiography.," *J. Thorac. Imaging*, vol. 18, pp. 148–164, 2003.

[182] A. Mencattini, M. Salmeri, R. Lojacono, M. Frigerio, and F. Caselli, "Mammographic images enhancement and denoising for breast cancer detection using dyadic wavelet processing," *IEEE Trans. Instrum. Meas.*, vol. 57, no. 7, pp. 1422–1430, 2008.

[183] S. Wu, Q. Zhu, Y. Yang, and Y. Xie, "Feature and contrast enhancement of mammographic image based on multiscale analysis and morphology," *2013 IEEE Int. Conf. Inf. Autom. ICIA 2013*, vol. 2013, pp. 521–526, 2013.